Journal of Contemporary
Water Research & Education

Issue 160
April 2017



The Importance of Scientific Publishing: Teaching an Undergraduate How to Swim the Entire Length of the Pool

UCOWR
UNIVERSITIES COUNCIL ON WATER RESOURCES

A publication of the Universities Council on Water Resources with support from Southern Illinois University Carbondale

JOURNAL OF CONTEMPORARY WATER RESEARCH & EDUCATION

Universities Council on Water Resources
1231 Lincoln Drive, Mail Code 4526
Southern Illinois University
Carbondale, IL 62901
Telephone: (618) 536-7571
www.ucowr.org

CO-EDITORS

Karl W. J. Williard
Southern Illinois University
Carbondale, Illinois 62901
williard@siu.edu

Jackie F. Crim
Southern Illinois University
Carbondale, Illinois 62901
crimjac@siu.edu

ISSUE EDITOR

Garey A. Fox
Biological and Agricultural Engineering
North Carolina State University
Raleigh, North Carolina 27695
garey_fox@ncsu.edu

ASSOCIATE EDITORS

Kofi Akamani
Policy and Human Dimensions
Southern Illinois University
k.akamani@siu.edu

Natalie Carroll
Education
Purdue University
ncarroll@purdue.edu

James Heaney
Water Use and Efficiency
University of Florida
heaney@ufl.edu

M.S. Srinivasan
Hydrology
National Institute of Water and
Atmospheric Research, New Zealand
MS.Srinivasan@niwa.co.nz

Kevin Wagner
Water Quality and Watershed Management
Texas A&M University
klwagner@ag.tamu.edu

Jonathan Yoder
Natural Resource Economics
Washington State University
yoder@wsu.edu

TECHNICAL EDITORS

Elaine Groninger
Southern Illinois University
Carbondale, Illinois 62901
egroninger@siu.edu

Shelly Williard
Southern Illinois University
Carbondale, Illinois 62901
swilliard@siu.edu

ISSN 1936-7031

Cover photos: Top Left: *Undergraduate Darya Anderson testing microbial carbon utilization in Arctic wetland samples*, Credit: Darya Anderson; Top Right: *Anna Vincent walking alongside Pratt Beach study site in Chicago, IL in October 2015*, Credit: Veronica Lourich; Bottom Left: *Auburn University students exhibiting at the 2016 National Sustainable Design Expo*, Credit: Paul Gray; Bottom Right: *Amy Schmidt presenting her undergraduate research at a poster session*, Credit: Lynne Lewis.
Back cover & inside back cover photos: Courtesy of Colorado State University

Subscription Information: The *Journal of Contemporary Water Research & Education* is published by the Universities Council on Water Resources. The annual subscription rate is $60 (domestic) and $100 (international). Prices per copy for past issues are $20 (domestic) and $40 (international). Members of UCOWR receive access to the *Journal of Contemporary Water Research & Education* as a part of their membership.

UCOWR is not responsible for the statements and opinions expressed by authors of articles in the *Journal of Contemporary Water Research & Education.*

Journal of Contemporary Water Research & Education

Issue No. 160 **April 2017**

The Importance of Scientific Publishing: Teaching an Undergraduate How to Swim the Entire Length of the Pool

The Importance of Scientific Publishing: Teaching an Undergraduate How to Swim the Entire Length of the Pool
Garey A. Fox, Emma L. Kuster, and Amanda K. Fox 1

The Cost of Stability: Consumption-Based Fixed Rate Billing for Water Utilities
Amy Schmidt and Lynne Lewis 5

Assessing Models of Arsenic Occurrence in Drinking Water from Bedrock Aquifers in New Hampshire
Caroline M. Andy, Maria Florencia Fahnestock, Melissa A. Lombard, Laura Hayes, Julia G. Bryce, and Joseph D. Ayotte 25

Searching for Antibiotic Resistance Genes in a Pristine Arctic Wetland
Krystalle S. Diaz, Virginia I. Rich, Jean E. McLain 42

Assessing Biomineral Formation by Iron-oxidizing Bacteria in a Circumneutral Creek
Nohemi Almaraz, Andrew H. Whitaker, Megan Y. Andrews, and Owen W. Duckworth 60

Anthropogenic Litter Abundance and Accumulation Rates Point to Seasonal Litter Sources on a Great Lakes Beach
Anna E.S. Vincent and Timothy J. Hoellein 72

A Method for Assessing Shoreline Stability of Alpine Lake, West Virginia
Carolina Rando, Leslie Hopkinson, Melissa O'Neal, and Jason Fillhart 85

Reduced Phytoplankton and Zooplankton Diversity Associated with Increased Cyanobacteria in Lake Champlain, USA
Katelyn A. Bockwoldt, Emily R. Nodine, Timothy B. Mihuc, Angela D. Shambaugh, and Jason D. Stockwell 100

Erodibility Parameters Derived from Jet and Flume Erosion Tests on Root-Permeated Soils
Bailey McNichol, Kayla Kassa, Garey Fox, Ron Miller, and Lucie Guertault 119

2D-Fe_3O_4 Nanosheets for Effective Arsenic Removal
Hongxi Luo, Fangwei Cheng, Weiming Hu, Jinpeng Wang, Shuting Xiang, and Maria Fidalgo de Cortalezzi 132

Design and Manufacturing of High Surface Area 3D-Printed Media for Moving Bed Bioreactors for Wastewater Treatment
Olivia Elliott, Stephanie Gray, Michael McClay, Bakr Nassief, Ann Nunnelley, Eric Vogt, Joseph Ekong, Kamran Kardel, Ali Khoshkhoo, Gabriel Proaño, David M. Blersch, and Andres L. Carrano 144

Universities Council on Water Resources
Journal of Contemporary Water Research & Education
Issue 160, Pages 1-4, April 2017

The Importance of Scientific Publishing: Teaching an Undergraduate How to Swim the Entire Length of the Pool

*Garey A. Fox[1], Emma L. Kuster[2], and Amanda K. Fox[3]

[1]*Professor and Department Head, North Carolina State University*
[2]*Program Coordinator, South Central Climate Science Center*
[3]*Mathematics Instructor and Researcher*
**Corresponding Author*

A number of programs are currently available to support undergraduate water research. For example, many academic institutions across the United States offer undergraduate research scholars' programs. The National Institutes for Water Resources (NIWR) helps the U.S. Geological Survey (USGS) meet the nation's water needs by "…transferring the latest tools and knowledge to water professionals around the country, training the next generation of water scientists, and tackling emerging water issues in collaboration with USGS scientists." Numerous projects funded by USGS and NIWR support undergraduate research assistants throughout the states and territories of the United States. The National Science Foundation (NSF) has invested significant resources into their Research Experience for Undergraduates (REU) programs across its directorates, providing key opportunities for undergraduates to participate in summer research experiences during a six- to ten-week period. The United States Department of Agriculture National Institute of Food and Agriculture (USDA NIFA) also funds undergraduate fellowship programs in key challenge areas. Furthermore, the U.S. Environmental Protection Agency (EPA) sponsors a People, Prosperity, and the Planet (P3) Student Design Competition.

Many assume that undergraduate research projects are not capable of generating enough high quality information to publish in peer-reviewed journals. Often undergraduates are simply acknowledged or less frequently added as lower order co-authors on papers to which they contributed. The students are often not engaged through the complete publication process. Unfortunately, this limits undergraduate students' opportunities for understanding the entire research paradigm and properly framing their contribution within existing scientific literature, until they get into graduate school. A graduate thesis is often the first major publication for a student.

Russell et al. (2007) noted that when undergraduates participate in research they increase their understanding of how to conduct research, their confidence in their research skills, and their awareness of what graduate school might be like. Linn et al. (2015) provided an in-depth review of undergraduate research opportunities, noting that past studies consistently document how students appreciate undergraduate research opportunities. However, they point out that very few studies are able to explicitly measure a student's understanding of the scientific practice or science concepts. They state that "…less than 10% of the studies validate self-reports with analysis of research products" such as presentations, reports, or publications. Having a goal to publish undergraduate research will more explicitly and thoroughly train an undergraduate to understand the scientific process, better prepare them for graduate studies, and more effectively assess undergraduate research programs.

Outlets for Publishing Undergraduate Research

While funding does not appear to be an impediment for engaging undergraduate students in water research projects, many students never reach the publication stage. The lack of an avenue to publish this undergraduate research is a primary reason for the limited publishing. Many states and even specific universities have undergraduate research journals that typically publish articles without copyright, but their success varies based on institutional support and the dedication of a few motivated individuals. Such journals struggle with finding adequate editors and reviewers for papers, and also struggle to support published researchers because of limited readership. More opportunities should be provided by key journals in water science and engineering to foster the publication of undergraduate research, and the authors applaud the *Journal of Contemporary Water Research and Education* for providing an avenue to demonstrate the ability of undergraduate students working in the multidisciplinary fields of water resources across the United States. As evidenced by the publications in this special issue, undergraduate students, when properly mentored, can contribute significantly to the peer-reviewed literature.

Key Strategies for Promoting Undergraduate Publishing

While the setup of undergraduate research programs can vary, an undergraduate student is typically paired with a faculty mentor to work as part of their research team, along with graduate students and postdoctoral scholars. The time frame of such experiences can be an impediment to generating enough research data or navigating through the entire research process to produce a peer-reviewed journal article. Several strategies exist to alleviate this roadblock. Of course, these strategies start with a highly motivated undergraduate student and a faculty mentor who understands the value of publishing for the student's career. The articles in this special issue of the *Journal of Contemporary Water Research and Education* serve as illustrative examples of the power of motivation and challenge the assumption that programs such as the NSF REUs are not long enough to produce high quality, publishable research.

Many undergraduate students are simply dedicated and substantially mentored and advised to publish their research even after completing short-term research experiences. For example, *Schmidt and Lewis* explored the use of consumption-based fixed rate pricing models to balance revenue stability versus conservation during times of water scarcity. They applied the pricing models to two case studies with data from Lomita, CA and Longmont, CO. *Andy et al.* evaluated the ability of multivariate logistic regression models to correctly estimate the probability of groundwater arsenic concentrations from bedrock drinking water wells in New Hampshire. The study specifically investigated three arsenic concentration thresholds (1, 5, and 10 μg/L). They also investigated the benefit of including additional variables in the models such as well type and casing length. They reported that the original multivariate logistic regression models performed well in identifying local spatial variability in arsenic concentrations. Another example is *Diaz et al.,* in which the researchers compared three distinct metagenomics-based methods for assessing the presence of antibiotic resistance genes along a permafrost thaw gradient in Abisko, Sweden. Funded by the Department of Energy, the goal was also to enhance our understanding of the presence of antibiotic resistance genes in natural environments. Finally, *Almarez et al.* describes research from a ten-week NSF REU focused on elucidating how water chemistry and iron oxidizing bacteria affect the formation of iron oxides in creeks with circumneutral pH. This research impacts our understanding of iron biogeochemical cycling. While the ten-week REU focused on data collection and analysis, a motivated undergraduate pushed the work through the publication process because of the opportunity to publish in this special issue focused on undergraduate research.

So what are potential strategies gleaned from these special issue publications that go beyond simply the requirement of a motivated undergraduate and mentor? First, design the research such that it builds upon a solid foundation

of previous work and creates an opportunity to collect significant data in an undergraduate research program. Publishing is an easier path for students with opportunities to work in laboratories funded through consecutive undergraduate scholars' programs. Previous studies specifically note that one key to successful undergraduate research is sustained as opposed to intermittent participation in research experiences (Thiry et al. 2012; Linn et al. 2015). The publication by *Vincent and Hoellein* is a prime example of this approach in which the undergraduate student worked with a faculty member for two and half years. They studied anthropogenic litter accumulation at a Lake Michigan beach in Chicago, IL, concluding that the fall season had higher accumulation rates and that infrequent sampling will underestimate total anthropogenic litter abundance.

Another option to ensure longer-term involvement is to extend the research experience by offering course credit through a research methods class or extend the research into a senior thesis or capstone project. An example of this model resulted in the publication by *Rando et al.* that focused on rapid stability assessments of lake shorelines to prioritize management. The rapid assessments include a number of metrics including shoreline bank height, bank angle, armoring, wind direction, and unconsolidated materials. Measured erosion rates generally corresponded well with the rapid assessment tool to identify locations at risk for instability and determine the most important attributes of management efforts. Similarly, the publication by *Bockwoldt et al.* was an example of sustained effort through both an initial NSF REU but also incorporating the REU research into a senior thesis at the undergraduate's home institution. The authors studied the relationship between zooplankton diversity and cyanobacteria in Lake Champlain. Cyanobacteria density was negatively correlated with phytoplankton richness, which was positively correlated with zooplankton diversity. The research concluded that cyanobacteria could directly affect zooplankton diversity and indirectly affect fish diversity.

Another strategy is to ensure that multiple summer projects overlap and/or build upon each other with co-authorship shared by multiple students. An example is the publication by *McNichol et al.* which combined undergraduate research projects from two years of a summer NSF REU. The two students worked on similar topics conducting jet erosion tests (JETs) to quantify the erodibility of root-permeated soils but in completely different summer REU sessions. The projects built upon each other by validating the JETs compared to the more traditional flume experiments and comparing soil erodibility derived from JETs in the field. While the students finished their specific parts of the NSF REU during their own ten-week experience, they remained engaged in the research process by continuing to work as a group to determine how to merge their work, review drafts of the manuscript, respond to reviewers' comments, and review the proof of the accepted manuscript.

In *Luo et al.*, the undergraduate student shared the project with two other students in order to complete the research. These authors investigated the use of nanosheets for arsenic removal with efficiencies that approached 94% at optimal pH. Similarly, two teams of undergraduates were merged to tackle aspects of the *Elliot et al.* project funded through the US EPA P3 student design competition. They used 3D printing to design and fabricate complex media designs (spherical gyroid) for biofilters. The manufacturing and post processing of hundreds of gyroid media units required a large and committed team of undergraduate students. Their work attempted to maximize specific surface area while also providing flow refugia where biofilms were protected from fluid shear stress. The research demonstrated that 3D printing can be used for media fabrication and optimization by creating unique flow pathways through the biofilter.

Once again, we applaud the *Journal of Contemporary Water Research and Education* for providing this opportunity to undergraduate students. We hope that mentors in academia, industry, and government will share this special issue with their students to demonstrate the potential of publishing their work in this and other peer-reviewed journals.

Acknowledgements

The authors acknowledge funding from the National Science Foundation through a Research Experience for

Undergraduates (REU) Site grant (EAR1358908) titled "REU Site: Evaluating the Effectiveness of Stream Restoration Projects Based on Natural Channel Design Concepts Using Process-Based Investigations."

Author Bio and Contact Information

Garey Fox, Ph.D., P.E., D.WRE is a Professor and Department Head in Biological and Agricultural Engineering at North Carolina State University. He joined North Carolina State University in January 2017 after 10 years on the faculty at Oklahoma State University, including three years as the Director and Berry Endowed Professor of the Oklahoma Water Resources Center. From 2015-2017, he served as a principal investigator (PI) on a NSF REU grant (EAR1358908). His research program focuses on surface water and groundwater interactions in influencing streamflow, sediment detachment and transport, and nutrient and pesticide transport in alluvial floodplains. He has received numerous university, state, and national teaching and research awards. He can be contacted by email at garey_fox@ncsu.edu.

Emma Kuster, M.A., is the Program Coordinator for the South Central Climate Science Center at the University of Oklahoma. She joined the South Central Climate Science Center in February 2017 after serving as the Program Coordinator for the Oklahoma NSF Experimental Program to Stimulate Competitive Research program at Oklahoma State University. She has a Master of Arts degree in Geography and a Bachelor of Science degree in Meteorology, both from the University of Oklahoma.

Amanda K. Fox, M.S., is an independent mathematics instructor and researcher in Cary, North Carolina. She has a Bachelor of Science degree in Mathematics and a Master of Science degree in Meteorology from Texas A&M University. She also has a Master of Science degree in Atmospheric Sciences from Colorado State University.

References

Linn, M.C., E. Palmer, A. Baranger, E. Gerard, and E. Stone. 2015. Undergraduate research experiences: Impacts and opportunities. *Science* 347: 1261757. DOI:10.1126/science.1261757. Accessed March 14, 2017.

Russell, S.H., M.P. Hancock, and J. McCullough. 2007. Benefits of undergraduate research experiences. *Science* 316: 548-549. DOI:10.1126/science.1140384. Accessed March 14, 2017.

Thiry, H., J. Weston, S. Laursen, and A.B. Hunter. 2012. The benefits of multi-year research experiences: Differences in novice and experienced students' reported gains from undergraduate research. *CBE Life Sciences Education* 11: 260-272. DOI:10.1187/cbe.11-11-0098: pmid: 22949423. Accessed March 14, 2017.

Universities Council on Water Resources
Journal of Contemporary Water Research & Education
Issue 160, Pages 5-24, April 2017

The Cost of Stability: Consumption-Based Fixed Rate Billing for Water Utilities

Amy Schmidt[1] and *Lynne Lewis[1]

[1]*Bates College, Lewiston, ME, USA*
**Corresponding author*

Abstract: Municipal water utilities in the United States face the challenge of balancing the potentially conflicting goals of sending signals about water scarcity and maintaining revenue stability. Times of extreme shortage such as the current extended drought in California seriously challenge and can jeopardize this delicate balance. Mandatory or voluntary conservation strategies can be detrimental to revenue stability. This study explores the ability of the Consumption-Based Fixed Rates (CBFR) pricing method to solve this dual dilemma of scarcity pricing and revenue stability in both normal times and times of drought. CBFR proposes using a proportional consumer pricing system directly based on utility supply costs. We utilize utility-side cost data from Lomita, CA and Longmont, CO, to estimate how consumer prices change under the CBFR method. Using simulations comparing current pricing mechanisms with the CBFR, we find that the latter solves the revenue problem, but creates greater problems with equity and scarcity versus the former. A modified structure of CBFR, with prices based partially on household income, seems to alleviate some of these problems and could prove to be a useful tool during times of drought.

Keywords: *municipal water pricing, revenue stability, water scarcity, Southwestern United States*

The United States depends heavily upon public infrastructure for its water supply; 83% of Americans rely on publicly owned, large-scale water utilities to supply them with potable water and treat their wastewater (Rahill-Marrier and Lall 2013). While American customers pay some of the lowest water rates among developed nations (Mehan and Kline 2012), the country's water infrastructure faces an annual 11 billion dollar deficit to replace aging facilities and bring water supply quality up to code with environmental health regulations (Rahill-Marier and Lall 2013).

While water providers face huge fixed costs to maintain and upgrade infrastructure, revenues depend largely upon variable factors. Fixed costs stay the same or increase year-to-year, but revenues fluctuate with water consumption, which varies based on changes in demand due to population growth, economic activity, and weather patterns.

Steady, reliable decreases in consumption due to better water conservation measures or other factors also pose problems for water utilities. As costs remain largely the same, water utilities may choose to raise their water prices to bring in necessary revenue. However, consumers may view increased prices as a "punishment" for their reduced consumption. Higher prices could also usher in more conservation, leaving the utility facing the same revenue shortfall it sought to avoid. Times of extreme drought provide an example of this scenario; during California's 2007-2009 drought, the Los Angeles Department of Water and Power faced a $70 million revenue shortfall as water consumption plunged 30% (Sedlak 2015). From a resource allocation perspective, it is tempting to think that perhaps a different pricing system could have prevented such a dire financial outcome.

One solution to the revenue stability problem is proposed by Spang et al. (2015). They introduce the theory of "consumption-based fixed rates" (CBFR), a pricing system following the supply-side pricing reform concept. In the CBFR system,

bills are calculated from the utility's costs, with customers paying a flat rate for fixed costs and a proportional rate for more variable costs. By calculating bills using overall system costs, the utility ensures stable, sufficient revenue regardless of the absolute level of water consumption.

This paper tests a water utility pricing model proposed by Spang et al. (2015) for consumption-based fixed rates as a means of pricing water to reflect scarcity and maintain equity for two cities (one in California and one in Colorado). We run simulations to evaluate the impacts of this technique with utility data in Longmont, Colorado and Lomita, California. We compare changes in billing rates for CBFR to the current pricing mechanism and examine the resulting impacts on consumer affordability, equity across different income groups, and the sensitivity of billing rates to changes in system costs or aggregate consumption. With the current severe drought in the state of California, managing water scarcity has become a top priority for water utilities across water scarce regions of the United States. Governor Jerry Brown's mandate for substantial reductions in water use by all California consumers (California State Water Board Emergency Regulations, Article 22.5, adopted Feb. 11, 2016) will likely have major, and as of yet unknown, impacts on water providers across the state.

Natural Monopoly and the Revenue "Catch-22"

Natural monopoly arises when the cost of supplying the market for a good is lower when all production comes from one firm, versus two or more firms splitting market production. In the case of a water utility, this structure holds true due to the high upfront costs of water service infrastructure, and, once a system is established, the relatively low cost of supplying additional units of water.

Shaked and Sutton (1987) propose that demand-side characteristics, in addition to industry cost structures, can also influence the establishment of a natural monopoly. In the case of a water utility, this type of "demand pull," as they term it, motivates the firm to incur more costs in order to expand system capacity, particularly peak capacity. This type of expansion can be modeled as a marginal capacity cost, or a 'jump' along the marginal cost curve, as the utility extends system capacity to accommodate an additional unit of consumption (Mann et al. 1979). Figure 1 provides an example of such a scenario, where average per unit cost is falling for all sources, but average cost overall is slowly rising as the upfront costs of bringing on a new supply source are incurred.

Due to the relative inflexibility in setting prices, in conjunction with the high fixed-cost nature of the market, water utilities are vulnerable to high revenue instability. Of particular interest for this study is the case of fluctuating consumption without price adjustments, which can lead to revenue out of alignment with costs. In other words, if decreases in consumption without pricing adjustments yield insufficient revenue to cover operating costs, is CBFR a possible solution? We test this question in this paper.

From a long-term perspective, a utility operating under conditions of severe drought, even with demand-side conservation efforts, likely faces an upward shift of its costs; the available yield for each water source falls below the expected value, and getting enough total water to meet demand thus becomes more expensive (Figure 2).

While this model remains theoretical, Tampa, Florida (Tampa Bay Water. Water Supply. http://www.tampabaywater.org/tampa-bay-seawater-desalination-plant.aspx), and Santa Barbara, California (City of Santa Barbara. Desalinization. http://www.santabarbaraca.gov/gov/depts/pw/resources/system/sources/desalination.asp), offer examples of utilities facing huge cost increases during drought by building large desalinization plants. For both utilities, desalinization became an economically viable option as the cost of securing water from other means increased. Costs increased over periods of drought even with lower consumption, because existing projects provided water levels severely below their predicted average yield. Thus, costs rose from both a "spike" in procurement costs for existing sources and the need to expand into new sources. Under these circumstances, falling consumption -- without billing adjustments sufficient to reflect the new costs -- could lead to a revenue shortage for the water utility. Figure 2 models this type of situation. As typical supply levels fall for all water

sources during a drought, the cost of extracting the necessary water volume from each source rises. If current sources cannot meet demand, new sources may be brought online which are then unnecessary in non-drought conditions.

If consumption decreases in response to drought-related conservation efforts/education, but only occurs during a drought-cycle, utilities would want to model long-term marginal costs along the same curve as before the reductions to get an accurate sense of what projects they will need to maintain or add, and when. In this case, a utility could develop one billing structure for normal periods (D_0) and one for drought periods (D').

By contrast, persistent changes in demand seem likely after extended periods of conservation, as consumers make long-term water-saving investments such as low-flow fixtures and xeriscaping. Additionally, new social norms and conservation habits (such as shorter showers) formed over the drought period could remain beyond the drought (Gregory and Di Leo 2003). If consumption cuts back sharply (D') and remains at that level, the utility faces a new cost structure where fewer procurement sources are needed. Permanent, severe declines could leave the utility with unnecessary infrastructure (reservoirs, water pipes, etc.) that can be phased out over time, leading to lower costs. Figure 3 shows that when drought-induced practices persist, fewer water sources may be necessary to meet average demand at all times. Thus, taking the sources necessary before drought-induced conservation offline could reduce utility costs.

Previous Literature

While an extensive amount of literature exists on the topic of water pricing mechanisms, the literature on water utility revenue instability--resulting from the industry's natural monopoly structure--gained traction in the late 1980s and early 1990s. Early papers, such as Chesnutt et al. (1996), explore the implications of revenue instability through reduced consumption and offer potential solutions. These proposals remain exogenous to actual water pricing systems; they do not consider the overall disconnect between the water utility's sources of cost and sources of

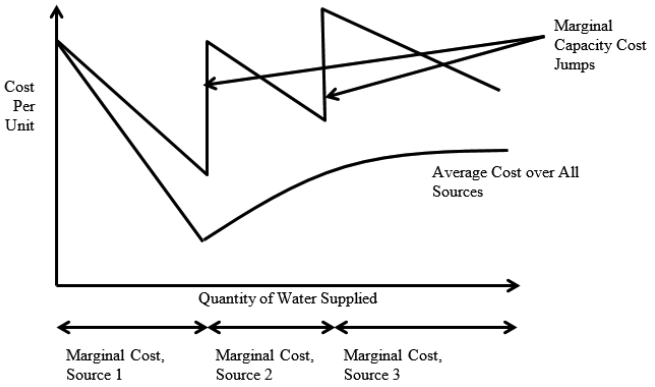

Figure 1. Theoretical model of a water utility cost structure (adapted from Hanemann 1998).

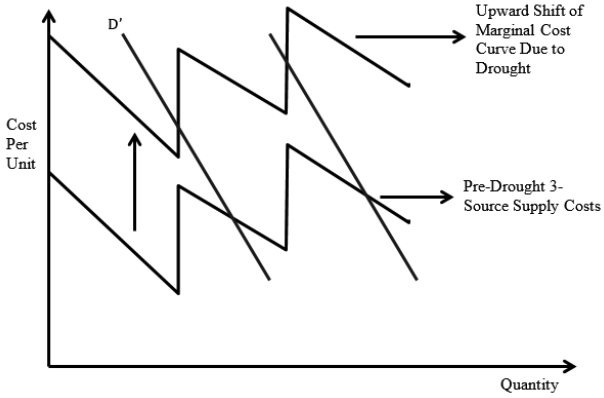

Figure 2. Utility supply costs under drought conditions. D_0 = demand under normal conditions. D' = demand during conservation period.

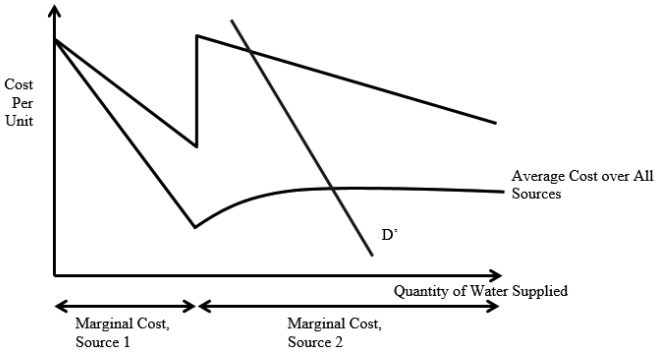

Figure 3. Post-drought cost planning, permanent consumption reduction. D' = new, lower demand (permanent reduction).

revenue. More recently, there has been an increase in both case studies and theoretical models of water pricing explicitly concerned with revenue stability via billing reform (Hoag and McKinley 2012; Rahill-Marier and Lall 2013; Schoengold and Zilberman 2014, for example).

Hoag and McKinley (2012), citing fears of inequality as a result of raising rates or fixed costs across the board, argue that the best option lies with a steeply increasing block price (IBR), as it conveys scarcity and encourages conservation. While this system provides more stability than a flat rate and more equality than indiscriminate rate hikes, IBR systems often do not fully incorporate system costs into a form of guaranteed revenue. Schoengold and Zilberman (2014) use a theoretical simulation to evaluate IBR pricing under different cost and scarcity conditions, in terms of both economic efficiency and social equity/affordability. The authors find that, in general, lower equity results in cases where the optimal minimum household price level lies above the maximum price that guarantees stable revenue without profits. Schoengold and Zilberman (2014) also find that pricing water with an IBR to ensure proper revenue requires adjusting rates frequently to account for changes in population, consumption level, supply sources, and technology. The CBFR system, by contrast, only requires that the utility have knowledge of its own cost structure to set prices.

Rahill-Marier and Lall (2013) and Olmstead et al. (2007) summarize some of the extensive literature on water pricing. Rahill-Marier and Lall (2013) analyze historical data from 190 water utilities within the United States. They find that, overall, water utilities where the primary water sources are from groundwater have the lowest average cost of supply, followed by surface water, a mix of the two, and utilities which rely on water purchases. This variation in costs provides context to understand what types of utilities might benefit most from a new form of consumer pricing such as CBFR.

Olmstead et al. (2007) analyze North American water consumption data for single-family households to measure price-elasticity of water demand under different pricing structures. Using a regression model for utility-maximizing households subject to a budget constraint, they find that price elasticity varies among different pricing mechanisms. However, they caution that these findings may result from either supply-side pricing decisions or demand-side responses to such prices. Olmstead and Stavins (2008) compare different price versus non-price mechanisms for water conservation in terms of equity and efficiency. While price-based mechanisms lead in efficiency, equity impacts remain highly dependent on design features for the program. Of particular concern, they mention that price elasticity is higher for low-income households; increases in price seem to result in greater consumption reductions among low-income users versus other groups. As a result, decreases in usage could come from low-use households who typically only consume to meet basic needs, versus those who consume water for luxury uses.

Renzetti et al. (2015) support these findings and show that price increases disproportionately affect low-income households (i.e., they pay a higher percentage of their income than other households). They hypothesize, for example, that the price increases will negatively affect equity of consumption; their results seem to support this hypothesis. These problems also arise with the Consumption-Based Fixed Rate model (Spang et. al. 2015), where the final impact on costs and equity depends upon the respective magnitudes of these two effects.

In the wake of the ongoing California drought, recent studies are evaluating California communities employing non-traditional water pricing structures. Barr and Ash (2015) focus on the Western Municipal Water District (WMWD) in the semi-desert inlands of Southern California. To solve problems with falling revenue despite the need for even greater conservation, the district adopted a "water budget" style of billing, where an efficient water amount for various activities (showering, cooking, cleaning, watering, etc.) is calculated for each customer based on household characteristics (number of occupants, ages, yard size, etc.), and steep charges are imposed for levels above one's "budget." The system has been successful in maintaining revenue, and receives high levels of customer satisfaction. However, potential problems with this system exist that are likely avoidable under the CBFR system. When

prices are based on a unique customer profile, high levels of tenant turnover would make it difficult to keep up with the changes in data required to calculate new water budgets. In the CBFR system, the only information required about the customer is the consumption level; such data are often already recorded. The CBFR system also does not directly limit how much water each customer may consume and may not have large impacts on household consumption patterns, considering that water tends to be a price inelastic resource (Klaiber et al. 2012).

While many articles raise concerns over water revenue stability, few propose any substantive customer price changes to help ensure the proportions of fixed versus variable charges more closely reflect the high fixed-cost nature of the water utility industry. The Consumption-Based Fixed Rates model by Spang et al. (2015) provides an explicit formula to align cost and revenue composition; this formulation will be tested on two utilities' operating costs, demand levels, and customer characteristics. In this paper, we test the Spang et al. (2015) pricing method with utility data from Longmont, Colorado and Lomita, California.

Consumption-Based Fixed Rates: Theoretical Background from Spang et al. (2015)

Spang et al. (2015) proposes a CBFR method designed to ensure appropriate utility revenue regardless of system use. The CBFR system distributes fixed costs faced by the utility across all users, such that the sum of all consumer bills yields revenue sufficient to cover operating costs (Equation 1).

$$\sum_{s_1}^{s_n} s_n C = C \qquad \text{(Equation 1)}$$

where s_n = consumer i's billing proportion and C = utility operating costs.

This relationship created by the structure of the billing calculations for each customer for each cost category (Table 1) is shown in Equations 2-4:

Fixed-Fixed Costs:

$$i\text{th customer's bill} = \frac{FF\ Costs}{X};$$

$$\left(\frac{FF\ Costs}{X}\right) * X = FF\ Costs \qquad \text{(Equation 2)}$$

Fixed-Fixed Costs:

$$i\text{th customer's bill} = FV\ Costs * \frac{A_n}{W};$$

$$\sum_{A_1}^{A_n} FV\ Costs * \frac{A_n}{W} = FV\ Costs \qquad \text{(Equation 3)}$$

Variable Costs:

$$i\text{th customer's bill} = V\ Costs * \frac{A_n}{W};$$

$$\sum_{A_1}^{A_n} V\ Costs * \frac{A_n}{W} = V\ Costs \qquad \text{(Equation 4)}$$

where X = Total Number of Utility Customers, A_n = Customer i's Consumption, and W = Total System Consumption.

Regardless of system demand, bills calculated for period *a* will always recoup the costs for period *a*. Thus, the bill sent at the start of time *a+1* will represent period *a* costs, with bills sent out at *a+2* representing *a+1* costs, etc. Periodically determining billing prices provides stable revenue to the utility and an up-to-date pricing signal for consumers. Further, it provides a community-level incentive to conserve, as any reductions in usage are realized in lower prices almost immediately.

Two Case Studies: Lomita, California and Longmont, Colorado

We present four simulations for two case studies in the West/Southwest United States. Simulation one utilizes the cost data for each utility to model

Table 1. Cost definitions and categorization.

Fixed-Fixed Costs: Constant regardless of system use	Compliance costs, safety checks, office personnel, treatment plant energy use, etc.
Fixed-Variable Costs: Exist regardless of system use, but change in magnitude based on system demand	Piping infrastructure, chemicals, repairs and maintenance, etc.
Variable Costs: Depend directly upon consumption levels	Water purchases, energy for water pumping, etc.

consumer prices in both Lomita, CA and Longmont, CO under the CBFR system. Simulation two experiments with different adjustments to the CBFR formula to address issues of fair consumer pricing and equity. Simulation three models prices under a completely proportional system. Simulation four explores the response of consumer prices to changes in the operating costs faced by the utility.

Lomita, California, located 22 miles from the City of Los Angeles, has a population of 20,596, with a median household income of $58,907, slightly below the state average of $60,190 (City-Data Lomita, California). Average yearly rainfall measures around 14 inches (Graphiq 2016).

The town's water is provided by a publicly owned utility operated by the city manager's office. The current billing structure consists of a bi-monthly meter fee and an IBR fee charged per hundred cubic feet (hcf, or 750 gallons). The data on utility costs and revenue used in this study come from a commissioned report by the consulting firm Black and Veatch (2013). The study includes observed data for fiscal year 2012-2013 costs and revenues, and projected levels for fiscal years 2013-2014 through 2016-2017. Projected data assume that growth in costs will be 3% per year, growth in fixed revenue (non-billing revenue) will be about 0.2%, and growth in consumption will be 0.25% per year.

The Lomita water utility collected insufficient revenue to fully cover its operation costs in FY 2012-2013; Black and Veatch (2013) also project shortfalls in the fiscal years 2013-2014 through 2016-2017. These results suggest that revenue needs might be better met under the CBFR system.

Longmont, Colorado, located 33 miles from Denver, has a population of approximately 89,919 with a median household income around $65,096, higher than the state average of $58,823 (City-Data Longmont, Colorado). Yearly rainfall averages 14.3 inches (US Climate Data 2016), similar to that of Lomita. Water service is provided by a publicly owned utility managed by the public works and natural resources department of the city government.

The Longmont Public Works and Natural Resources Department provided data for utility operation costs, as well as data on the number of customers serviced at each meter size, from 2011 to 2014. The city website (https://www.longmontcolorado.gov/departments/departments-n-z/water/rates-and-fees) provides information on billing rates. Table 2 shows the cost categories used in this study.

Tables 3 and 4 show how the different cost categories are classified (fixed-fixed, fixed-variable, or variable) for the purposes of the following simulations.

Simulations

Simulation 1: Consumer Cost Impacts of CBFR

The first simulation compares consumer bills under the IBR system currently in place in each city with consumer bills under the CBFR method. IBR bills are calculated with the assumption that residential users (single family homes) pay for meters within the 5/8" to 3/4" range for Lomita (the size of over 50% of all meters) and 5/8" for Longmont (the size of 90% of all meters).

The amount of water consumed per month (based on the Black and Veatch estimates of high, average, and low use) is multiplied by the cost/unit within the consumer's block; yearly consumption costs are presented as this value multiplied by 12. Total yearly costs equal the monthly consumption cost multiplied by 12 plus the bi-monthly meter cost multiplied by 6. The same consumption levels designated as high, average, and low are used in both the Lomita and Longmont calculations. While this study lacks the necessary data to firmly conclude that customer usage is similar for these two utilities, analysis of some additional data (Yolles 2016) suggests that this is a reasonable approach. Household level water consumption data for Sharon, MA, Los Angeles, CA, and West Palm Beach, FL, suggest that average rainfall impacts total water consumption. West Palm Beach receives an average 61 inches of precipitation per year (U.S. Climate Data-Palm Beach 2016), and average monthly water consumption stands at 8 hcf. Sharon receives around 49 inches of precipitation per year (U.S. Climate Data-Sharon 2016); average water use for those households is 10 hcf per month. Los Angeles, however, receives the same amount of average yearly precipitation as Lomita, around 14 inches (Los Angeles Almanac

Table 2. Water utility cost categories per fiscal year.

Lomita, California	Longmont, Colorado
All Personnel	Regulatory Compliance
Debt Service	Water Administration: Offices and Personnel
WRD Assessment Expense	Water Plant Personnel
Safety Compliance	Water Distribution Personnel
Power and Utilities	Water Quality Laboratory: Personnel
Chemicals, Fuels, Supplies	Instrumentation: Personnel
Repair and Maintenance	Survey Engineers: Personnel
Contract Services	Distribution System Rehab
Capital Outlay	Water Distribution Supplies
Water CIP Projects	Water Quality Laboratory: Supplies
Miscellaneous	Instrumentation: Supplies
Water Purchases	Survey Supplies
	St. Vrain Pipe Project
	Operation and Maintenance Costs
	Water Plant Chemicals, Energy, Misc. Supplies

2016), and average household water consumption measures around 34 hcf a month. These two cities, with identical rainfall, have similar monthly household consumption levels. Therefore, it seems reasonable to assume that Longmont, with average rainfall also around 14 inches, could also have an average usage of about 35 hcf per customer.

Water bills for high, average, and low consumption users under the CBFR system were calculated using data on costs and revenues for each city. Table 1 shows how costs were divided for this study. While there is no definitive way to partition costs, this study attempts to follow the recommendation in Spang et al. (2015). For the fixed-fixed category, each consumer's bill equals the total cost of this category divided by the total number of users. Both the fixed-variable and the variable category cost sums are multiplied by a consumer's proportion of overall water consumption (consumer/Lomita total) to determine his/her bill. While the example bills provided in the study apply at the residential level, non-residential customers and their consumption are included in the CBFR definitions of total system use (W) and total number of customers (X). Dividing these yearly billing amounts by 12, and adding the quotients, provides an estimate for a monthly bill.

Yearly costs for each level of consumption were also divided by median household income for each city, in order to estimate the affordability of water costs under the CBFR; the EPA recommends that yearly water expenses account for 2% or less of median household income or MHI (Meiburg et al. 2006). The results of this calculation show that the CBFR fits within the boundaries recommended by the EPA; no estimated costs, for any level of use, exceed 1% of MHI.

Overall, consumers face lower average billing charges under the CBFR system versus the current IBR plus meter charge system. At an "average use" level of 35 hcf per month, a consumer would pay $37.11 per billing period with the CBFR system; he/she would pay around $100 under the current system. For the average user, the new system decreases billing costs by 64%.

While both high- and low-use customers over

Table 3. Lomita utility costs per fiscal year categorized for CBFR system.

Fixed-Fixed Category	Fixed-Variable Category	Variable Cost
All Personnel	Power and Utilities	Water Purchases
Debt Service	Chemicals, Fuels, Supplies	
WRD Assessment Expense	Repair and Maintenance	
Safety Compliance	Contract Services	
(Predictable Revenue)*	Capital Outlay	
	Water CIP Projects	
	Miscellaneous	

*Predictable revenue includes all utility revenues accrued regardless of total water consumption. This value was subtracted from the sum of the fixed-fixed costs category in order to decrease the value of the portion of the consumer's bill unrelated to personal consumption.

Table 4. Longmont utility cost categories per fiscal year.

Fixed-Fixed Category	Fixed-Variable Category	Variable Cost
Regulatory Compliance	Distribution System Rehab	Water Plant Chemicals Energy
Water Administration: Offices and Personnel	Water Distribution Supplies	Misc. Supplies
Water Plant Personnel	Water Quality Laboratory: Supplies	
Water Distribution Personnel	Instrumentation: Supplies	
Water Quality Laboratory: Personnel	Survey Supplies	
Instrumentation: Personnel	St. Vrain Pipe Project	
Survey Engineers: Personnel	Operation and Maintenance Costs	

this same time period would also see decreases in their monthly water bill, the CBFR formula actually provides a greater magnitude of savings for high-use versus low-use consumers. This is the result of splitting fully fixed costs evenly across all consumers. A smaller portion of the bill changes with consumption level in the CBFR system versus the current system.

In the case of Longmont, high users see their bills decrease by about 60% under the CBFR versus the *status quo*. However, average and low users face substantial bill increases; bills under the CBFR are almost twice their current value for average consumption and three times their current value for low consumption. This disparity between different user groups, and the magnitude of the increase, stands in marked contrast to the Lomita example. These results suggest that the CBFR method, in its current form, would not be suitable for use in Longmont. The next simulation explores

possible alterations to the cost categorization that might better maintain price levels like those under the IBR system, affordability, and conservation incentives for high users. Table 5 shows the results of Simulation 1; Figures 4 and 5 present the results for Lomita and Longmont, respectively.

Alternative Distribution of Fixed Costs in CBFR Formula. The distribution of costs to different categories defined by CBFR remains largely subjective; different utility managers will likely have different opinions of what constitutes a fully fixed cost versus a partially fixed cost. To understand the level of sensitivity of consumer bills to changes in cost categorization, consumer bills for three different categorizations are compared to the CBFR bills from Simulation 1 (see supplemental tables for results).

Moving two costs from fixed-variable to fixed-fixed increased the former cost by 5%; the latter decreased by 45%. This re-categorization shows how increasing the absolute value of the fixed-fixed cost category has a strong impact on consumer bills. Not only do bills for all levels of use increase, the increase also affects low-use bills the most. The increased fixed-fixed cost more than offsets the decrease in the fixed-variable category cost.

Table 5. Consumer prices under CBFR system, FY 2013-2014.

Monthly Bills Simulation 1		
High (50 hcf)	**Lomita**	**Longmont**
Fixed-Fixed Charge	$25.62	$19.88
Fixed-Variable Charge	$6.35	$1.81
Variable Charge	$9.71	$0.67
Monthly Bill	$41.68	$22.36
Total Paid Over 12 Billing Cycles	$500.16	$268.36
% IBR System	30%	35%
Average (35 hcf)	**Lomita**	**Longmont**
Fixed-Fixed Charge	$25.62	$19.88
Fixed-Variable Charge	$4.44	$1.27
Variable Charge	$6.80	$0.47
Monthly Bill	$36.86	$21.62
Total Paid Over 12 Billing Cycles	$442.36	$259.43
% IBR System	40%	171%
Low (15 hcf)	**Lomita**	**Longmont**
Fixed-Fixed Charge	$25.62	$19.88
Fixed-Variable Charge	$1.90	$6.52
Variable Charge	$2.91	$2.41
Monthly Bill	$30.44	$20.63
Total Paid Over 12 Billing Cycles	$365.29	$247.53
% IBR System	63%	268%

For Lomita, increasing the value of the fixed-variable costs category not only lowers consumer bills, but leads to greater savings for low-use versus high-use. This is the opposite of what occurs when fixed-fixed costs are increased. The greater the value of fixed-variable costs versus fixed-fixed costs, the more pricing corresponds to usage and therefore the greater the difference among consumer types.

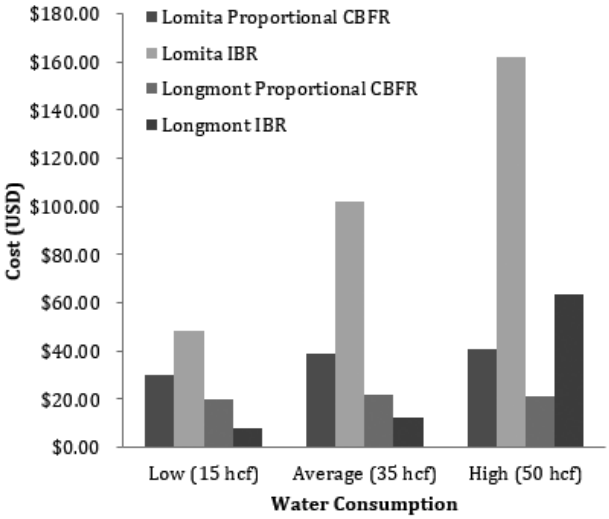

Figure 4. Monthly billing rate: IBR versus Standard CBFR in Longmont and Lomita, FY 2013-2014.

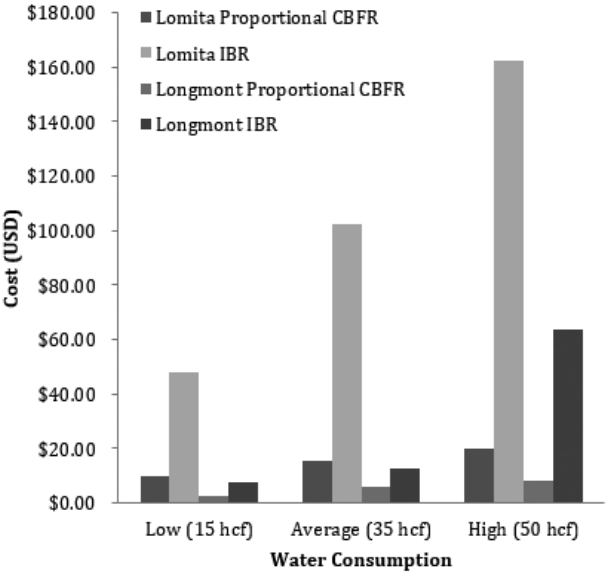

Figure 5. Monthly billing rate: IBR versus Entirely Proportional CBFR in Longmont and Lomita, FY 2013-2014.

In Longmont, personnel accounts for a large portion of costs. This simulation measures the impact of moving personnel costs from the fixed-fixed section to the fixed-variable section. The result is a more equitable system with prices similar to those under the current IBR plan.

These results suggest that a substantial change in costs categorization is necessary to make the CBFR system benefit customers of the Longmont utility. Even under this system the benefits are greatest for the highest use customers; the pricing mechanism fails to encourage conservation.

Simulation 2: Altering the Formula of CBFR

Simulation 2 explores modifications to the CBFR formula that provide water services at a more affordable rate for low-income users. Studies suggest that, beyond drinking and cleaning based on household size, greater water consumption is driven by the use of luxury goods like pools or irrigated landscaping (Mini et al. 2014). The unequal burden for low-income or low-use households stems from the CBFR system's relationship to the utility costs as a whole: the more water a household consumes, the lower the per unit cost they pay as they distribute the fixed-fixed cost section over more and more units of water. Only the fixed-fixed portion of the costs (as it is not already scaled by use to help lower-income users) will be altered: The original value for the category is multiplied by 2/3 for low income and 4/3 for high income. Average income costs remain unchanged. Low-income constitutes earnings at or below 75% of MHI; median includes those making between 75 and 150% or more of MHI; high-income is defined as any income at or above 150% of the MHI.

The public data set excludes consumer-level data, so this simulation uses 'fabricated' consumers with low, middle, and high income. The low-income household makes 50% of the MHI, the average income household makes exactly the MHI, and the high-income household makes 200% of the MHI. Providing different pay scales for different income levels improves affordability for low-income groups by keeping prices below 2% of income, but still allows high-income users to pay a smaller share of their income for water.

Using this proportional pricing method in Longmont lowers bills by about 30% for low-

income groups and also ensures that, for up to 50 hcf of use, bills remain below 2% of an income of $32,548.

The proportional method raises high-income user bills by about 30%; these bills still account for well below 2% of household income. These results suggest that a modified CBFR billing system based on income can keep bills fairly close to their pre-CBFR levels, as a proportion of the household's income. Table 6 shows the results of pricing in a low income model, and Table 7 shows the results of a high income model.

Simulation 3: An Entirely Proportional System

Given that the original CBFR system eliminates any conservation incentive (the more water consumed, the lower the per-unit price of water), a fully proportional system seems worth exploring. In this case (Simulation 3), the lump-sum costs for the utility in time *t* are distributed using the formula:

$$\text{Customer } i\text{'s Bill} = C * \frac{A_i}{W} \qquad \text{(Equation 5)}$$

where C equals total utility system costs, A_i equals customer i's consumption, and W equals total system consumption. The results of this system are shown in Table 8 and Figure 5.

Simulation 4: Sensitivity of Consumer Bills to Changes in Utility Operation Costs

The CBFR method makes consumer costs much more sensitive to changes in utility operation costs than a traditional increasing block rate. In fact, the relationship between changes in utility costs and increases in consumer bills is 1-to-1. Given this quality of the CBFR, Simulation 4 seeks to provide a limit at which increases in utility costs yield consumer bills in excess of 2% of MHI. These values are calculated for the FY 2012-2013 data.

Lomita. This simulation raises all costs simultaneously until the average use customer's bill exceeds 2% of MHI. Performing calculations with the Lomita, CA data suggests that costs could increase by up to 250% to ensure that average or conserving consumers bills remain below 2% of Lomita HMI. This suggests that CBFR bills remain at reasonable rates even if certain utility costs were to spike due to an increase in energy prices, a large unforeseen repair project, etc.

Longmont. For Longmont, utility costs could more than triple and still keep bills within 2% of MHI range. This suggests that CBFR bills remain at reasonable rates even if certain utility costs were to spike.

Extension: Lomita Consumer Costs over Time with 25% Decreased Consumption over Five Years

The benefit of the CBFR method of pricing centers around its ability to ensure income to cover operating costs regardless of fluctuations in consumption. In this simulation, using the costs for fiscal years 2012-2013 to 2016-2017, the effects of a 25% reduction in consumption over five years (via a 5% yearly reduction) are compared in the traditional versus the CBFR system. For all costs classified as fixed-fixed and fixed-variable, total yearly costs for FY 2012-2013 will be used over the five-year period. Water purchases are assumed to have a constant marginal cost/hcf, which will be used to estimate total water purchase costs per year. With this assumption that average cost equals the marginal cost of water purchases, the cost of water purchases for a given year equals $2.32 per hcf.

Given the lack of consumer-level data, the estimates of revenue shortfalls from a 25% consumption decrease under the current system are rough estimates. The values shown below assume that, on average, each unit of water consumed is charged at the middle block rate of 21/35 hcf/month. Assuming that no meters are added or removed over the 5-year period, yearly meter revenue can be calculated with near-certainty.

Table 9 reports the revenue shortfalls per year with the current billing structure and constant costs; table 10 shows shortfalls with an estimated 2% decrease in costs for the fixed-variable category.

For the CBFR scenario, the same formulas from Simulation 1 were used. Assuming costs remain stable, the only changes to a consumer's bill will come from the fixed-variable and variable categories. Since these costs are multiplied by the consumer's proportion of total consumption, a decrease in overall consumption increases the proportion represented by each "generic" customer profiled here. Table 11 models cost impacts with no change in utility costs.

Table 6. CBFR consumer prices, low income model.

High (50 hcf)	**Lomita**	**Longmont**
Yearly Fixed-Fixed	$204.99	$159.07
Yearly Cost	$397.67	$188.88
Monthly Cost (assume 1 bill/month)	$33.14	$15.74
% MHI	1.35%	0.15%
Average (35 hcf)	**Lomita**	**Longmont**
Yearly Fixed-Fixed	$204.99	$159.07
Yearly Cost	$339.86	$179.88
Monthly Cost (assume 1 bill/month)	$28.32	$14.99
% MHI	1.15%	0.14%
Low (15 hcf)	**Lomita**	**Longmont**
Yearly Fixed-Fixed	$204.99	$159.07
Yearly Cost	$262.79	$168.00
Monthly Cost (assume 1 bill/month)	$21.90	$14.00
% MHI	0.89%	0.13%

Table 7. CBFR consumer prices, high income model.

High (50 hcf)	**Lomita**	**Longmont**
Yearly Fixed-Fixed	$409.98	$318.14
Yearly Cost	$602.66	$347.88
Monthly Cost (assume 1 bill/month)	$50.22	$28.99
% MHI	0.51%	0.27%
Average (35 hcf)	**Lomita**	**Longmont**
Yearly Fixed-Fixed	$409.98	$318.14
Yearly Cost	$544.85	$339.00
Monthly Cost (assume 1 bill/month)	$45.40	$28.25
% MHI	0.46%	0.26%
Low (15 hcf)	**Lomita**	**Longmont**
Yearly Fixed-Fixed	$409.98	$318.14
Yearly Cost	$467.78	$327.12
Monthly Cost (assume 1 bill/month)	$38.98	$27.26
% MHI	0.40%	0.25%

Table 8. Completely proportional pricing system.

High (50 hcf)	**Lomita**	**Longmont**
Fixed-Fixed Charge	$5.48	$5.83
Fixed-Variable Charge	$4.74	$1.81
Variable Charge	$9.54	$0.70
Total Paid over 12 Billing Cycles	$237.24	$100.41
Monthly Bill	$19.77	$8.34
% of IBR Bill	14%	13%
Average (35 hcf)	**Lomita**	**Longmont**
Fixed-Fixed Charge	$5.48	$4.12
Fixed-Variable Charge	$3.32	$1.27
Variable Charge	$6.68	$0.47
Total Paid over 12 Billing Cycles	$185.76	$70.29
Monthly Bill	$15.48	$5.86
% of IBR Bill	15%	46%
Low (15 hcf)	**Lomita**	**Longmont**
Fixed-Fixed Charge	$5.48	$1.77
Fixed-Variable Charge	$1.42	$0.55
Variable Charge	$2.86	$0.20
Total Paid over 12 Billing Cycles	$117.24	$30.12
Monthly Bill	$9.77	$2.51
% of IBR Bill	20%	33%

Table 9. Consumption and revenue with 25% decrease over five years, 0 inflation.

Fiscal Year	**12-13**	**13-14**	**14-15**	**15-16**	**16-17**
Total Consumption (hcf)	$903,813.85	$813,432.47	$768,241.77	$723,051.08	$677,860.39
Estimated Total Consumption Revenue	$3,678,250.85	$3,310,425.77	$3,126,513.22	$2,942,600.68	$2,758,688.14
Estimated Revenue Shortage	$455,043.15	$1,214,553.24	$1,842,159.83	$2,121,829.13	$2,657,870.83

Table 10. Consumption and revenue with 25% decrease over five years and 2% yearly decrease in fixed-variable costs, 0 inflation.

Fiscal Year	12-13	13-14	14-15	15-16	16-17
Total Consumption (hcf)	$903,814	$813,432.47	$768,241.77	$723,051.08	$677,860
Estimated Total Consumption Revenue	$3,678,250.85	$3,310,425.77	$3,126,513.22	$2,942,600.68	$2,758,688.14
Estimated Revenue Shortage	$399,731.97	$571,390.10	$664,989.63	$759,455	$859,057

These results support the assumption that, as consumption decreases, consumers face larger CBFR bills to cover system costs. However, individual bills do not increase proportionally to consumption decreases: a 25% system-wide decrease in consumption over five years raises a high user's bill by 8%, an average user's bill by 6%, and a low user's bill by 3%.

The result that greater users face greater price increases over time also suggests that some amount of progressive pricing is built into the system, for as overall community consumption decreases, those who persist in using high volumes of water will account for a larger fraction of the total and face higher bills as a result. This explains why high-use bills increase more than low-use bills. No bill value exceeds the 2% of MHI limit recommended by the EPA.

If fixed-variable costs decrease in absolute value by at least 2% per year, CBFR bills should be lower for all users versus the status quo with no conservation. Table 12 shows the results of such a simulation.

At any level of consumption, decreasing the fixed-variable costs over time decreases the consumer's bill. Compared to the *status quo* from Simulation 1, lowering costs and consumption lowers bills by 6% for high users, 5% for average users, and 2.6% for low users.

In contrast to the scenario with no change in utility costs, this scenario provides a greater savings the greater the amount of water used. This suggests that the yearly cost decreases overpower increases in the proportion of the total accounted for by the high-use consumer. While all consumers see a decrease in bills, the disproportionate benefit provided to high-income users may conflict with other goals like equity and conservation-focused billing.

Based on the significant difference in billing prices for CBFR between Lomita and Longmont, it is clear that the results of switching to the CBFR system are largely dependent upon the current utility pricing situation and community characteristics. For Lomita, the CBFR system lowered billing costs to customers, whereas in Longmont, the system decreased bills for high users but increased bills for low and average use customers. Comparing the IBR systems employed by each utility reveals some key differences in current pricing that ultimately make the CBFR either helpful or harmful to customers. In the case of Lomita, the current system imposes a large meter cost ($218/year) but then charges similar costs for its three blocks; the difference between the first block and the top (third) block is 44%. With a high fixed cost and relatively low penalties for increased consumption, this billing system more closely mirrors the cost structure for the water utility itself, with its costs predominately fixed regardless of consumption. As a result, the CBFR's slight positive increase on the fixed portion of the bill is more than offset by the much lower per-unit costs.

Table 11. Billing impacts of a 25% total decrease in consumption FY 2014-2015.

High (50 hcf)	
Fixed-Fixed Charge	$25.62
Fixed-Variable Charge	$7.90
Variable Charge	$9.68
Monthly Bill	$43.20
Total Paid Over 12 Billing Cycles	$518.42
% of MHI	0.88%
Average (35 hcf)	
Fixed-Fixed Charge	$25.62
Fixed-Variable Charge	$5.53
Variable Charge	$6.78
Monthly Bill	$37.93
Total Paid Over 12 Billing Cycles	$455.14
% of MHI	0.77%
Low (15 hcf)	
Fixed-Fixed Charge	$25.62
Fixed-Variable Charge	$2.37
Variable Charge	$2.90
Monthly Bill	$30.90
Total Paid Over 12 Billing Cycles	$370.76
% of MHI	0.63%

Table 12. Billing impacts of a 25% decrease in consumption with an absolute decrease in fixed-variable costs of 2% per year, FY 2014-2015.

High (50 hcf)	
Fixed-Fixed Charge	$25.62
Fixed-Variable Charge	$3.92
Variable Charge	$9.68
Monthly Bill	$39.22
Total Paid Over 12 Billing Cycles	$470.68
% of MHI	0.80%
Average (35 hcf)	
Fixed-Fixed Charge	$25.62
Fixed-Variable Charge	$2.74
Variable Charge	$6.78
Monthly Bill	$35.14
Total Paid Over 12 Billing Cycles	$421.72
% of MHI	0.72%
Low (15 hcf)	
Fixed-Fixed Charge	$25.62
Fixed-Variable Charge	$1.18
Variable Charge	$2.90
Monthly Bill	$29.70
Total Paid Over 12 Billing Cycles	$356.44
% of MHI	0.61%

The current IBR system in Longmont is almost the opposite of the Lomita system. The meter cost is only $58.80/year, while the consumption cost increases by 145% between the first block and the final (fourth) block (the amount of water included in each block is reasonably consistent for the two utilities to allow for this type of comparison). The CBFR method greatly upsets the IBR and its greater variation in the consumption-based portion of a customer's bill; low-use customers in Longmont who no longer benefit from conserving suffer the most under the CBFR system. The severity of the change from switching to CBFR highlights the difference between Longmont's pricing system and the typical water utility's cost structure.

Conclusion

Were a utility to consider the CBFR method, system planners would need to be highly confident in their cost categorizations: failing to allocate the system properly could have unnecessarily negative impacts on consumer bills, especially for low users. Given the negative effects on low-use customers, utilities should be very cautious about if and when to pursue the CBFR system. The similarity between the CBFR bill and the

water utility's cost structure disadvantages low-use customers; just like the utility, the fixed-fixed portion of their bill is spread over fewer units of water, so they pay a higher per-unit cost than high-use customers. Equity remains an issue in a system where all types of users face the same, substantial, fixed cost bill component. In addition, the higher price elasticity for low-income users (Olmstead et al. 2007) suggests that lower-use households could end up reducing consumption more than higher-use (high-income) homes. More conservation might come from lower-cost households who already use smaller amounts of water. Thus, equity concerns in the CBFR system stem from the high proportion of a user's bill accounted for by the fixed-fixed charge, and how low-use, low-income households may decrease consumption by a larger amount than other households.

Given the difference between high and low users, weighting the value of each user's fixed-fixed cost bill based on income could help mitigate potential equity problems. Especially for Longmont, the current system, with its steep blocks and its minimal meter fee, allows customers to save money by using less water. Multiplying the fixed-fixed bill by 2/3 for low income and 4/3 for high income ensures that all customers making at least 50% of the MHI will not pay more than 2% of their income to consume up to 50 hcf of water. However, even this type of scale lets high-income groups pay a smaller portion of their income overall versus other users. While income scalars certainly ease the burden for low-income groups, they need to be highly complex in order to ensure all customers pay an equal portion of their income for any given consumption amount. Furthermore, the burden on the utility to obtain income information for all customers could be severe; other methods like census tract data are certain to have errors. Any attempt to base price on income is also likely to be politically controversial.

Experimentation with the Lomita data shows that all users' bills inevitably increase under the CBFR with a system-wide consumption decrease. However, cost increases are of a lower magnitude than the consumption decrease: reducing system consumption by 25% does not raise bills by more than 10%, up to monthly consumption of 50 hcf. High-use customers also see their bill rise more than low-use customers; costs increase by 8% at 50 hcf/month, 6% at 35 hcf/month, and just 3% at 15 hcf/month. With the magnitude of the increase higher for high-use customers, the CBFR system seems like an effective means of incentivizing high users to decrease use in the face of community-wide conservation; customers who ignore the conservation trend will have to shoulder more of the costs for running the system. Higher volume users tend to have more price elastic demand (more luxury water uses) and as such might be most responsive to these incentives. Under extreme conservation measures, like the 25% reduction call currently faced in California, some utilities could employ a CBFR system to guarantee revenue to cover costs, and also send conservation signals to their high-use consumers.

Both Lomita and Longmont consumer bills prove remarkably resilient to utility cost fluctuations. Increases in operating costs of up to 250% for Lomita and 300% for Longmont still keep consumer bills within the "affordable" range defined by the EPA, or 2% of MHI. The magnitude of the increase in consumer bills is significantly lower than the increase in utility operating costs, but still provides sufficient revenue to cover these greater costs.

This study finds that the CBFR ensures stable revenue at the cost of equitable billing and conservation pricing. The CBFR pricing mechanism is not a good solution for water utilities over the long term. However, the system could be useful in times of severe drought, where utilities face a large threat of revenue shortfalls. For example, if consumption reductions are determined exogenously, such as the current situation in California, the CBFR appears to be the simplest way to ensure that utilities can cover their high fixed costs. In particular, the system would be best applied to drought-stricken communities where income is largely homogenous for all customers.

Further research is needed to explore the ideal scalar system, or to explore any other methods for making the CBFR system more equitable and conservation-focused. While a proportional system yields bills more responsive to a customer's consumption, it depresses prices too much below the IBR rates such that any conservation or scarcity pricing currently in place is eliminated. With water

prices accounting for only 0.5 to 0.6% of the average U.S. family's household budget (Mehan III and Kline 2012), higher, not lower prices seem necessary to induce water conservation--especially for high-income consumers-- in water-scarce environments. For now, a "SCBFR" (Scaled Consumption-Based Fixed Rates) system seems the best option for ensuring revenue stability for the water utility without jeopardizing affordability for low-income households.

Acknowledgments

Thanks to Cal Youngberg of Longmont Public Works and Natural Resources, and Peter Yolles of WaterSmart Software, for sharing data for this project.

Author Bio and Contact Information

Amy Schmidt graduated from Bates College in 2016 with a B.A. in Environmental Studies, concentrating in Environmental Economics. She would like to thank Professor Lewis and her wonderful family and friends for their support.

Lynne Lewis is the Elmer W. Campbell Chair of Economics at Bates College. She is an environmental economist with primary research interests in water, ecosystem services and climate change. She coauthors the textbook Environmental and Natural Resource Economics with Tom Tietenberg. She is also a former board member of UCOWR. She may be contacted at llewis@bates.edu.

Supplemental Tables (S1 - S3)

Table S1. Alternative distribution of fixed costs in CBFR formula. Impact of moving "capital outlay" and "misc. costs" from fixed-variable to fixed-fixed on consumer bills FY 2014-2015.

High (50 hcf)	**New**	**Previous**	**% Change**
Fixed-Fixed Charge	$27.71	$25.62	8.13
Fixed-Variable Charge	$5.89	$6.35	-7.17
Variable Charge	$9.71	$9.71	0.00
Total Amount Due	$43.31	$41.68	3.90
Average (35 hcf)	**New**	**Previous**	**% Change**
Fixed-Fixed Charge	$27.71	$25.62	8.13
Fixed-Variable Charge	$4.12	$4.44	-7.17
Variable Charge	$6.80	$6.80	0.00
Total Amount Due	$38.63	$36.86	4.79
Low (15 hcf)	**New**	**Previous**	**% Change**
Fixed-Fixed Charge	$27.71	$25.62	8.13
Fixed-Variable Charge	$1.77	$1.90	-7.17
Variable Charge	$2.91	$2.91	0.00
Total Amount Due	$32.39	$30.44	6.39

Table S2. Alternative distribution of fixed costs in CBFR formula. Impact of movement of "safety compliance" and "WRD assessment expense" categorization on consumer bills FY 2014-2015.

High (50 hcf)	**New**	**Previous**	**% Change**
Fixed-Fixed Charge	$24.60	$25.62	-3.98
Fixed-Variable Charge	$6.57	$6.35	3.51
Variable Charge	$9.71	$9.71	0.00
Total Amount Due	$40.88	$41.68	-1.91
Average (35 hcf)	**New**	**Previous**	**% Change**
Fixed-Fixed Charge	$24.60	$25.62	-3.98
Fixed-Variable Charge	$4.60	$4.44	3.51
Variable Charge	$6.80	$6.80	0.00
Total Amount Due	$36.00	$36.86	-2.34
Low (15 hcf)	**New**	**Previous**	**% Change**
Fixed-Fixed Charge	$24.60	$25.62	-3.98
Fixed-Variable Charge	$1.97	$1.90	3.51
Variable Charge	$2.91	$2.91	0.00
Total Amount Due	$29.49	$30.44	-3.13

Table S3. Alternative distribution of fixed costs in CBFR formula. Movement of personnel from fixed-fixed to fixed-variable: impact on bills.

High (50 hcf) 2014	
Fixed-Fixed Charge	$61.62
Fixed-Variable Charge	$82.06
Variable Charge	$8.03
Total Paid over 12 Billing Cycles	$151.71
Monthly Bill	$12.64
% of MHI	0.23%
% of Status quo	20%
Average (35 hcf) 2014	
Fixed-Fixed Charge	$61.62
Fixed-Variable Charge	$57.45
Variable Charge	$5.62
Total Paid over 12 Billing Cycles	$124.69
Monthly Bill	$10.39
% of MHI	0.19%
% of Status quo	82%
Low (15 hcf) 2014	
Fixed-Fixed Charge	$61.62
Fixed-Variable Charge	$24.62
Variable Charge	$2.41
Total Paid over 12 Billing Cycles	$88.65
Monthly Bill	$7.39
% of MHI	0.14%
% of Status quo	96%

References

Barr, T. and T. Ash. 2015. Sustainable water rate design at the western municipal water district: The art of revenue recovery, water use efficiency, and customer equity. *Global Issues in Water Policy* 9: 373-392.

Black and Veatch. 2013. *Water Utility Cost of Service Report.* Lomita, California.

Chesnutt, T.W., C. McSpadden, and J. Christianson. 1996. Revenue instability induced by conservation rates. *American Water Works Association* 88: 52-63.

City Data. Lomita, California. Available at: http://www.city-data.com/city/Lomita-California.html. Accessed February 27, 2017.

City Data. Longmont, Colorado. Available at: http://www.city-data.com/city/Longmont-Colorado.html. Accessed February 27, 2017.

Gregory, G.D. and M. Di Leo. 2003. Repeated behavior and environmental psychology: The role of personal involvement and habit formation in explaining water consumption. *Journal of Applied Social Psychology* 33: 1261-1296.

Graphiq Inc. 2016. Lomita, California Average Rainfall. *Weather DB.* Available at: https://rainfall.weatherdb.com/l/15135/Lomita-California. Accessed February 27, 2017.

Hanemann, M.W. 1998. Price and rate structures. Chapter 5 In: *Urban Water Demand Management and Planning*, D.Baumann, J. Boland, and W.M. Hanemann (Eds.). McGraw-Hill.

Hoag, G. and R. McKinley. 2012. Money matters: Managing cashflow instability under conservation-based rates. *American Water Works Association* 104: 28-30.

Klaiber, H.A., V.K. Smith, M. Kaminsky, and A. Strong. 2012. Measuring Price Elasticities for Residential Water Demand with Limited Information. NBER Working Papers. Available at: http://www.nber.org/papers/w18293. Accessed February 28, 2017.

Los Angeles Almanac. 2016. Total Seasonal Rainfall. Available at: http://www.laalmanac.com/weather/we13.htm. Accessed February 28, 2017.

Mann, P.C. and J.L. Mikesell. 1979. Cost behavior and water systems. *Journal of the American Water Resources Association* 15: 1301–1307. DOI:10.1111/j.1752-1688.1979.tb01129.x.

Mehan III, T. and I. Kline. 2012. Pricing as a demand side management tool: Implications for water policy and governance. *American Water Works Association* 104: 61-66.

Meiburg, S.A., P. Domenici, T. Agriss, J.A. Barnes, J. Belaga, J. Boland, G. Butcher, D. Correll, and M. Curley. 2006. Affordable Rate Design for Households. Environmental Financial Advisory Board.

Olmstead, S.M., W.M. Hanemann, and R.N. Stavins. 2007. Water demand under alternative price structures. *Journal of Environmental Economics and Management* 54: 181-198.

Olmstead, S.M. and R.N. Stavins, 2008. Comparing price and nonprice approaches to urban water conservation. *Water Resources Research* 45.

Rahill-Marier, B. and U. Lall. 2013. America's Water: An Exploratory Analysis of Municipal Water Survey Data. Columbia Press.

Renzetti, S., D.P. Dupont, T. Chitsinde. 2015. An empirical examination of the distributional impacts of water pricing reforms. *Utilities-Policy* 34: 63-69.

Schoengold, K. and D. Zilberman. 2014. The economics of tiered pricing and cost functions: Are equity, cost recovery, and economic efficiency compatible goals? *Water Resources and Economics* 7: 7.

Sedlak, D. 2015. Why your water bill must go up. *San Francisco Chronicle*. Available at: http://www.sfchronicle.com/opinion/article/Why-your-water-bill-must-go-up-6207560.php. Accessed February 28, 2017.

Shaked, A. and J. Sutton. 1987. Product differentiation in industrial structure. *The Journal of Industrial Economics* 36: 131-146.

Spang, E.S., S. Miller, M. Williams, and F.J. Loge. 2015. Consumption-based fixed rates: Harmonizing water conservation and revenue stability. *American Water Works Association* 107: 164-173.

U.S. Climate Data. 2016. Climate-Longmont, Colorado. Available at: http://www.usclimatedata.com/climate/longmont/colorado/united-states/usco0243. Accessed February 28, 2017.

U.S. Climate Data. 2016. Climate-Walpole, Massachusetts. Available at: http://www.usclimatedata.com/climate/walpole/massachusetts/united-states/usma0437. Accessed February 28, 2017.

U.S. Climate Data. 2016. Climate-West Palm Beach, Florida. Available at: http://www.usclimatedata.com/climate/west-palm-beach/florida/united-states/usfl0512. Accessed February 28, 2017.

Yolles, P. 2016. WaterSmart Software, Personal Correspondence.

Universities Council on Water Resources
Journal of Contemporary Water Research & Education
Issue 160, Pages 25-41, April 2017

Assessing Models of Arsenic Occurrence in Drinking Water from Bedrock Aquifers in New Hampshire

Caroline M. Andy[1], Maria Florencia Fahnestock[2], *Melissa A. Lombard[1,2], Laura Hayes[1], Julia G. Bryce[2], and Joseph D. Ayotte[1]

[1]U.S. Geological Survey, Pembroke, NH, USA
[2]Department of Earth Sciences, University of New Hampshire, Durham, NH, USA
**Corresponding author*

Abstract: Three existing multivariate logistic regression models were assessed using new data to evaluate the capacity of the models to correctly predict the probability of groundwater arsenic concentrations exceeding the threshold values of 1, 5, and 10 micrograms per liter (µg/L) in New Hampshire, USA. A recently released testing dataset includes arsenic concentrations from groundwater samples collected in 2004-2005 from a mix of 367 public-supply and private domestic wells. The use of this dataset to test three existing logistic regression models demonstrated enhanced overall predictive accuracy for the 5 and 10 µg/L models. Overall accuracies of 54.8, 76.3, and 86.4 percent were reported for the 1, 5, and 10 µg/L models, respectively. The state was divided by counties into northwest and southeast regions. Regional differences in accuracy were identified; models had an average accuracy of 83.1 percent for the counties in the northwest and 63.7 percent in the southeast. This is most likely due to high model specificity in the northwest and regional differences in arsenic occurrence. Though these models have limitations, they allow for arsenic hazard assessment across the region. The introduction of well-type (public or private), well depth, and casing length as explanatory variables may be appropriate measures to improve model performance. Our findings indicate that the original models generalize to the testing dataset, and should continue to serve as an important vehicle of preventative public health that may be applied to other groundwater contaminants in New Hampshire.

Keywords: *arsenic prediction, bedrock groundwater, geogenic arsenic, water supply wells, logistic regression*

Arsenic is linked to important public health concerns, including liver, lung, bladder, and kidney cancers as well as developmental defects, cardiovascular disease, neurotoxicity, and diabetes (Smith et al. 1992; World Health Organization 2012). Arsenic is present in excess of maximum contaminant levels in domestic water supplies around the world, and can be elevated due to anthropogenic (e.g., agricultural or industrial) or geogenic sources. In New Hampshire, and the larger northeastern United States region of New England, geogenic arsenic is of great concern in drinking water supplies in bedrock aquifers (Ayotte et al. 2003; Moore 2004; Ayotte et al. 2006; Ayotte et al. 2011; Flanagan et al. 2012; Zheng and Ayotte 2015; Baris et al. 2016). In New Hampshire, nearly half of the state's population depends on a domestic well water supply, where at least 75 percent comes from drilled bedrock wells and the rest from shallow glacial aquifer wells (U.S. Census Bureau 1999). As many as 30 percent of these bedrock wells, supplying potentially 120,000 people, may have arsenic concentrations above 10 micrograms per liter (µg/L), the federally and internationally advised limit for safe drinking water (Ayotte et al. 2003; Peters and Blum 2003; Moore 2004; Ayotte et al. 2011). Elevated mortality rates for bladder cancer within New England date back to 1950, possibly implicating regionally specific domestic well use (Ayotte et al. 2006) and

exposure to naturally occurring inorganic arsenic as a contributor (Baris et al. 2016). As a matter of public health, predicting the probability of arsenic exceeding multiple thresholds as a function of various environmental parameters is an essential step in assessing exposure risk and promoting safe drinking water accessibility in the northeastern United States.

Efforts to predict arsenic content in bedrock-hosted drinking water include the use of statistical models and routine laboratory analyses of private and public drinking water supplies. Logistic regression models have been used for estimating the probability of various groundwater contaminants exceeding certain thresholds at various spatial scales and locations, including volatile organic compounds in the United States (Squillace et al. 1999), pesticides in California (Teso et al. 1996), nitrate in the United States (Nolan et al. 2002), and arsenic in New England (Ayotte et al. 2006; Yang et al. 2012). Logistic regression models, in comparison to linear regression models, facilitate predicting the probability of exceedance when much of the dependent variable dataset is reported as below some threshold, usually the laboratory reporting level or a human health benchmark (Hosmer and Lemeshow 2000).

This study assesses three multivariate logistic regression models that were developed to estimate the probability of arsenic exceeding three threshold concentrations (1, 5, or 10 µg/L) in New Hampshire. These models were developed by use of a training dataset of 1,715 samples describing arsenic concentrations in groundwater and from testing of 374 potential predictor variables. These variables, by design, are publicly accessible, continuous and mappable features that were applied across New Hampshire to facilitate the creation of statewide maps showing the predicted probability of arsenic exceeding 1, 5, and 10 µg/L in groundwater. Thus far, the models evaluated here have been used for public health applications including a study on the geospatial association between adverse birth outcomes and arsenic presence in groundwater in New Hampshire (Shi et al. 2015). For this reason, assessment of the model's predictive application to a new dataset is of increased importance.

Explanatory variables representing geologic, geochemical, hydrologic, land use, and other categories of relevant features were important in predicting the probability of arsenic in groundwater. For example, a continuous variable describing proximity to granitic plutons is related to arsenic probability, particularly in the 5 and 10 µg/L threshold models (Ayotte et al. 2011). This and similar explanatory variables may be surrogate variables representing soluble arsenic minerals that may exist near these plutons as a result of hydrothermal alteration during late-stage pegmatite formation (Peters and Blum 2003). Binary explanatory variables also include the presence or absence of a well in a particular bedrock unit, whereas continuous numerical explanatory variables include the mean annual precipitation from 1971 to 2000. These explanatory variables exemplify just a few of the many mappable features that estimate arsenic hazard (Ayotte et al. 2011).

Groundwater contaminant models are seldom evaluated with independent data—an indication of how accurately the model represents the study area, particularly in originally unsampled regions. This study, a comparative analysis using new data not available during the development of the original models, serves to (1) evaluate the predictive capacity of three existing multivariate logistic regression models that estimate the probability of arsenic exceeding 1, 5, and 10 µg/L in groundwater in New Hampshire, (2) examine the prevalence of any regional differences in model accuracy, and (3) propose possible adjustments in modeling type and explanatory variable selection in order to enhance model efficacy.

Methods

Sample Collection and Arsenic Analysis

In this study we assess three existing models developed using data collected for 1,715 wells located throughout New Hampshire; we refer to this dataset as the model training dataset (Table 1). The models were assessed using data collected from 367 wells independent of the model training dataset; we refer to this dataset as the model testing dataset (Table 1) (Lombard et al. 2017). The locations and arsenic concentrations for the training dataset and testing dataset are shown in Figures 1a and 1b, respectively. Both datasets contain public-supply wells and private domestic

Table 1. Percentage of wells with arsenic concentrations below model threshold values for model training and model testing datasets.

Arsenic Concentration (model threshold value)	Training Data (percent)	Testing Data (percent)
< 1 µg/L	31	57
< 5 µg/L	66	81
< 10 µg/L	79	89

wells. In the training dataset, 960 (56 percent) are from public-supply wells and 755 (44 percent) are from private domestic wells. In the testing dataset, 102 samples (28 percent) are from public-supply wells, and 265 (72 percent) are from private domestic wells. In both datasets there is a clear distinction between the southeastern part of the state (Belknap, Hillsborough, Merrimack, Rockingham, and Strafford counties) where arsenic concentrations are more often high but also are more variable, and the northwestern part (Carroll, Cheshire, Coos, Grafton, and Sullivan counties) where concentrations are often low; for this reason we divide the state into two regions (Figure 1, inset) reflecting those differences for some of the analyses.

The samples used in the testing dataset were originally collected for use in an earlier study on methyl *tert*-butyl ether (MTBE) occurrence in drinking-water resources in New Hampshire (Ayotte et al. 2008). Five hundred and forty eight samples from that research were analyzed for arsenic (Fahnestock et al. 2017). Duplicate samples and locations included in the training dataset were excluded from the testing dataset. As a result, 367 of the 548 samples from public- and private-supply wells were used in this study (Lombard et al. 2017).

The testing dataset samples were collected from 2004 to 2005 in accordance with U.S. Geological Survey (USGS) procedures. During sampling, 250-mL polypropylene bottles were used to collect unfiltered water samples from a stainless steel flow-reducing port attached to existing plumbing as close as possible to the wellhead. In the few instances where height restraints did not allow for attaching the stainless steel flow-reducing port, samples were collected using clean Teflon lines with stainless steel fittings or existing plumbing lines (Ayotte et al. 2005). Sampling occurred after pH, specific conductivity, dissolved oxygen, and water temperature had met stabilization criteria as outlined in the USGS National Field Manual (U.S. Geological Survey 2005).

The testing dataset samples were analyzed for arsenic between December 2012 and February 2014. Prior to analysis, samples were visually inspected for sealed caps, clean storage conditions, and evidence of evaporation. Though no evidence of evaporation was present, an evaporation of 2.5 mL would equate to 1 percent loss of sample volume and would therefore only artificially increase the reported arsenic concentration by 1 percent. The presence of any color, staining, precipitate, or biological materials was also noted.

The samples were not acidified at the time of sample collection as is recommended for sample preservation of ambient water samples for trace metals analyses (U.S. Environmental Protection Agency 1996). Although delayed acidification and holding time are potential complications to quantitative analysis, previous studies indicate that extended holding times and delayed acidification of trace metal samples may not significantly influence accurate measurements of metal concentrations (Feldmann et al. 1992; Graney and Landis 2013). We addressed the potential issue of arsenic adsorption on container surfaces by conducting a series of stepwise acidification experiments in which nitric acid was added incrementally to the samples before arsenic analysis. This sequential leaching approach included analyses of a subset of five samples picked at random and subjected to sequential acidification (5-, 10-, and 15-percent nitric acid) and subsequent week-long equilibration times. Analyses of five samples demonstrated a > 99 percent yield for the total arsenic in the system during the first acidification step (i.e., 5 percent

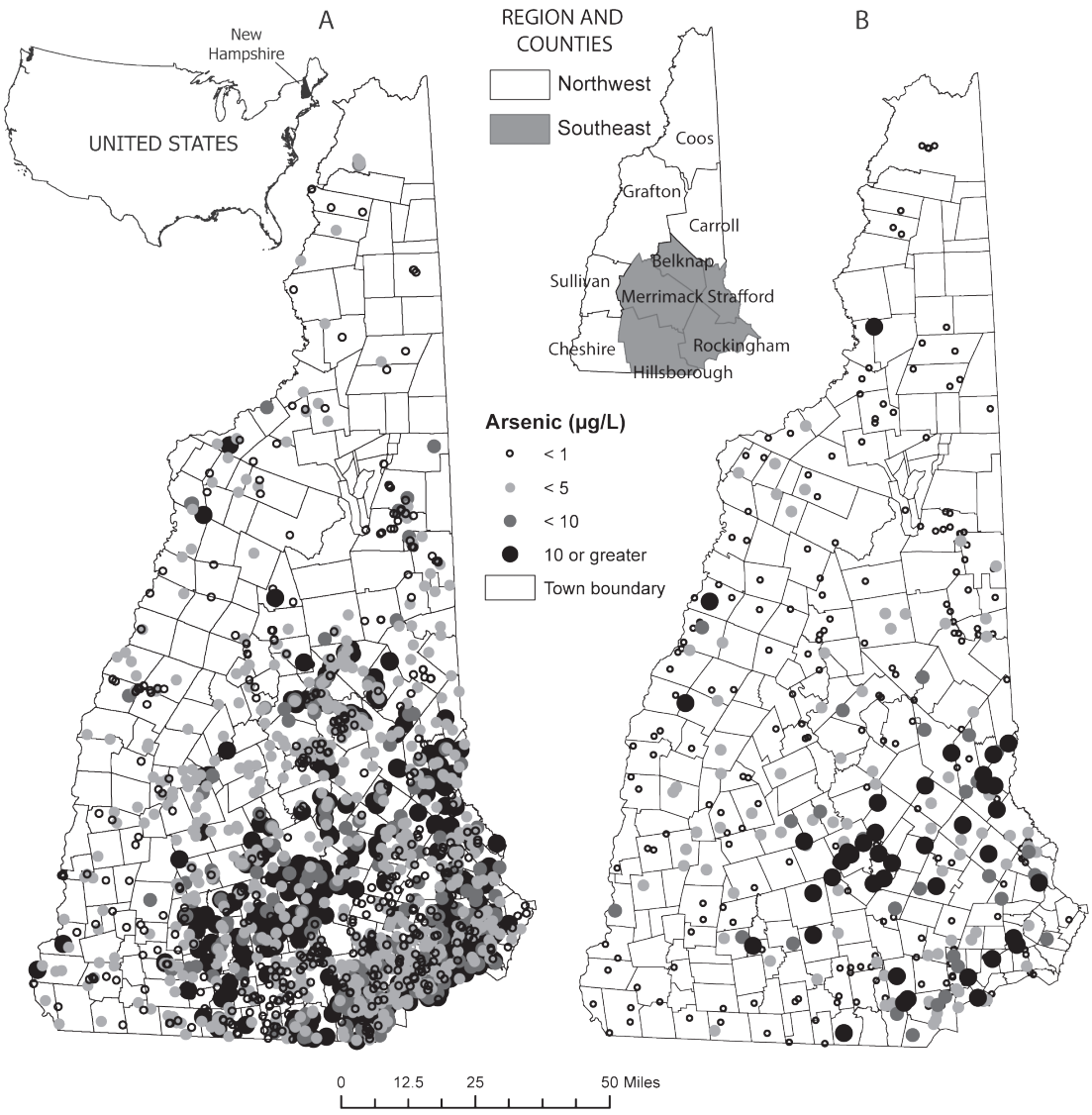

Figure 1. Concentrations of arsenic (µg/L) for the (A) model training (n = 1,715) and (B) testing (n = 367) datasets in New Hampshire. The model training dataset was originally collected for Ayotte et al. (2011) and is mapped beside the model testing data, collected independently for this study, in order to highlight differences in sample spatial distribution around the state.

nitric). Accordingly, 5 percent acidification was adopted in the laboratory procedures for the remainder of the samples, and though the sequential approach was not carried out for every sample, we interpret the data with the assumption of minimal sampling bias associated with sample shelf life.

Laboratory Procedures and Data Quality Control Assessment

Arsenic analyses on the samples used in the testing dataset were carried out in the geochemistry laboratory in the Department of Earth Sciences at the University of New Hampshire (UNH). Samples were analyzed via a hydride generator-inductively coupled plasma mass spectrometer (HG-ICP-MS) using a Cetac HGX-200 plumbed into a Nu Instruments Attom high-resolution inductively coupled plasma mass spectrometer, following procedures adapted from Klaue and Blum (1999). Diluted aliquots of samples were run in triplicate, and the reported uncertainty is two times the standard deviation on the mean (2σ) of these

analyses. Generally, the data have a reporting limit of quantitation (LOQ) of ~ 0.2 µg/L as determined from repeated assessment of analytical blanks and using the conventional approach of defining limit of quantitation as the mean blank + ten times the standard deviation around the mean blank. Though field blanks were not collected, prior arsenic sampling procedures indicate the unlikelihood that environmental source arsenic, unlike other metals, is present to contaminate samples during collection, a conclusion supported by the lack of contamination in field blanks for similar samples from domestic wells in New Hampshire (Flanagan et al. 2014). Samples with arsenic concentrations lower than the dilution-corrected LOQ on a given analytical session were ascribed as being below quantification level (bql). Threshold-based arsenic concentrations are used in the model with a conservative value of < 1 µg/L, thereby mitigating any influence of differences between the LOQ and bql.

To mitigate the absence of sequential field replicate samples, 14 samples with arsenic concentrations ranging from < 0.2 µg/L to > 30 µg/L were analyzed in triplicate as described above to assess the reproducibility of the results under different analytical sessions. Arsenic concentrations and their associated 2σ values are reported for each individual replicate (Appendix Table 1A). We interpret the assessment of duplicates to demonstrate that samples are reproducible within uncertainties of < ~10% (Appendix Table 1A).

To assess the accuracy and precision of the data, internationally certified reference materials were repeatedly analyzed during the course of analyses, generally yielding results in excellent agreement with accepted or recommended most probable values. Arsenic concentrations and their associated F-pseudosigma (fps) or 2σ values are reported for each individual replicate (Appendix Table 2A). The non-parametric fps approximates the standard deviation of traditional statistics when the data have a Gaussian distribution. The exception to this generalization lies in the one USGS standard close to the LOQ where the mean plus standard deviation fell just below the calculated most probable value (Appendix Table 2A). For the purpose of this study, larger uncertainties on low (< 0.5 µg/L) arsenic concentrations do not influence the use of these concentration data in the models since threshold-based arsenic concentrations are used as opposed to a continuous range of concentrations. Furthermore, it is important to note that the public health issues pertaining to safe drinking-water accessibility rely mostly on the 10 µg/L model—the internationally advised arsenic limit and highest arsenic concentration threshold modeled.

Probability Modeling

The original study used the SAS® System statistical software for logistic regression model development (SAS Institute, Inc. 2008; Ayotte et al. 2011). In this study, the models were tested and evaluated using R statistical software (R Core Team 2014). The original models, which identified the significant explanatory variables for each arsenic concentration threshold, were verified and subsequently tested in R system software as a mechanism of model validation. The multivariate logistic regression model operates on the assumption that the independent variables are directly related to the log-odds of the model, and is the appropriate alternative to a general linear model when dichotomous variables are involved (Hosmer and Lemeshow 2000; Menard 2002; Greene et al. 2005). The logistic regression models, which are a compilation of the most significant explanatory variables for a given threshold, take the following form:

$$P_{[y=1|x]} = \frac{e^{(\beta_0+\beta_1 x_1+\beta_2 x_2+\ldots+\beta_{kn} x_{kn})}}{1+e^{(\beta_0+\beta_1 x_1+\beta_2 x_2+\ldots+\beta_{kn} x_{kn})}} \quad \text{(Equation 1)}$$

where P is the predicted probability of arsenic concentrations in groundwater exceeding a specific threshold (1, 5, or 10 µg/L); y is an indicator (threshold) variable which denotes one of the two binary results (y=1 denoting arsenic occurrence above a given threshold, y=0 denoting arsenic presence at concentrations below a given threshold); $x_1, x_2, \ldots, x_k$ represent the significant explanatory or independent variables; $\beta_0, \beta_1, \ldots, \beta_k$ represent non-standardized variable coefficients; and n is the number of explanatory variables.

The three models are independent expressions of the predicted probabilities of arsenic exceeding three threshold concentrations of 1, 5, or 10 µg/L. As such, the models include only the most significant of the 374 potential explanatory

variables originally tested at that given threshold and contain differing combinations of explanatory variables and associated β coefficients represented in the logistic regression function. The number of explanatory variables used in each model ranges from 22 to 24 and they are described fully in Ayotte et al. (2011). These model-specific variables and beta coefficients from Ayotte et al. (2011) comprise the logistic regression models tested in this study.

Arsenic probabilities were predicted by the models for each observation in the testing dataset. The "predict" function in R was used to develop the arsenic probabilities given the coded multivariate logistic regression model and the set of selected explanatory variables that were associated with the sample locations for the testing dataset using a geographic information system (GIS) (Lombard et al. 2017). These predicted probabilities were converted into a binary variable based on a cutoff point of 0.5; that is, the value 0 was assigned to probabilities < 0.5 and the value 1 was assigned for probabilities ≥ 0.5. To determine the ability of the original model to generalize to the new testing dataset, the binary probabilities were then compared to the actual presence or absence of arsenic at or above each threshold concentration.

Using the testing dataset, the percentage rate that the models correctly predicted the probability of arsenic concentrations to be at or above a threshold, and below a threshold, was determined, and is defined in this study as "total accuracy."

The predictive accuracy of the models was also evaluated through the use of two other statistical constructs: sensitivity and specificity. Sensitivity refers to the frequency at which the model correctly identifies true positives, which is the rate of arsenic values at or above the threshold value. Specificity is the frequency of obtaining true negatives, which is the rate of arsenic values below the threshold value.

To evaluate model performance, three additional statistics were computed. The Pearson residual coefficients for each data point were calculated and mapped by threshold concentration and dataset. Residual coefficients ranging from -2 to 2 were defined as indicators of reasonably good model performance. Those outside of this range were denoted visually on maps to highlight points of significant under or over prediction. Another indicator of model performance is the area under the receiver operating characteristics (ROC) curve and is a measure of concordance (c statistic) or model discrimination. Values for the c statistic are between 0 and 1, with a value of 1 indicating that the model will always predict the correct outcome. Acceptable values for the c statistic are between 0.7 and 0.8, with excellent values between 0.8 and 0.9 (Hosmer and Lemeshow 2000). These calculations facilitated an evaluation of the overall fit of the multivariate logistic regression models to the testing data, thereby denoting the strengths and limitations of the models in predicting the probability of arsenic occurrence at various thresholds. In addition to accuracy, we use the Kappa (κ) statistic, which is a measure of agreement between model predictions and model observations, and also describes expected accuracy under chance agreement. Kuhn and Johnson (2013) used it as a metric for comparing binary prediction against observations. Values of κ range from -1 to 1, where values < 0 indicate little agreement, and those approaching 1 are in nearly complete agreement (Kuhn and Johnson 2013); many attempts to characterize acceptable values of κ have resulted in somewhat arbitrary thresholds.

Results

Three arsenic concentration thresholds (1, 5, and 10 µg/L) were used in the development of the original models. The percentage of samples where concentrations of arsenic were below the model threshold values differs between the model training dataset and model testing dataset (Table 1). The model training dataset has a larger percentage of samples with high (> 10 µg/L) arsenic concentrations. Only 31 percent of model training samples contain arsenic at less than 1 µg/L compared with 57 percent of the model testing samples. Twenty-one percent of the model training samples have arsenic concentrations greater than 10 µg/L compared to 11 percent of the model testing wells (Table 1).

The difference in arsenic concentrations between training and testing dataset samples is likely a reflection of the differences in geographic distribution among locations where samples were collected as opposed to other differences, such

as differences in data collection or laboratory procedures. Only 20.1 percent of the model training dataset are from the northwestern region of New Hampshire, while the remaining 79.9 percent of these data are from the southeastern region of the State (Figure 1). The testing dataset samples were intended originally for analysis of MTBE concentration in New Hampshire drinking water sources (Ayotte et al. 2005; 2008). As such, sample distribution was broader and more evenly spread across the state for the testing dataset than the training dataset used for arsenic model development; about 42 percent of the testing dataset are from the northwestern region of the state, and 58 percent are from the southeastern counties. The geographic differences in sample distribution across datasets enable model evaluation in previously less sampled regions.

Accuracy and Discrimination by Model Threshold and Dataset

Evaluation of the arsenic probability models with the testing dataset determined the ability of the models to resolve local spatial variability in arsenic concentrations and to predict to unsampled areas. Model accuracy increased with threshold concentration for the testing dataset (Table 2). Model accuracy increased between the training and testing dataset from 71.5 to 76.3 percent and 80.4 to 86.4 percent for the 5 µg/L and 10 µg/L models, respectively. The 1 µg/L threshold model, however, decreased in accuracy from 74.8 to 54.8 percent (27 percent decrease) from the training to the testing datasets. Compared to the 1µg/L threshold model, the 5 µg/L and 10 µg/L models performed better in terms of specificity for both the model training and testing datasets. However, the 1 µg/L model had greater sensitivity, demonstrating its heightened ability to differentiate where arsenic concentrations exceed the 1 µg/L threshold.

In terms of model discrimination, the 5 µg/L and 10 µg/L threshold models had comparable c-statistic values (ROC) in the training and testing datasets. The c-statistic value for the 1 µg/L was much lower for the testing data compared to the training data. The training data c-statistic increases with increasing model threshold concentration (Table 3), likely a reflection of the shifting proportion of non-events with increasing arsenic threshold. The 1 µg/L model may have a higher training c-statistic due to the relatively bigger difference between the ratio of events to non-events in the training and testing datasets compared to the other modeled thresholds (Table 1). Kappa statistic values are relatively low but have worth in the evaluation of their changes over the range of modeled thresholds for training and testing datasets and comparison to other model performance statistics. The testing data for the 10 µg/L threshold model have the lowest κ (0.101) but the highest accuracy value (Table 2). The low κ value likely reflects the small proportion of events above the 10 µg/L threshold indicated by the very low sensitivity value and high specificity value. The largest κ for the testing data is for the 5 µg/L threshold. This reflects the high specificity and moderate sensitivity values for that model. The κ values suggest that the best model is the one developed for the 5 µg/L threshold (Viera and Garret 2005).

Model Accuracy by Region

Evaluation of model accuracy by region (Figure 1, inset) indicated potentially important geographic differences in the ability of the models to correctly predict the probability of arsenic exceeding threshold concentrations. Differences in overall accuracy by region ranged from 4.0 to 34.4 percent depending upon the threshold arsenic concentration (Table 4). On average, the five northwestern counties had 83.1 percent accuracy across the three models, whereas the five southeastern counties had 63.7 percent accuracy.

Model results from the northwestern New Hampshire counties had the highest overall accuracies for all three threshold models with standard deviations ranging from 2.2 to 11.4 (average 5.5) (Figure 2 and Table 4). The southeastern counties, by contrast, had standard deviations ranging from 13.0 to 16.0 (average 14.1) — over two times that of the northwest (Figure 2 and Table 4). Though the standard deviations for the accuracy of the 1 µg/L model are similar between the northwest and southeast (11.4 and 13.0, respectively), standard deviations of accuracies between regions increase for the 5 and 10 µg/L models (Table 4). This reflects, in part, the fact that model accuracy is lower where arsenic concentrations are high, and have characteristically

Table 2. Summary of model performance (in percent) based on a 0.5 probability cutoff point.

Dataset	Accuracy (%)	Sensitivity (%)	Specificity (%)	Number of Observations
Arsenic concentrations ≥ 1 microgram per liter				
Training	74.8	92.3	40.9	1,543
Testing	54.8	68.6	44.5	367
Arsenic concentrations ≥ 5 micrograms per liter				
Training	71.5	38.3	88.4	1,689
Testing	76.3	29.4	87.0	367
Arsenic concentrations ≥ 10 micrograms per liter				
Training	80.4	19.2	96.6	1,691
Testing	86.4	12.5	95.4	367

Table 3. Summary of Kappa and c statistics for the 1, 5, and 10 micrograms per liter threshold logistic regression models for training and testing datasets.

Arsenic Concentration Threshold	Kappa Statistic, κ		c Statistic (area under receiver operating characteristics curve)	
	Training data	Testing data	Training data	Testing data
1 µg/L	0.372	0.124	0.772	0.574
5 µg/L	0.295	0.173	0.757	0.736
10 µg/L	0.211	0.101	0.770	0.771

high well-to-well variability. In areas with concentrations of arsenic that are predominantly low or below the threshold concentrations, the standard deviation is less and the results of the models are more accurate.

Differences in Pearson residuals are observable in the model training and testing datasets and high residuals (> 2 or < -2) are mapped for each threshold and dataset (Figure 3). Overall, the models fit the training dataset better than the model testing dataset, but this is in part due to the prevalence of non-events in the testing dataset. The residuals emphasize that the testing dataset performed relatively well for the 1 µg/L threshold model but that the larger positive and negative residuals in both the testing and training dataset were located dominantly in the southeast, suggesting a regional pattern to model performance metrics for the testing dataset consistent with the training dataset residuals. Regional patterns of Pearson residuals from the testing dataset indicate model performance and possible improvements to future models (Figure 3). For example, larger Pearson residuals from the testing dataset are more prevalent in the southeastern region of the state (Figure 1) for all threshold models, where arsenic concentrations also are more variable.

Discussion and Conclusion

Accuracy by Threshold Model and Study Dataset: A Reflection of Specificity Bias

The development and use of statistical models of contaminants seldom include the use of an

Table 4. Model accuracy (in percent) by region using the testing dataset [NA, not applicable].

Region	County	1 µg/L model			5 µg/L model			10 µg/L model		
		Accuracy	Sensitivity	Specificity	Accuracy	Sensitivity	Specificity	Accuracy	Sensitivity	Specificity
Northwestern New Hampshire	Coos	62.5	100	60.9	95.8	0	100	95.8	0	100
	Grafton	55.8	28.6	65.8	92.3	0	98.0	96.2	0	100
	Sullivan	47.4	71.4	33.3	100	NA	100	100	NA	100
	Cheshire	68.4	33.3	75.0	94.7	0	100	100	NA	100
	Carroll	40.0	50.0	36.7	97.5	100	97.4	100	NA	100
	Average ± 1σ	**54.8±11.4**	**56.7±29.5**	**54.3±18.4**	**96.1±2.9**	**25±50**	**99.1±1.3**	**98.4±2.2**	**0**	**100**
Southeastern New Hampshire	Belknap	31.3	55.6	0	68.8	25.0	83.3	87.5	0	100
	Merrimack	45.1	58.1	25.0	70.6	17.6	97.1	74.5	15.4	94.7
	Hillsborough	63.6	88.9	46.2	65.9	50.0	97.3	93.2	50.0	97.5
	Rockingham	60.3	91.9	15.4	69.8	41.2	80.4	79.4	0	92.6
	Strafford	53.8	69.2	23.1	33.3	25.0	39.1	59.0	11.1	73.3
	Average ± 1σ	**50.8±13.0**	**72.7±16.9**	**21.9±16.8**	**61.7 ± 16.0**	**31.8±13.4**	**79.4±23.8**	**78.7±13.2**	**15.3±20.6**	**91.6±10.6**

independent dataset to test their predictive performance. The independence of the new testing dataset and the differences in the spatial and concentration distributions were useful in assessing the performance of the previously published arsenic probability models. The model performance metrics of the testing dataset support the ability of the models to reasonably predict using independent data.

The shift of the testing dataset distribution curve towards lower concentrations relative to the training dataset indicates a divergence that may contribute to the heightened overall accuracy associated with the testing dataset (Figure 4). This is likely because only 31 percent of the model training dataset had concentrations less than 1 µg/L as compared to 57 percent of the testing dataset. It is likely that the enhanced model performance indicated by the new testing dataset is overwhelmingly reflective of model specificity bias — a product of the alignment of the multivariate logistic regression model with the more dominating population of lower arsenic concentrations. A heightened propensity to correctly discern where these low-arsenic samples occur allows the model to more accurately predict arsenic probability in a dataset dominated by low arsenic concentrations.

The increase in overall accuracy with concentration threshold may too be an indicator of enhanced model specificity. Whereas the frequency of high arsenic concentrations is lowest when considering the highest concentration threshold, the accuracy of the 10 µg/L threshold model also is the highest; relative to the other threshold models, it is more sensitive to the proportion of arsenic samples below a given threshold. It is likely, therefore, that patterns in model-specific accuracy are another reflection of the strengths and limitations of arsenic logistic regression modeling - specificity and sensitivity, respectively.

Regional Differences in Accuracy: Topics of Specificity and Inclusion of Additional Explanatory Variables

In addition to accuracy variation by threshold concentration (computed by county) for the testing dataset (Figure 5), the models showed regional differences in predictive accuracy (Table 4). The accuracy of overall predictive performance for the

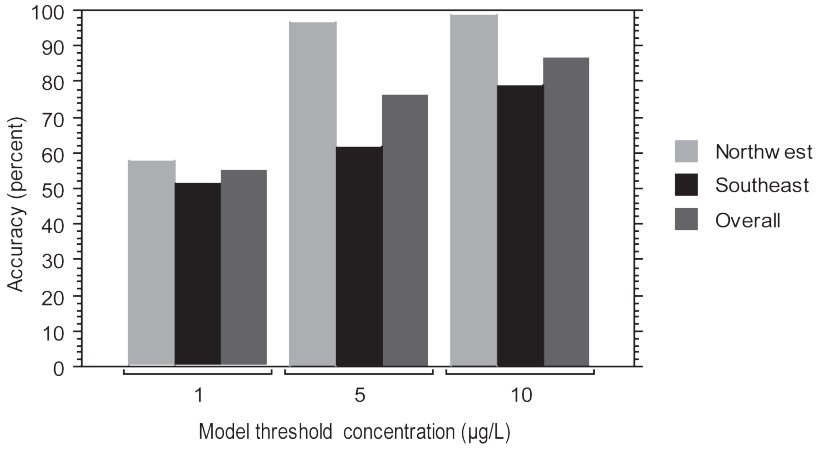

Figure 2. Accuracy (percent) of the 1, 5, and 10 µg/L arsenic concentration threshold models using the testing dataset (n = 367) separated regionally into southeastern, northwestern, and statewide data selections.

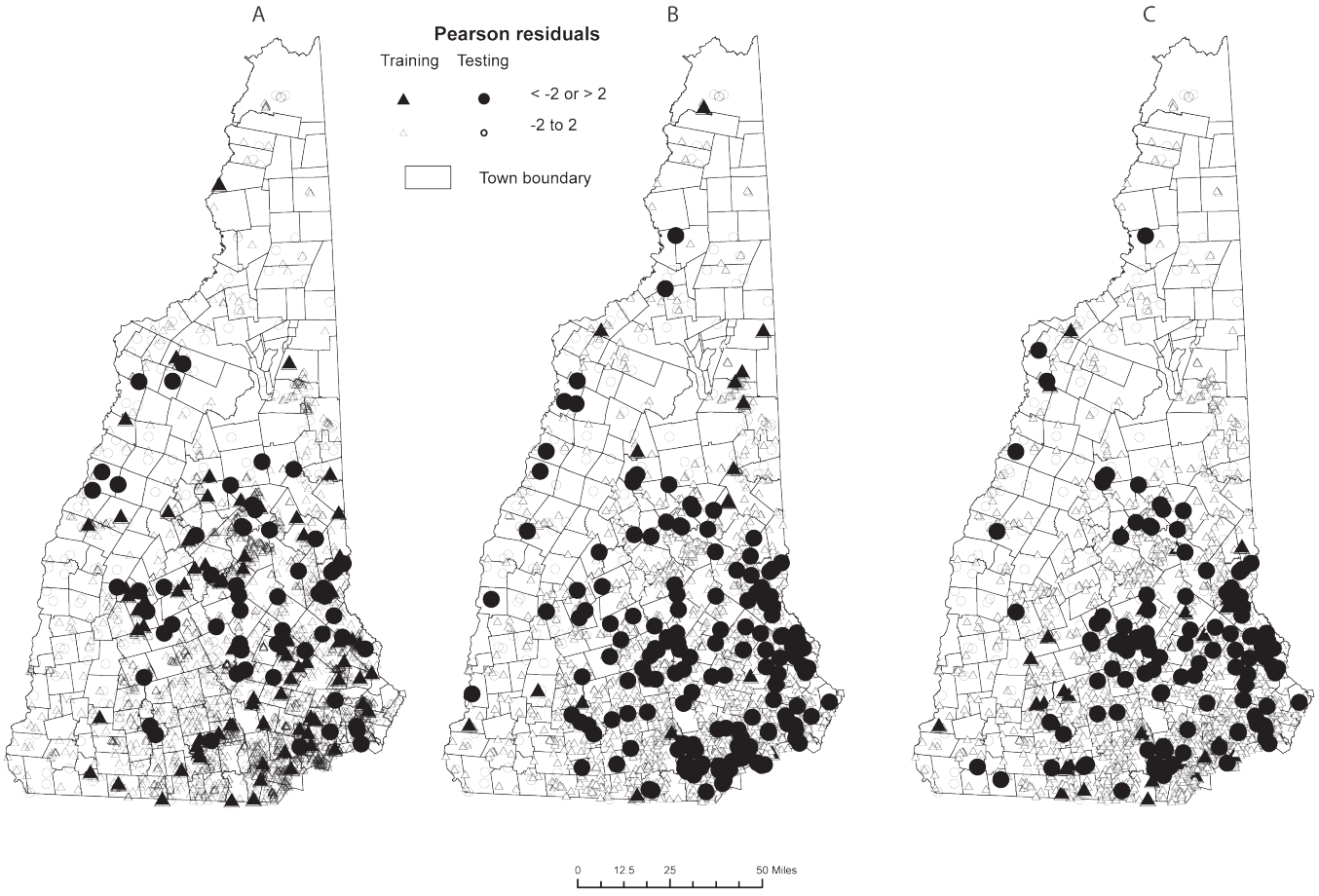

Figure 3. Model residuals by dataset and model threshold concentration for the (A) 1 µg/L, (B) 5 µg/L, and (C) 10 µg/L models.

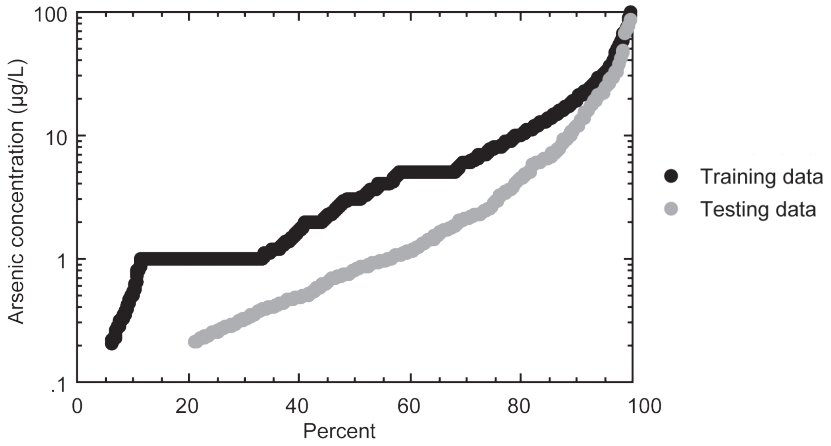

Figure 4. Cumulative distribution plot of arsenic concentration (µg/L) for the model training and testing datasets.

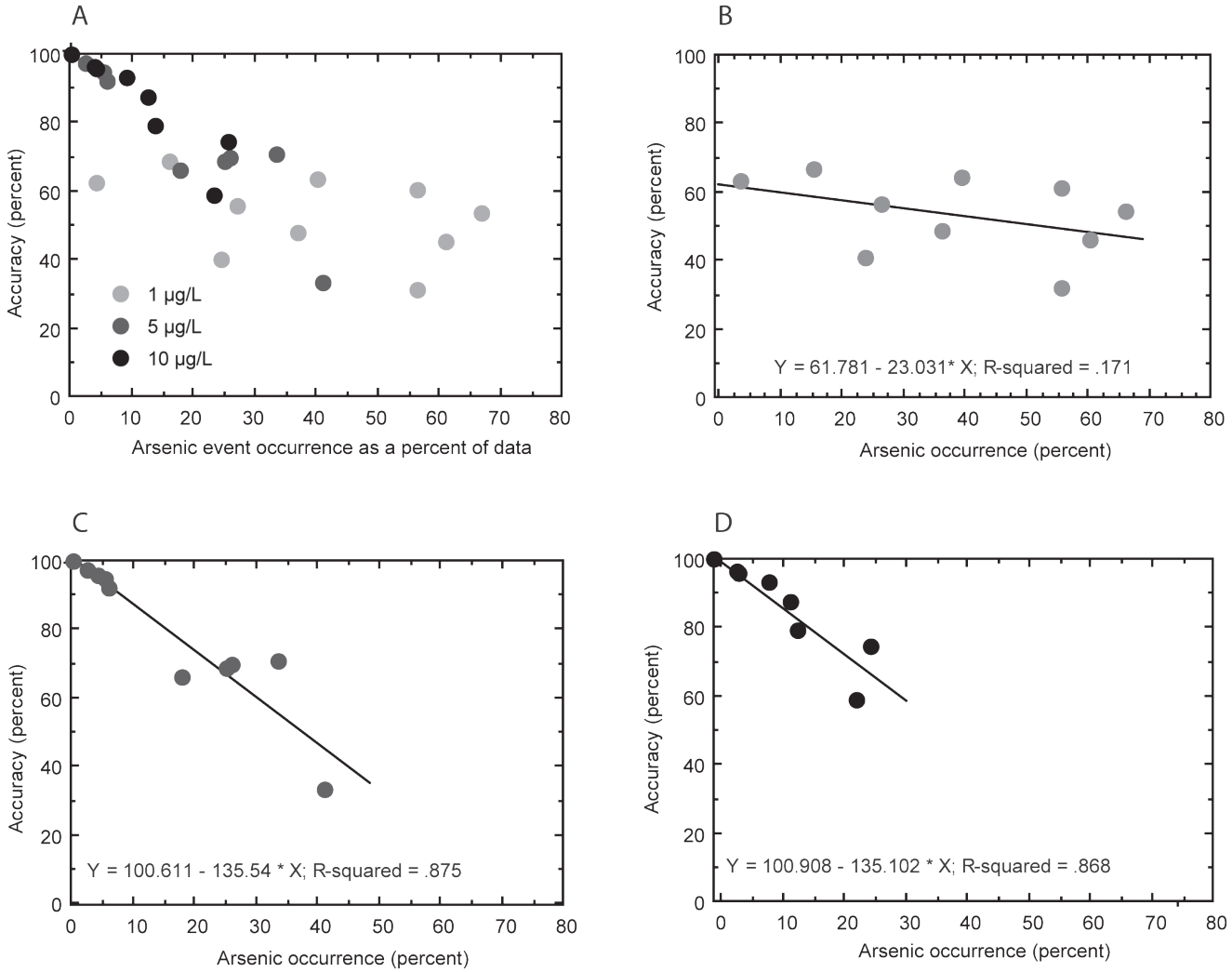

Figure 5. Accuracy (percent) as a function of arsenic occurrence for the testing dataset (n = 367) where each point represents the samples collected from a given county and accuracy and arsenic occurrence (A) all model threshold concentrations, (B) 1 µg/L model threshold concentration, (C) 5 µg/L model threshold concentration, and (D) 10 µg/L model threshold concentration.

models for the northwestern counties was higher than that for the southeastern region of the state—a result contrary to initial expectations based on distribution of the training and testing dataset samples by county. The majority of samples with inaccurate arsenic predictions were predominantly localized in the southeast. Thus, it appears that the regional difference in overall predictive performance can, in part, be attributed to improved specificity and the regional patterns of arsenic occurrence in the testing dataset.

It is possible that certain local geologic and geochemical explanatory variables present in select regions may play an important role in predicting local arsenic probability. If this is true, then future models may benefit from a design that better accounts for these regional differences, such is the case with ensemble-based regression tree models. It is also possible that yet unidentified locally important features related to arsenic occurrence (potential explanatory variables) have not been accounted for in the data or the model. Although both the model training and testing datasets appeared to have relatively comparable distributions of arsenic concentrations, closer examination by well type (public versus private domestic wells) reveals differences in sample distribution that may be of importance in model performance. Although no conclusive pattern was discerned regarding well type and arsenic presence in the model training dataset, private domestic wells had systematically higher concentrations of arsenic compared with public wells in the testing dataset (Figure 6).

The discernible spatial pattern in the distribution of arsenic by well type for the testing dataset seems to suggest that well type may indeed bear some capability to predict arsenic occurrence. Should this be the case, well type, unaccounted for in the original model, may be contributing to the lower instances of model performance and, as a result, may be an appropriate addition to maximize model performance. Furthermore, the varying geographic distribution of private domestic well use in New Hampshire may have some bearing on the differences in model accuracy by region.

Study Limitations

Model performance results using the testing dataset indicate a decrease in sensitivity, suggesting limited effectiveness in predicting the probability of arsenic in groundwater exceeding a specific threshold. Model inconsistencies may be traced back to varying sample spatial distribution between the original training and new testing datasets, distinctive geochemical and geological properties between the geographical areas sampled in the two different datasets, and natural temporal variability in groundwater arsenic (Ayotte et al. 2014). It is important to note that, although the quality of testing dataset used in our study is high overall, outlier inaccuracies in laboratory analysis would potentially have the effect of lowering the perceived model predictive performance.

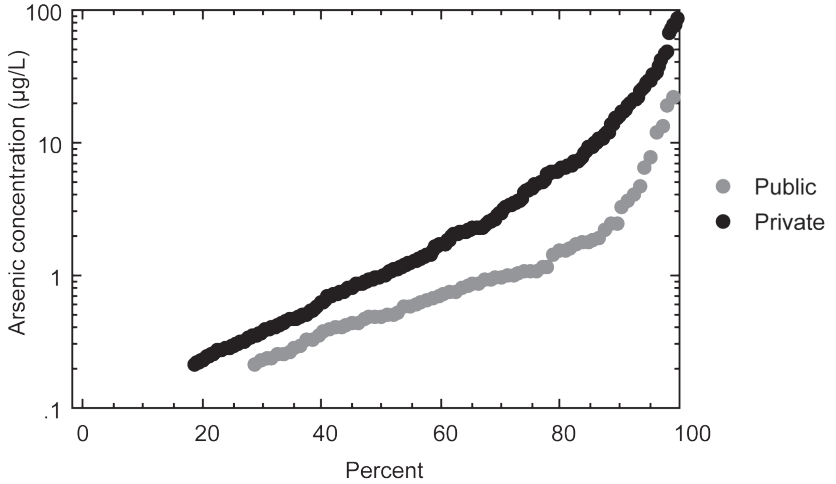

Figure 6. Cumulative distribution plot of arsenic concentration (µg/L) for the testing dataset, by well-type.

Other studies suggest the relevance of three-dimensional spatial characterization of samples as an explanatory variable of importance in arsenic prediction models (Flanagan et al. 2012; Ayotte et al. 2016). This model, taking into account only two-dimensional coordinate points, may be improved upon by considering sample depth as a potential explanatory variable. Flanagan et al. (2012) suggest well casing length as an important predictor of arsenic occurrence. Deep wells with long casings, drilled through deep bedrock fractures, facilitate the collection of old groundwater, which is typically alkaline and has arsenic concentrations leached from adjacent bedrock fracture surfaces. As groundwater well systems have increased in casing length and depth by an average of nearly 1 foot and 6 feet per year, respectively, over the past 30 years, the age of the well may also bear an effect on arsenic content in acting as a surrogate explanatory variable for aquifer depth (Ayotte et al. 2010). Although the age of the well was not reported in either the model training or testing datasets, it is possible that this explanatory variable is influential in predicting arsenic occurrence. Consideration of these features may be appropriate in designing a model with improved accuracy in future studies.

Such wide ranging variability in model predictive performance across regions and model thresholds may suggest limitations of logistic regression models in describing groundwater arsenic probability. Development of other types of models may improve predictive accuracy and ultimately may enhance preventative public health action in ensuring safe drinking water accessibility around the world. Recent studies suggest that, although logistic regression modeling is suitable for developing models of arsenic probability, sensitivity may be enhanced through the use of ensemble gradient boosting modeling techniques such as the boosted regression tree methods (Elith et al. 2008; Kuhn 2014; Nolan et al. 2015; Ridgeway 2015; Ayotte et al. 2016).

Nevertheless, it is important to note that the probability models evaluated here have provided New Hampshire with public health improvement potential that goes beyond individual well assessment. Specifically, they provide a statewide snapshot of the predicted probability of arsenic concentrations in groundwater exceeding specific thresholds in New Hampshire that may be used in conjunction with other data, such as disease outcome data, to ultimately guide outreach and education efforts as well as evaluation of exposure risk and resource allocation. This and other modeling procedures, reliant upon well-established, accessible, and mappable explanatory variables, provide a potentially powerful tool in reducing arsenic-associated, regionally specific rates of disease. Furthermore, evaluation of models with independent data, as demonstrated here, may help with the assessment and improvement of our understanding of arsenic in other areas around the globe and may be instrumental in the characterization of other hazardous environmental contaminants.

Acknowledgments

We thank the private citizens and public utilities participating in sample collection for this study. Funding for CMA's work in this study from the USGS Office of Science Quality and Integrity's Youth and Education in Science Program is gratefully acknowledged. We also thank Leslie DeSimone and Gardner Bent for their help with data-quality evaluation and the two anonymous journal reviewers for their contributions. We thank John Clark for assisting with arsenic analysis of well water samples used in this study. The authors also thank Anna Glover and Eliza Gross with the U.S. Geological Survey and two anonymous reviewers for constructive editorial review. Funding for the analytical work cited in this paper was provided by the USGS Water Resources Research Institute and the University of New Hampshire to JGB. Any use of trade, firm, or product names is for descriptive purposes only and does not imply endorsement by the U.S. Government.

Author Bio and Contact Information

Caroline M. Andy is a biological chemistry undergraduate student at Bates College. She can be contacted at U.S. Geological Survey, New England Water Science Center, New Hampshire-Vermont Office, 331 Commerce Way, Suite 2, Pembroke, NH 03275 or by email at candy@usgs.gov or at Bates College, 2 Andrews Road, Lewiston, Maine 04240, email candy@bates.edu.

Maria Florencia Fahnestock is a Research Scientist at the University of New Hampshire with expertise in analytical geochemistry. She can be contacted at Department of Earth Sciences, University of New

Hampshire, 56 College Road, 214 James Hall, Durham, NH 03824 or by email at Florencia.fahnestock@unh.edu.

Melissa A. Lombard is a lecturer at the University of New Hampshire and is affiliated with the U.S. Geological Survey. She can be contacted at Department of Earth Sciences, University of New Hampshire, 56 College Road, 214 James Hall, Durham, NH 03824 or by email at Melissa.Lombard@unh.edu or at the U.S. Geological Survey, New England Water Science Center, New Hampshire-Vermont Office, 331 Commerce Way, Suite 2, Pembroke, NH 03275, email at mlombard@usgs.gov.

Laura Hayes is a Physical Scientist and GIS Specialist in the USGS New England Water Science Center. She can be contacted at U.S. Geological Survey, New England Water Science Center, New Hampshire-Vermont Office, 331 Commerce Way, Suite 2, Pembroke, NH 03275 or by email at lhayes@usgs.gov.

Julia G. Bryce is a Professor of Geochemistry at the University of New Hampshire. She can be contacted at Department of Earth Sciences, University of New Hampshire, 56 College Road, 214 James Hall, Durham, NH 03824 or by email at julie.bryce@unh.edu.

Joseph D. Ayotte is a Supervisory Hydrologist for the Groundwater Quality Studies Section in the USGS New England Water Science Center. He can be contacted at U.S. Geological Survey, New England Water Science Center, New Hampshire-Vermont Office, 331 Commerce Way, Suite 2, Pembroke, NH 03275 or by email at jayotte@usgs.gov.

Appendix

Table 1A. Duplicate analysis of New Hampshire drinking water samples.

UNH ID	USGS Obs ID	Date of Analysis (month/day/year)	As, µg/L	2σ
44	208	12/1/2012	0.3	0.02
		1/1/2013	0.3	0.01
		Mean	0.3	
		RPD (%)	2	
46	213	11/1/2013	5.0	0.2
		11/1/2013	4.8	0.4
		Mean	4.9	
		RPD (%)	3	
120	387	11/1/2013	0.1	0.02
		11/1/2013	0.1	0.00
		Mean	0.1	
		RPD (%)	3	

Table 1A Continued.

UNH ID	USGS Obs ID	Date of Analysis (month/day/year)	As, µg/L	2σ
281	233	1/1/2013	1.3	0.08
		2/1/2014	1.5	0.02
		Mean	1.4	
		RPD (%)	11	
363	610	1/1/2013	1.2	0.04
		2/1/2014	1.2	0.04
		Mean	1.2	
		RPD (%)	4	
365	737	1/1/2013	11.1	0.3
		2/1/2014	10.9	0.6
		Mean	11.0	
		RPD (%)	2	
388	758	1/1/2013	30.0	1.0
		2/1/2014	29.6	0.7
		Mean	29.8	
		RPD (%)	1	
389	327	1/1/2013	0.6	0.02
		2/1/2014	0.7	0.01
		Mean	0.7	
		RPD (%)	6	
411	766	1/1/2013	65.9	2.2
		2/1/2014	70.7	5.5
		Mean	68.3	
		RPD (%)	7	
446	745	11/1/2013	0.3	0.01
		11/1/2013	0.3	0.00
		Mean	0.3	
		RPD (%)	7	
455	-	1/1/2013	4.7	0.1
		3/1/2013	4.5	0.4
		Mean	4.6	
		RPD (%)	4	
468	-	5/1/2013	12.4	0.5
		5/1/2013	11.7	0.1
		Mean	12.0	
		RPD (%)	6	
499	876	5/1/2013	1.0	0.01
		5/1/2013	1.0	0.02
		Mean	1.0	
		RPD (%)	6	
511	851	2/1/2014	58.7	1.7
		2/1/2014	61.1	0.6
		Mean	59.9	
		RPD (%)	4	

Table 2A. Quality Control Standards analyzed for total Arsenic.

Quality Control Standard (QCS)	Number of Analyses	Mean As (µg/L)	2σ (µg/L)	QCS Accepted As (µg/L)	f-pseudosigma (fps)	Accuracy[b] (%)
NIST 1643e	154	61.9	3.0	60.5	0.7[a]	98
USGS RR T187	59	1.3	0.7	1.2	0.1	91
USGS RR T201	39	26.2	2.0	24.4	1.6	93
USGS RR T211	15	5.5	1.0	5.0	0.5	90
USGS RR T213	33	1.0	0.3	1.0	0.06	96
USGS RR T215	12	0.4	0.1	0.5	0.1	81
USGS RR T217	13	5.9	0.5	6.0	0.4	98

[a]Expanded uncertainty based on 1σ.
[b]Accuracy (%) defined as the ratio of the mean measured value to the accepted value.

References

Ayotte, J.D., D.M. Argue, and F.J. McGarry. 2005. Methyl *tert*-butyl ether occurrence and related factors in public and private wells in southeast New Hampshire. *Environmental Science and Technology* 39: 9-16. DOI: 10.1021/es049549e. Accessed March 3, 2017.

Ayotte, J.D., D.M. Argue, F.J. McGarry, J.R. Degnan, L. Hayes, S.M. Flanagan, and D.R. Helsel. 2008. Methyl *tert*-butyl ether (MTBE) in public and private wells in New Hampshire: Occurrence, factors, and possible implications. *Environmental Science and Technology* 42: 677-684. DOI: 10.1021/es071519z. Accessed March 3, 2017.

Ayotte, J.D., M. Belaval, S.A. Olson, K.R. Burow, S.M. Flanagan, S.R. Hinkle, and B.D. Lindsey. 2014. Factors affecting the temporal variability of arsenic in groundwater used for drinking water supply in the United States. *Science of the Total Environment* 505: 1370-1379. DOI: 10.1016/j.scitotenv.2014.02.057. Accessed March 3, 2017.

Ayotte, J.D., M. Cahillane, L. Hayes, and K.W. Robinson. 2011. *Estimated Probability of Arsenic in Groundwater from Bedrock Aquifers in New Hampshire.* U.S. Geological Survey Scientific Investigations Report 2012-5156. Available at: https://pubs.usgs.gov/sir/2012/5156/. Accessed March 3, 2017.

Ayotte, J.D., B.M. Kernen, D.R. Wunsch, D.M. Argue, D.S. Bennett, and T.J. Mack. 2010. *Preliminary Assessment of Trends in Static Water Levels in Bedrock Wells in New Hampshire, 1984 to 2007*. U.S. Geological Survey Open-File Report 2010-1189. Available at: http://pubs.usgs.gov/of/2010/1189/. Accessed March 3, 2017.

Ayotte, J.D., D.L. Montgomery, S.M. Flanagan, and K.W. Robinson. 2003. Arsenic in groundwater in eastern New England: Occurrence, controls, and human health implications. *Environmental Science and Technology* 37(10): 2075-2083. DOI: 10.1021/es026211g. Accessed March 3, 2107.

Ayotte, J.D., B.T. Nolan, J.R. Nuckols, K.P. Cantor, G.R. Robinson, Jr., D. Baris, L. Hayes, M. Karagas, W. Bress, D.T. Silverman, and J.H. Lubin. 2006. Modeling the probability of arsenic in groundwater in New England as a tool for exposure assessment. *Environmental Science and Technology* 40 (11): 3578-3585. DOI: 10.1021/es051972f. Accessed March 3, 2017.

Ayotte, J.D., B.T. Nolan, and J.A. Gronberg. 2016. Predicting arsenic in drinking water wells of the Central Valley, California. 2016. *Environmental Science and Technology* 50(14): 7555-7563. DOI 10.1021/acs.est.6b01914. Accessed March 3, 2017.

Baris, D., R. Waddell, L.E.B. Freeman, M. Schwenn, J.S. Colt, J.D. Ayotte, M.H. Ward, J. Nuckols, A. Schned, B. Jackson, C. Clerkin, N. Rothman, L.E. Moore, A. Taylor, G. Robinson, G.M.M. Hosain, K.R. Armenti, R. McCoy, C. Samanic, R.N. Hoover, J.F. Fraumeni, Jr., A. Johnson, M.R. Karagas, and D.T. Silverman. 2016. Elevated bladder cancer in northern New England: The role of drinking water and arsenic. *Journal of the National Cancer Institute* 108(9). DOI: 10.1093/jnci/djw099. Accessed March 3, 2017.

Elith, J., J.R. Leathwick, and T.J. Hastie. 2008.

A working guide to boosted regression trees. *Journal of Animal Ecology* 77(4): 802-813. DOI: 10.1111/j.1365-2656.2008.01390.x. Accessed March 3, 2017.

Fahnestock, M.F., M.A. Lombard, J.C. Clark, J.G. Bryce, and J.D. Ayotte. 2017. *Concentrations of Arsenic in Water from Public-Supply and Domestic Wells in New Hampshire*. U.S. Geological Survey data release. Available at: http://dx.doi.org/10.5066/F7JM27R9. Accessed March 3, 2017.

Feldmann, C.R., J.B. Walasek, and L.B. Lobring. 1992. Procedure for preserving lead in drinking water samples. *American Water Works Association* 84(7): 89-91.

Flanagan, S.M., J.D. Ayotte, and G.P. Robinson, Jr. 2012. *Quality of Water from Crystalline Rock Aquifers in New England, New Jersey, and New York, 1995-2007*. U.S. Geological Survey Scientific Investigations Report 2011-5220. Available at: http://pubs.usgs.gov/sir/2011/5220/. Accessed March 3, 2017.

Flanagan, S.M., M. Belaval, and J.D. Ayotte. 2014. *Arsenic, Iron, Lead, Manganese, and Uranium Concentrations in Private Bedrock Wells in Southeastern New Hampshire, 2012-2013*. U.S. Geological Survey Fact Sheet 2014-3042. Available at: https://dx.doi.org/10.3133/fs20143042. Accessed March 3, 2017.

Graney, J.R. and M.S. Landis. 2013. Coupling meteorology, metal concentrations and Pbisotopes for source attribution in archived precipitation samples. *Science of the Total Environment* 448: 141-150. DOI: 10.1016/j.scitotenv.2012.07.031. Accessed March 3, 2017.

Greene, E.A., A.E. LaMotte, and K-A. Cullinan. 2005. *Ground-Water Vulnerability to Nitrate Contamination at Multiple Thresholds in the Mid-Atlantic Region Using Spatial Probability Models*. U.S. Geological Survey Scientific Investigations Report 2004-5118. Available at: http://pubs.usgs.gov/sir/2004/5118/. Accessed March 3, 2017.

Hosmer, D.W. and S. Lemeshow. 2000. *Applied Logistic Regression*, 2nd Ed. John Wiley and Sons, New York.

Klaue, B. and J.D. Blum. 1999. Trace analyses of arsenic in drinking water by inductively coupled plasma mass spectrometry: High resolution versus hydride generation. *Analytical Chemistry* 71(7): 1408-1414.

Kuhn, M. 2016. The 'caret' Package. Available at: http://topepo.github.io/caret/index.html. Accessed March 3, 2017.

Kuhn, M. and K. Johnson. 2013. *Applied Predictive Modeling*, 1st Ed. Springer, New York.

Lombard, M.A, L. Hayes, C.M. Andy, M.F. Fahnestock, J.G. Bryce, and J.D. Ayotte. 2017. *Testing Data Set for Independent Analysis of New Hampshire Arsenic Model*. U.S. Geological Survey data release. Available at: https://www.sciencebase.gov/catalog/item/5877e09be4b0b8c259c4875b. Accessed March 3, 2017.

Menard, S. 2002. *Applied Logistic Regression Analysis*, 2nd Ed. Sage University Papers Series on Quantitative Applications in the Social Science, series no. 07-106. Sage Publications, Inc., Thousand Oaks, California.

Moore, R.B. 2004. *Quality of Water in the Fractured-Bedrock Aquifer in New Hampshire*. U.S. Geological Survey Scientific Investigations Report 2004-5093. Available at: http://pubs.usgs.gov/sir/2004/5093/. Accessed March 3, 2017.

Nolan, B.T., K.J. Hitt, and B.C. Ruddy. 2002. Probability of nitrate contamination of recently recharged groundwaters in the conterminous United States. *Environmental Science and Technology* 36: 2138-2145.

Nolan, B.T., M.N. Fienen, and D.L. Lorenz. 2015. A statistical learning framework for groundwater nitrate models of the Central Valley, California, USA. *Journal of Hydrology* 531 (part 3): 902-911. DOI: 10.1016/j.jhydrol.2015.10.025. Accessed March 3, 2017.

Peters, S.C. and J.D. Blum. 2003. The source and transport of arsenic in a bedrock aquifer, New Hampshire, USA. *Applied Geochemistry* 18(11): 1328-1333. DOI: 10.1016/S0883-2927(03)00109-4. Accessed March 3, 2017.

R Core Team. 2014. R: A language and environment for statistical computing. R Foundation for Statistical Computing, Vienna, Austria. Available at: http://www.R-project.org/. Accessed March 3, 2017.

Ridgeway, G. 2015. Package 'gbm', The R Project for Statistical Computing. Available at: https://cran.r-project.org/web/packages/gbm/gbm.pdf. Accessed March 3, 2017.

SAS Institute Inc. 2008. SAS OnlineDoc 9.1.3: SAS Institute, Inc. Available at: http://support.sas.com/onlinedoc/913/docMainpage.jsp. Accessed March 3, 2017.

Shi X., J.D. Ayotte, A. Onda, S. Miller, J. Rees, D. Gilbert-Diamond, T. Onega, J. Gui, M. Karagas, and J. Moeschler. 2015. Geospatial association between adverse birth outcomes and arsenic in groundwater

in New Hampshire, USA. *Environmental Geochemistry and Health* 37(2): 333-351. DOI: 10.1007/s10653-014-9651-2. Accessed March 3, 2017.

Smith, A.H., C. Hopenhayn-Rich, M.N. Bates, H.M. Goeden, I. Hertz-Picciotto, H.M. Duggan, R. Wood, M.J. Kosnett, and M.T. Smith. 1992. Cancer risks from arsenic in drinking water. *Environmental Health Perspectives* 97: 259-267.

Squillace, P.J., M.J. Moran, W.W. Lapham, C.V. Price, R.M. Clawges, and J.S. Zogorski. 1999. Volatile organic compounds in untreated ambient groundwater of the United States, 1985-1995. *Environmental Science and Technology* 33: 4176-4187.

Teso, R.R., M.P. Poe, T. Younglove, and P.M. McCool. 1996. Use of logistic regression and GIS modeling to predict groundwater vulnerability to pesticides. *Journal of Environmental Quality* 25: 425-432.

U.S. Census Bureau. 1999. Historical Census of Housing Tables - Sources of Water. Available at: http://www.census.gov/hhes/www/housing/census/historic/water.html. Accessed March 3, 2017.

U.S. Environmental Protection Agency. 1996. *Method 1669: Sampling Ambient Water for Trace Metals at EPA Water Quality Criteria Levels*. Available at: https://nepis.epa.gov/Exe/tiff2png.cgi/P100536O.PNG?-r+75+-g+7+D%3A%5CZYFILES%5CINDEX%20DATA%5C95THRU99%5CTIFF%5C00001998%5CP100536O.TIF. Accessed March 3, 2017.

U.S. Geological Survey. 2006. Collection of water samples (ver. 2.0). In: *U.S. Geological Survey Techniques of Water-Resources Investigations*, Book 9, Chapter A4. Available at: http://pubs.water.usgs.gov/twri9A4/. Accessed March 3, 2017.

Viera, A.J. and J.M. Garret. 2005. Understanding interobserver agreement: The kappa statistic. *Family Medicine* 37(5): 360-363.

World Health Organization. 2012. Arsenic. World Health Organization Fact Sheet.

Yang, Q., H.B. Jung, R.G. Marvinney, C.W. Culbertson, and Y. Zheng. 2012. Can arsenic occurrence rates in bedrock aquifers be predicted? *Environmental Science and Technology* 46(4): 2080-2087.

Zheng, Y. and J.D. Ayotte. 2015. At the crossroads: Hazard assessment and reduction of health risks from arsenic in private well waters of the northeastern United States and Atlantic Canada. *Science of The Total Environment* 505: 1237-1247.

Universities Council on Water Resources
Journal of Contemporary Water Research & Education
Issue 160, Pages 42-59, April 2017

Searching for Antibiotic Resistance Genes in a Pristine Arctic Wetland

Krystalle S. Diaz[1,4], Virginia I. Rich[2], *Jean E. McLain[3]

[1]University of New Hampshire, Molecular, Cellular, and Biomedical Sciences, [2]Ohio State University, Department of Microbiology, [3]University of Arizona, Water Resources Research Center, [4]Work conducted at The University of Arizona, Department of Soil, Water, and Environmental Science
**Corresponding author*

Abstract: Antibiotics are the foundation of modern medicine, and the sustainability of antibiotic use depends on overcoming the challenge of antibiotic resistance (AR). This may be extremely difficult, given that antibiotic production by environmental microbiota is a natural process and AR is widespread in nature. AR has been shown to spread readily and quickly, as well as to exist in the absence of anthropogenic forcing (i.e., the application of antibiotics by humans). This study compared a range of approaches to identify AR gene sequences in microbial community genomes in three habitats (Palsa, Bog, and Fen) across a permafrost thaw gradient in Abisko, Sweden. Depending on the search algorithm used, we found a range of 0.72-1.29% AR protein-coding genes across all habitats, with model-based search algorithms resulting in greater sensitivity than traditional identity-based approaches for identifying AR sequences. Though each habitat within the permafrost gradient showed different cell densities, pH, bioavailable carbon, water content, nutrient availability, and other factors that impact microbial life, the difference in overall AR protein abundance between habitats was not significant. Examination of AR at this location will contribute to our understanding of AR presence in natural environments and how AR may be impacted by permafrost thawing related to global warming.

Keywords: *metagenomics, microbial communities, climate change, soil resistome, permafrost*

In recent years, there has been rising global concern regarding the emergence and increase of antibiotic resistant pathogens (Allen et al. 2010; D'Costa et al. 2011; World Health Organization 2014). While these concerns have been centered in health care settings, there is growing awareness that human use of antibiotics in medical, veterinary, agricultural, and wastewater treatment settings may lead to environmental spread of antibiotic resistance (AR) that is anthropogenic in origin. The spread of AR via reclaimed wastewater irrigation and its potential subsequent spread into the human health chain is an especially pressing concern in arid and semiarid ecosystems, where such irrigation is common. In the Southwest United States, reclaimed wastewater is used for environmental remediation, irrigation of golf courses and other recreational areas, and also irrigation of food crops. While bacterial indicator levels allowed in reclaimed water for different uses are carefully controlled, the levels of antibiotics and AR genes are wholly unregulated. Only the most modern municipal wastewater treatment plants are able to eliminate emerging microparticles such as antibiotics (McLain and Williams 2014), and thus antibiotics present in reclaimed wastewater could, in theory, induce survival of resistant bacteria (Wright 2007; Martinez 2009; Allen et al. 2010; Martinez 2012; Li et al. 2015). However, establishing the potential for antibiotic usage to induce AR in surrounding environments requires a clear understanding of natural, "default" AR levels and diversity existing prior to anthropogenic forcing.

Resistance to antibiotics is ancient, and evolutionary mechanisms that confer resistance in the wild are often similar to clinical variants (D'Costa et al. 2011). AR has been found in natural

environments such as caves, deep and ancient ice cores, and permafrost (reviewed in D'Costa et al. 2011). It is hypothesized that pressures such as resource competition, microbial signal trafficking, and/or detoxification may facilitate AR spread in natural environments (Dantas et al. 2008; Davies and Davies 2010; D'Costa et al. 2011; Nesme et al. 2014). Thus, assessing the potential for anthropogenically-produced antibiotics to increase resistance in natural environments must take into account the confounding factor of natural AR.

Despite the well-known presence of AR in the natural environment, studies analyzing AR spread in the environment due to anthropogenic activities such as reclaimed wastewater use or agricultural antibiotic use often lack control sites unimpacted by human activities. Though this could lead to erroneous conclusions about potential impacts of human-induced AR development, it is becoming increasingly clear that AR levels are often higher in human-impacted sites than in natural environments (Li et al. 2015). A critical research task highlighted by recent work (e.g., Durso et al. 2012; Nesme et al. 2014) is the establishment of a baseline of natural AR abundance. Such information will be crucial in addressing the question of anthropogenic influence on AR spread in natural and human-created environments alike. If AR levels and diversity in human-impacted sites differ from those in natural sites, it follows that there is basis for claims of anthropogenic AR.

A limited number of studies have analyzed AR presence in natural environments using next generation sequencing tools. Next generation sequencing tools allow scientists to analyze microbial community genes (metagenomics) and gene products and to estimate the abundance of target genes with improved accuracy. AR studies which have used metagenomic methods have found AR in clinical, agricultural, veterinary, and treated wastewater samples as well as in natural environments (Durso et al. 2012; Hu et al. 2013; Nesme et al. 2014). These studies use identity-based methods, primarily BLAST (Basic Local Alignment Search Tool), to identify similar regions between protein, DNA, or RNA sequences (Johnson et al. 2008).

Published AR sequences in gene and protein databases are dominated by AR variants from clinical samples, but environmental datasets invariably contain uncharacterized bacteria whose AR variants may prevent their identification through traditional identity-based searches. Newer, model-based approaches increase search sensitivity for metagenomic data, which is particularly useful in datasets whose sequence variants are likely to be divergent from published AR sequences. In general, environmental AR studies use permissive BLAST cutoffs (ex: ≥35% identity to known sequences), as compared to the ≥80% or ≥97% identity cutoffs typically used for classification of sequences. This allows for better identification of sequences in environmental datasets that will differ from their clinical, published counterparts.

Three metagenomics AR studies, two environmental (Durso et al. 2012; Nesme et al. 2014) and one clinical (Hu et al. 2013), have most informed the current work. In these three studies, the range of AR genes in environmental, agricultural, gut, and fecal metagenomes was 0.05-7.4% of overall metagenome content, with the highest diversity of AR found in soil metagenomes. Each of these studies uses identity-based methods. None of them analyze AR spread within or to natural habitats, only AR gene presence within publically available metagenomes. Recently, AR studies using next generation sequencing methods to analyze community AR have become more common (Fouhy et al. 2015; Li et al. 2015; Johnson et al. 2016). Johnson et al. (2016) found that AR genes on swine farms clustered together, leading to multiple AR enriched bacterial communities, regardless of bacterial community composition. The authors state such enrichment is likely due to high selective pressures from farm usage of a subset of chemicals to which the clusters confer resistance, leading to enrichment of already available genes.

Here, we demonstrate a potentially more effective method to identify AR-coding genes in metagenomic datasets than methods used in traditional identity-based approaches. In order to gauge a baseline for AR in a natural wetland, our study mined three arctic wetland metagenomes (Woodcroft et al. in prep) for predicted AR genes and their products. Examination of AR in the Swedish permafrost sites will contribute to understanding AR presence and diversity in natural wetlands. This

is critical before addressing concerns regarding human-induced AR, as human-impacted sites are expected to differ from their natural counterparts. Mere AR presence or similar AR levels would not necessarily mean AR spread, but a difference between natural and impacted AR diversity and level would be expected. The present study tested four algorithms for analyzing metagenomic data, two of them identity-based (BLAST) methods commonly used in AR metagenome studies, and two model-based (via hidden Markov models) methods, to assess the presence of AR genes along a relatively pristine permafrost thaw gradient in Abisko, Sweden. For the purposes of this paper, "pristine" includes natural sites impacted by climate change. Abisko is the site of a research station studying the impact of climate change in the region. Changes in climate have induced permafrost thaw globally (Intergovernmental Panel on Climate Change 2014), and its impact on habitat greenhouse gas emissions (McCalley et al. 2014), soil organic matter (Hodgkins et al. 2014), and microbiota (Mondav et al. 2014).

Methods

Study Site

The study site is Stordalen Mire, a thawing permafrost mosaic system near the Abisko Research Station in Abisko, Sweden. The Mire is relatively pristine, with minimal recorded human impacts, and is composed of three main habitats spanning a permafrost thaw gradient (Figure 1). These habitats are Palsa (intact permafrost which is ~30-40 cm below the surface, dry, dominated by ericaceous shrubs); Bog (intermediate permafrost thaw which is 60-90 cm below the surface, with a perched rainwater-fed water table, and dominated by *Sphagnum spp.* peat moss); and Fen (fully thawed with no detectable permafrost in the upper meter, inundated, continuous with groundwater, and dominated by sedges). In addition to thaw and water content gradients, there is also a nutrient content and microbial diversity gradient, with an increase in both from the Palsa to the Fen (McCalley et al. 2014; Mondav et al. 2014). Material was collected from triplicate cores from each of the habitats in June 2012, from three depths (Table 1) through the active surface layer of the soil above the permafrost (where present) subject to annual thaw.

DNA Extraction, Sequencing, and Metagenome Processing

DNA was extracted using a variation of the PowerMax DNA Isolation Kit #12966-10 (Mo Bio Laboratories, Inc., USA), retaining the preservation solution during lysis, as in Mondav et al. (2014). This kit extracts genomic DNA as well as plasmids, which house many known AR genes (Martinez 2008; Allen et al. 2010; D'Costa et al. 2011; McArthur et al. 2013). Bulk DNA extracts were sequenced on an Illumina HiSeq (Illumina Inc., USA), with paired-end reads. All sequences from each habitat were pooled and assembled with the Australian Centre for Ecogenomics (ACE) Assembly Pipeline (as in Mondav et al. 2014), resulting in assemblies with 567,790 contigs (overlapping sequence data reads ≥500 bp) in the Palsa, 400,114 contigs in the Bog, and 749,828 contigs in the Fen (Table 1). Metagenome annotation and protein-coding sequence prediction were carried out with Prokka (v.1.11) (Seemann 2014), using the *--metagenome* flag and otherwise default parameters. These data are summarized in Table 1, and are part of a larger dataset that describes the shifting microbiology over space and time in this ecosystem (Woodcroft et al., in preparation). The sequences recovered in this study are available at https://github.com/ksdiaz/AR_project/.

Overall Workflow

To locate AR genes in the habitat datasets, we used (i) BLAST for comparison to published studies, and (ii) the HMMer (v3.0) software package (Finn et al. 2015). HMMer employs a model-building method that compares known variants of a specific gene or protein and models conserved versus variable sites, with more weight given to matches for the conserved sites. Profile HMMs (hidden Markov models) in HMMer are statistical models of sequence alignments based on consensus of protein structure and conservation. Although many AR genes evolve naturally in soils, clinical AR sequences are likely to have diverged from their wild counterparts. However, the active sites of the proteins still accomplish the same biological tasks and are likely conserved. Thus,

environmental AR genes may be identified by homology-based approaches when they cannot be identified using identity-based measures, making an HMM-based method a useful complementary approach. Other studies have lowered BLAST cutoffs to permissive thresholds (≥35% and ≥40% identity) to circumvent the likely divergence of known AR from environmental sequences; to our knowledge, only Pehrsson et al. (2016) have targeted functionally homologous sequences.

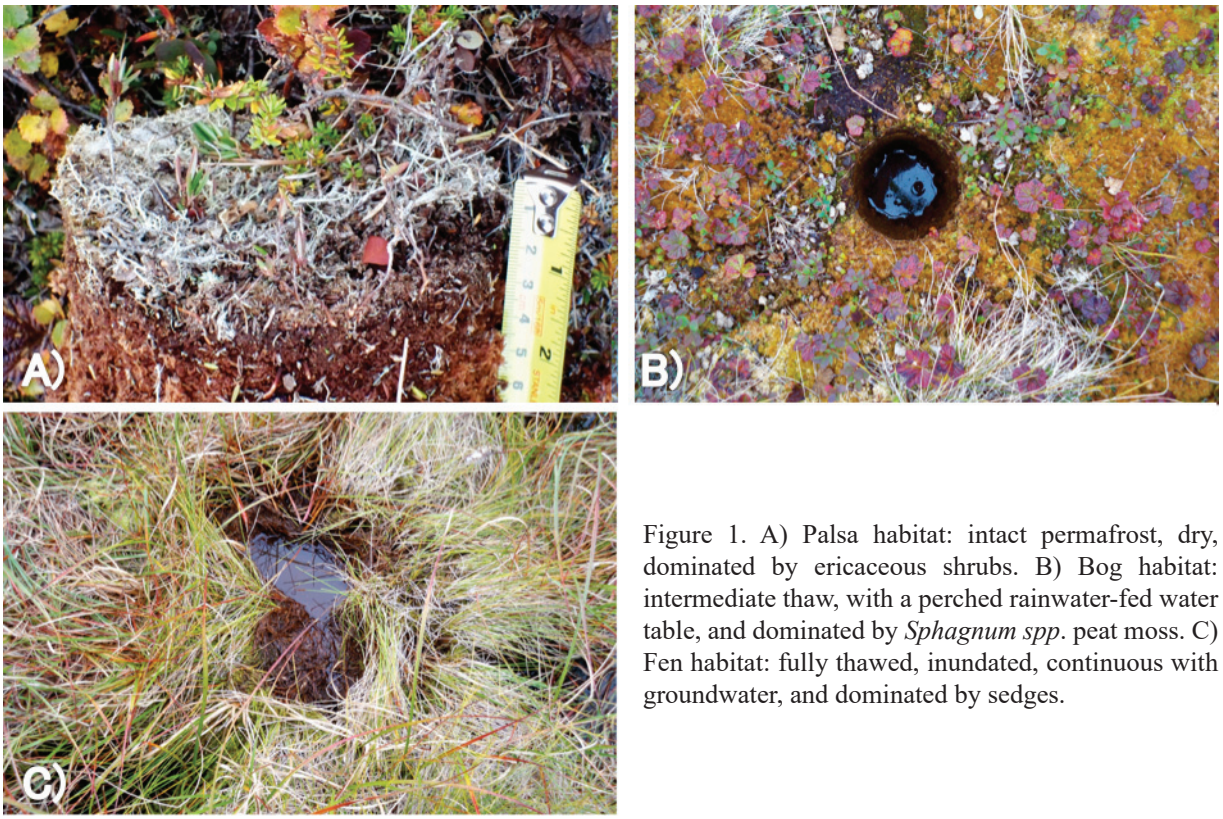

Figure 1. A) Palsa habitat: intact permafrost, dry, dominated by ericaceous shrubs. B) Bog habitat: intermediate thaw, with a perched rainwater-fed water table, and dominated by *Sphagnum spp*. peat moss. C) Fen habitat: fully thawed, inundated, continuous with groundwater, and dominated by sedges.

Table 1. Comparison of metagenome outputs to the original assemblies, generated from paired-end reads. All samples were collected in the field on 3 June 2012. The multiple sequencing depths were assembled into a single metagenome.

Habitat	Depth (name)	Depth (cm)	Megabases in raw reads	Contigs	Megabases in contigs	Prokka-predicted proteins
Palsa	Surface	1-4	1,741	567,790	289	228,334
	Middle	7-10	1,491			
	Deep	14-17	1,385			
Bog	Surface	1-4	1,994	400,114	472	685,553
	Middle	4-7	1,556			
	Deep	14-17	1,869			
Fen	Surface	1-4	1,653	749,828	995	2,038,823
	Middle	5-8	1,317			
	Deep*	11-14	15,029			

*The Fen Deep assembly was sequenced to a higher depth.

Resistance Database

The Comprehensive Antibiotic Resistance Genes Database (CARD, http://arpcard.mcmaster.ca/) contains 4,120 genes in 24 antibiotic classes for antibiotic biosynthesis, resistance, and inhibition of resistance, with 3,111 genes specific to resistance in 18 antibiotic classes (Table 2) (McArthur et al. 2013). The polypeptide and nucleotide versions of the CARD were downloaded 3 February 2015. To streamline workflow and improve search speed, the nucleotide version of the CARD was dereplicated using UCLUST's *derep_fulllength* command to remove exact copies via full-sequence matching. The dereplicated nucleotide CARD was then translated in all six reading frames using *transeq* in EMBOSS (Rice et al. 2000), and appended to the polypeptide version of the database to create a concatenated CARD with all possible representations of a given sequence (Figure 2, C1 & D1). This translation step was conducted because the metagenomes were annotated with Prokka, which predicts proteins from a given metagenome, and these would be searched against a BLAST algorithm that translates gene sequences in all six reading frames (*BLASTx*) before searching them against the provided database. This *BLASTx* algorithm was used in Hu et al. (2013) and Nesme et al. (2014). The translation step allowed for more direct comparability of HMMer results to *BLASTx*. Finally, this concatenated CARD was dereplicated again for a total of 14,808 AR polypeptide sequences. Thus, a non-redundant database with all possible versions of a known AR sequence was created. Further edits were made downstream for use in HMMer searches.

BLAST Searches: Identity-Based Methods

Identity-based searches were performed using two different BLAST algorithms (NCBI's BLAST+ v. 2.2.30) to search the metagenome assemblies for AR coding genes. Both algorithms search a protein database. *BLASTp*, is for a protein query while *BLASTx*, used for comparison to published studies (Hu et al. 2013; Nesme et al. 2014), uses a nucleotide query that it translates prior to conducting searches and assigning likelihood scores. Stricter filtering was used for *BLASTp* for a more accurate, narrower identification of potential AR-coding sequences with higher identity-based confidence, as a representation of a basic BLAST search with these data.

Lenient parameters: *BLASTx* (Figure 2, A) searched the concatenated polypeptide CARD against the prokka-predicted genes from the metagenomes, using an E-value cutoff of <1e-5, in the range of what is typical in the literature. Results were filtered for the top BLAST match for each query sequence, with percent identities ≥35% and bitscores ≥60. This level of leniency for positive matches allowed comparability to Hu et al. (2013) and Nesme et al. (2014).

Strict parameters: *BLASTp* (Figure 2, B) searched the concatenated polypeptide version of the CARD against the translations of the Prokka-predicted genes from the metagenomes. An E-value cutoff of <1e-5 was again used, but outputs were filtered to ≥80% identity, ≥70% query coverage, and bitscore ≥60 (Hu et al. 2013; Nesme et al. 2014). Unlike *BLASTx*, *BLASTp* uses input sequences that are already in protein format, so it does not translate the query into proteins in all six reading frames as it searches, thus the matches it makes are more direct and less inclusive than *BLASTx*. This search assumes the correctness of the Prokka-predicted genes in the metagenome.

Hidden Markov Models with HMMer 3.0

Model-based searches were performed using two HMM-based methods in the HMMer software suite (v3.0). At its simplest, HMMer identifies conserved versus variable regions when analyzing proteins and is designed to be a homology-based approach. Such a model may also be able to effectively capture functional similarities due to convergent evolution, and shared evolutionary histories. However, because clinical AR variants often have an environmental source (Martinez 2009; Martinez et al. 2009), targeting homology is a key approach in identifying AR analogs in the environment.

The *hmmsearch* algorithm (Figure 2, C) searches protein HMM profiles, built from a multiple sequence alignment, against a target query sequence database (Finn et al. 2011). In order to best target homologous sequences, protein profile HMMs require relatedness or functional similarity in the input protein sequences. To build the profile HMMs, the concatenated polypeptide

CARD was split into 18 antibiotic classes (Figure 2, C1 & D1; Table 2). These AR classes were grouped according to the ontology provided in the CARD download files. Only 18 of the available 24 classes denoted in the ontology files were associated with resistance genes, while the other six classes were associated with antibiotic target or biosynthesis sequences. All sequences with annotations indicating resistance to more than one antibiotic class were regrouped into the multiple

Table 2. Antibiotic classes used to create the HMMs from AR-coding and AR-associated sequences in the CARD.

Profile HMM name	Polypeptides used to build profile HMM	AR genes used to build profile HMM (CARD descriptions)
aminocoumarin	282	Point mutations to DNA gyrase subunit B (gyrB) can result in resistance to aminocoumarins. In some cases, expression of parY(R), which encodes an aminocoumarin resistant topoisomerase IV, can also confer aminocoumarin resistance.
aminoglycoside	1,170	Genes conferring resistance to aminoglycoside antibiotics.
beta-lactam	8,058	Genes conferring resistance to beta-lactams. Genes that directly or indirectly modulate beta-lactam resistance.
chloramphenicol	54	Genes conferring resistance to chloramphenicol.
ethambutol	42	Genes conferring resistance to ethambutol.
fluoroquinolone	1,236	Genes conferring resistance to fluoroquinolones.
fosfomycin	78	Genes conferring resistance to fosfomycin.
glycopeptide	408	Genes conferring resistance to glycopeptides.
lincosamide	78	Genes conferring resistance to lincosamides.
macrolide	186	Genes or their products conferring resistance to macrolide antibiotics.
multiple[a,b]	2,040	Resistance to antibiotics is often conferred by single nucleotide polymorphisms (SNPs) and other mutations in target genes. Efflux proteins that pump antibiotic out of a cell to confer resistance. Enzyme that catalyzes the inactivation of an antibiotic resulting in resistance. Inactivation includes chemical modification, destruction, etc. Genes that directly or indirectly change rates of antibiotic efflux. Enzymes that confer resistance by modifying antibiotic targets. Genes involved in restructuring of the cell wall.
polymyxin	18	Genes conferring resistance to polymyxins.
rifampin	132	Genetic determinants which confer resistance to rifampin.
streptogramin	492	Genes conferring resistance to streptogramin antibiotics.
sulfonamide	300	Genes conferring resistance to sulfonamide antibiotics.
tetracycline	66	Genes conferring resistance to tetracycline antibiotics.
tunicamycin	6	Genes that confer resistance to tunicamycin.
unspecified[a]	162	A gene whose product inactivates an antibiotic by formation of a complex, preventing interaction of the antibiotic with its target. Genes that are involved in conferring self resistance to antibiotics. Genes directly or indirectly reducing overall permeability to antibiotics.

[a]Searched against UniProt if not linked to a specific antibiotic class. Gene products that led back to a single, specific class were re-assigned their category before building the profile HMM.
[b]Multiple includes any gene product associated with two or more distinct classes of antibiotics.

resistance category, and those without specificity to an antibiotic class but annotated as "antibiotic resistance" in CARD were classed as unspecified AR sequences. *Hmmsearch* requires an alignment from which to build profile HMMs, so each CARD subset database was aligned using the algorithms Muscle, Mafft, and Clustal Omega, so that there were three multiple sequence alignments (Figure 2, C2). Muscle creates pairwise alignments between protein sequences, scores them, and chooses the best alignment before repeating the step until it has found the best match, then moves on to the next set of alignments (Edgar 2004). Mafft aligns on the basis of sequence similarity, but builds evolutionary information into its alignment strategy (Katoh and Standley 2013). Clustal Omega uses HMMs to build its alignments (Sievers et al. 2011). Using these three aligners minimizes the chance of false positives.

Mafft was run on each of the CARD subset databases using the parameters *mafft --localpair --maxiterate* 1000, as recommended for <200 sequences in the Mafft manual. For Muscle, each CARD subset database was run with defaults and the *-maxiters 2* for large datasets and better accuracy and speed. Default parameters were

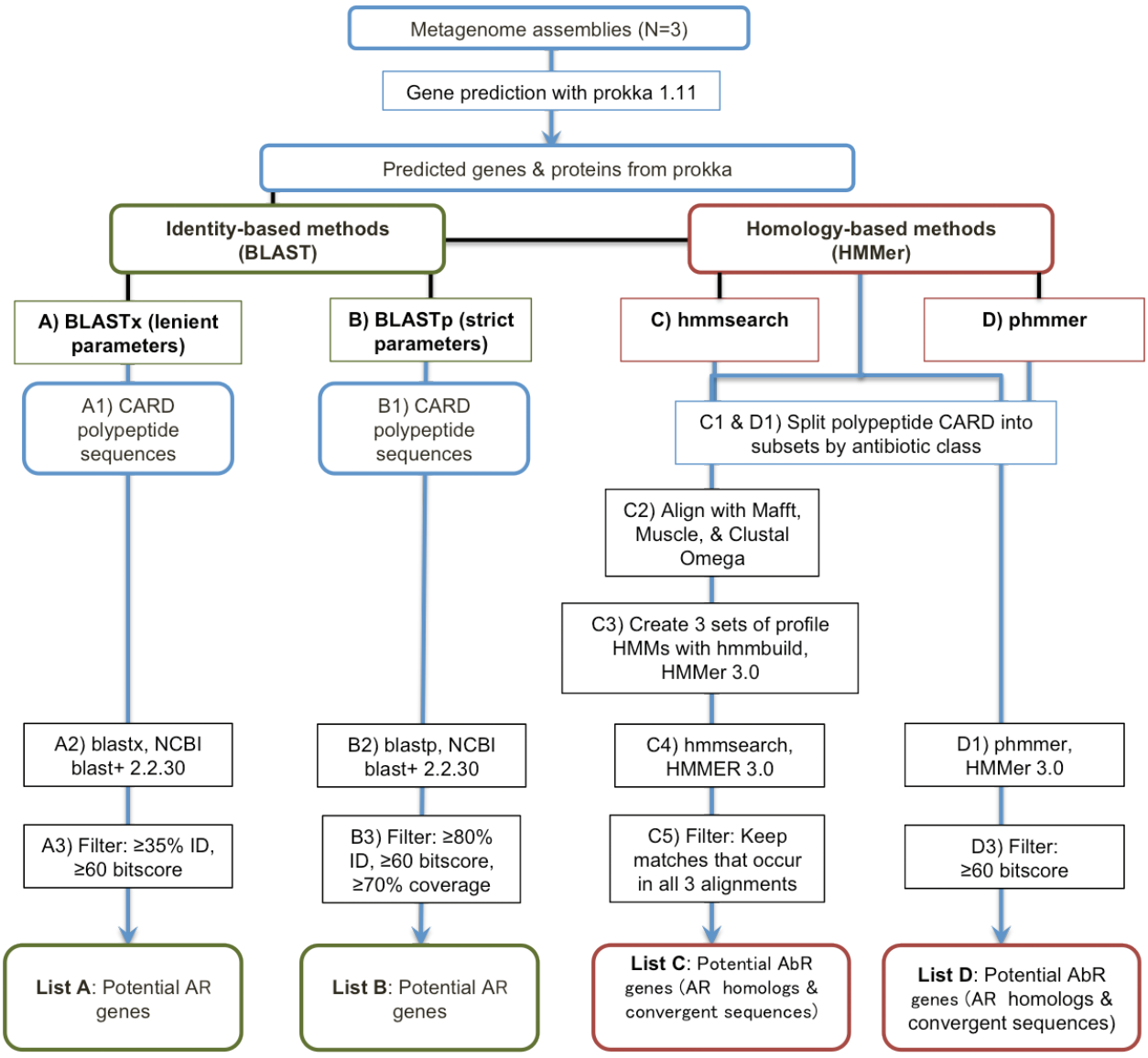

Figure 2. Bioinformatic workflow to identity potential AbR-coding sequences and homologs in wetland metagenomes.

used for Clustal Omega. Following the initial runs, all three AR alignment sets were run through HMMer's *hmmbuild* ("profile HMM construction from multiple sequence alignments") to create three profile HMMs, one from each aligner, for each set of AR proteins (Figure 2, C3). These profile HMMs were then used to search the metagenomes in *hmmsearch*, using command *hmmsearch -o <logfile.txt> --tblout <output_table.txt> -E 1e-5 --cpu 2 <query hmm file> <target seqfile>*. *Hmmsearch* outputs two bitscores, one for the sequence-HMM match and one for the best-scoring domain in the sequence, both of which we filtered to ≥60. In order to maintain a conservative dataset, only sequences that matched CARD profile HMMs from all three aligners were retained (Figure 2, C5).

Similar to *BLASTp*, *phmmer* (Figure 2, D) takes protein sequences as a query and searches them against a database, but *phmmer* converts the query sequences into profile HMMs as it searches for matches. The polypeptide CARD sequences were used to build the profile HMMs during the *phmmer* search (Figure 2, D1). Metagenomes were utilized as a database when running *phmmer*, as this results in searches of the metagenome for homologs to known AR sequences and iteratively generates metagenome-specific HMMs used to then collect more matches. The alternative of scanning known AR sequences for homologs to protein-coding sequences in an environmental dataset could lead to a higher frequency of spurious identifications.

Five Key Resistance Proteins

In order to gain a clearer idea of genetic diversity of microorganisms within the habitats, four frequently occurring AR-conferring proteins and an additional protein conferring resistance to vancomycin and teicoplanin were chosen for more detailed analysis (Table 3). These were DHPS (dihydropteroate synthase), DNA gyrA (DNA gyrase subunit A), MdtC (multidrug resistance protein MdtC), BepG (efflux pump membrane transporter BepG), and VanA (vancomycin/teicoplanin A-type resistance protein VanA). Vancomycin and teocoplanin are two broad-spectrum glycopeptide class antibiotics used in clinics to combat *Clostridium* infections and methicillin-resistant *Staphylococcus aureus*.

Results

In the literature, the range of AR abundances in gut, fecal, agricultural, and environmental metagenomes ranges from 0.05-7.4% of total gene content, with a trend of lower abundance but higher diversity in environmental samples, and higher abundance but predictable diversity in agricultural and fecal samples (Durso et al. 2012; Hu et al. 2013; Nesme et al. 2014). In our study, *hmmsearch* (model-based; Figure 2, List C) and *BLASTp* (identity-based; Figure 2, List B) returned results consistently below 0.05%, but *BLASTx* (identity-based; Figure 2, List A) and *phmmer* (model-based; Figure 2, List D) searches returned abundances between 0.72-0.75% and 0.84-1.29%, respectively, consistent with the current literature.

With both identity- and model-based methods, no significant differences were found in overall AR abundance between habitats (one-way ANOVA, n=3 habitats, p=0.96). There were, however, differences in AR class and gene types between habitats. The Bog metagenome yielded more instances of two efflux pump-related genes, BepG and MdtC, than did the other habitats, at 0.03% overall gene abundance for MdtC and 0.01% for BepG as calculated by *phmmer*. The other habitats do not display this trend (Supplemental Figure 1). Search method significantly impacted the identification of potential AR sequences, with *phmmer* consistently returning the highest AR diversity and abundance (ANOVA, $p<0.001$).

In *BLASTx*, the AR class in the highest proportion, out of total Prokka-predicted genes, was multiple antibiotic resistance (average=0.33%), followed by aminocoumarin (average=0.09%), macrolide (average=0.07%), and glycopeptide (average=0.05%) resistance (Figure 3). *Phmmer* returned a similar distribution of AR classes for multiple (average=0.56%), aminocoumarin (average=0.09%), macrolide (average=0.12%), and glycopeptide (average=0.07%) resistance. Too few matches were obtained from *BLASTp* and *hmmsearch* to identify any trends. Despite similar overall AR, protein types within AR classes (multiple resistance, aminocoumarin resistance, macrolide resistance, etc.) in the *phmmer* and *BLASTx* results had differing protein identifications within their AR matches in all of the habitats

Table 3. Five key resistance-conferring proteins and the antibiotic or antibiotic class they confer resistance to. DHPS, DNA gyrA, and MdtC are ordinarily targets of the antibiotics in the table, but these proteins are resistant mutants. All information from UniProt (http://www.uniprot.org/) and InterPro (http://www.ebi.ac.uk/interpro/) databases.

Abbreviation	Protein name	Resistance to	Function	Description
DHPS	Dihydropteroate synthase	sulfonamides	cellular metabolic process	Enzyme that catalyzes the second to last step in folic acid biosynthesis.
DNA gyrA	DNA gyrase subunit A	fluoroquinolones	DNA topological change, ATP binding, DNA binding	DNA gyrase negatively supercoils closed circular double-stranded DNA in an ATP-dependent manner and also catalyzes the interconversion of other topological isomers of double-stranded DNA rings, including catenanes and knotted rings.
MdtC	Multidrug resistance protein MdtC	novobiocin (aminocoumarin), deoxycholate, acriflavine, beta-lactams, chloramphenicols	efflux pump, multidrug resistance	The MdtABC tripartite complex confers resistance against novobiocin and deoxycholate. Multidrug resistance proteins are molecular pumps that participate in a low energy shock adaptive response in some bacteria. The MdtBC complex is iInvolved in the resistance of gram negative bacteria to novobiocin, deoxycholate and beta-lactams.
BepG	Efflux pump membrane transporter BepG	deoxycholate, nalidixic acid (fluoroquinolone), other	efflux pump, transporter activity	May contribute to resistance to some drugs, such as deoxycholate, sodium dodecyl sulfate, and nalidixic acid, in the absence of BepD and BepE.
VanA	Vancomycin/ teicoplanin A-type resistance protein VanA	glyocpeptides (vancomycin & teicoplanin)	peptidoglycan biosynthesis, ATP binding, DNA binding	Required for high-level resistance to glycopeptide antibiotics. D-Ala- -D-Ala ligase of altered specificity which catalyzes ester bond formation between D-Ala and various D-hydroxy acids; produces a peptidoglycan which does not terminate in D-alanine but in D-lactate, thus preventing vancomycin or teicoplanin binding.

(Supplemental Figure 3), with an average of 39% shared protein identifications (Supplemental Figure 2).

Four Top AR Classes

In order to analyze the completeness of pathways with AR involvement within the site metagenomes, we focused a more detailed analysis on the four most abundant AR classes in the data: multiple, macrolide, aminocoumarin, and glycopeptide resistance. The KEGG (Kyoto Encyclopedia of Genes and Genomes) is a resource for understanding high-level functions of microorganisms and their utility to ecosystem function from molecular information, especially large-scale molecular datasets generated by genome sequencing and other high-throughput experimental technologies (Tanabe and Kanehisa 2012). Across the four resistance classes, in all three habitats KEGG molecular pathways from the *phmmer* results were consistently more complete than the *BLASTx* results, with an average of 46.0% of the multiple, 79.2% of the macrolide, 59.5% of the aminocoumarin, and 58.9% of the

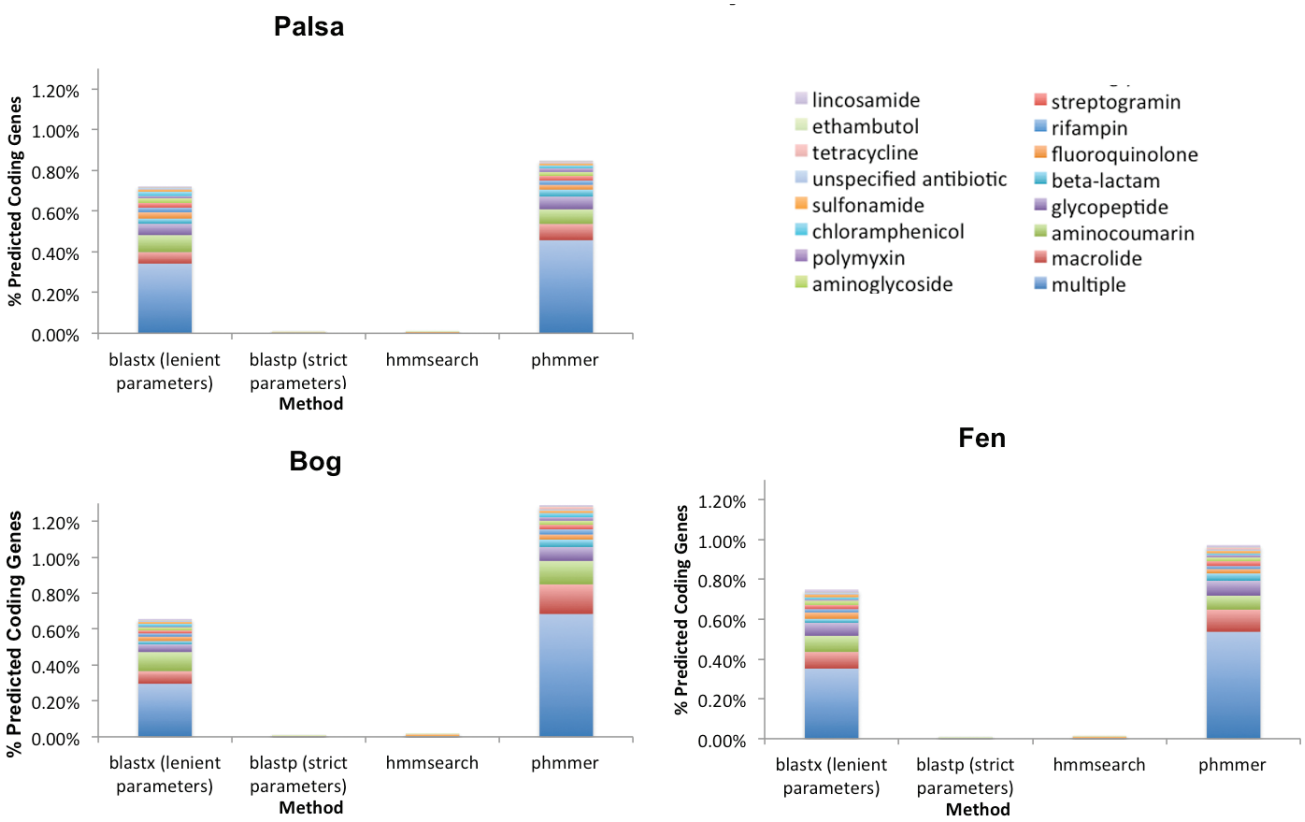

Figure 3. Abundance of hits, by AR detection method, normalized to their respective habitats. Both *BLASTx* and *phmmer* returned results within the ranges expected from the literature, with similar overall abundances to particular antibiotic classes, but their individual hits were quite different (Supplemental Figures 1-6).

glycopeptide *phmmer* matches annotated to a KEGG functional category. In comparison, 38.5% of the multiple, 71.4% of the macrolide, 36.8% of the aminocoumarin, and 34.8% of the glycopeptide *BLASTx* matches were annotated on average (Supplemental Figures 4-7). This is possibly due to the HMM building involved in HMMer. KEGG maps of the pathways in the multiple, macrolide, aminocoumarin, and glycopeptide matches demonstrate some difference in pathways available to pump out antibiotics from a bacterial cell, with more pathways present in the *phmmer* matches than in the *BLASTx* matches, all in either the two-component system or the ABC transporter system. The two-component system is a stimulus-response system, and the ABC transporter system is a protein family that transports microbial substrates. Multiple, aminocoumarin, and glycopeptide resistance matches mapped to the two-component system. Multiple resistance and macrolide matches mapped to pathways in the ABC transporter system

Five Key Resistance Proteins

With the five key Prokka-predicted proteins DHPS, DNA gyrA, MdtC, BepG, and VanA, abundances of each gene chosen were relatively stable among the three habitats for *phmmer* and *BLASTx*, but not for *hmmsearch* or *blastp,* due to the low number of AR identifications. BepG and VanA were not represented in the *hmmsearch* and *BLASTp* hits of any habitat (Supplemental Figure 1). There were more MdtC identifications in *phmmer* for the Bog than for the other habitats and methods (≥0.01% in the Bog, 0.01% in the Palsa and Fen habitats, versus the *BLASTx* results of 0.01% for Palsa and Fen and 0.02% in the Bog). There were two hits to vancomycin resistance in the Palsa with both *BLASTx* and in *phmmer* (≤0.01% abundance). Interestingly, despite the low VanA hits, vancomycin pathways were found in all of the glycopeptide hits for each habitat, although they were less complete in the *BLASTx* hits than in the *phmmer* hits.

Discussion

Although each habitat has different cell densities, pH, bioavailable carbon, water content, nutrient availability, and other factors that impact microbial life, the difference in overall AR proteins between habitats was not significant. Difference in resistance to the four most abundant classes (multiple, macrolide, aminocoumarin, and glycopeptide resistance) was also not significant. In the Abisko permafrost mosaic system, the overall AR gene product abundance was constant across habitats. Multiple resistance was the most abundant category due to efflux pumps, which, although not plasmid-encoded, serve a general purpose in the cell, thus making any change in response to any individual antibiotic a potential shift to resistance to multiple antibiotic classes (Webber & Piddock 2003; Martinez et. al 2009). KEGG functional annotations of the multiple macrolide, aminocoumarin, and glycopeptide resistance matches in each habitat did indicate some difference in pathways available for potential AR responses.

Conclusion

We have demonstrated a more effective method with higher sensitivity than traditional BLAST-based approaches for identifying potential AR genes in metagenomic datasets, particularly for environmental datasets whose sequence variants are most likely to be divergent from the CARD and other gene and protein databases. The *phmmer* algorithm yielded more potential matches to the CARD database, and those matches spanned more complete KEGG pathways than their *BLASTx*-derived counterparts. Results using this methodology provide valuable information about the presence and completeness of AR pathways, but they do not yield information regarding the activity or non-activity of those processes in the metagenome sites. Additional study using metaproteomics or metatranscriptomics would enhance information regarding AR, enabling a contrast between what genes are available and what genes are being expressed, as it is conceivable that AR itself may not be occurring even if AR genes are spread into a habitat due to human activities. Such a case would open another set of public health and environmental health concerns regarding the potential for anthropogenically-induced AR spread.

Further research on the topic would allow for examination of environments where AR is suspected to have spread. Culturing samples for this sort of analysis is not practical, but sequencing small samples to analyze with HMMer, using comparable environmental AR levels and diversities, could establish the presence of AR potentially changed from a prior state. This has practical applications as well. For example, in Arizona and the Southwestern United States, reclaimed wastewater irrigation in agriculture is a common practice to conserve water resources (Arizona Department of Water Resources 2014), and there is concern about AR spreading within an irrigated field and to the surrounding environment via runoff, similar to concerns regarding disposal of medical and veterinary waste. Bacterial indicator levels allowed in reclaimed water for different uses are carefully controlled in the Southwest, but the levels of antibiotics and AR genes are unregulated, and thus antibiotics present in reclaimed wastewater could induce survival of resistant bacteria (Wright 2007; Martinez 2009; Allen et al. 2010; Martinez 2012; Li et al. 2015). Currently, these are only concerns, not all of which have been addressed, and there are currently no standardized tests to analyze any possible effects if antibiotics are present in the environment (Roose-Amsaleg and Laverman 2015). As AR continues to evolve in the clinic, it is time to begin addressing these concerns and anticipate those that will arise.

Acknowledgements

We thank Drs. Gene Tyson and Ben Woodcroft of the Australian Ecogenomics Centre for kindly sharing their unpublished metagenomic data for this study.

Author Bio and Contact Information

Krystalle Diaz is pursuing a Master's Degree in Microbiology at the University of New Hampshire. She has a Bachelor of Science in Environmental Science from the University of Arizona, where she began undergraduate research in the soil microbial ecology laboratory of Virginia Rich, (Ph.D.). This work led to

interest in the microbial community genomics in natural environments experiencing change from anthropogenic influence and their potential recoveries. She may be contacted at ksdiaz17@gmail.com or Gregg Hall 431, University of New Hampshire, 36 Colovos Road, Durham, New Hampshire 03820.

Virginia Rich has been an Assistant Professor of Microbiology at Ohio State since June 2015 after moving from the University of Arizona. Virginia's lab uses molecular microbial ecology techniques and strong partnerships with biogeochemists, informaticians, and modelers to investigate how microbes respond to, and mediate, environments undergoing anthropogenic change. Her team works towards a "systems-level" understanding of microbial community interactions with the environment. Virginia holds a Bachelor of Arts degree from the University of California at Berkeley, with majors in Integrative Biology and in Molecular and Cell Biology: Genetics. She earned a Ph.D. in Microbial Oceanography from the Joint Program of the Massachusetts Institute of Technology and Woods Hole Oceanographic Institute. She may be contacted at virginia.isabel.rich@gmail.com or 105 Biological Sciences Building, 484 W. 12th Ave, Columbus, OH 43210.

Jean McLain has been the Associate Director and an Associate Research Scientist at University of Arizona Water Resources Research Center since 2011 following a 10-year career with the USDA-Agricultural Research Service. Jean's work in environmental microbiology includes managing an international research program focused on establishing the human health and environmental risks of using recycled municipal wastewater for crop irrigation, replenishment of surface water, and groundwater recharge. Jean holds a Bachelor of Science Degree in Forestry from the University of Vermont, and a Master's Degree in Forest Science from Yale University. She received her Ph.D. from Duke University in Microbial Ecology in 2002. She may be contacted at mclainj@email.arizona.edu or 350 N. Campbell Avenue, Tucson, Arizona 85719.

Supplemental Figures (S1-S7)

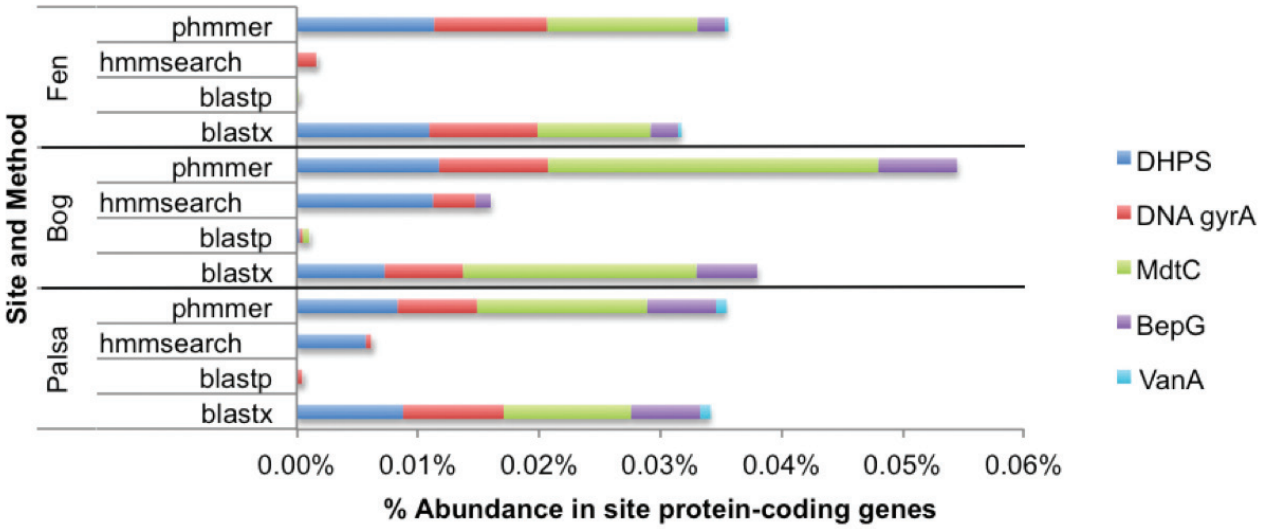

Figure S1. Five key resistance proteins, chosen for their conferring of AR, and their identification in each method and habitat.

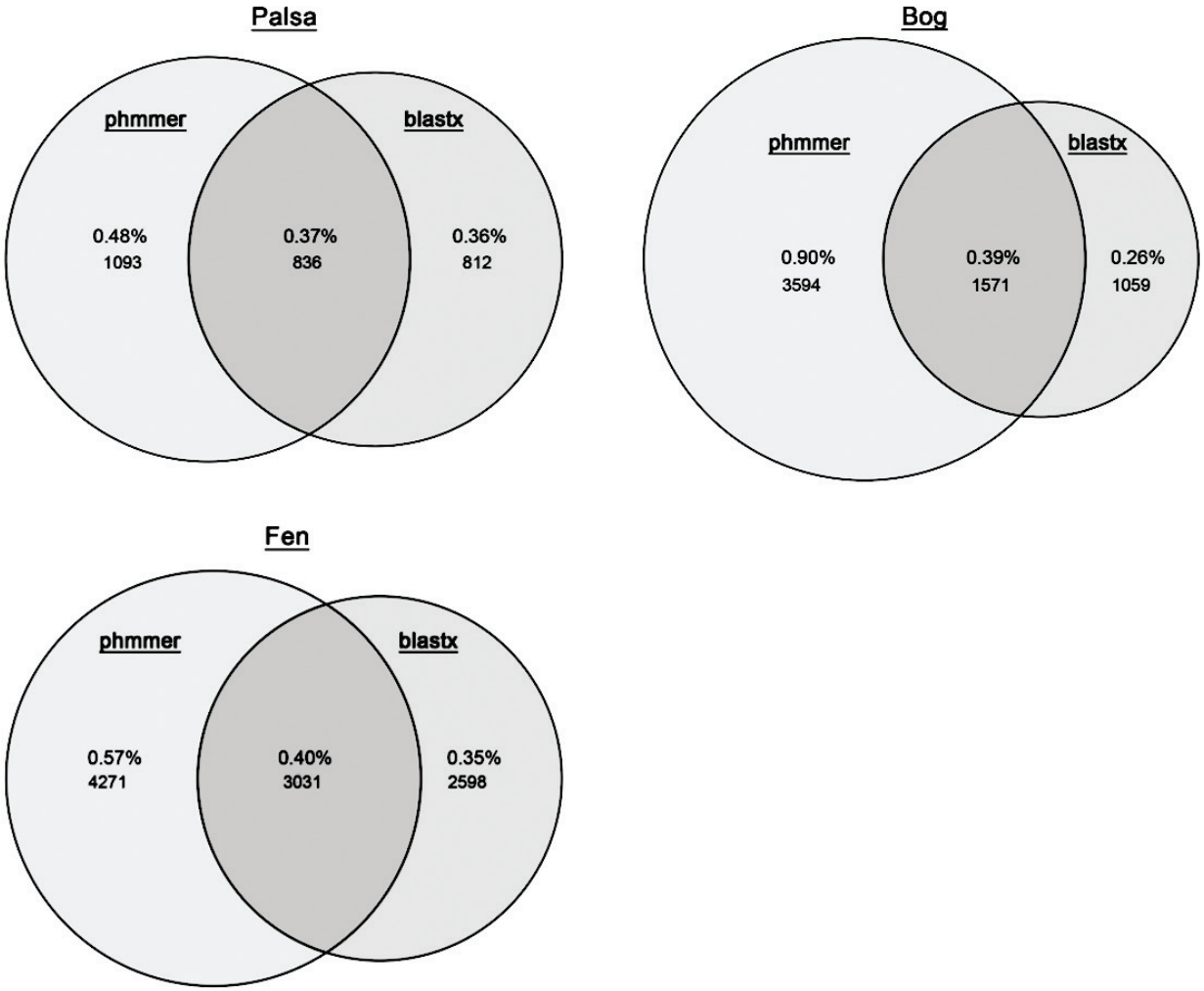

Figure S2. Prokka-predicted proteins caught by *phmmer* and *BLASTx* searches. Percentages are normalizations to the habitat's prokka-predicted proteins, not to the overall AR abundance.

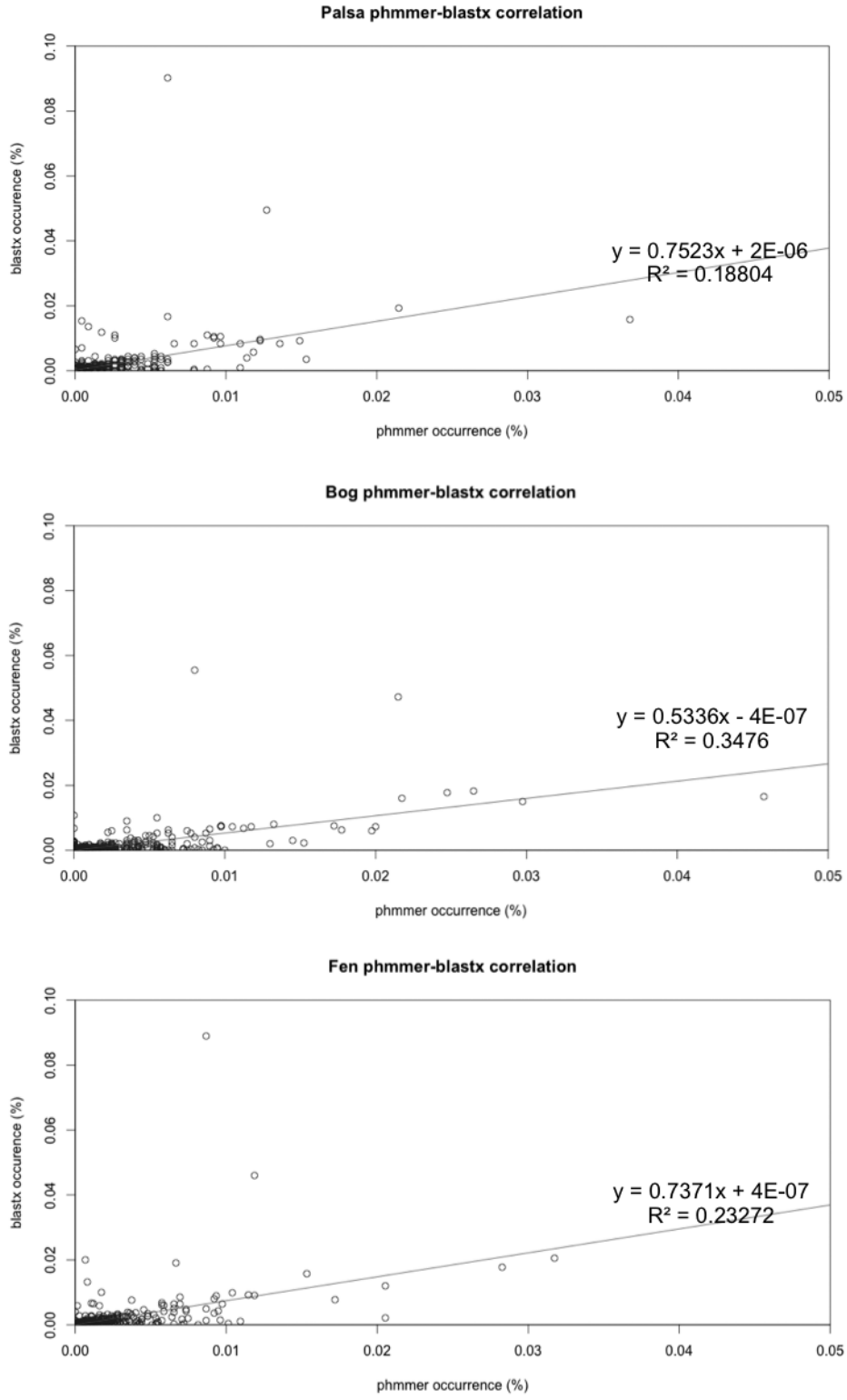

Figure S3. Correlations between *phmmer* and *BLASTx* results for each unique protein in antibiotic classes.

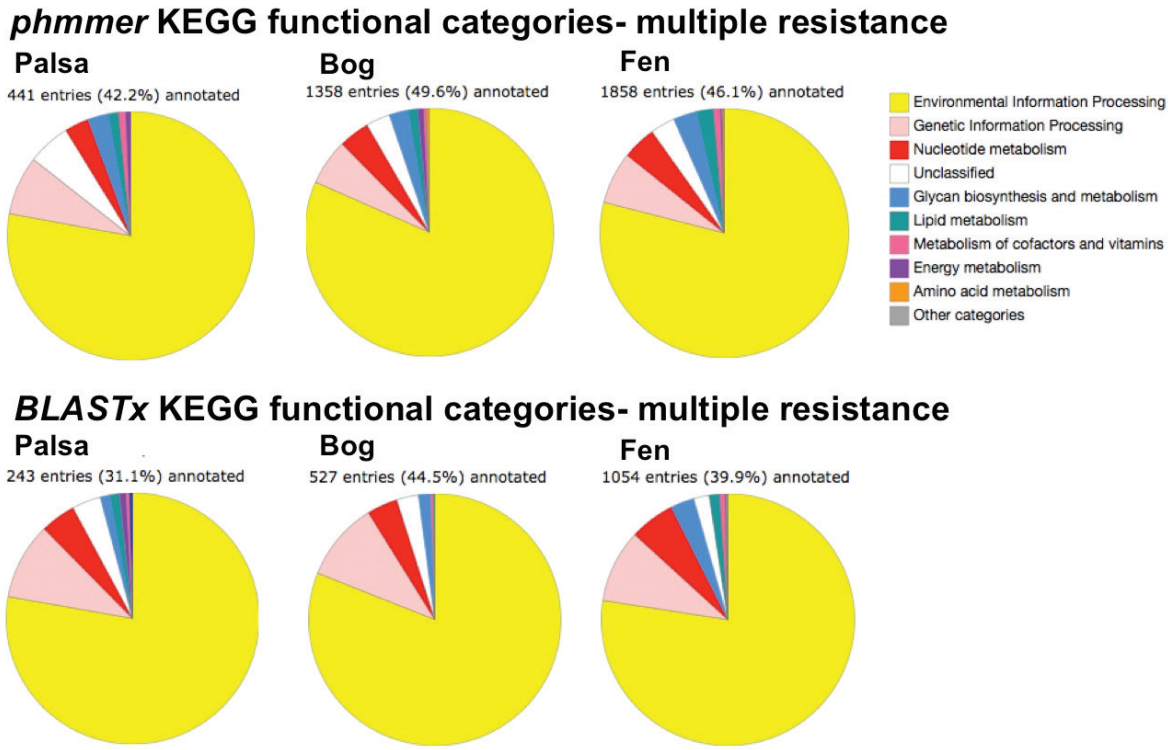

Figure S4. KEGG pie charts, displaying the number of sequences and the percent of hits from that subset of data that KEGG was able to link to a particular function. Note that despite being very similar in overall distribution, a higher percentage of sequences was able to be mapped in *phmmer* than in *BLASTx*.

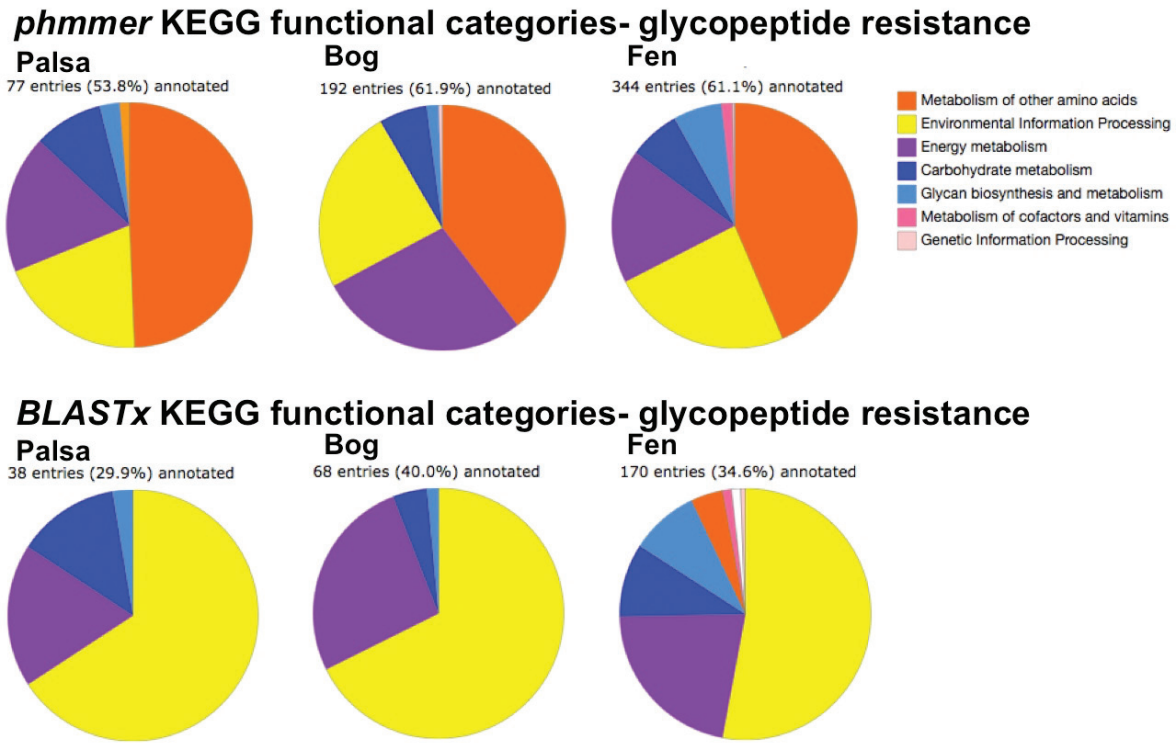

Figure S5. KEGG functionality pie charts, displaying the number of sequences and the percent of hits from that subset of data that KEGG was able to link to a particular function. A higher percentage of sequences was able to be mapped in *phmmer* than in *BLASTx*. Unlike the other antibiotic classes, distribution of functionality between *BLASTx* and *phmmer* hits was quite different in the glycopeptides than in the other classes.

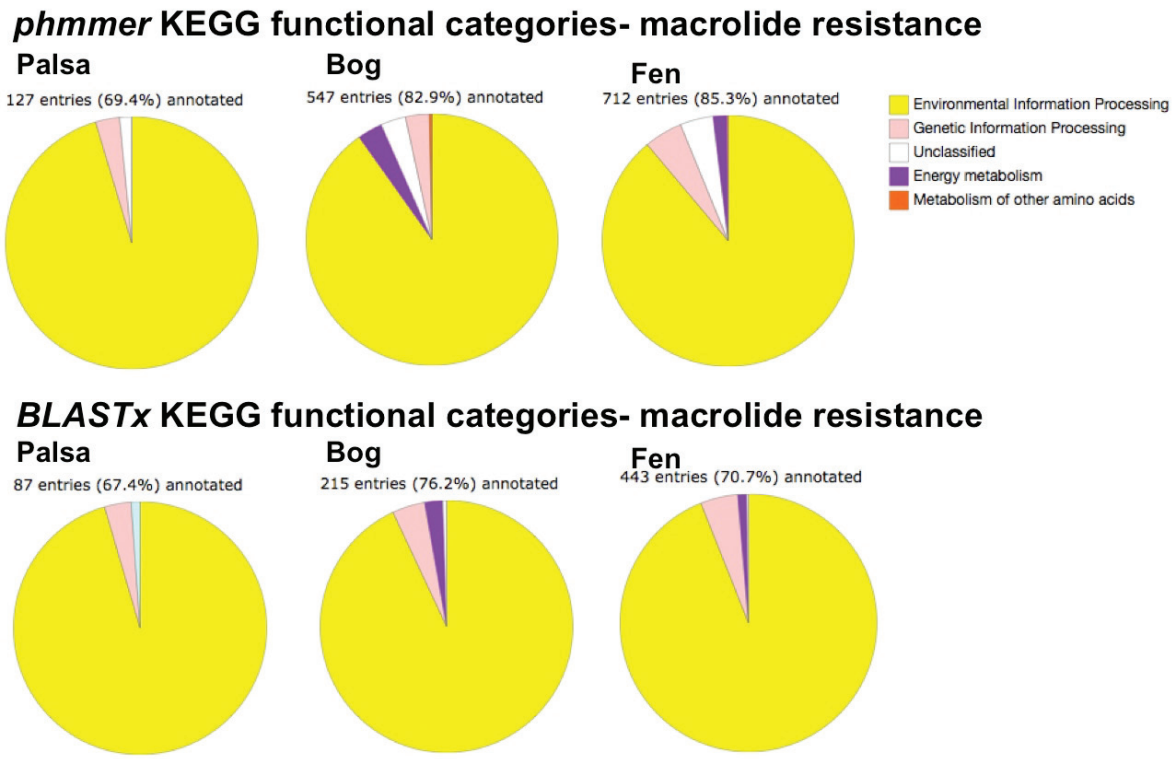

Figure S6. KEGG functionality pie charts, displaying the number of sequences and the percent of hits from that subset of data that KEGG was able to link to a particular function. Note that despite being very similar in overall distribution, a higher percentage of sequences was able to be mapped in *phmmer* than in *BLASTx*.

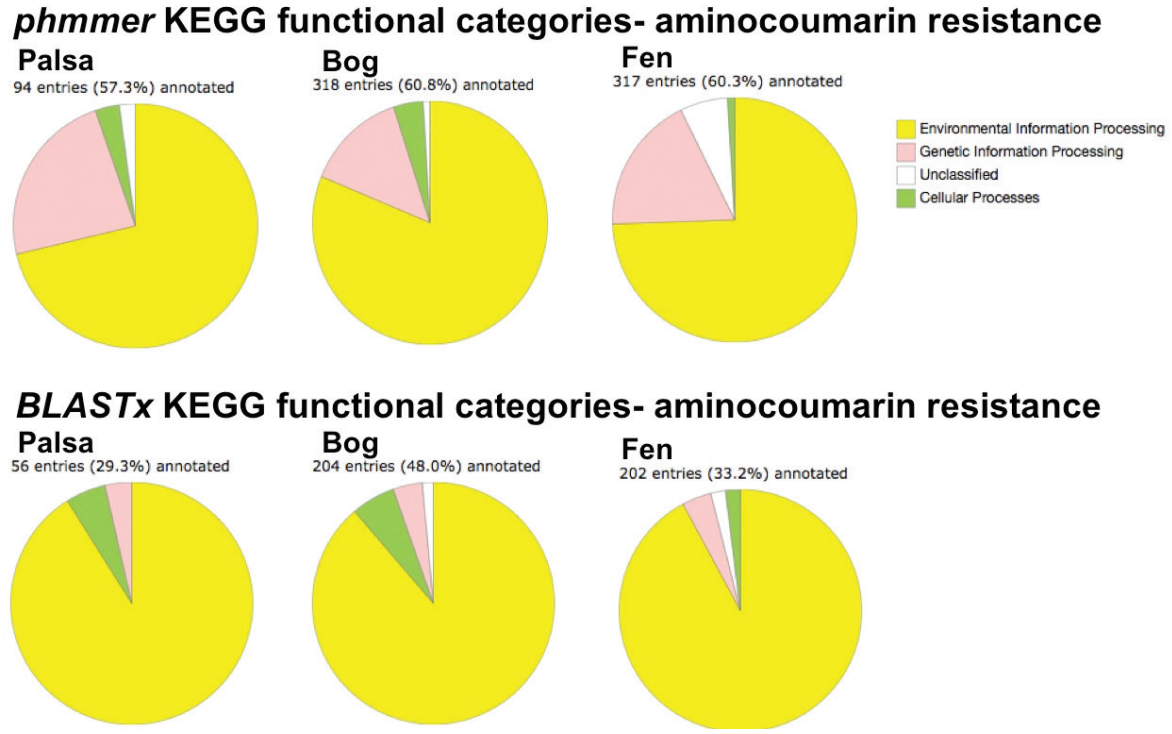

Figure S7. KEGG functionality pie charts, displaying the number of sequences and the percent of hits from that subset of data that KEGG was able to link to a particular function. Note that despite being very similar in overall distribution, a higher percentage of sequences was able to be mapped in *phmmer* than in *BLASTx*.

References

Arizona Department of Water Resources. 2014. Active Management Area Water Supply - Effluent and Contamination Sites. Available at: http://www.azwater.gov/azdwr/StatewidePlanning/WaterAtlas/ActiveManagementAreas/PlanningAreaOverview/WaterSupplyEffluent.htm. Accessed February 21, 2017.

Allen, H.K., J. Donato, H.H. Wang, K.A. Cloud-Hansen, J. Davies, and J. Handelsman. 2010. Call of the wild: Antibiotic resistance genes in natural environments. *Nature Reviews Microbiology* 8(4): 251-259. Available at: http://dx.doi.org/10.1038/nrmicro2312. Accessed February 21, 2017.

D'Costa, V.M., C.E. King, L. Kalan, M. Morar, W.W.L. Sung, C. Schwarz, D. Froese, G. Zazula, F. Calmels, R. Debruyne, G.B. Golding, H.N. Poinar, and G.D. Wright. 2011. Antibiotic resistance is ancient. *Nature* 477(7365): 457-461. Available at: http://dx.doi.org/10.1038/nature10388. Accessed February 21, 2017.

Dantas, G., M.O.A. Sommer, R.D. Oluwasegun, and G.M. Church. 2008. Bacteria subsisting on antibiotics. *Science* 320(5872): 100-103.

Davies, J. and D. Davies. 2010. Origins and evolution of antibiotic resistance. *Microbiology and Molecular Biology Reviews: MMBR 74*(3): 417-433. Available at: http://doi.org/10.1128/MMBR.00016-10. Accessed February 21, 2017.

Durso, L.M., D.N. Miller, and B.J. Wienhold. 2012. Distribution and quantification of antibiotic resistant genes and bacteria across agricultural and non-agricultural metagenomes. *PLoS ONE* 7(11): 1-12.

Edgar, R.C. 2004. MUSCLE: Multiple sequence alignment with high accuracy and high throughput. *Nucleic Acids Research* 32(5): 1792-1797. Available at: http://doi.org/10.1093/nar/gkh340. Accessed February 21, 2017.

Finn, R.D., J. Clements, W. Arndt, B.L. Miller, T.J. Wheeler, F. Schreiber, A. Bateman, and S.R. Eddy. 2015. HMMER web server: 2015 update. *Nucleic Acids Research* 43(W1): W30-W38. Available at: http://nar.oxfordjournals.org/lookup/doi/10.1093/nar/gkv397. Accessed February 21, 2017.

Finn, R.D., J. Clements, and S.R. Eddy. 2011. HMMER web server: Interactive sequence similarity searching. *Nucleic Acids Research* 39(suppl_2): W29-W37. Available at: https://academic.oup.com/nar/article-lookup/doi/10.1093/nar/gkr367. Accessed February 21, 2017.

Fouhy, F., C. Stanton, P.D. Cotter, C. Hill, and F. Walsh. 2015. Proteomics as the final step in the functional metagenomics study of antimicrobial resistance. *Frontiers in Microbiology* 6(March): 1-6. Available at: http://journal.frontiersin.org/article/10.3389/fmicb.2015.00172. Accessed February 21, 2017.

Hodgkins S.B., M.M. Tfaily, C.K. McCalley, T.A. Logan, P.M. Crill, S.R. Saleska, et al. 2014. Changes in peat chemistry associated with permafrost thaw increase greenhouse gas production. *Proceedings of the National Academy of Sciences USA* 111: 5819-24.

Hu, Y., X. Yang, J. Qin, N. Lu, G. Cheng, N. Wu, Y. Pan, J. Li, L. Zhu, X. Wang, Z. Meng, F. Zhao, D. Liu, J. Ma, N. Qin, C. Xiang, Y. Xiao, L. Li, H. Yang, J. Wang, R. Yang, G.F. Gao, J. Wang, and B. Zhu. 2013. Metagenome-wide analysis of antibiotic resistance genes in a large cohort of human gut microbiota. *Nature Communications* 4: 2151. Available at: http://www.ncbi.nlm.nih.gov/pubmed/23877117. Accessed February 21, 2017.

International Panel on Climate Change. 2014: *Climate Change 2014: Synthesis Report. Contribution of Working Groups I, II and III to the Fifth Assessment Report of the Intergovernmental Panel on Climate Change* [Core Writing Team, R.K. Pachauri and L.A. Meyer (eds.)]. IPCC, Geneva, Switzerland.

Johnson, M., I. Zaretskaya, Y. Raytselis, Y. Merezhuk, S. McGinnis, and T.L. Madden. 2008. NCBI BLAST: A better web interface. *Nucleic Acids Research* 36(Web Server issue): W5-W9. Available at: https://www.ncbi.nlm.nih.gov/pmc/articles/PMC2447716/. Accessed February 21, 2017.

Johnson, T.A., R.D. Stedtfeld, Q. Wang, J.R. Cole, S.A. Hashsham, T. Looft, Y.-G. Zhu, and J.M. Tiedje. 2016. Clusters of antibiotic resistance genes enriched together stay together in swine agriculture. *mBio* 7(2): e02214-15. Available at: http://mbio.asm.org/content/7/2/e02214-15.full. Accessed February 21, 2017.

Katoh, K. and D.M. Standley. 2013. MAFFT multiple sequence alignment software version 7: Improvements in performance and usability. *Molecular Biology and Evolution* 30(4): 772-780.

Li, B., Y. Yang, L. Ma, F. Ju, F. Guo, J.M. Tiedje, and T. Zhang. 2015. Metagenomic and network analysis reveal wide distribution and co-occurrence of environmental antibiotic resistance genes. *The ISME Journal (9)*: 2490-2502. Available at: http://dx.doi.org/10.1038/ismej.2015.59. Accessed February 21, 2017.

Martínez, J.L. 2008. Antibiotics and antibiotic resistance genes in natural environments. *Science* 321(5887): 365-367.

Martinez, J.L. 2009. The role of natural environments in the evolution of resistance traits in pathogenic bacteria. *Proceedings. Biological Sciences / The Royal Society* 276(1667): 2521-2530.

Martínez, J.L. 2012. Natural antibiotic resistance and contamination by antibiotic resistance determinants: The two ages in the evolution of resistance to antimicrobials. *Frontiers in Microbiology* 3(JAN): 2010-2012.

Martínez, J.L., M.B. Sánchez, L. Martínez-Solano, A. Hernandez, L. Garmendia, A. Fajardo, and C. Alvarez-Ortega. 2009. Functional role of bacterial multidrug efflux pumps in microbial natural ecosystems. *FEMS Microbiology Reviews* 33(2): 430-449.

McArthur, A.G., N. Waglechner, F. Nizam, A. Yan, M.A. Azad, A.J. Baylay, K. Bhullar, M.J. Canova, G. De Pascale, L. Ejim, L. Kalan, A.M. King, K. Koteva, M. Morar, M.R. Mulvey, J.S. O'Brien, A.C. Pawlowski, L.J.V. Piddock, P. Spanogiannopoulos, A.D. Sutherland, I. Tang, P.L. Taylor, M. Thaker, W. Wang, M. Yan, T. Yu, and G.D. Wright. 2013. The comprehensive antibiotic resistance database. *Antimicrobial Agents and Chemotherapy* 57(7): 3348-3357.

McCalley, C.K., B.J. Woodcroft, S.B. Hodgkins, R.A. Wehr, E.H. Kim, R. Mondav, P.M. Crill, J.P. Chanton, V.I. Rich, G.W. Tyson, and S.R. Saleska. 2014. Methane dynamics regulated by microbial community response to permafrost thaw. *Nature* 514(7523): 478-481. Available at: http://www.ncbi.nlm.nih.gov/pubmed/25341787. Accessed February 21, 2017.

McLain, J. and C. Williams. 2014. Sustainability of water reclamation: Long-term recharge with reclaimed wastewater does not enhance antibiotic resistance in sediment bacteria. *Sustainability* 6(3): 1313-1327. Available at: http://www.scopus.com/inward/record.url?eid=2-s2.0-84897046113&partnerID=tZOtx3y1. Accessed February 21, 2017.

Mondav, R., B.J. Woodcroft, E.H. Kim, C.K. McCalley, S.B. Hodgkins, P.M. Crill, J. Chanton, G.B. Hurst, N.C. VerBerkmoes, S.R. Saleska, P. Hugenholtz, V.I. Rich, and G.W. Tyson. 2014. Discovery of a novel methanogen prevalent in thawing permafrost. *Nature Communications* 5: 3212. Available at: http://www.ncbi.nlm.nih.gov/pubmed/24526077. Accessed February 22, 2017.

Nesme, J., S. Cécillon, T.O. Delmont, J.-M. Monier, T.M. Vogel, and P. Simonet. 2014. Large-scale metagenomic-based study of antibiotic resistance in the environment. *Current Biology* 24(10): 1096-1100.

Pehrsson E.C., P. Tsukayama, S. Patel, M. Mejía-Bautista, G. Sosa-Soto, and K.M. Navarrete. 2016. Interconnected microbiomes and resistomes in low-income human habitats. *Nature* 533: 212-216.

Rice, P., I. Longden, and A. Bleasby. 2000. EMBOSS: The European molecular biology open software suite. *Trends in Genetics* 16(6): 276-277.

Roose-Amsaleg, C. and A.M. Laverman. 2015. Do antibiotics have environmental side-effects? Impact of synthetic antibiotics on biogeochemical processes. *Environmental Science and Pollution Research*. Available at: http://link.springer.com/10.1007/s11356-015-4943-3. Accessed February 22, 2017.

Seemann, T. 2014. Prokka: Rapid prokaryotic genome annotation. *Bioinformatics* 30(14): 2068-2069.

Sievers F., A. Wilm, D. Dineen, T.J. Gibson, K. Karplus, and W. Li. 2011. Fast, scalable generation of high-quality protein multiple sequence alignments using Clustal Omega. *Molecular Systems Biology* 7. e-pub ahead of print DOI: 10.1038/msb.2011.75.

Tanabe, M. and M. Kanehisa. 2012. Using the KEGG database resource. *Current Protocols in Bioinformatics* (SUPPL.38): 1-54.

Walsh, F., S.G.B. Amyes, and B. Duffy. 2013. Challenging the concept of bacteria subsisting on antibiotics. *International Journal of Antimicrobial Agents* 41(6): 558-563. Available at: http://dx.doi.org/10.1016/j.ijantimicag.2013.01.021. Accessed February 22, 2017.

Webber, M.A. and L.J.V. Piddock. 2003. The importance of efflux pumps in bacterial antibiotic resistance. *Journal of Antimicrobial Chemotherapy* 51(1): 9-11.

World Health Organization. 2014. *Antimicrobial Resistance. Global Report on Surveillance 2014*. World Health Organization, Geneva, Switzerland.

Woodcroft B., C. Singleton, P. Evans, R. Wilson, S. Hodgkins, J. Chanton, S. Saleska, V.I. Rich, and G.W. Tyson. Microbial community response to permafrost thaw across a natural gradient via shallow metagenome profiling. In preparation.

Wright, G.D. 2007. The antibiotic resistome: The nexus of chemical and genetic diversity. *Nature Reviews. Microbiology* 5(3): 175-186.

Universities Council on Water Resources
Journal of Contemporary Water Research & Education
Issue 160, Pages 60-71, April 2017

Assessing Biomineral Formation by Iron-oxidizing Bacteria in a Circumneutral Creek

Nohemi Almaraz[1,2], Andrew H. Whitaker[1], Megan Y. Andrews[1,3], and *Owen W. Duckworth[1]

[1]*Department of Crop and Soil Sciences, North Carolina State University, Raleigh, NC, USA*
[2]*Department of Civil and Environmental Engineering, Colorado School of Mines, Golden, CO, USA*
[3]*Current Address: Center for Integrated Fungal Research, North Carolina State University, Raleigh, NC, USA*
**Corresponding Author*

Abstract: Iron oxidizing bacteria and environmental conditions influence the formation of iron biominerals in aquatic environments. This 10-week Research Experience for Undergraduates (REU) study focused on elucidating how water chemistry and iron oxidizing bacteria affect the formation of iron oxides in creeks with circumneutral pH. Two locations, each with multiple microenvironments containing abundant iron oxide deposits, were studied. Water chemistry was assessed via both in situ and laboratory analysis over a 5-week period, revealing correlations between aqueous components that indicate differing groundwater sources may feed nearby discharge points. Microscopy of iron oxide deposits reveals morphologies consistent with the presence of iron oxidizing bacteria. Although efforts to isolate iron oxidizing bacteria did not produce pure cultures, 16S ribosomal DNA analysis also suggests the presence of iron oxidizing bacteria in these sites. Taken together, these results show the diversity of iron oxide forming microenvironments in spatially collocated sites, which may result in unique formations of iron oxide structures, microbial communities, and aqueous chemical cycling.

Keywords: *iron (hydr)oxides, water chemistry, neutrophilic, gradient tubes, iron oxidation, groundwater*

Iron oxidation is an ubiquitous phenomenon in aqueous environments that may control pH (Blowes et al. 2003) and the mobility of nutrients and contaminants (Jambor and Dutrizac 1998). The formation of iron (oxyhydr)oxides (from here on out referred to as "iron oxides") may be driven by the abiotic and biotic oxidation of ferrous (Fe^{2+}) to ferric iron (Fe^{3+}) in the presence of oxygen. These processes commonly occur simultaneously upon mixing of iron-rich, anoxic groundwater with oxygen-rich surface water (Druschel et al. 2008). Iron biomineral formation from microbially mediated processes has been identified in diverse aqueous environments, including acid mine drainage sites (Colmer et al. 1950; Baker et al. 2009; Johnson and Hallberg 2015), hydrothermal vents (Emerson et al. 1999; Peng et al. 2011; Toner et al. 2012), and circumneutral pH surface waters (Emerson and Moyer 1997; Duckworth et al. 2009; Emerson et al. 2010; Fleming et al. 2014). In many circumneutral pH waters, abiotic oxidation is in direct competition with neutrophilic iron oxidizing bacteria (FeOB), organisms that exist at oxic-anoxic interfaces and have metabolic capabilities that promote rapid iron oxidation (Druschel et al. 2008). Multiple neutrophilic, microaerophilic FeOB, such as *Leptothrix*, *Gallionella,* and *Sideroxydans,* have been identified and studied to understand biotic-abiotic interactions in diverse environments (Duckworth et al. 2009; Fleming et al. 2014).

Generally, less is known about the formation and chemistry of these minerals, as well as microbes that oxidize iron at circumneutral pH, than most other aspects of iron biogeochemistry. The importance of FeOB and iron oxides originates from their sorptive capacity and influence on delivered water quality in distribution systems through pipe oxidation (Cullimore and McCann 1978; Søgaard et al. 2001; Fleming et al. 2014; Sowers et al. 2017), importance in microbial

ecology and evolution (Posth et al. 2014), and potential for use in soil remediation (Emerson et al. 2010). These applications, combined with their natural abundance, motivated our interest in understanding the physical, chemical, and biological characteristics of environments capable of supporting biogenic formation of iron oxides. In this study, we analyzed water chemistry and microbial composition of streams in North Carolina over the summer of 2015.

Materials and Methods

Field Site

The first sampling area was located on two small tributaries of Walnut Creek (WC: 35° 45' 45.4" N, 78° 40' 19.7" W) in Raleigh, North Carolina. The sampling sites consisted of a groundwater spring and a midstream site in the first tributary (WC1S and WC1M), and the midstream of the second tributary (WC2). The water was relatively shallow (<10 cm), with the exception of small ponds formed along the streams, and had variable flow (dependent on rainfall) for both tributaries. There was a high abundance of canopy vegetation that limited light penetration. The second location was Rocky Branch Creek (RBC: 35° 46' 48.6" N, 78° 40' 1.9" W) located on North Carolina State University Campus in Raleigh, North Carolina (Andrews and Duckworth 2016; Sowers et al. 2017). There were two site locations along the south side of the creek bank (RBC1 and RBC2), as well as a seep located downstream on the north side of the creek (RBC3) and a midstream location (RBCM). Water depth in RBC1-2 was greater than that observed in WC sites (approximately 50 cm) and had a more continuous flow. RBC3 depth was approximately 5 cm. Iron oxide formation occurred near the bank where the presence of rocks reduced water flow rates. The WC and RBC sites are approximately 1.9 miles apart, and are assumed to be fed by distinct water sources.

*S*ample Collection

Temperature and pH measurements, as well as stream water and iron oxide samples, were obtained weekly on site from June 6, 2015 to July 8, 2015 in Raleigh, North Carolina. Temperature was measured with a portable, analogue thermometer (Fisher) submerged at half depth until temperature equilibrated. The pH was measured on site using pH strips and in the laboratory using a calibrated Accumet excel XL20 pH meter equipped with a combination electrode (Fisher). Temperature and pH measurements were taken in every sampling location. Water samples were collected at half stream depth with a 25 mL polypropylene syringe, and immediately filtered with 0.22 µm filters into 50 mL polypropylene conical centrifuge tubes. Biomass was collected using 25 mL polypropylene syringes. Excess water was decanted to maximize the amount of biomass collected. Samples were stored at -4˚C until further analysis.

Organic and Inorganic Analysis

Samples were thawed and allowed to equilibrate to room temperature before analysis. Samples for dissolved organic carbon (DOC) and metals analysis were acidified with hydrochloric acid and nitric acid, respectively, to a pH ≤ 2. A Shimadzu total organic carbon analyzer was used to measure DOC, and a Thermo Scientific iCE 3000 series flame atomic absorption spectrometer was used to quantify iron (Fe), manganese (Mn), magnesium (Mg), calcium (Ca), and potassium (K). For metal ions, a six-point calibration (0.0–8.0 mg/L in 1% nitric acid (HNO_3)) was performed for each element with a linear fit ($R^2 > 0.995$). Blanks (1% HNO_3) were tested after every 10 samples for quality control. Samples with values over the range of the calibration curve were diluted and re-analyzed.

Statistical Testing

Correlations between measured constituents were tested through regression analysis to determine the relationships between each of the measured constituents, followed by two-tailed t-tests to determine correlation significance (Table 1). Regression analysis was performed in Microsoft Excel.

Growth Media

Gradient tubes, suboxic microcosms that may be utilized to isolate iron oxidizing bacteria, were employed to grow cultures from stream samples (Emerson and Moyer 1997; Emerson and Floyd 2005). The bottom layer of iron sulfide mineral

Table 1. Matrix of correlation (R) between measured constituents.

	Fe	Mn	Ca	Mg	K	Fe	Mn	Ca	Mg	K
			RBCM					**WC1S**		
Fe	1.00	0.18	0.79	0.69	0.56	1.00	0.59	0.61	0.68	0.31
Mn		1.00	0.08	0.05	0.15		1.00	***0.98***	0.42	0.48
Ca			1.00	***0.94***	0.44			1.00	0.44	0.35
Mg				1.00	0.15				1.00	0.34
K					1.00					1.00
			RBC1					**WC1M**		
Fe	1.00	***0.94***	0.66	0.59	0.30	1.00	0.45	0.51	0.44	0.43
Mn		1.00	0.57	0.77	0.24		1.00	***0.97***	0.56	0.42
Ca			1.00	0.06	0.23			1.00	0.68	0.43
Mg				1.00	0.29				1.00	0.57
K					1.00					1.00
			RBC2					**WC2**		
Fe	1.00	0.66	0.68	0.64	0.57	1.00	***0.91***	***0.81***	0.24	0.53
Mn		1.00	0.55	***0.91***	0.39		1.00	***0.96***	0.41	0.68
Ca			1.00	0.25	***0.97***			1.00	0.56	***0.80***
Mg				1.00	0.04				1.00	0.27
K					1.00					1.00
			RBC3							
Fe	1.00	***0.86***	0.75	***0.85***	0.58					
Mn		1.00	0.77	***0.95***	***0.80***					
Ca			1.00	***0.92***	0.27					
Mg				1.00	0.63					
K					1.00					

Correlation significance (p) of correlation coefficient (R) was analyzed using a two-tailed statistical test with Df = N-2, N represents the 5 data points used to calculate R. Values of R>0.8 have significance of p>0.1 (shown in bold italics).

was made using 11.6g of $FeSO_4$, and 9.9g of Na_2S. The cleaned minerals were then mixed with 3.75g of agar mixed in 250 mL of deionized water. The media was composed of 0.75g NH_4Cl, 0.15g $MgSO_4 \cdot 7H_2O$, 0.075g $CaCl_2 \cdot 2H_2O$, 750 mL of deionized water, 0.0375g K_2HPO_4, and 0.315g $NaHCO_3$ (Wolfe's modified mineral media (Wolin et al. 1963)) with 2.25g of 0.3% low melt agarose. All chemicals were obtained from Fisher Scientific and were of analytical grade or higher purity. Media and mineral mixtures were autoclaved then cooled to 60˚C before 1 µL of ATCC vitamin and trace mineral supplement were added to the media.

Bacterial Isolation

Biomass for inoculation was collected on June 12, 2015 throughout each individual site. All tubes and pipette tips were autoclaved, and all aseptic transfers were conducted in a dead air box (Fisher Optimizer PCR workstation). Gradient tubes were made by pipetting 4 mL of the iron sulfide mineral agar solution into 40 mL glass tubes. Following solidification, 12 mL of medium was added to

form a stratified tube. While the top layer was semi-solid, it was purged with N_2 for one minute. Tubes were tightly covered with caps and a rubber septum and stored at 4˚C.

Before inoculation, the gradient tubes were purged with CO_2 at 10 psi for five seconds to obtain neutral pH and provide a carbon source and small amounts of O_2. Using sterile 1 ml syringes equipped with 22-gauge hypodermic needles, 500 µL of biomass (sites with no biomass accumulation were inoculated with collected water samples) sample from each site were inoculated into each tube (first generation). Two negative controls, one without purging and inoculation and one without inoculation, were kept for quality control. Each sample was made in triplicate and incubated at ambient benchtop conditions. Further purification (second generation gradient tubes) was achieved by transferring biomass into new tubes after significant iron oxides (as noted by formation of a distinct red band in the media) were detected in the tubes (timeframe of one to four weeks).

Preliminary identification of iron oxidizing bacteria was conducted on the second generation of gradient tubes. Biomass was harvested from the oxidized band in the gradient tubes. Genomic DNA was extracted using FastDNA® SPIN Kit for Soil (MP Biomedical) following manufacturer instructions. The polymerase chain reaction was utilized to amplify portions of the 16S ribosomal DNA gene (8F and 1492R) primers using a Veriti 96 Well Thermal Cycler (Applied Biosystem). Sequences were examined and trimmed using FinchTV (Geospiza). Unaligned sequences were compared to the National Center for Biotechnology Information (NCBI) database using the BLAST search algorithm to find closely related sequences (Table 2).

Microscopic Analysis

Microscope slides were prepared in an aseptic environment during the transfer of isolated iron oxidizing bacteria from incubated tubes into new gradient tubes. Approximately 5 µL of biomass from incubated tubes was transferred into microcentrifuge tubes and diluted 1:5 with deionized water. Samples were evenly mixed and 5 µL of dilute sample was transferred onto a microscope slide, covered, and dried overnight. Images were taken with an EVOS XL microscope (Life Technologies) at 40× magnification.

Results

Water and Oxide Chemistry

In Situ Data. Through five weeks of field sampling, the pH ranged from 6.7–6.8 and 6.3–6.7 in WC and RBC sites, respectively. The average water temperature was 24˚C in all sites. Regular episodic rainfall events were observed throughout the summer, resulting in loss of iron oxide biomass, but these events were followed by rapid regeneration of deposits. The sites with iron oxides (noted by bright orange deposit, as shown in Figure 1) were sites RBC1-3 and the spring site at WC (WC1S).

Abundance, color, texture, and density of the iron oxides throughout sites RBC1-3 and the seep at site WC1S were visually different. Figure 1 shows the bright orange color of RBC3 (Figure 1A), in contrast to the light brown and dark red appearance of site RBC1 (Figure 1D) and RBC2 (Figure 1B, C), respectively. Additionally, deposits in site RBC3 were visually denser than the other sites. In WC, billowy iron oxides formed around and downstream of the groundwater seep before the intersection with the WC2 tributary. Iron oxides were not observed in the second tributary (site WC2), but samples were collected to assess the water chemistry in comparison to sites at WC1.

Solute Concentrations. Trends in metal and DOC elemental concentrations throughout the sampling period at WC and RBC sites are shown in Figures 2A and 2B, respectively. The DOC in RBC averaged 3.82, 3.62, 2.78, and 3.44 mg/L DOC in RBCM, RBC1, RBC2, and RBC3, respectively. In WC, concentrations of DOC were an average of 4.55, 4.40, and 3.90 mg/L DOC in WC1S, WC1M, and WC2, respectively. These average values were reasonably consistent throughout the five weeks of the study.

The elemental analysis in WC revealed the presence of Fe and Mn at smaller concentrations than Ca, K, and Mg. Fe concentrations ranged from 0–0.25 mg/L, whereas Mn concentrations ranged from 0–0.10 mg/L. In contrast, Ca, Mg, and K concentrations ranged from 2.2–5.6, 1.5–3.2, and 2.4–4.2 mg/L, respectively. The concentrations

Table 2. DNA sequencing data from RBC and WC. The National Center for Biotechnology Information (NCBI) Nucleotide BLAST tool was used to identify the closest isolate. Isolates in bold are known or putative iron oxidizing bacteria.

Location	Identified Isolates	Fragment Size (bp)	% Identity	Accession
RBC1	*Propionivibrio dicarboxylicus* strain*	635	94%	NR_026477.1
	Dechlorosoma* sp. AH	870	96%	AY171616.1
	Rhodocyclus sp. HOD 5**	869	96%	AY691423.1
RBC2	***Sideroxydans lithotrophicus* ES-1***	636	89%	CP001965.1
	Propionivibrio sp. Smarlab*	986	94%	AY643079.1
	Propionivibrio dicarboxylicus strain**	793	92%	NR_026477.1
	Rhodocyclus sp. HOD 5**	1017	95%	AY643079.1
RBC3	Beta proteobacterium**	826	96%	AB376632.1
WC1S	*Herbaspirillum huttiense* strain*	673	79%	KF515669.1
	Sideroxydans lithotrophicus* strain ES-1*	717	95%	NR_074731.1
WC1M	*Acholeplasma oculi* strain*	669	90%	NR_025960.1
	Sideroxydans lithotrophicus* strain ES-1*	1221	84%	NR_074731.1
WC2	*Propionivibrio dicarboxylicus* strain*	787	92%	NR_026477.1
	Candidatus Accumulibacter phosphatis clade**	834	96%	CP001715.1
	Herbaspirillum sp. NR 3-04*	472	91%	KM253112.1
	Thiobacter subterraneus strain C55**	588	93%	NR_024834.1

*Sequence from forward primer (8F). **Sequence from reverse primer (1492R), sequences with similar identified isolates are only presented once.

of Ca, Mn, and Fe tended to increase during the sampling period, whereas Mg and K did not clearly trend with time.

Similarly, lower Fe and Mn concentrations in comparison to other elements were also observed in RBC, where Fe, Mn, Ca, Mg, and K were 0–2.38, 0.07–1.55, 6.3–33.4, 3.3–11.7, and 4.0–11.8 mg/L, respectively. Concentrations of Fe and Mn were more variable at sites containing oxide deposits than at the midstream sampling location. Also, it is notable that the concentrations of all elements in WC are lower than that of the corresponding concentration at RBC.

Bacterial Assessment

Gradient Tube Isolation. Tubes inoculated with samples from WC and RBC sites yielded discrete red bands, indicative of the presence of iron oxidizing bacteria (Figure 3). Interestingly, gradient tubes inoculated from sites with no visible iron oxides (WC2 and RBCM) also yielded iron oxidizing bacteria in gradient tubes. Bacterial growth (as judged by the formation of discrete red bands) in the first generation of gradient tubes was relatively slow in comparison to the second generation. Therefore, transfer of oxidizing organisms occurred after four weeks of growth for the first generation and two weeks for the second generation. Furthermore, the first generation of gradient tubes had a less defined growth zone in comparison to the second generation, which had a defined band of oxidation at a specific media depth (cf. Figure 3A and 3B).

A preliminary DNA assessment of the iron



Figure 1. Iron oxides at the Rocky Branch Creek (RBC) sample area. (A) Bright orange and thick iron oxides at site RBC3 (B) Location of sites RBC1 and RBC2 in the bank and adjacent to each other (C) Iron sheen and dark red iron oxides at site RBC2 (D) Billowy light brown iron oxides in site RBC1.

oxidizing bacteria isolation cultures was conducted on the second generation of gradient tubes using 16S rDNA. Sequencing results produced chromatograms (not shown) with overlapping peaks after 472-1221 base pairs (bp), suggesting a mixed culture is present in the tubes.

Microscale Morphological Assessment. Iron oxide structures observed under a microscope showed string-like structures seen throughout all samples, consistent with previously observed morphologies of bacteriogenic iron oxides. Isolated filamentous (sheath-like) and small globular structures, previously noted in optical micrographs of iron oxide biofilms (Duckworth et al. 2009), were also observed in the samples (Figure 4). String-like structures decreased in frequency from the first generation of gradient tubes to the second generation (images not shown).

Discussion

Aqueous Constituents Correlations

A detailed heat map representing the regression coefficients of correlations (R) is shown in Table 1. Significant correlations ($p < 0.1$; Table 1 values in bold italics) were found between Mn-Ca at all WC sites, and between Fe-Mn, Fe-Ca, and Ca-K at WC2. At RBC, significant correlations were established at RBCM between Ca-Mg, at RBC1 between Fe-Mn, at RBC2 between Mn-Mg and Ca-K, and at RBC3 between Fe-Mn, Fe-Mg, Mn-Mg, Ca-Mg, and Mn-K.

In RBC3, more frequent significant correlations between constituents were found compared to the other sites. Based on the unique location on the north side of the creek (as compared to the other RBC sites), it is likely that the groundwater discharge at this site is fed by a different water

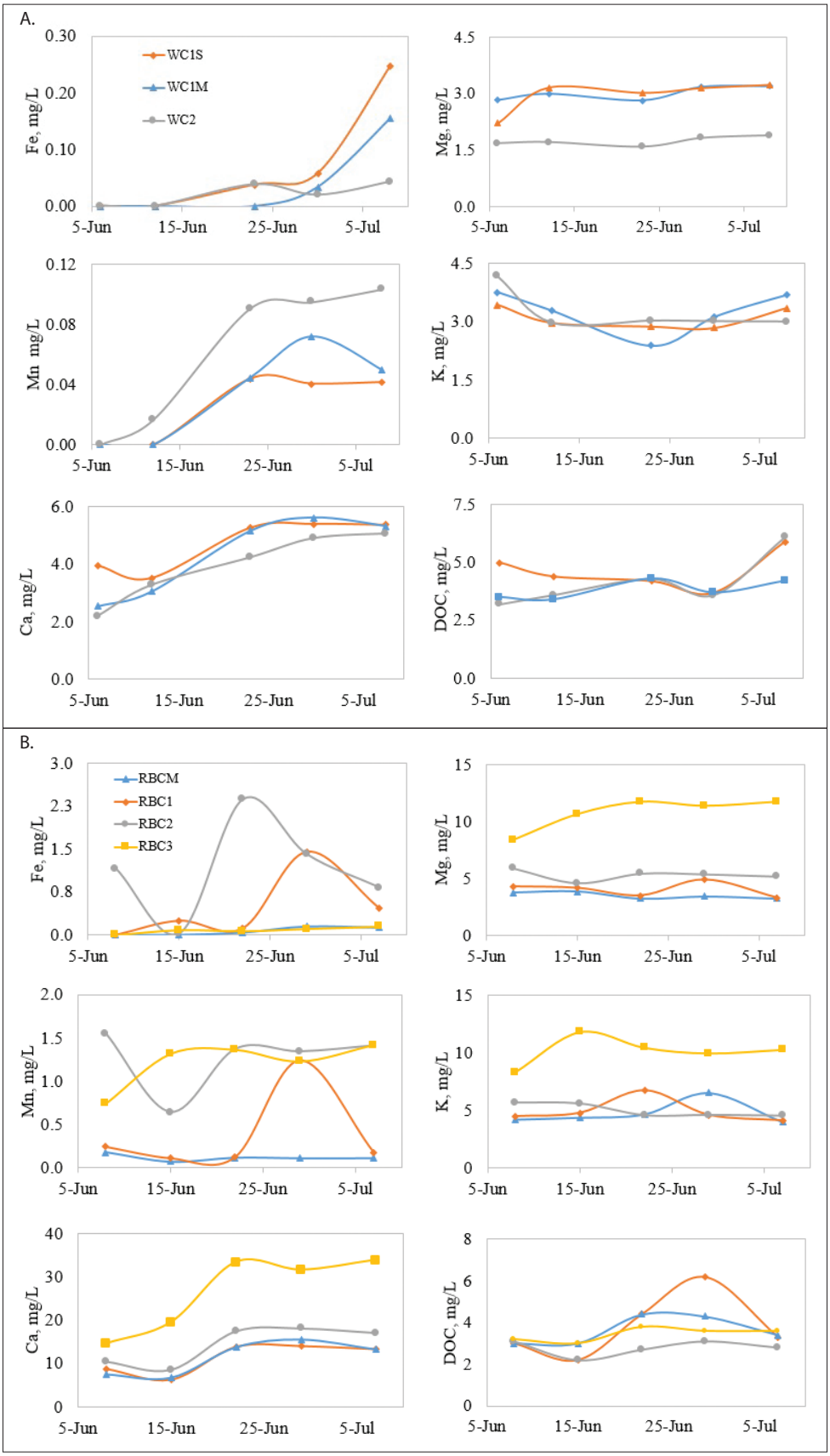

Figure 2. Temporal changes in element concentrations throughout the summer in (A) WC and (B) RBC.

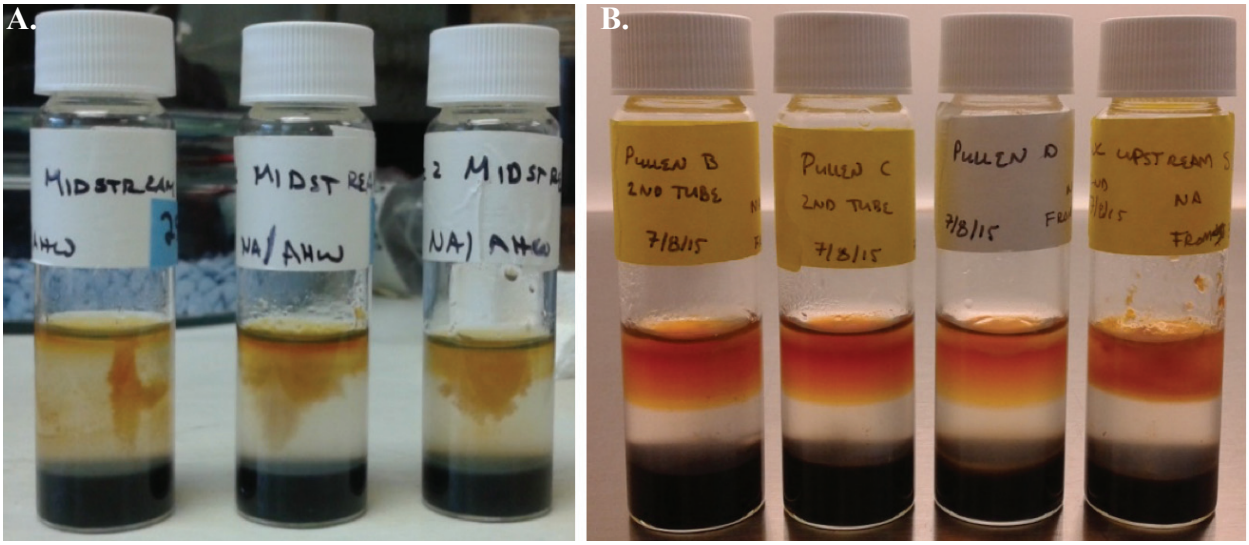

Figure 3. Gradient tubes depicting the distinct growth pattern of the (A) first generation and (B) second generation gradient tubes.

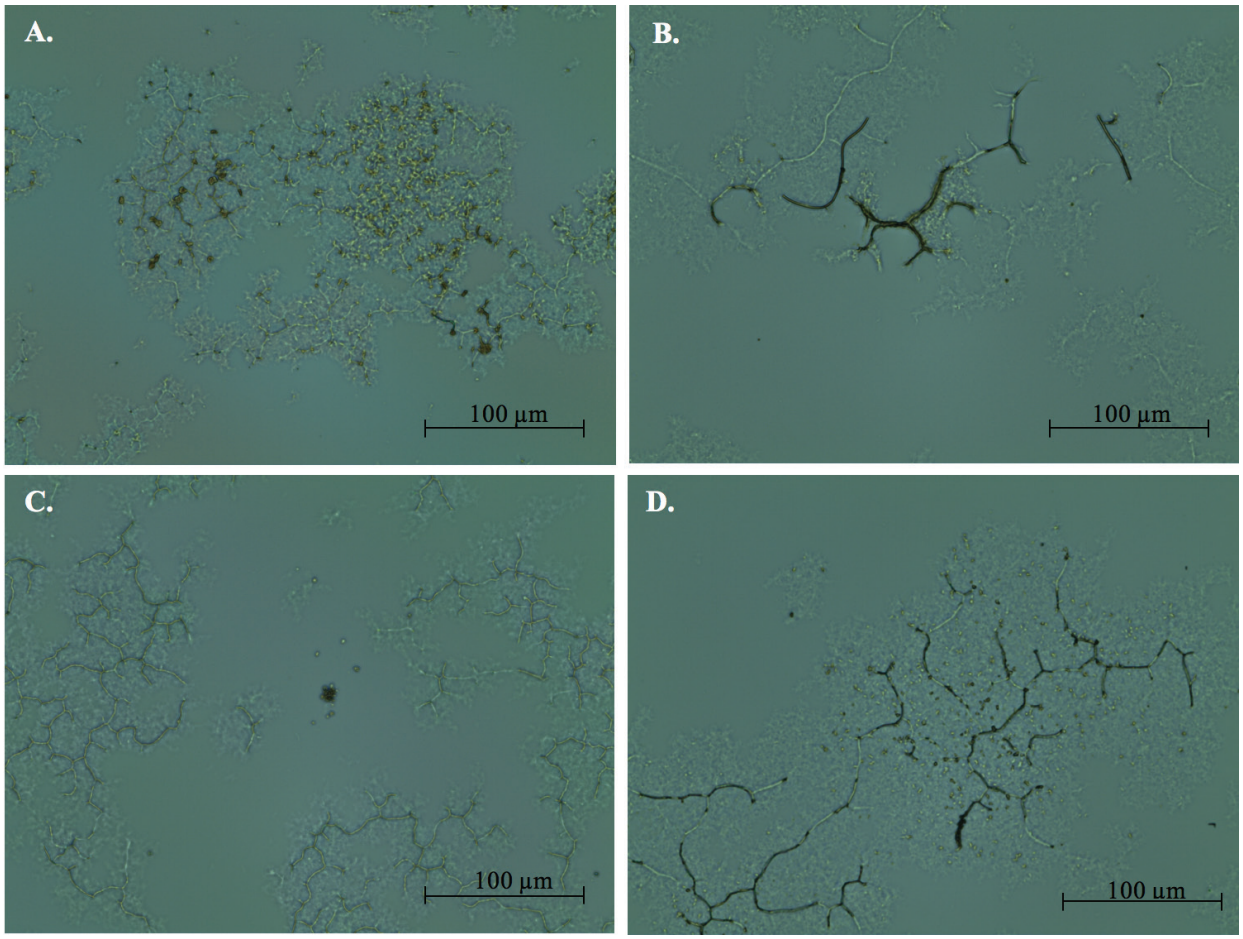

Figure 4. Morphological characteristics of each site's first generation of gradient tubes. (A) WC1M, (B) WC1S, (C) RBC1, and (D) RBC3.

source than RBC1 and RBC2. In addition, these correlations can provide information on coupled chemical processes associated with specific constituents that have similar concentration patterns and significant correlations. Significant correlations between elements that are collocated in similar crystallographic sites in minerals (such as Ca and Mg in clays and carbonates) can be indicative of rock-weathering interactions that contribute to the water's composition (Duckworth et al. 2009), as well as chemical interactions and mineral cycling. We also note that the RBC site is bordered to the north by athletic fields that receive inputs of fertilizer and other chemicals, as well as a greenway and a road to the south. Indeed, Figure 2 shows the relatively higher concentrations of most constituents in RBC compared to WC, with Ca concentrations being almost twice as large, especially in RBC3.

Concentrations of Fe and Mn in all sites were smaller and more variable relative to the other constituents. These observed concentrations are possibly an effect of an assortment of reactions and interactions between the dissolved metals and microorganisms. Precipitation of oxides (governed by low solubility) can result in low concentrations of iron; however, we note that iron concentrations can be highly influenced by the presence of colloidal or chelated iron (Duckworth et al. 2009), and thus be present at concentrations above predicted solubility.

In WC, concentrations of Mg, K, and DOC were consistent throughout the summer. This pattern may result from a higher contribution from groundwater sources and not surface streams. The strong chemical similarities between WC1S and upstream WC1M (Figure 2) was not expected because the spring downstream had water mixing from surface and groundwater sources (where oxides form) that we did not observe upstream.

Establishing the groundwater and surface water contributions to stream water are important in understanding the limiting and driving factors of physical and biological iron oxidation which can be influenced by water chemistry. Based on the formation of iron oxides in gradient tubes (Figure 3) from sites that did not have any on the field (Table 2), it seems likely that the metabolic capability to produce biogenic oxide is widespread in these streams, and thus multiple limiting factors and constantly changing environments play a major role in the formation of iron oxides where FeOB are present.

Microbial Communities

DNA sequences varied in read length with multiple signals interfering in the chromatograms. The poor quality was an indication of the presence of multiple organisms in the gradient tubes. As a result, DNA sequences were not assembled nor aligned and each individual sequence from the 8F and 1492R primers were only BLAST scanned for identification of the most similar isolate (not clone) sequence.

Table 2 shows the closest isolate match to DNA fragments taken from second generation gradient tubes. It should be noted that BLAST results do not necessarily indicate the presence of a bacterium closely related to the organism (due to mixture of DNA sequences in samples), but closest matches do provide some evidence for the presence of related organisms. This mixed nature of DNA is emphasized by the lack of match on forward and reverse sequences of the sample.

Although microbes associated with fermentative metabolisms were frequent (e.g., *Herbaspirillium* and *Propionvibrio* sp.), three tubes contain sequences that are similar to those of the iron oxidizing organisms *Sideroxydans lithotrophicus* and *Dechlorosoma* sp. (Lack et al. 2002; Emerson and Floyd 2005). Interestingly, one tube contained a sequence similar to that of *Thiobacter subterranus*, a bacterium associated with redox cycling of sulfur (Hirayama et al. 2005).

The morphological signatures seen under the microscope can provide additional information on the bacterial communities responsible for the formation of filamentous and globular structures observed under the microscope (Figure 4). The predominant iron oxidizing bacteria identified in environments similar to those described in this study (circumneutral, microaerophilic environment) are *Betaprotobacteria* (Emerson et al. 2010; Maamar et al. 2015) belonging to the *Gallionella*, *Leptothrix,* and *Sideroxydans* genera (Cullimore and McCann 1978; Emerson et al. 2010). The sheath-like filamentous structures (Figure 4) observed under the microscope are

characteristic of *Leptothrix* (Emerson et al. 2010; Fleming et al. 2011; Fleming et al. 2014). These bacteria are neutrophilic, microaerophilic, and grow at ideal temperatures ranging from 20–25° (Cullimore and McCann 1978; Emerson et al. 2010). A study by Fleming et al. (2014) observed the formation of sheath-like structures associated with *Leptothrix ochracea* during the summer and the succession of *Gallionella* in the spring. This study further supports the possible presence and contribution of *Leptothrix* to the environments of our study, which was conducted in warm (24°C daytime temperature) waters during the summer (it should be noted that *Leptothrix ochracea* is currently uncultured, thus not in 16S databases (Fleming et al. 2011)). In addition, the globular structures observed may be a mix of cell matter and precipitates that adhere to iron oxides, or encrusted iron oxides similar to those in the *Sideroxydans* genera (Duckworth et al. 2009).

The observed formation of biogenic iron oxides in gradient tubes inoculated from sites without visible oxide deposits indicates that other factors may limit the accumulation of iron oxides environments. Complex microbial communities can reduce the dominance of one specific organism and reduce microbial mediated biomineral formation. The slow growth of organisms with iron oxide bands in the first generation of gradient tubes compared to the second generation may be an indication of the diversity of microbial communities in that niche that compete for resources and limit the formation of iron oxides.

Conclusion

Understanding the chemistry of diverse environments where iron oxidizing bacteria can harness energy through the precipitation of biominerals (i.e., iron oxides) is key to understanding iron biogeochemical cycling. Through an overall analysis of the water chemistry conducted in this study the following observations were made: 1) the concentrations of measured constituents were significantly higher in RBC compared to WC, yet some microenvironments in both sites sustained constant iron oxide formation; 2) concentrations of Fe and Mn were relatively lower and more variable than other measured constituents; and 3) presence of iron oxidizing bacteria was established through preliminary DNA analysis and microscopic examination of the biofilm collected from these sites, including those with no visible oxides.

Despite the close proximity of some of these sites, iron oxides only form in certain locations due to unknown limiting factors. As noted previously, the microbial community and aqueous chemistry of microsites may affect the formation and accumulation of oxide biofilms. Indeed, the chemistries of sites near each other were observed to be variable, as was our ability to identify iron oxidizing organisms. However, the physical environment at these locations (e.g., hydraulic conditions) may not be favorable for appreciable accumulation of iron oxide bearing biofilms. Oxygen concentrations in these sites are influenced by water depth, gas boundary diffusion, and fluid mixing processes. The shallow and variable stream flow in these sites may result in large fluctuations of oxygen concentration areas, potentially making areas transiently or permanently unsuitable for FeOB that require selective oxygen gradients for metabolic activities. The research presented herein was part of a 10-week research experience for undergraduates which limited the scope of the research to this timeframe. Future work will include further purification of gradient tubes to conduct DNA assessment of the FeOB isolates, and attempts to better constrain groundwater composition.

Acknowledgements

We thank Tyler Sowers, Wayne Roper, and Terrance Gardner for assistance on this project. We thank the National Science Foundation (1255158 and 1358938) for funding and support of this project.

Author Bio and Contact Information

Nohemi Almaraz is a Civil and Environmental Engineering Masters Student at Colorado School of Mines where she studies analytical techniques to quantify organic compounds in complex waste streams. She may be contacted at nalmaraz@mines.edu.

Andrew H. Whitaker is a Ph.D. student in Soil Biogeochemistry in the Department of Crop and Soil Science at North Carolina State University. He studies the formation and structure of iron biominerals and their

impact on contaminant dynamics in circumneutral pH waterways. He may be contacted at ahwhitak@ncsu.edu.

Megan Y. Andrews is the Project Manager for the Center for Integrated Fungal Research and the Plant Soil Microbial Community Consortium at North Carolina State University. She may be contacted at megan_andrews@ncsu.edu.

Owen W. Duckworth is an Associate Professor of Soil Biogeochemistry in the Department of Crop and Soil Science at North Carolina State University. He serves as Co-director of the Basic and Environmental Soil Science Training (BESST) Research Experiences for Undergraduates (BESST REU) program at NC State University. He may be contacted at owen_duckworth@ncsu.edu or by phone at 919-513-1577.

References

Andrews, M.Y. and O.W. Duckworth. 2016. A universal assay for the detection of siderophore activity in natural waters. *Biometals* 29: 1085-1095.

Baker, B.J., G.W. Tyson, L. Goosherst, and J.F. Banfield. 2009. Insights into the diversity of eukaryotes in acid mine drainage biofilm communities. *Applied and Environmental Microbiology* 75: 2192-2199.

Blowes, D.W., C.J. Ptacek, J.L. Jambor, and C.G. Weisener. 2003. The geochemistry of acid mine drainage. In: *Treatise on Geochemistry*, K.K. Turekian (Ed.). Pergamon, Oxford, pp. 149-204.

Cullimore, D.R. and A.E. McCann. 1978. The identification, cultivation, and control of iron bacteria in groundwater. In: *Aquatic Microbiology*, Skinner & Shewan (Eds.). Academic Press, New York, pp. 219-262.

Colmer, A.R., K.L. Temple, and M.E. Hinkle. 1950. An iron-oxidizing bacterium from the acid drainage of some bituminous coal mines. *Journal of Bacteriology* 59: 317-328.

Druschel, G.K., D. Emerson, R. Sutka, P. Suchecki, and G.W. Luther. 2008. Low-oxygen and chemical kinetic constraints on the geochemical niche of neutrophilic iron(II) oxidizing microorganisms. *Geochimica et Cosmochimica Acta* 72: 3358-3370.

Duckworth, O.W., S.J.M. Holmström, J. Peña, and G. Sposito. 2009. Biogeochemistry of iron oxidation in a circumneutral freshwater habitat. *Chemical Geology* 260: 149-158.

Emerson, D., E.J. Fleming, and J.M. McBeth. 2010. Iron-oxidizing bacteria: An environmental and genomic perspective. *Annual Review of Microbiology* 64: 561-583.

Emerson, D. and M.M. Floyd. 2005. Enrichment and isolation of iron-oxidizing bacteria at neutral pH. *Methods in Enzymology* 397: 112-123.

Emerson, D. and C. Moyer. 1997. Isolation and characterization of novel iron-oxidizing bacteria that grow at circumneutral pH. *Applied and Environmental Microbiology* 63: 4784-4792.

Emerson, D., J.V. Weiss, and J.P. Megonigal. 1999. Iron-oxidizing bacteria are associated with ferric hydroxide precipitates (Fe-Plaque) on the roots of wetland plants. *Applied and Environmental Microbiology* 65: 2758-2761.

Fleming, E.J., I. Cetinić, C.S. Chan, D.W. King, and D. Emerson. 2014. Ecological succession among iron-oxidizing bacteria. *The ISME Journal* 8: 804-815.

Fleming, E.J., A.E. Langdon, M. Martinez-Garcia, R. Stepanauskas, N.J. Poulton, E.D.P Masland, and D. Emerson. 2011. What's new is old: Resolving the identity of *Leptothrix ochracea* using single cell genomics, pyrosequencing and FISH. *PLoS ONE* 6: 1-10.

Hirayama, H., K. Takai, F. Inagaki, K.H. Nealson, and K. Horikoshi. 2005. *Thiobacter subterraneus* gen. nov., sp. nov., an obligately chemolithoautotrophic, thermophilic, sulfur-oxidizing bacterium from a subsurface hot aquifer. *International Journal of Systematic and Evolutionary Microbiology* 55: 467-472.

Jambor, J.L. and J.E. Dutrizac. 1998. Occurrence and constitution of natural and synthetic ferrihydrite, a widespread iron oxyhydroxide. *Chemical Reviews* 98: 2549-2586.

Johnson, D.B. and K.B. Hallberg. 2015. Acid mine drainage remediation options: A review. *Science of the Total Environment* 338: 3-14.

Lack, J.G., S.K. Chaudhuri, R. Chakraborty, L.A. Achenbach, and J.D. Coates. 2002. Anaerobic biooxidation of Fe(II) by *Dechlorosoma suillum*. *Microbial Ecology* 43: 424-431.

Maamar, S.B, L. Aquilina, A. Quaiser, H. Pauwels, S. Michon-Coudouel, V. Vergnaud-Ayraud, T. Labasque, C. Roques, B.W. Abbott, and A. Dufresne. 2015. Groundwater isolation governs chemistry and microbial community structure along hydrologic flowpaths. *Frontiers in Microbiology* 6.

Peng, X., S. Chen, H. Zhou, L. Zhang, Z. Wu, J. Li, J. Li, and H. Xu. 2011. Diversity of biogenic minerals in low-temperature Si-rich deposits from a newly discovered hydrothermal field on the ultraslow spreading Southwest Indian Ridge. *Journal of Geophysical Research: Biogeosciences* 116: 1-18.

Posth, N.R., D.E. Canfield, and A. Kappler. 2014. Biogenic Fe(III) minerals: From formation to diagenesis and preservation in the rock record. *Earth-Science Reviews* 135: 103-121.

Sowers, T.D., J.M. Harrington, M.L. Polizzotto, and O.W. Duckworth. 2017. Sorption of arsenic to biogenic iron (oxyhydr)oxides produced in circumneutral environments. *Geochimica et Cosmochimica Acta* 198: 194-207.

Søgaard, E.G., R. Aruna, J. Abraham-Peskir, and C.B. Koch. 2001. Conditions for biological precipitation of iron by *Gallionella ferruginea* in a slightly polluted ground water. *Applied Geochemistry* 16: 1129-1137.

Toner, B.M., T.S. Berqu, F.M. Michel, J.V. Sorensen, A.S. Templeton, and K.J. Edwards. 2012. Mineralogy of iron microbial mats from Loihi Seamount. *Frontiers in Microbiology* 3.

Wolin, E.A., M.J. Wolin, and R.S. Wolfe. 1963. Formation of methane by bacterial extracts. *Journal of Biological Chemistry* 238: 2882-2886.

Universities Council on Water Resources
Journal of Contemporary Water Research & Education
Issue 160, Pages 72-84, April 2017

Anthropogenic Litter Abundance and Accumulation Rates Point to Seasonal Litter Sources on a Great Lakes Beach

*Anna E.S. Vincent[1] and Timothy J. Hoellein[1]

[1]*Department of Biology, Loyola University Chicago, Chicago, IL, USA*
**Corresponding author*

Abstract: The ecology of anthropogenic litter (AL) (i.e., trash) in marine ecosystems is a growing field of research. Freshwater and marine ecosystems have similar AL densities, but research on the assemblage and accumulation rates of AL in freshwater environments is less common. We studied AL accumulation at Pratt beach, located on Lake Michigan in Chicago, IL, USA. The beach has a concrete pier at the south end, with two areas of grass bisected by a walking path. Pratt beach receives many daily visitors, but unlike other urban beaches, it has no daily municipal beach grooming. We established five 60 m transects parallel to the shoreline, with increasing distance to the shoreline. Each transect was divided into four habitat zones (i.e., pier, south vegetation, path, and north vegetation). All AL within 1 m of each transect was collected biweekly from March-November 2015. AL density (No. m^{-2}) and input rate (No. m^{-2} day^{-1}) were highest at the pier, regardless of distance from the shoreline. Fall had the highest AL density relative to spring or summer. We concluded AL inputs at the pier were dominated by direct littering and the retention of wind- and wave-blown AL at the pier's wall. The study beach had much higher AL than adjacent beaches which received municipal AL cleaning, suggesting cleaning is effective at reducing AL density. This study suggests that, given the mobile nature of AL by natural processes, infrequent sampling may underestimate total AL abundance. Management efforts for AL should be directed towards the greatest AL accumulation sites within a beach, and at prevention of direct littering from visitors.

Keywords: *marine debris, urban, Lake Michigan, trash, glass, pollution, beach maintenance*

Abundance of anthropogenic litter (AL) and the ecological and economic consequences of AL are well documented in marine environments (Abu-Hilal and Al-Najjar 2009; Cózar et al. 2014; Kühn et al. 2015). Recent studies in lakes and rivers confirm that AL is abundant in freshwaters and its density is comparable to marine ecosystems (Hoellein et al. 2014; Driedger et al. 2015; Rech et al. 2015; McCormick and Hoellein 2016). However, more research is needed to examine the ecological dimensions of AL, such as rates of input, output, and breakdown, as well as biological interactions. For example, repeated measurements of AL density over time are needed to document AL movement and to quantify the anthropogenic and natural factors driving its redistribution (Ryan et al. 2009; Carson et al. 2013; McCormick and Hoellein 2016).

Anthropogenic litter represents a complex assemblage of material types, some of which are highly mobile. For example, McCormick and Hoellein (2016) tracked individual AL items to show that the most common AL types in the riparian zone of an urban river (e.g., cans, bottles, plastic bags) had a turnover time of about one year. Export of AL was driven by flooding, seasonality, and capacity for materials to become entrained in debris dams and vegetation (McCormick and Hoellein 2016). Similarly, Bowman et al. (1998) recorded AL abundance and material (e.g., plastic, metal, glass, paper, wood, cloth) to track AL mobility on Mediterranean beaches. The short AL

turnover rate at those sites, less than six months, indicated that beaches are not the final resting place for AL, but rather a brief interruption in the constant movement of AL in aquatic environments. These studies conclude that AL density on a single date is not descriptive of total AL inputs over time. While it may appear that the same amount of AL is present over repeated visits, it is apparent from these studies that some portion of the AL standing stock has arrived and departed, so gross input may not be represented.

The Laurentian Great Lakes are the largest contiguous body of freshwater in the world, a critical resource for communities and industries in the region, and an emerging site of focus for AL ecology in surface waters, sediment, and beaches (Zbyszewski and Corcoran 2011; Zbyszewski et al. 2014; Driedger et al. 2015; Hoellein et al. 2015). Assessments of AL density and composition on Great Lakes beaches have used a diversity of approaches to assess spatial variation, and thereby infer its sources and movement. For example, citizen-science datasets have been used to address AL density on Lake Michigan beaches to show positive correlations between beach-goer activity, proximity to urban centers, and AL abundance (Hoellein et al. 2015). Other studies followed a transect-based study design to examine spatial patterns of AL abundance on Great Lakes beaches, with a focus on the plastic component of AL (Zbyszewski and Corcoran 2011; Zbyszewski et al. 2014). Those results suggested proximity to AL sources including urban environments and industrial manufacturing, combined with lake currents, drive distribution of plastic AL on beaches. Finally, Hoellein et al. (2014) used transects to study AL abundance on a Lake Michigan beach, and compared those values to the benthic and riparian zones of an urban river. Overall, research on Great Lakes AL density and composition is in its early stages, and to our knowledge, no studies have returned to permanent transects to measure temporal patterns in AL abundance and quantify net input rates on Great Lakes beaches.

The purpose of this study was to examine AL composition over time using permanent transects. Our objectives were to 1) measure spatial and temporal patterns in AL density, distribution, and accumulation rates; 2) examine temporal changes in AL to infer primary sources; 3) scale up net input rates to determine annual load of AL; and 4) directly compare AL density on Lake Michigan beaches with data collected via different methods (i.e., transect-based and citizen-science-based) and at sites which experience different municipal management (i.e., beach grooming or no beach grooming). With respect to spatial patterns, we hypothesized that AL would be highest next to a pier which delineated the south end of the beach, and closest to the water's edge. We also hypothesized that AL density would be highest in summer and lowest in fall and spring, as beach visitors were likely the dominant AL source. We expected that AL density would be higher when measured using a transect-based study design, as opposed to using citizen-science data, as volunteer scientists may be more likely to underestimate total AL density. Finally, we hypothesized that AL density would be higher on the study beach, which receives no municipal cleaning, relative to beaches that receive regularly scheduled maintenance.

Methods

Study Site

Data collection was completed at Pratt beach, a public beach and dunes restoration area in a densely populated urban neighborhood in Chicago, IL that covers an area of 11,366 m^2 (Figure 1). The dunes restoration area is surrounded by public beaches, and was established in 2003 to serve as a sanctuary for native plants and migratory birds. There are no stormwater outlets, combined sewer outflows, or streams near the restoration area. Public beaches are maintained by the Chicago Park District from Memorial Day (last Monday of May) to Labor Day (first Monday of September; Hoellein et al. 2015). However, the dunes restoration area at Pratt beach is not actively cleaned by the city of Chicago or by volunteers. We established five 60 m long permanent transects parallel to the shoreline. The transects were spaced 11-47 meters apart and divided into four habitat zones: pier, south vegetation, path, and north vegetation. The pier at Pratt beach is a solid concrete structure spanning the entire south edge of the restoration area. The south and north vegetation areas consist of re-emergent native dune grasses, and the beachgoers

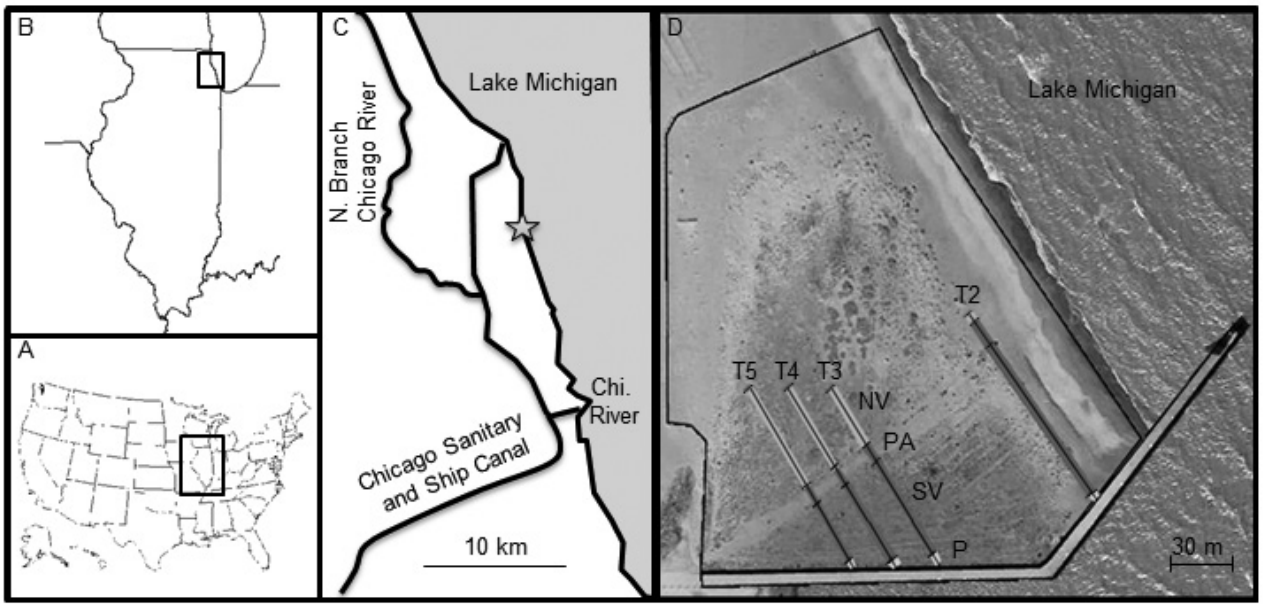

Figure 1. Lake Michigan study site located at Pratt beach in northeastern Illinois. (D) Location of transects (T2-T5) in pier (P), south vegetation (SV), path (PA), and north vegetation (NV) habitat zones.

path consists of sand and bisects the vegetation zones. Transect 1 was eliminated from the analysis after it was inundated by lake level rise soon after the start of the project.

Data Collection and Categorization

All AL visible to the naked eye located within 1 m of each transect line was collected biweekly from March 19, 2015 until November 18, 2015. Collection dates were classified by season, where spring dates spanned from March 19, 2015 to Memorial Day (May 25, 2015), summer collections fell between Memorial Day and Labor Day (September 7, 2015), and fall collections occurred from Labor Day to November 18, 2015. We were unable to collect AL during winter due to consistent snow and ice coverage. AL was categorized, counted, and weighed in the laboratory. The AL categories were created by the Ocean Conservancy and Alliance for the Great Lakes to be used in citizen-science data collection during beach clean ups (Hoellein et al. 2015). The seven categories are food-related AL, smoking-related AL, small AL (i.e., AL ≤2.5 cm), medical/personal hygiene, waterway activities, dumping activities (e.g., large appliances and construction materials), and 'other' (e.g., fireworks). We calculated density as number of AL items and AL mass on an aerial basis (No. m^{-2} and g m^{-2}, respectively). The number of days between each collection was recorded and used to determine net accumulation rates of AL by number of items and mass accumulation rates (No. m^{-2} day^{-1} and g m^{-2} day^{-1}, respectively) for each habitat zone (McCormick and Hoellein 2016). We note the net accumulation is the balance between gross accumulation rates and export. Net accumulation assumes the material present on a collection date is the net input of new AL since the preceding collection date, as some amount of the gross accumulation was exported during the days between collection dates (Bowman et al. 1998; McCormick and Hoellein 2016).

Scaling Up Transects to Total Beach Area

Annual net accumulation for the dune restoration area was determined using beach area and total number of items. We calculated total area of all habitats and transects using Google Earth Pro by extending the length of each transect to the edge of the restoration zone and considering the width of each transect to extend to the halfway point between transects. Beach zone area was multiplied by the zone accumulation rate, and the number of days since the previous collection date. Finally, we

summed across all collection dates (C; excluding the first collection) and zones to estimate the number of AL items accumulated (Equation 1).

$$\text{No. items accumulated} = \sum_{i=1}^{c} (\text{accumulation rate} * \text{area} * \text{days}) \quad \text{(Equation 1)}$$

This represents the total number of items that arrived on Pratt beach over the course of one year in each habitat and each transect. We report these values in terms of annual accumulation, but our results are conservative as they do not account for winter accumulation. AL collection was not possible during the winter due to snow cover throughout the beach and shifting ice mounds at the water's edge, limiting access. We would estimate winter accumulation rates to be low given our conclusion that beach visitors are the main source of AL. Other sites with ice and snow would likely experience similar complications for annual AL budget calculations.

Precipitation and Wind Data

We gathered precipitation and wind speed data from the online daily climate database issued by National Weather Service at the closest location we could identify to our study site. All data were recorded at the Weather Forecast Office (WFO) Chicago-O'Hare field station, approximately 20.5 km from the study site (NOAA 2015). In 2015, the annual precipitation daily average was 0.11 inches, and the average wind speed was 9.8 mph. We calculated peak precipitation and wind speed between consecutive collection dates using daily weather data from the WFO. Peak precipitation refers to the heaviest rainfall event between consecutive collection dates. Peak wind speed is defined as the highest recorded wind speed between collection dates. Of the 16 dates where we recorded the peak wind speed, seven dates had wind from the North, five from the West, and four from the South.

Data Analysis

We compared AL density (No. m^{-2}) and AL mass (g m^{-2}) among the four habitats and transects using 2-way ANOVA. AL density and mass were analyzed individually in spring, summer, and fall. Following a significant interaction between habitats and transects, we utilized 1-way ANOVA to compare AL density among the four habitats in each transect individually, and accounted for multiple comparisons with a Bonferonni correction ($\alpha = 0.05/4 = 0.013$). Temporal patterns of AL density and AL mass across all collection dates were analyzed using repeated measures ANOVA. We analyzed AL composition to determine the most abundant categories for each season, transect, and habitat. Small AL was examined separately by material (e.g., glass and other) to determine the dominant material in each habitat. We used simple linear regressions to quantify the relationships between mean AL density (No. m^{-2}) of each habitat and transect, and peak precipitation and wind speed that occurred during the preceding collection interval. All statistical analyses were completed using SYSTAT 13 and SigmaPlot 10.0.

Results

Spatial and Temporal Variation of AL

AL density was different among habitat types and transects, and these patterns were similar across the three seasons. In spring, AL density in the pier zone was higher than the other habitats (2-way ANOVA $p<0.001$; Figure 2A). In summer and fall, there was a significant transect x habitat interaction (2-way ANOVA $p<0.001$ and $p=0.006$, respectively; Figure 2), so we analyzed differences among habitats for each transect individually. The transect 2 section of the pier zone was higher in AL density during the summer than the other habitats (ANOVA $p=0.001$). In the summer measurements of transects 3-5, the pier zone was highest in AL density, the path was intermediate, and the vegetation zones were lowest (Figure 2B). In fall, transects 3 and 5 showed similar patterns as summer where the pier was highest (ANOVA $p=0.007$ and $p<0.001$, respectively), while transects 2 and 4 had no significant differences among habitats (ANOVA $p=0.028$ and $p=0.132$, respectively; Figure 2C). Across all transects and collection dates, the greatest AL density occurred in the pier zone during the fall, and the lowest AL density occurred in the south vegetation zone during spring (Figure 2).

AL mass showed fewer differences among transects or seasons than AL density. AL mass was higher in transect 2 relative to the other transects

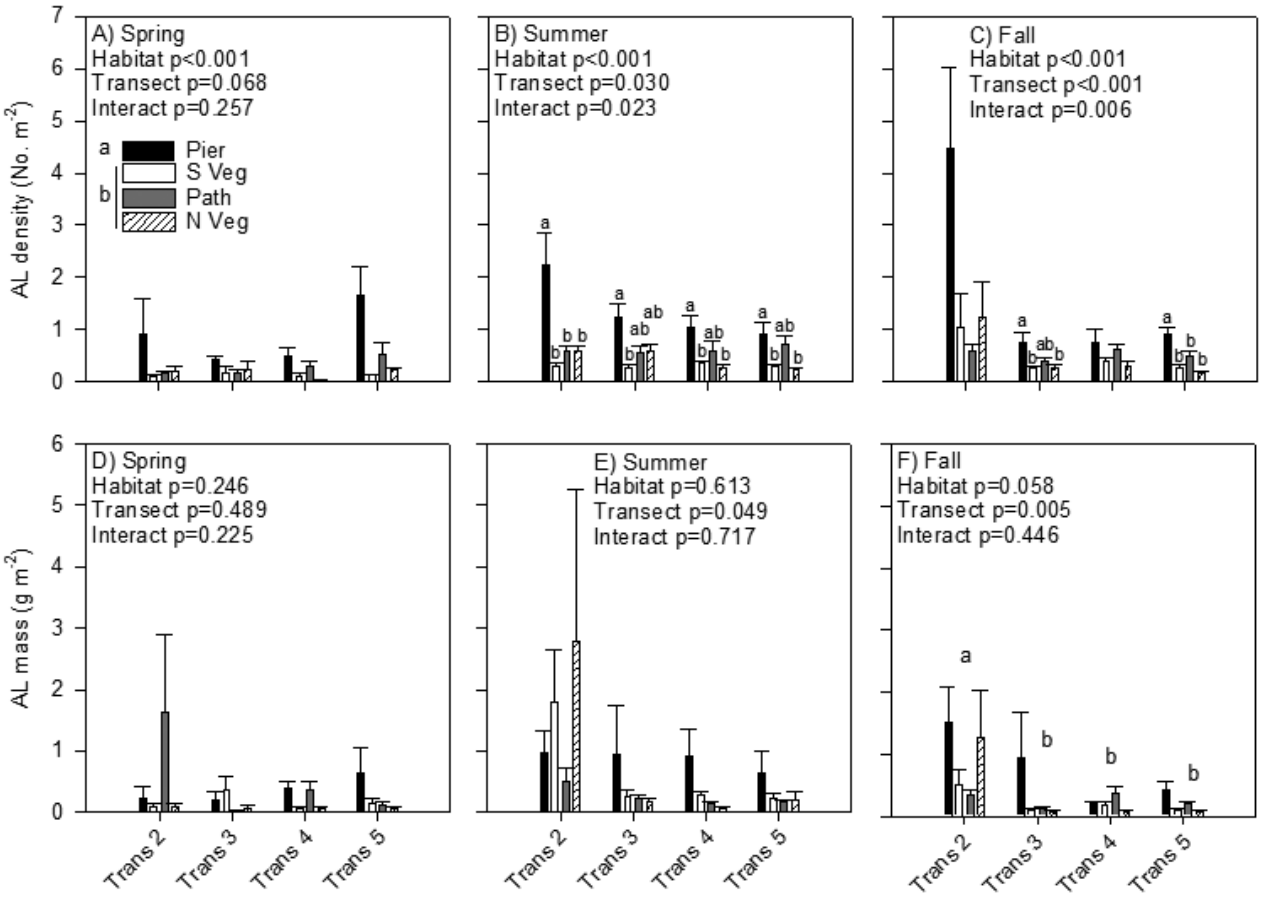

Figure 2. Anthropogenic litter (AL) density for all habitats and transects in (A) spring, (B) summer, and (C) fall. Mass of AL for all habitats and transects are shown in (D) spring, (E) summer, and (F) fall. The p-values are from 2-way ANOVA among habitats and transects in each season. Small letters next to legend in panel A indicate differences among habitats from Tukey's multiple comparison test. Small letters in panels B and C indicate differences among habitats in each transect from Tukey's multiple comparison test, completed after significant habitat x transect interaction. Small letters in panel F indicate differences among transects.

in the fall only (2-way ANOVA p=0.005; Figure 2F). During the fall, AL mass was highest in the pier zone and generally the lowest in the north vegetation zone (Figure 2F). In spring and summer, there was no difference in AL mass among habitats and transects, and there were no significant transect x habitat interactions (Figure 2).

We also considered patterns in AL density and mass over time. Total AL density in the pier zone was higher than the other habitats (R-M ANOVA p=0.036), however, AL density was not significantly different among collection dates (R-M ANOVA p=0.061; Figure 3). In contrast, AL mass showed no differences in habitat (R-M ANOVA p=0.625), but significant differences among collection dates (R-M ANOVA p=0.025; Figure 3), attributed to two peaks of AL mass in early July. There was no significant date x transect interaction in AL density or AL mass (R-M ANOVA p=0.350 and p=0.233, respectively).

Relative Composition of AL by Category

The categories of small AL, smoking-related AL, and food-related AL contributed most to total AL composition across all seasons and habitats. Small AL contributed 55-60% of all collected material, while smoking- and food-related AL represented 20-25% in spring, summer, and fall (Figure 4A). The relative amount of smoking-related AL was higher in fall (~20%) than in spring (~10%) or summer (~15%). By habitat, the contribution of small AL to total AL was relatively consistent

at ~55% in the pier, south vegetation, and path habitats, but was ~65% of all AL in the north vegetation (Figure 4B). The amount of smoking- and food-related AL was ~35% in the pier, 20-25% in the south vegetation and path habitats, and ~10% in the north vegetation. The composition of small AL was largely glass (~70% of small items; Figure 4C), with foam, metal, and plastic as the remainder (~30% of small items). Items from waterway activities, medical/personal hygiene, dumping activities, and other miscellaneous items were rare across all habitats and seasons (~5%; Figure 4A, 4B).

Relationship between AL and Weather

We used simple linear regressions to quantify the relationship between weather patterns and AL density in all transects and habitat zones. There

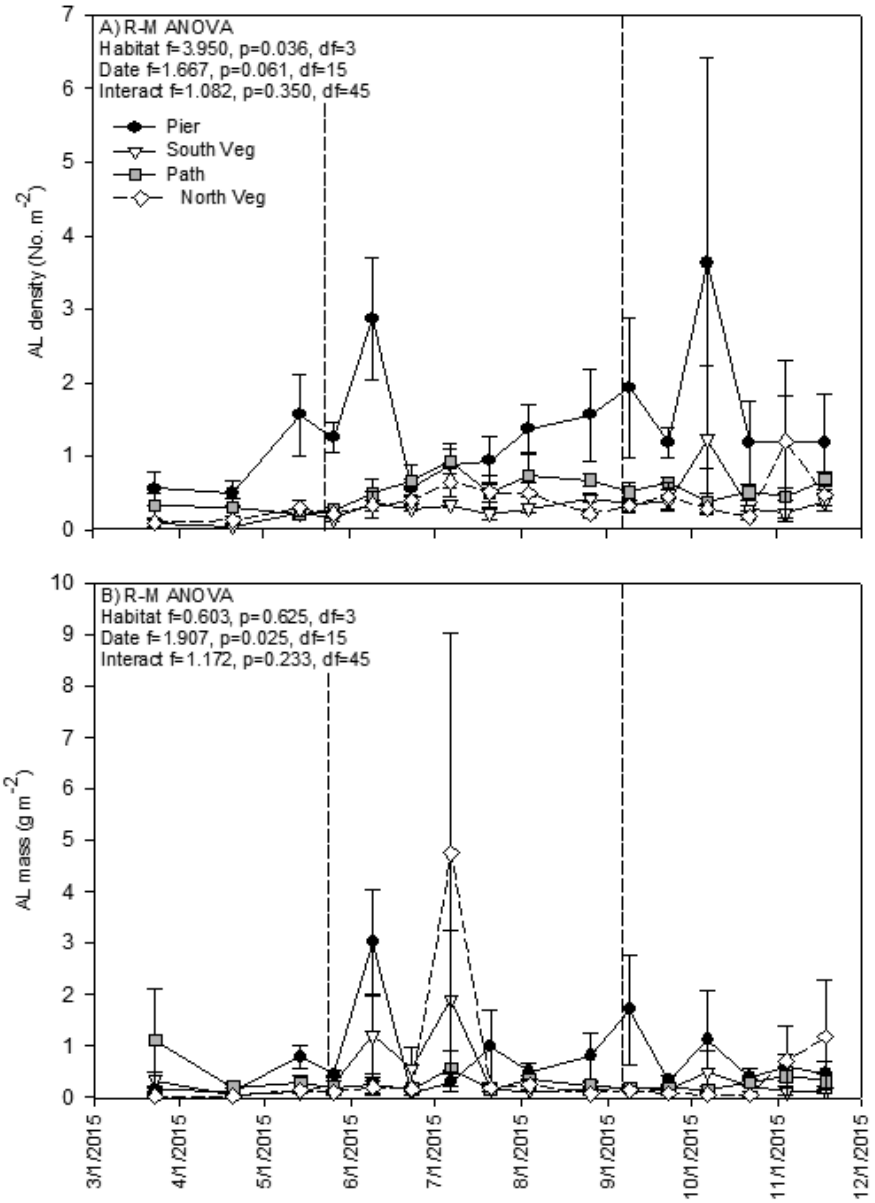

Figure 3. Mean (±SE) anthropogenic litter (AL) (A) density and (B) mass by habitat across all collection dates. From left to right, dashed lines represent changes in season (American holidays of Memorial Day, May 25, 2015 and Labor Day, September 7, 2015, respectively). These dates serve as a reference point, representing the start and end of beach maintenance on municipally maintained beaches. *P*-values are from repeated measures ANOVA.

were no significant linear correlations between AL density and precipitation or wind (Table 1). The strongest linear relationship, albeit statistically insignificant, showed a decreasing trend between AL density in the pier zone and peak precipitation since the previous collection date (R^2=0.191, p=0.091), a trend which may indicate that high precipitation is correlated with lower net AL accumulation.

Scaling Up Transects to the Whole Beach

We scaled up our results to the area covered by each transect and habitat on the beach. The dunes restoration area (total area = 11,366 m^2) had a total net accumulation of 79,915 AL items in 2015. The north vegetation zone was the largest of the four habitats (7,490 m^2, Table 2) and had an annual net accumulation of 50,209 items; south vegetation was the next largest (2,945 m^2) with a net accumulation of 17,537 items; the pier and path zones were the smallest (374 m^2 and 556 m^2, respectively) and had an annual net accumulation of 7,562 items and 4,606 items, respectively. By mass, Pratt beach had a total annual net accumulation of 99,498 g of AL. The north vegetation and south vegetation zones had an annual net accumulation of 67,234 g and 25,131 g, respectively. The pier and path zones had the lowest net accumulation by mass with an annual net accumulation of 4,125 g and 3,008 g, respectively. Finally, the total net accumulation of 'non-small AL' items versus 'small AL' items was different for density and mass. Pratt beach had a total net accumulation of 42,060 non-small items and 37,855 small items. However, the small items represented much of the mass, or 90,361 g, while non-small AL items were 9,138 g.

Discussion

Spatial Patterns in AL Abundance

Patterns in spatial variation of AL followed our hypothesis, as the pier zone had the highest AL density for all habitats and seasons. The prevailing lake and wind currents in Chicago (i.e., the southwest side of Lake Michigan) are from north to south (Beletsky et al. 1999), thus any litter deposited on the beach, especially on the north side of the pier, is likely to accumulate along the pier wall. Like natural materials (i.e., leaf litter and

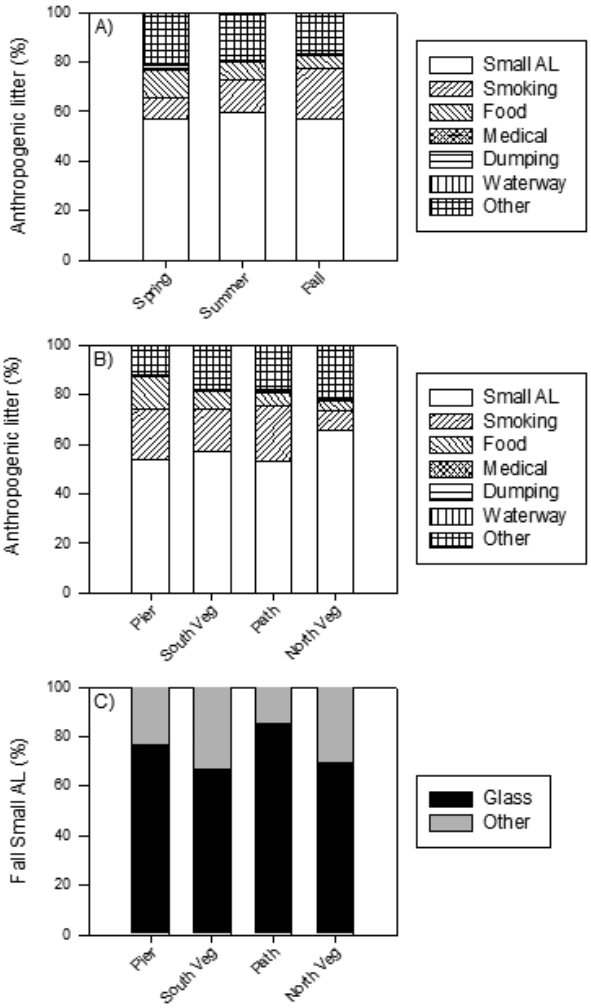

Figure 4. Composition of anthropogenic litter (AL) by (A) season, (B) habitat zone, and (C) AL 1-2.5 cm, analyzed by habitat in fall.

Table 1. R^2 (*p*-value) from simple linear regressions between weather patterns and anthropogenic litter (AL) density (No. m^{-2}) by transect and habitat. Peak precipitation (in) and peak wind speed (mi/hr) were measured between consecutive collection dates.

	Peak Precipitation	Peak Wind Speed
Transect 2	0.068 (0.330)	0.070 (0.321)
Transect 3	0.082 (0.282)	0.084 (0.275)
Transect 4	0.053 (0.392)	0.010 (0.717)
Transect 5	0.043 (0.441)	0.019 (0.607)
Pier	0.191 (0.091)	0.046 (0.426)
South Veg	0.023 (0.576)	0.044 (0.438)
Path	0.139 (0.155)	0.068 (0.329)
North Veg	0.038 (0.472)	0.009 (0.734)

Table 2. Annual net accumulation (number of items) of anthropogenic litter (AL) for all transects and habitats.

	Area (m^2)	Total No. (All Items)	Total No. (Small AL)	Total No. (Non-small AL)
Transect 2	3,605	40,144	25,685	14,459
Transect 3	3,478	20,628	13,368	7,260
Transect 4	1,384	6,004	3,811	2,193
Transect 5	2,899	13,140	8,144	4,996
Pier	374	7,562	4,159	3,403
South Veg	2,945	17,537	10,172	7,366
Path	556	4,606	2,533	2,073
North Veg	7,490	50,209	34,142	16,067

algae), AL in the environment is not stationary, but is redistributed by natural processes throughout the ecosystem and can accumulate on barriers, including natural or anthropogenic structures (Bowman et al. 1998; McCormick and Hoellein 2016). Similarly, some items from the lake were stranded on the beach during periods of high wind and waves, and eventually accumulated along the pier. We observed that AL along the pier was mixed with senesced, filamentous green algae.

We hypothesized that AL density would be highest in Transect 2, which was located nearest to the lake above the high-water mark. However, there were no significant differences among transects in spring, and in fall and summer there was a significant interaction between transect and habitat. This shows that distance from the water and AL density are only related at the pier habitat in transect 2. Because of higher accumulation along the pier at the transect closest to the water, waves seem to increase AL accumulation (Silva-Cavalcanti et al. 2009). In this study, our plan for an additional assessment of the effect of distance from the water's edge on AL distribution was confounded by ongoing lake-level rise throughout 2015. For example, we had initially established another transect closest to the water's edge and collected data there for several weeks, but it remained completely submerged for the remainder of the data collection period and could thus not be considered for analysis here.

Results from studies elsewhere also show that comparing AL density on different beaches, or among different locations on the same beach, can illustrate the effects of visitor density, physical structures, and wind and wave dispersal. A recent analysis of engineered shorelines throughout coastal Chile indicated that artificial breakwaters retain more AL than unmodified shorelines (Aguilera et al. 2016). Hoellein et al. (2015) demonstrated that AL density on beaches throughout Lake Michigan was positively correlated with population density. Similar results were observed on marine beaches in South America (Portz et al. 2011; Thiel et al. 2013), and the Mediterranean (Poeta et al. 2016). Last, Zbyszewski et al. (2014) showed higher plastic AL in proximity to industrial pollution sources, especially downstream of prevailing currents, indicating AL movement via water affects its distribution on Great Lakes shorelines.

Temporal Patterns in AL Density

We hypothesized that summer would have the highest AL density, but found fall had the highest AL density among seasons. This may be related to beach maintenance. Beaches managed by the Chicago Park District receive daily maintenance during the summer, which appears to reduce AL density (Hoellein et al. 2015). However, we observe that good weather conditions continue to draw visitors to Chicago-area beaches for fishing and swimming after regular cleaning ceases in

early September, but acknowledge that we do not have beach visitor data. The combination of high visitation rates in September and no regular cleaning schedule could explain higher AL density in the fall than during the summer on sandy beaches with municipal maintenance. This result was similar to Hoellein et al. (2015), who also found AL density was higher in fall on other Lake Michigan beaches by analyzing a citizen science-generated dataset on beaches that have municipal cleaning. Similarly, Topçu et al. (2013) concluded that AL density on tourist beaches was highest in the fall, which they attributed to fishing practices, seasonal climatic variations (e.g., heavy rains), strong wave action, and wind-driven surface currents. While the adjacent public beach receives scheduled maintenance, the dunes restoration area of Pratt beach did not receive any cleaning. Therefore, we hypothesized summer would have higher density as that is the period of greatest visitation. However, it appears that some aspect of seasonality influenced this un-groomed beach in a similar fashion to the adjacent, groomed beaches. Thus, we estimate that the AL density on the study beach was affected by AL from the areas directly surrounding it. This includes beachgoers that could directly litter near the pier zone, as well as the transport of light AL items (e.g., cigarette butts and food wrappers) from nearby beaches via wind. To support this inference, we attempted to relate wind speed and AL density, but found no significant patterns. However, we note our wind speed data were recorded at a National Weather Service field station at O'Hare International Airport, approximately 20.5 km from Pratt beach. Superior results could be attained using wind speed data collected on the beach, and we predict that AL input rates could show a positive correlation with wind speeds in future studies.

Beach Visitors as a Source of AL

We considered smoking-related, food-related, and many of the items in the "other" category (e.g., fireworks, hair ties) to most likely be generated by beach visitors. Anecdotally, we observed many of the smoking- and food-related items to be unweathered suggesting their recent deposition. In accordance with other studies, two of the most common AL categories were smoking- and food-related (Santos et al. 2005; Hoellein et al. 2015). We acknowledge that some smoking and food-related AL may have been generated elsewhere and been moved to the study beach by wind and waves. Previous AL studies on Great Lakes beaches (Hoellein et al. 2014; Hoellein et al. 2015), estuarine shorelines (Thornton and Jackson 1998), and tourist beaches in Latin America (Nagelkerken et al. 2001; Silva-Iñiguez and Fischer 2003; Wetzel et al. 2004; Araújo and Costa 2006; Bravo et al. 2009; Thiel et al. 2013) also concluded that beach visitors are the primary source of AL, based upon the assemblage of AL types and observation of beach-goers' activity. In contrast, studies conducted in more remote areas away from tourist centers found that fishing- and shipping-related activities were the major sources of AL (Nagelkerken et al. 2001; Kusui and Noda 2003; Hinojosa and Thiel 2009; Santos et al. 2009; Thiel et al. 2013).

Our 'small AL' category includes AL items composed of glass or other materials that were ≤2.5 cm in size. Glass represented ~70% of all small AL items. We surmise that these glass particles are most likely from consumer goods (i.e., glass containers), rather than manufacturing or industry sources. We conclude this because there are no major manufacturing centers for glass on Lake Michigan shorelines up-current (i.e., north) of the study site, and because of the irregular shapes of the glass items. We can also draw some inferences about the age and biological interactions of small glass AL. Many of the glass pieces had been present for some time as they were smoothed over from water and sand abrasion. From a biological perspective, these small glass items may represent less of a concern to beach organisms than small pieces of plastic, which could be directly consumed and leach or adsorb persistent organic pollutants (Rochman et al. 2013). Finally, small heavy AL items such as glass pieces were likely to be buried and uncovered by sand throughout the year. Thus, finding small AL in the transect might not always represent input of new AL items, but simply that some previously buried items were revealed between collection dates. We acknowledge this might also occur with larger items or lighter materials, but burial is likely most common with small, dense pieces of glass or plastic. This could be assessed by measuring AL

in sand cores, but to our knowledge has not been included in previous AL research. Zbyszewski et al. (2014) noted degradation of plastic on Lakes Erie and St. Clair shorelines due to sunlight and shifting sands. The disparity found between glass and other materials on Pratt beach may be the result of direct deposition of glass items (e.g., beverage bottles) on the beach or in the water near the shoreline.

Comparison of AL Density to Literature Values

Results from this and two recent Lake Michigan AL abundance beach studies suggest that municipal cleaning is effective at reducing AL density (Figure 5; Hoellein et al. 2014; Hoellein et al. 2015), and that citizen science-generated data adequately captured AL density compared to more rigorous, transect-based collection. AL density on the study site was close to an average literature value for marine beaches with no city-sanctioned cleaning (1.83 items m^{-2}; Figure 5; Hoellein et al. 2015). However, an adjacent beach, Hartigan beach, which experienced municipal maintenance had a much lower AL density (0.007 items m^{-2}), when measured using the same transect-based approach as the current study (Hoellein et al. 2015). Finally, similar AL density results were obtained from citizen science and transect-based collections on maintained beaches, which further suggests that AL density can be reduced by effective cleaning strategies (Figure 5; Hoellein et al. 2014; Hoellein et al. 2015).

Management Implications

Due to the protected nature of the dunes restoration area at the study site, the use of large machinery to collect AL is prohibited. Despite the growth of vegetation, accumulation of AL within the site occurs at relatively high rates, consistent with results from marine beaches (Figure 5). Reducing AL density on Pratt beach and similar beaches elsewhere will require a multifaceted approach. We confirm the value of current beach maintenance operations, and suggest that local management agencies enhance AL collection with manual clean-up within protected areas and in sites adjacent to human-engineered structures that may promote AL accumulation. In this way, quantitative analyses of the spatial and temporal patterns of

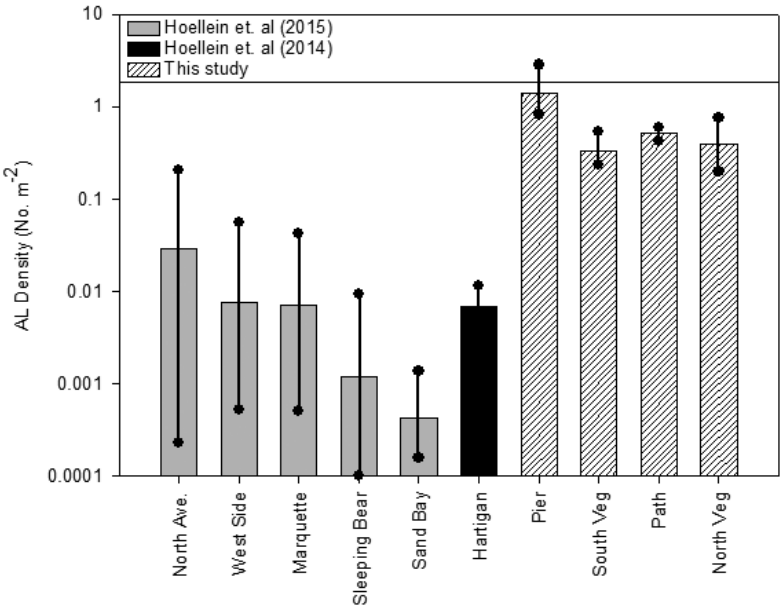

Figure 5. Comparison of mean (± range) AL density on Lake Michigan beaches from citizen science studies (Hoellein et al. 2015) and transect-based collection studies (Hoellein et al. 2014; this study). AL density from Lake Michigan beach studies is compared to a mean AL density for marine beaches worldwide, indicated by a solid line (1.83 items m^{-2}; Garrity and Levings 1993; Thornton and Jackson 1998; Nagelkerken et al. 2001; Kusui and Noda 2003; Silva-Iñiguez and Fischer 2003; Abu-Hilal and Al-Najjar 2004; Bravo et al. 2009; Slavin et al. 2012; Topçu et al. 2013).

AL in urban beaches will directly contribute to the refinement of efficient management practices. Additional prevention measures may include addition of garbage receptacles, adjustments of beach combing technology, and innovative measures similar to the 'vote with your butt' ashtrays installed by the Alliance for the Great Lakes. For this novel approach to litter prevention, beach goers are presented with an opportunity to 'vote' on local topics (e.g., sports teams or food choices) by placing their smoking-related litter on one side or another of a plexiglass ashtray. Future studies should examine resident and tourist populations separately to address disparities in knowledge of local AL management practices. Finally, continued educational outreach and interactive clean-up measures by beach management agencies can draw attention to the harmful effects of AL and provide the necessary incentives to alter beach visitor behavior.

Acknowledgments

We thank Lisa Kim, Catherine Rovegno, Veronica Lourich, Claudia Urban, Anthony Overhiser, Megan Westhoven, Erin O'Connell, and Mike Hassett for their assistance with data collection and processing. We appreciate the support of the Loyola University Chicago Department of Biology and the Alliance for the Great Lakes. Many thanks to the Loyola Undergraduate Research Opportunities Program, the Women in Science Enabling Research (WISER) fellowship program, and the Mulcahy Scholarship Program for funding to AV. Historical and beach maintenance information for the Loyola dunes restoration area was provided by Ann Whelan.

Author Bio and Contact Information

Anna Vincent is an undergraduate student in the College of Arts and Sciences and Interdisciplinary Honors Program at Loyola University Chicago. She is working toward her Bachelor of Science in Biology (Ecology emphasis) with a minor in Environmental Science. Her undergraduate research focuses on the impact of anthropogenic actions in urban aquatic ecosystems. Her other interests include nutrient cycling in freshwater ecosystems, sustainable ecosystem management, and conservation of ecosystem biodiversity. She may be contacted at avincent1@luc.edu or Department of Biology, Loyola University Chicago, 1032 W Sheridan Rd, Chicago IL, USA.

Timothy Hoellein is an Associate Professor in the Department of Biology at Loyola University Chicago. His teaching and research focus on biogeochemistry and ecosystem ecology. Much of his work involves metrics of ecosystem function and seasonal dynamics for evaluation of human impacts and restoration in urban aquatic ecosystems. He is particularly interested in understanding the ecological dimensions of nitrogen cycling and the accumulation, assemblage, and movement of anthropogenic litter. He may be contacted at thoellein@luc.edu or Department of Biology, Loyola University Chicago, 1032 W Sheridan Rd, Chicago IL, USA.

References

Abu-Hilal, A.H. and T. Al-Najjar. 2004. Litter pollution on the Jordanian shores of the Gulf of Aqaba (Red Sea). *Marine Environmental Research* 58: 39-63.

Abu-Hilal, A.H. and T. Al-Najjar. 2009. Marine litter in coral reef areas along the Jordan Gulf of Aqaba, Red Sea. *Journal of Environmental Management* 90: 1043-1049.

Aguilera, M.A., B.R. Broitman, and M. Thiel. 2016. Artificial breakwaters as garbage bins: Structural complexity enhances anthropogenic litter accumulation in marine intertidal habitats. *Environmental Pollution* 214: 737-747.

Araújo, M.C.B. and M.F. Costa. 2006. The significance of solid wastes with land-based sources for a tourist beach: Pernambuco, Brazil. *Pan-American Journal of Aquatic Sciences* 1: 28-34.

Beletsky, D., J.H. Saylor, and D.J. Schwab. 1999. Mean circulation in the Great Lakes. *Journal of Great Lakes Research* 25(1): 78-93.

Bowman, D., N. Manor-Samsonov, and A. Golik. 1998. Dynamics of litter pollution on Israeli Mediterranean beaches: A budgetary, litter flux approach. *Journal of Coastal Research* 14(2): 418-432.

Bravo, M., M.D. Gallardo, G. Luna-Jorquera, P. Nunez, N. Vasquez, and M. Thiel. 2009. Anthropogenic debris on beaches in the SE Pacific (Chile): Results from a national survey supported by volunteers. *Marine Pollution Bulletin* 58: 1718-1726.

Carson, H.S., M.R. Lamson, D. Nakashima, D. Toloumu, J. Hafner, N. Maximenko, and K.J. McDermid. 2013. Tracking the sources and sinks of local marine debris in Hawai'i. *Marine Environmental Research* 84: 76-83.

Cózar, A., F. Echevarría, J.I. González-Gordillo, X. Irigoien, B. Úbeda, S. Hernández-León, Á.T.

Palma, S. Navarro, J. García-de-Lomas, A. Ruiz, and M.L. Fernández-de-Puelles. 2014. Plastic debris in the open ocean. *Proceedings of the National Academy of Sciences* 111(28): 10239-10244. DOI: 10.1073/pnas.1314705111. Accessed September 12, 2016.

Driedger, A.G., H.H. Dürr, K. Mitchell, and P. Van Cappellen. 2015. Plastic debris in the Laurentian Great Lakes: A review. *Journal of Great Lakes Research* 41(1): 9-19.

Garrity, S.D. and S.C. Levings. 1993. Marine debris along the Caribbean coast of Panama. *Marine Pollution Bulletin* 26: 317-324.

Hinojosa, I.A. and M. Thiel. 2009. Floating marine debris in fjords, gulfs and channels of southern Chile. *Marine Pollution Bulletin* 58: 341-350.

Hoellein, T., M. Rojas, A. Pink, J. Gasior, and J. Kelly. 2014. Anthropogenic litter in urban freshwater ecosystems: Distribution and microbial interactions. *PLoS ONE* 9(6): e98485. DOI: 10.1371/journal.pone.0098485. Accessed September 20, 2016.

Hoellein, T.J., M. Westhoven, O. Lyandres, and J. Cross. 2015. Abundance and environmental drivers of anthropogenic litter on 5 Lake Michigan beaches: A study facilitated by citizen science data collection. *Journal of Great Lakes Research* 41(1): 78-86.

Kühn, S., E. Rebolledo, and J. van Franeker. 2015. Deleterious effects of litter on marine life. In: *Marine Anthropogenic Litter*, M. Bergmann, L. Gutow, and M. Klages (Eds.). Springer International Publishing, Switzerland, pp. 75-116.

Kusui, T. and M. Noda. 2003. International survey on the distribution of stranded and buried litter on beaches along the Sea of Japan. *Marine Pollution Bulletin* 47: 175-179.

McCormick, A.R. and T.J. Hoellein. 2016. Anthropogenic litter is abundant, diverse, and mobile in urban rivers: Insights from cross-ecosystem analyses using ecosystem and community ecology tools. *Limnology and Oceanography* 61: 1718-1734.

Nagelkerken, I., G. Wiltjer, A.O. Debrot, and L. Pors. 2001. Baseline study of submerged marine debris at beaches in Curacao, West Indies. *Marine Pollution Bulletin* 42: 786-789.

National Oceanic and Atmospheric Administration (NOAA) and National Weather Service. 2015. WFO Monthly/Daily Climate Data. Available at: http://forecast.weather.gov/product.php?site=LOT&issuedby=ORD&product=CF6& format=CI& version=15&glossary=0. Accessed June 8, 2016.

Poeta, G., L. Conti, M. Malavasi, C. Battisti, and A.T.R. Acosta. 2016. Beach litter occurrence in sandy littorals: The potential role of urban areas, rivers and beach users in central Italy. *Estuarine, Coastal and Shelf Science* 181: 231-237.

Portz, L., R.P. Manzolli, and J. Ivar do Sul. 2011. Marine debris on Rio Grande do Sul north coast, Brazil: Spatial and temporal patterns. *Journal of Integrated Coastal Zone Management* 11: 41-48.

Rech, S., V. Macaya-Caquilpán, J. Pantoja, M. Rivadeneira, D. Jofre Madariaga, and M. Thiel. 2015. Rivers as a source of marine litter—A study from the SE Pacific. *Marine Pollution Bulletin* 82: 66-75.

Rochman, C.M., E. Hoh, T. Kurobe, and S.J. Teh. 2013. Ingested plastic transfers hazardous chemicals to fish and induces hepatic stress. *Scientific Reports* 3: 3263.

Ryan, P.G., C.J. Moore, J.A. van Franeker, and C.L. Moloney. 2009. Monitoring the abundance of plastic debris in the marine environment. *Philosophical Transactions of the Royal Society of London B: Biological Sciences* 364(1526): 1999-2012.

Santos, I.R., A.C. Friedrich, M. Wallner-Kersanach, and G. Fillmann. 2005. Influence of socioeconomic characteristics of beach users on litter generation. *Ocean & Coastal Management* 48: 742-752.

Santos, I.R., A.C. Friedrich, and J.A. Ivar do Sul. 2009. Marine debris contamination along undeveloped tropical beaches from northeast Brazil. *Environmental Monitoring and Assessment* 148: 455-462.

Silva-Cavalcanti, J.S., M.C.B. de Araújo, and M.F. da Costa. 2009. Plastic litter on an urban beach—A case study in Brazil. *Waste Management & Research* 27(1): 93-97.

Silva-Iñiguez, L. and D.W. Fischer. 2003. Quantification and classification of marine litter on the municipal beach of Ensenada, Baja California, Mexico. *Marine Pollution Bulletin* 46: 132-138.

Slavin, C., A. Grage, and M.L. Campbell. 2012. Linking social drivers of marine debris with actual marine debris on beaches. *Marine Pollution Bulletin* 64: 1580-1588.

Thiel, M., I.A. Hinojosa, L. Miranda, J.F. Pantoja, M.M. Rivadeneira, and N. Vasquez. 2013. Anthropogenic marine debris in the coastal environment: A multi-year comparison between coastal waters and local shores. *Marine Pollution Bulletin* 71: 307-316.

Thornton, L. and N.L. Jackson. 1998. Spatial and temporal variations in debris accumulation and composition on an estuarine shoreline, Cliffwood Beach, New Jersey, USA. *Marine Pollution Bulletin* 36: 705-711.

Topçu, E.N., A.M. Tonay, A. Dede, A.A. Öztürk, and B. Öztürk. 2013. Origin and abundance of marine litter along sandy beaches of the Turkish Western Black Sea Coast. *Marine Environmental Research* 85: 21-28.

Wetzel, L., G. Fillmann, and L.F.H. Niencheski. 2004. Litter contamination processes and management perspectives on the southern Brazilian coast. *International Journal of Environment and Pollution* 21: 153-165.

Zbyszewski, M. and P.L. Corcoran. 2011. Distribution and degradation of fresh water plastic particles along the beaches of Lake Huron, Canada. *Water, Air, & Soil Pollution* 220: 365-372.

Zbyszewski, M., P.L. Corcoran, and A. Hockin. 2014. Comparison of the distribution and degradation of plastic debris along shorelines of the Great Lakes, North America. *Journal of Great Lakes Research* 40: 288-299.

Universities Council on Water Resources
Journal of Contemporary Water Research & Education
Issue 160, Pages 85-99, April 2017

A Method for Assessing Shoreline Stability of Alpine Lake, West Virginia

Carolina Rando[1], *Leslie Hopkinson[1], Melissa O'Neal[2], and Jason Fillhart[2]

[1]*Civil and Environmental Engineering, West Virginia University*
[2]*West Virginia Water Research Institute*
**Corresponding author*

Abstract: Rapid stability assessments are tools commonly applied to stream reaches to evaluate potential for instability and are often used to prioritize management strategies. In this work, a rapid stability assessment was created to evaluate the stability of the shoreline of Alpine Lake in West Virginia, USA. First, the assessment tool was created considering the metrics of bank height, bank angle, erosion, armoring, wind and wave action, unconsolidated materials, protection measures, vegetation, and accretion. The resulting tool was applied to 83 reaches (20-100 m in length) of the lake shoreline. The reaches were rated in terms of potential instability: very low (14%), low (42%), moderate (33%), high (10%), and very high (1%). Second, erosion rates were monitored at eight locations using erosion pins. Average erosion rates up to 0.22 mm/d were observed. Measured erosion rates generally supported the rapid assessment results, but there were some exceptions. Additional categories that consider human activity along the lakeshore for recreation should be added. If used without continued erosion monitoring, the rapid assessment should be completed multiple times because the stability of the banks with little vegetation buffer varied by season. Lastly, reclamation strategies are discussed.

Keywords: *rapid stability assessment, erosion, lakeshore*

Rapid geomorphic assessments are common tools used to characterize stream reaches and evaluate the sensitivity of channels to disturbance. Many rapid assessment tools exist for the riverine environment (e.g., channel instability index: Simon and Downs 1995; bank erosion hazard index: Rosgen 2001; Oklahoma Ozark streambank erosion potential index: Heeren et al. 2012). The metrics utilized vary by assessment tool, but most follow the same basic methods. The river of interest is divided into reaches with similar morphological characteristics. Each reach is then evaluated using metrics defined in the tool through field work, observation, analysis of climate or hydrologic data, and/or GIS methods (e.g., Simon and Downs 1995; Rinaldi et al. 2013).

Simon and Downs (1995) developed an approach to assess the potential for channel instabilities referred to as the channel instability index. The variables considered in the index include bed material, bed protection, stage of channel evolution, percent of channel constriction, number of piers in channel, percent blockage, bank erosion, meander impact, pier skew, mass wasting, high-flow angle of approach, and percent woody vegetative cover. Each variable is evaluated and assigned a score; high aggregate scores ($\geq$ 20) identify highly unstable stream reaches. It was originally developed to evaluate the potential for bridge scour and related channel instabilities but can be applied to additional disturbance areas by modifying the variables and altering the ranking system (Simon and Downs 1995). As such, it has been commonly used in altered forms (e.g., Simon and Klimetz 2008; Mukundan et al. 2011; Heeren et al. 2012).

For example, Heeren et al. (2012) applied the channel instability index to streambank reaches in Oklahoma to identify sites in most need of streambank stabilization. Because the index does not consider streambank cohesion and the difficulty in assessing some variables, a modified version was developed called the Oklahoma Ozark streambank erosion potential index (OSEPI). The modified index included variables to consider streambank cohesion and stream curvature. This modified form had high correlation with observed streambank erosion.

Like the OSEPI, assessments have been developed for specific locations. Rinaldi et al. (2013) presented the Morphological Quality Index (MQI) developed to classify stream morphological quantity in Italy. Longitudinal and lateral continuity, channel pattern, cross-sections, bed structure, and the riparian corridor are evaluated in the MQI using 28 variables (e.g., longitudinal continuity in sediment and wood flux, hillslope-river corridor connectivity, structure of channel bed, upstream alteration of flows, vegetation management). The tool was tested on 102 Italian rivers and provides a framework for prioritizing management strategies.

The abovementioned assessment tools have been used to evaluate channel stability. In this work, we extend the assessment tools to evaluate shoreline stability at Alpine Lake, a small (0.6 km^2), man-made lake, in West Virginia. Like streambank retreat, shoreline retreat is a complex process that results from a combination of mass failure, subaerial processes, water level fluctuations, overland flow, groundwater processes, and wave action. The factors vary in importance, depending on reservoir characteristics (Lawson 1985).

Shoreline retreat can result in property damage (Gabriel 2004), and there is concern about shoreline processes at Alpine Lake affecting infrastructure. Alpine Lake has many residential and recreational uses (e.g., fishing, boating, swimming, hiking, cross-country skiing, golfing). The lake is essential for the recreational activities at Alpine Lake resort; however, shoreline erosion is beginning to affect infrastructure critical to recreation, and there is a desire to stabilize the shoreline. We developed a rapid stability assessment tool to apply to the shoreline, compared the assessment results to observed erosion rates, and discuss potential reclamation strategies.

Methods

A rapid stability assessment was developed for Alpine Lake and applied to the shoreline. Erosion was monitored using erosion pins to evaluate the assessment tool.

Alpine Lake Watershed Description

Alpine Lake Resort is a planned community in Preston County, WV, USA on approximately 2,000 wooded acres (8.1 km^2) (Figure 1). A 0.6 km^2 man-made lake is the focus of the community. Amenities include an 18-hole golf course, beach, boating, cross-country skiing, fishing, and lodge (restaurant, pool, and conference center). Boating is allowed on the lake, but no gas-powered engines are permitted (Alpine Lake Resort 2016). There have been few changes in infrastructure to the area in the last 20 years.

The Alpine Lake watershed (4.85 km^2) has a total of streams length of 6.9 km. Most of the developed area includes single-family homes, many of which are only seasonally inhabited, and the infrastructure to support the development. The impervious areas in the watershed (<5% by area) are primarily located in close proximity to the lake and are mainly attributed to roads and houses. In the southern portion of the watershed, the two largest areas of impervious surfaces are due to the Alpine Lake Resort Lodge and a clubhouse associated with the resort (Figures 1 and 2). Forested areas (85% by area) and grassed lawns (7% by area) make up most of the watershed. Approximately 60% of the watershed is underlined by Dekalb soil series. The topography is relatively mild with elevations ranging from approximately 366 m to 975 m above mean sea level (Figure 2). The annual average precipitation is 1.4 m and is relatively evenly distributed with a drier summer/fall season. The water elevation is relatively stable throughout the year but decreases during the dry season. Mean monthly temperatures range from -2.7°C to 20.3°C (NRCC 2016).

Rapid Stability Assessment

A rapid stability assessment tool was developed to assess erosion hazard levels along the lake shoreline (= 4.39 km). The assessment was based on methods by Simon and Downs (1995), Guthrie

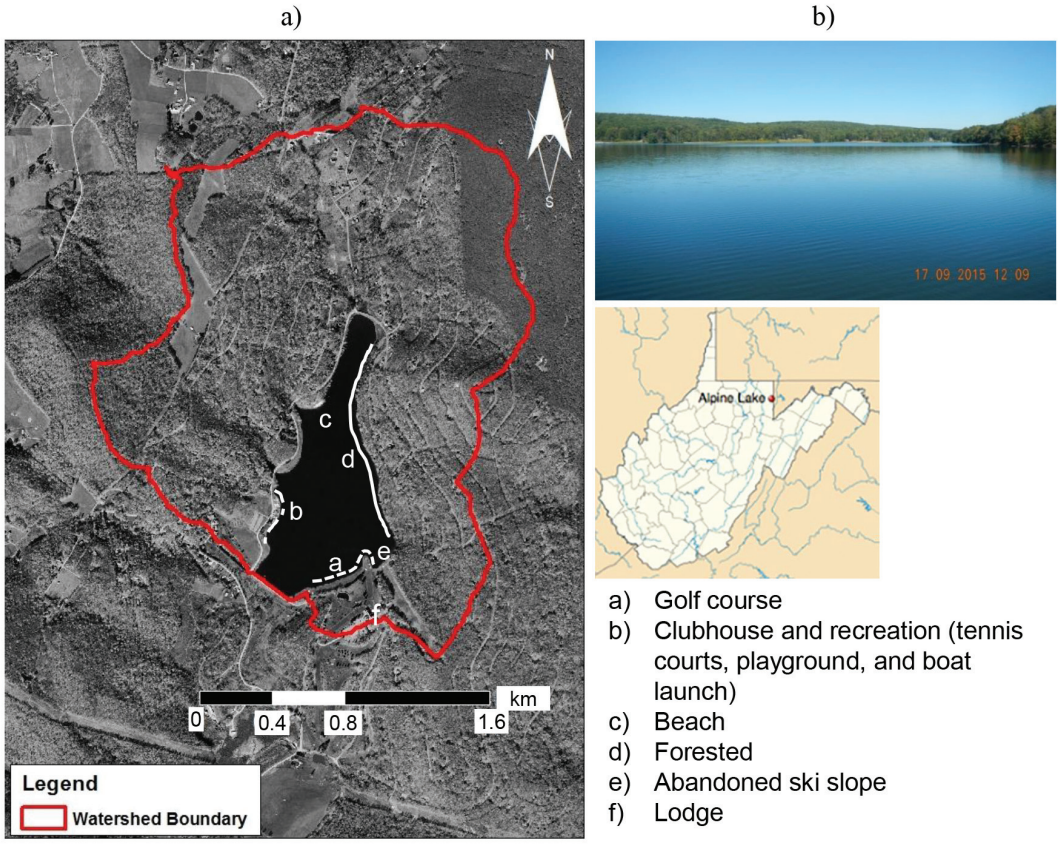

Figure 1. a) Alpine Lake watershed showing major amenities, and b) Alpine Lake located in Preston County, WV, USA.

and Law (2005), Simon and Klimetz (2008), and Heeren et al. (2012). After several field visits, the following metrics were identified as necessary to include in the assessment: 1) bank height, 2) exposed bank length, 3) bank angle, 4) evidence of mass wasting, 5) armoring, 6) wind and wave action, 7) unconsolidated material, 8) shoreline protection, 9) vegetation, and 10) accretion. Table 1 describes the metrics and notes any necessary field measurements. Like prior assessment tools (i.e., Johnson 2005), the intent was to limit the amount of field measurements to minimize evaluation time and not require extensive training to complete.

Each metric was assigned a score where higher values represented a greater potential of erosion or instability. The aggregate score (maximum score = 85) characterized the overall stability value using the following categories: ≤ 30 = very low; 30.5 - 40 = low; 40.5 - 50 = moderate; 50.5 - 60 = high; and ≥ 60.5 = very high. The final version of the rapid stability assessment is available in the Appendix.

The rapid stability assessment (Appendix) was then applied to the shoreline of Alpine Lake by a team of four people (two groups of two) during one week in August 2015 (August 5-11, 2015); training was provided before work began. The lake perimeter was divided into reaches of 20-100 m in length that had similar characteristics. Each factor was rated, and an overall shoreline erosion/stability rating was assigned to each reach. The results were then mapped using GIS. The earthen dam at the southern end of the lake and the shoreline covered by a clubhouse and man-made beach were not included in the evaluation (Figure 1).

Erosion Monitoring

Erosion was monitored in eight locations to evaluate the rapid stability assessment tool. The locations were selected to represent the range of bank conditions observed around the lake. Erosion pins were installed during September 2015 following methods reported by Staley et al. (2006).

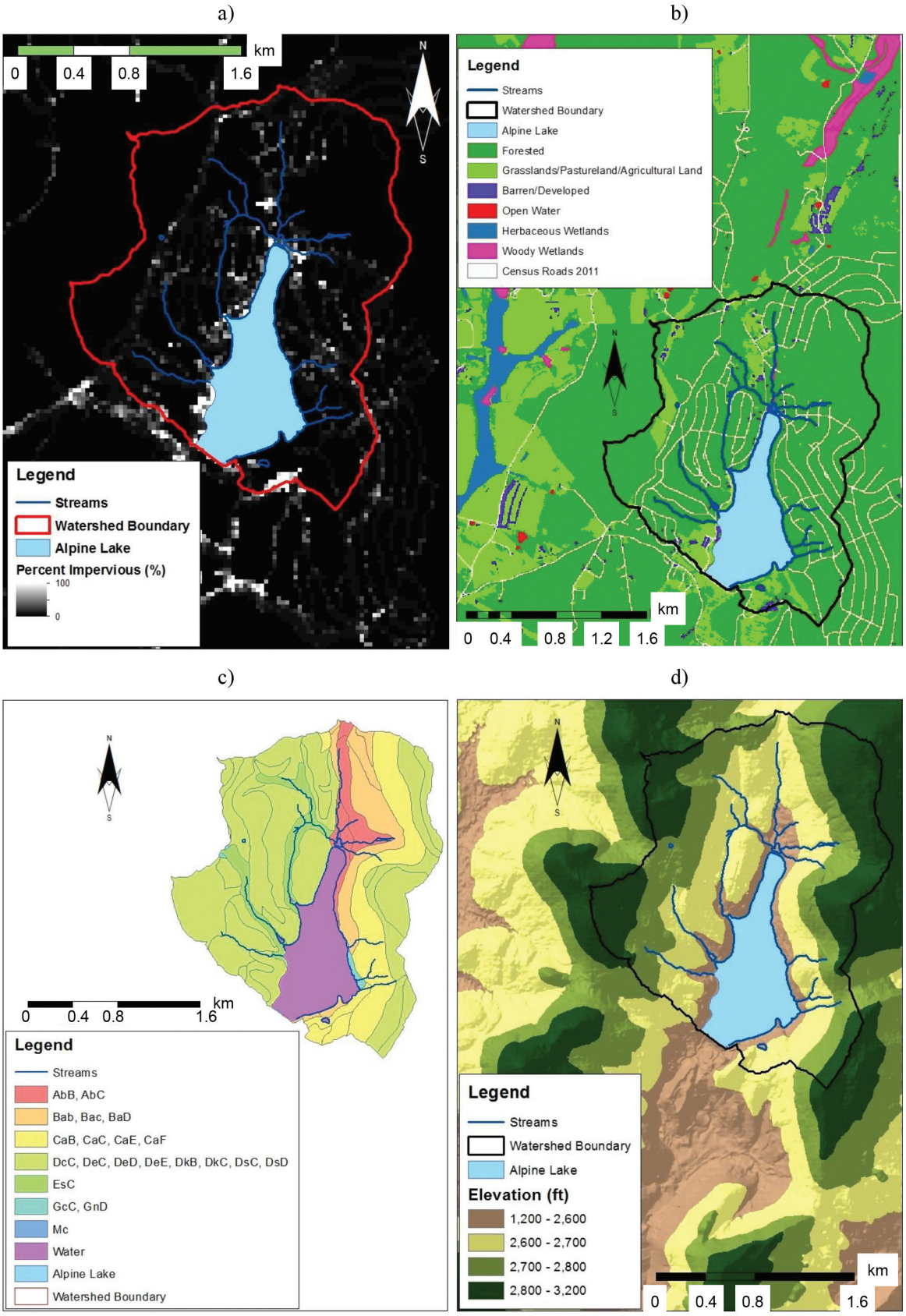

Figure 2. Alpine Lake watershed characteristics: a) impervious surface, b) land use, c) soil type, and d) elevation.

Table 1. Metrics included in rapid stability assessment.

	Description	Equipment
Bank height	Vertical elevation of shoreline	Field tape
Bank angle	Angle of bank measured against the horizontal	Survey equipment or clinometer
Evidence of recent mass wasting/erosion	Observed characteristics of mass wasting (e.g., slough banks, overhanging banks, exposed roots)	*
Evidence of armoring	Coarse gravel or larger particles (D50>16 mm) protecting bank toe	Gravelometer
Wind and wave action	Observed wind direction and wave strength	Compass
Unconsolidated materials	Texture of bank sediment	*Feel method (Soil Survey Staff 2014)
Shoreline protection	Existing protection measures, man-made or natural (e.g., riprap, vegetation)	*
Vegetation contributing to instability	Large vegetation adding weight to bank	*
Occurrence of accretion	Evidence of sediment settling near toe	*

*Field tape needed to determine percent of shoreline affected.

The pins were made of unpolished steel rods (4.8-mm in diameter, 30.5-cm long) and positioned perpendicular to the bank with an initial exposed distance of 3-8 cm. The exposed distance was greater in areas where vegetation was dense so that the pins could be located. The exposed portion of the pins was marked with orange paint. Because the bank height varied among locations, the spacing between erosion pins was not constant and varied from 30 to 70 cm. Locations 1, 2, 3, 4, 5, 6, 7, and 8 had 4, 4, 6, 8, 8, 6, 6, and 5 pins, respectively. The number of pins in the vertical direction ranged from one to three depending on bank height. The number of pins in the horizontal direction varied from two to four (Figure 3). Exposed length was measured once before winter (October 2015) and quarterly beginning in spring 2016 (March, June, and September) with a total monitoring period of one year. The protocol suggested by Staley et al. (2006) was followed and the pins were re-set as necessary during measurements. Erosion rates were calculated for each monitoring period.

Results

Rapid Stability Assessment

The rapid stability assessment was applied to 83 reaches along the shoreline. Stability scores ranged from 17.5 to 62.5. The majority of the locations were considered to have low to moderate potential for erosion (89%). Ten percent of the locations were considered to have high potential for erosion, and one location was identified as having very high potential for erosion (Figures 4 and 5).

There was little variability in the score for the metrics of unconsolidated material, vegetation instability, and accretion (Figure 6). The bank material was primarily cohesive sediment; therefore, more than 75% of the locations had a minimum score for unconsolidated material. Locations with high scores for unconsolidated material were primarily located near the boathouse and beach on the west side of the lake. More than 75% of the locations also had the minimum score

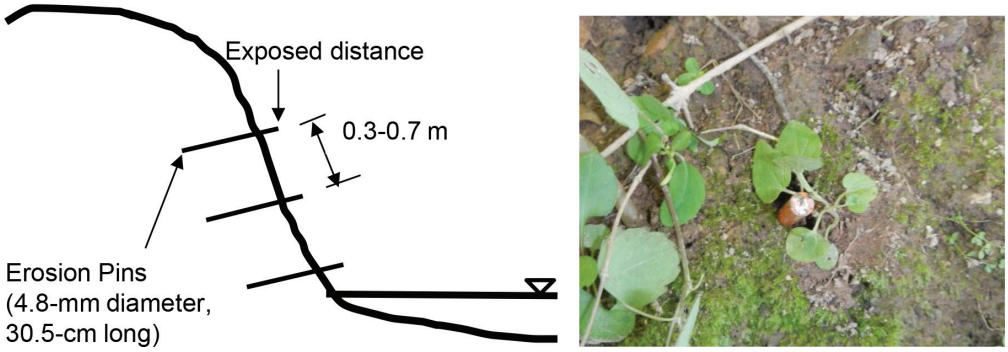

Figure 3. General erosion pin placement with a picture of the exposed erosion pin colored orange.

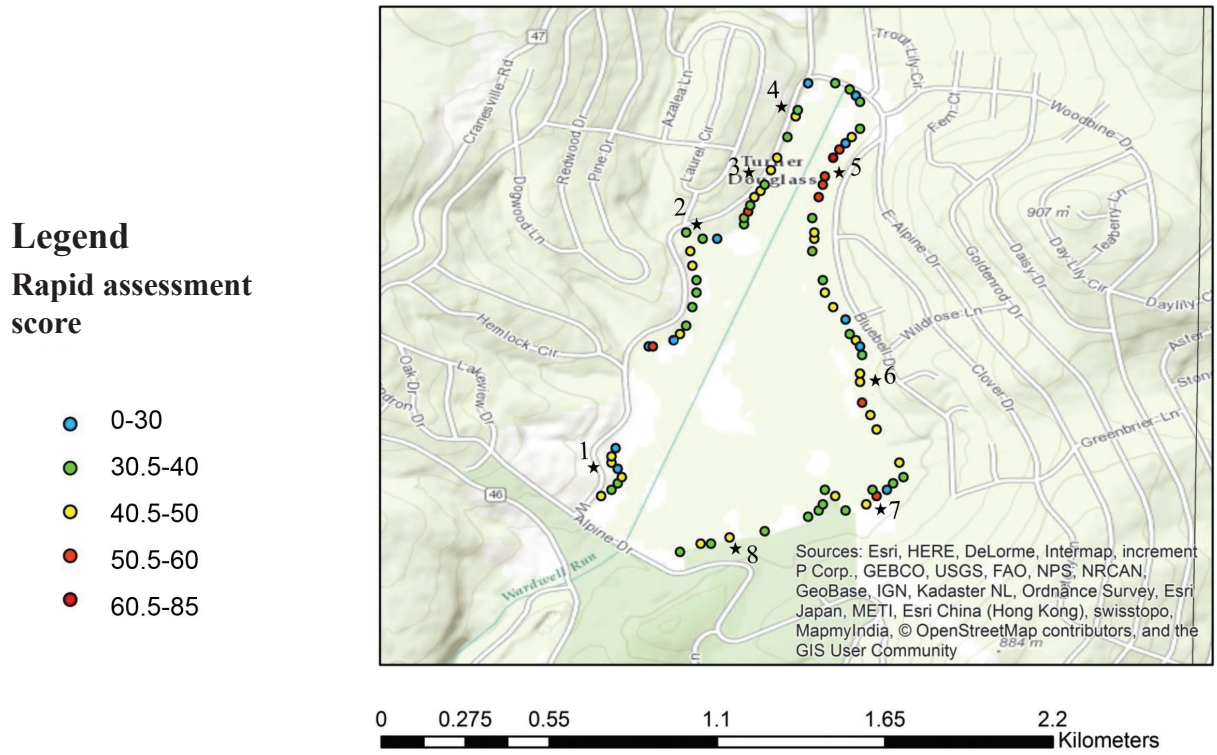

Figure 4. Spatial distribution of overall stability score resulting from rapid stability assessment; stars note erosion pin monitoring locations.

for vegetation adding to instability. The entire west portion of the lake had grass and shrub vegetation that did not contribute to instability. Some trees along the shoreline on the eastern, forested side of the lake had leaning trees along the water's edge. These sites were rated as having high potential for instability shown in Figure 4. Depositing sediment was only observed at a few locations, mainly near the man-made beach, so most locations received the maximum score for the accretion metric (Figure 6).

Bank stability, bank angle, evidence of mass wasting, wind and wave action, armoring, and shoreline protection had more variability in assigned scores. Most of the banks were nearly vertical; some were overhanging which led to a high score. Evidence of mass wasting was observed at varying degrees around the lake. It

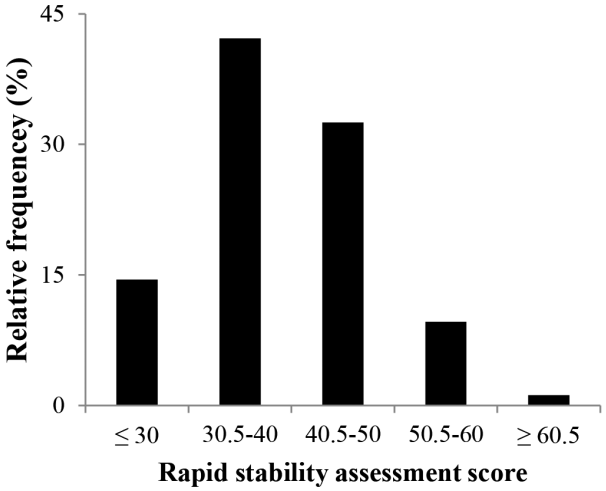

Figure 5. Overall stability score divided by stability classifications; ≤ 30 = very low; 30.5 - 40 = low; 40.5 - 50 = moderate; 50.5 - 60 = high; ≥ 60.5 = very high.

existed in the short, grass-line banks, in the taller banks with shrubs, and along the forested banks. High scores of wind and wave action were located near the boathouse on the west side of the lake and near the protruding land mass in the south portion of the lake. Armoring was evident primarily along the forested portion of the shoreline but existed in locations around the lake.

Measured Erosion

Measured erosion was primarily observed at locations 1, 3, 7, and 8. Negative erosion rates were observed at locations 2, 3, 4, 5, 6, and 7 (Figure 7). These negative erosion rates denote that the erosion pins were partially covered during the monitoring period and represent aggradation. At most locations, localized mass wasting events were the cause of the negative rates. Sediment present at the bank toe was observed at location 2 during the 3/11-6/21 monitoring period. The deposited sediment resulted from a large mass wasting event. This location had a short bank (< 0.5 m), and the entire bank experienced a mass failure event. The mass wasting may have continued but the pins were missing during the final data collection. This site is a common fishing location, and the pins were likely removed by recreation users. The heavy foot traffic in this area also contributes to the mass wasting events, a category not considered in the rapid geomorphic assessment tool.

Discussion

Comparison of Rapid Stability Assessments and Erosion Pins

Both rapid stability assessments and erosion monitoring were needed to assess the stability of the shoreline. The placement of the erosion pins potentially overestimated the erosion rates because the measurements were localized into a few-meter section. Four to eight erosion pins were used to characterize the erosion rates of a 5-10 m reach. The rapid stability assessments were used to assess 20-100 m reaches. The rapid assessments were helpful in identifying overall instability features of the reaches; common contributions to instability were identified to similar reaches around the lake perimeter. The erosion pins showed whether erosion or aggradation occurred in point locations and provided long-term information.

The erosion pins at locations 1 and 2 were both located on the west side of the lake. Both locations had short shoreline bank heights (< 0.5 m) and grass along the shoreline that is mowed frequently (< 15 cm in height observed). There is no natural, un-mowed buffer in either location. Location 2 is near a man-made beach, a common fishing location, and adjacent to a reach lined with riprap.

Low to moderate stability was expected at locations 1 and 2 based on the rapid stability assessments (rapid stability assessment score ≤ 50, Figure 4). On average, the erosion rates at location 1 were low (≤ 0.04 mm/d). This rate could likely be reduced by allowing for a natural vegetation buffer near the water surface. During March to June, large mass failure events occurred at location 2, resulting in the large negative erosion rate value (mean erosion rate = -0.52 mm/d, Figure 7). This large rate was the maximum absolute rate observed. While the bank height here is small, the shoreline is actively adjusting. Riprap is placed on the shoreline near location 2 which is effective in reducing erosion at that site. Fishing and human traffic in this location were unaccounted for in the assessment and should be considered in the future.

Similarly, low to moderate instability was expected at locations 3 and 4 based on the stability assessment (Figure 4). Erosion pins in these locations were positioned on similar banks with large bank heights (> 2 m), natural dense shrub

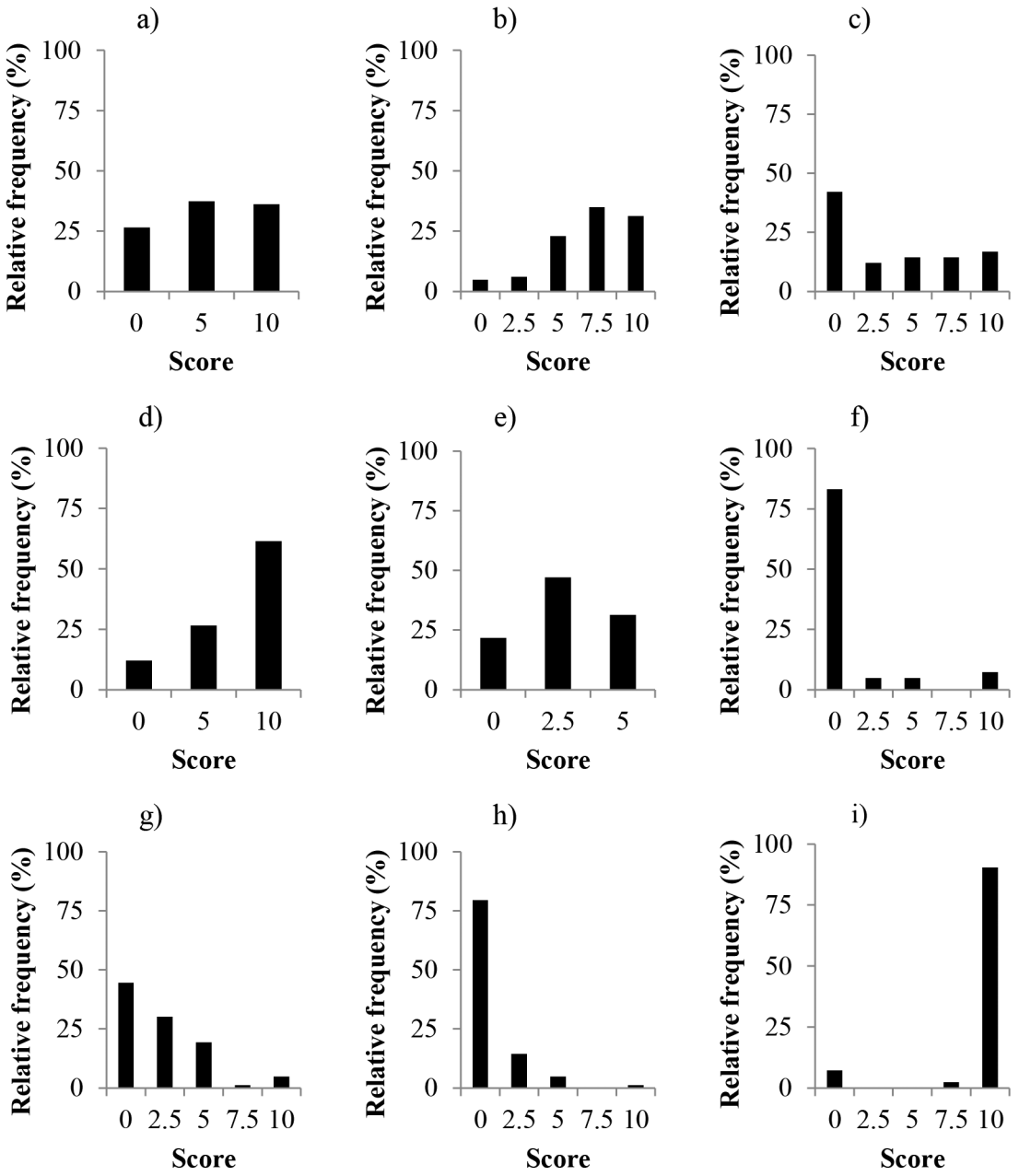

Figure 6. Distribution of score for the metrics in the rapid stability assessment: a) bank height, b) bank angle, c) evidence of mass wasting, d) evidence of armoring, e) wind and wave action, f) unconsolidated material, g) evidence of shoreline protection, h) vegetation contributing to instability, and i) evidence of accretion.

vegetation, and a road near the bank. On average, low erosion rates were observed at location 3 (≤ 0.5 mm/d, Figure 7). The erosion pins spanned the entire bank height at this location and provided a good overall picture of the erosion of the bank; the rapid stability assessment represented the low degree of instability well.

The erosion rates at location 4 were greater than location 3 (mean erosion rate = -0.17-0.11 mm/d, Figure 7), but the pins were not positioned in an area that represented the entire bank. We targeted the placement of the erosion pins near the water surface as we expected the upper part of the bank to be stable; therefore, while the erosion rates

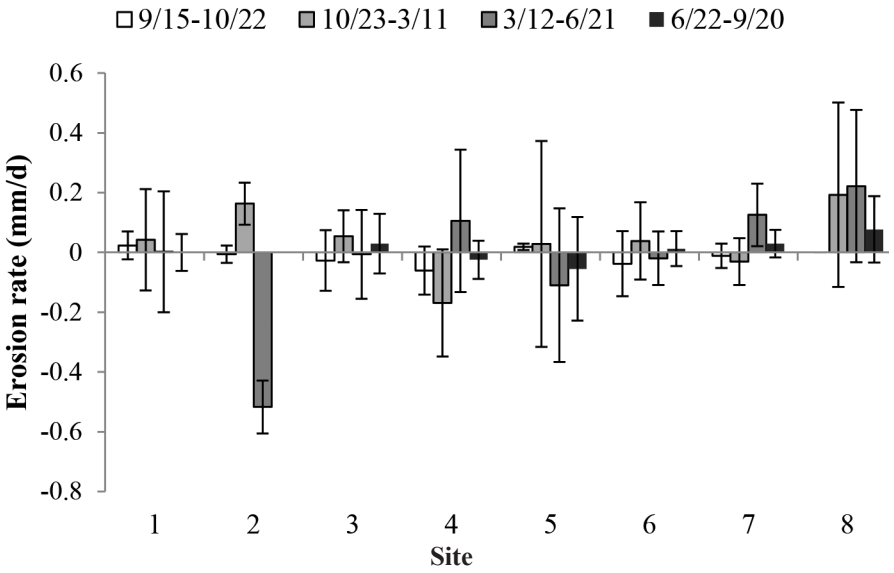

Figure 7. Mean erosion rates for each monitoring period; error bars show standard deviation. (No data for site 2 during 6/22-9/22; pins removed).

measured at this location indicated high instability, the rates were likely overestimated.

Locations 5 and 6 were positioned along the forested east side of the lake. The rapid stability assessments suggest moderate to high instability in these regions. On average the erosion rates in these locations ranged from -0.11 to 0.04 mm/d. However, the variability in erosion rates was among the greatest of all the locations (Figure 7). The trees provide stability, but there was substantial localized erosion around large vegetation (exposed roots, stems, etc.).

Location 7 was at the downslope of a ski slope that is no longer in use. There are areas of erosion especially around drain features (as indicated by the single "high" instability reach in Figure 4). Substantial erosion rates occurred in this location during the wet period (0.12 mm/d) likely due to the runoff from the ski slope (Figure 7).

The final set of erosion pins (location 8) were on a tall (> 1 m) bank adjacent to a golf course. Moderate instability was expected here based on the stability assessment (Figure 4). Vegetation existed on the bank surface at the time of rapid assessment, but there was little vegetation when the erosion measurements were taken during the spring and summer. No erosion was recorded during the first measurement period, but the highest erosion rates and variability in erosion rates were measured in this location during October to June (mean erosion rate = 0.19-0.22 mm/d, Figure 7). The bank is stable during summer months when the water recedes and allows vegetation to establish on the bank. High erosion rates occurred when the bank was bare of vegetation, indicating that multiple assessments may be needed.

Observed Instability Features and Recommendations

Common features of instability were observed around the lake. The lake can be divided into five regions with the following recommended reclamation approaches (Figure 8):

1. *Southwest*: The shoreline in the southwest area of the lake was primarily characterized with low banks (< 0.5 m) and grass vegetation. The grass was frequently mowed to a short height (< 15 cm) all the way to the shoreline. Exposed near-vertical or overhanging bank faces were common, and both fluvial entrainment and mass wasting were observed.

   The impact of shoreline vegetation on bank retreat is complex. Herbaceous vegetation, like that observed in the southwest section of Alpine Lake, absorbs rainfall impact, increases roughness,

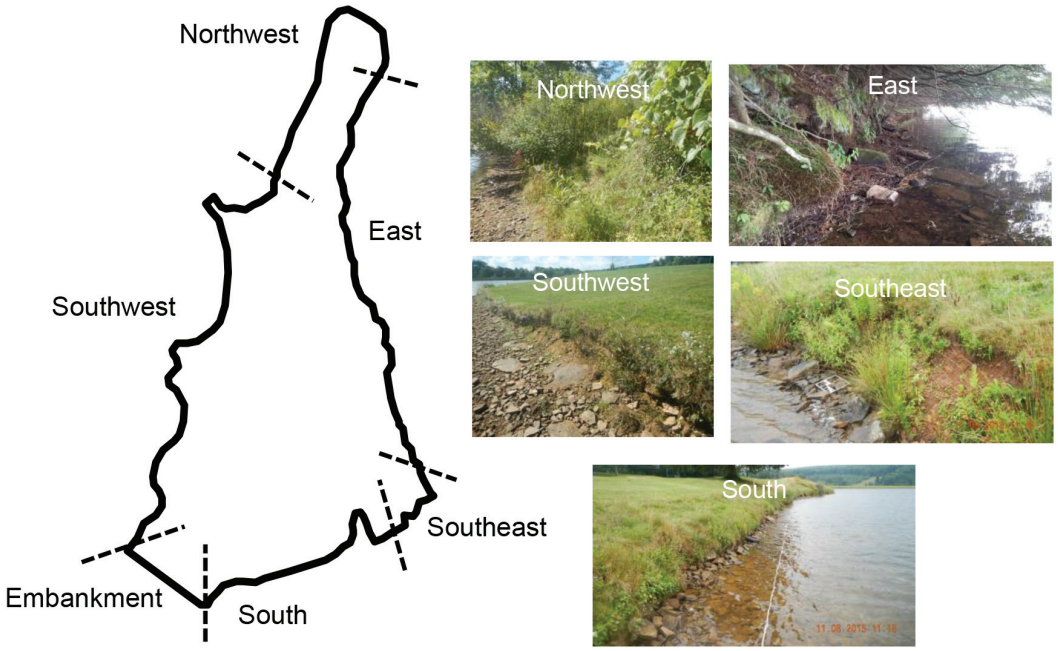

Figure 8. Representative shoreline pictures for each area with common characteristics: southwest, northwest, east, southeast, and south.

influences bank soil temperature and moisture content, and provides root strength through reinforcement (Thorne 1998; Mamo and Bubenzer 2001a, 2001b; Wynn and Mostaghimi 2006). While the vegetation in this location added root strength through reinforcement (Mamo and Bubenzer 2001a, 2001b), roots of herbaceous vegetation only reinforce the top 30 cm or less (Wynn et al. 2004). Further, the low mowing height can lead to reduced root length and increased dead root length (Liu and Huang 2002), limiting root reinforcement benefits.

The stability of this portion of the shoreline could be improved by allowing a vegetation buffer to establish along the shoreline. By reducing the mowing frequency and mowing to a greater height, a greater benefit from shoreline vegetation will be achieved. Active approaches like riprap or vegetation plantings may be needed in the locations near recreation locations (e.g., common fishing locations) where vegetation is less likely to naturally establish in the absence of mowing.

2. *Northwest*: The shoreline in the northwest area of the lake was primarily characterized by high banks (> 2 m) with herbaceous vegetation. Some trees exist but it is not considered forested. A road is in close proximity to the shoreline through this region. The herbaceous vegetation on the bank surface is natural and not mowed and there was little exposed soil during the time of rapid assessment data collection. Compared to areas with exposed soil, vegetated areas have less erodibility, more shear strength, and lower detachment rates (Mamo and Bubenzer 2001a, 2001b). The vegetation absorbs rainfall impact, provides resistance, moderates temperature fluctuations, alters the bank moisture content, and adds root reinforcement (Thorne 1998; Mamo and Bubenzer 2001a, 2001b; Wynn and Mostaghimi 2006).

Because the vegetation along this bank is dense and varied in species, additional plantings would not likely promote greater stability. Observed erosion rates in this region were low (locations 3-4, Figure 7)

so no reclamation strategy is likely needed unless the road is undermined by shoreline adjustment.

3. *East:* The shoreline ground surface elevation increased gradually. This feature is consistent with forested stream systems; forested streams are typically wider than grassed channels and slower to erode than grass-lined channels (Zimmerman et al. 1967; Davies-Colley 1997; Trimble 1997; Allmendinger et al. 2005). Localized fluvial entrainment around exposed roots and woody vegetation was observed, but measured erosion rates were low. A large buffer region exists between the shoreline and community infrastructure. Based on the rapid stability assessment and erosion measurements, there are no recommendations for reclamation in this region.
4. *Southeast:* The shoreline in the southeastern portion of the lake is between the forested section and the area adjacent to the golf course. The banks are generally tall (> 1 m), and runoff from a former ski slope likely contributes to fluvial entrainment of the bank. Because there is more area for reclamation without interfering with community infrastructure, a series of plantings and a reduction of the shoreline angle would be appropriate for this location.
5. *South*: The banks on the southern region of the lake were tall (>1 m), had exposed bank material, and are adjacent to the community golf course. Fluvial entrainment of the exposed bank material as well as localized mass wasting during wet months was observed. Because the adjacent land is a golf course, the full benefit of the grass vegetation is not attained as it is maintained at a low height (Liu and Huang 2002). An active approach to reclamation like riprap is likely needed because the banks have little room to adjust before impacting the infrastructure (i.e., golf course). Reducing the bank angle and planting vegetation would encroach on land used for golfing greens.

Substantial erosion rates were observed in this location even though the stability assessment indicated that the banks were relatively stable (Figures 4 and 7). This inconsistent result highlights the need of multiple assessment techniques to adequately characterize shoreline stability. The rapid stability assessment was completed during the fall in a stable period; no erosion was recorded following the rapid stability assessment, but continued erosion monitoring showed the continued bank adjustment (Figure 7).

Conclusion

A rapid stability assessment tool was developed to evaluate the stability of the shoreline of Alpine Lake. Assessment categories included bank height, exposed bank length, bank angle, evidence of mass wasting, armoring, wind and wave action, unconsolidated material, shoreline protection, vegetation, and accretion. The tool identified locations at risk for instability as well as determined common attributes to consider for designing management efforts. Some limitations were identified and are summarized hereafter:

- The rapid stability assessment was developed over the summer months. The data collection for the rapid assessment of the entire shoreline was completed within one week during August, the driest time of year. The rapid assessment tool was evaluated using erosion measurements collected over a one-year period. The vegetation was fully established on the shoreline bank face in some locations during the rapid assessment data collection where it does not exist during other times of the year. Some reaches, especially near the golf course, were rated as having low to moderate potential for instability with the assessment tool. Later in the year, high erosion rates were observed at some of these locations. Therefore, if the rapid assessment tool is used alone, it should be repeated during the year to confirm the aggregate score and ratings.

- Additional categories may be needed in future versions of the Alpine Lake Rapid Stability Assessment Tool. The current version did not account for the impact of human activity on the bank stability. Mass failures partly caused by foot traffic were observed at popular fishing locations. Recreation activities should be considered in the future.

In summary, the rapid stability assessment tool proved to be an effective tool for identifying the means by which the banks are adjusting, identifying commonalities around the lake, and prioritizing future management techniques. In the absence of erosion pin monitoring, multiple rapid assessments during different seasons would be useful to best quantify the erosion potential. Like previous riverine assessment tools, it could be modified for larger lakes by adding and removing categories.

Acknowledgments

The authors would like to thank Alpine Lake Resort for supporting this work. CAPES, Science without Borders, and WVU CEE provided partial support for the undergraduate research.

Author Bio and Contact Information

Carolina Rando is a former Undergraduate Research Assistant in the Civil and Environmental Engineering Department at West Virginia University sponsored by CAPES Foundation (Ministry of Education of Brazil, Brasilia - DF, Zip Code 70040-020). She is a senior year undergraduate student in Civil Engineering at Escola de Engenharia de Piracicaba in Brazil. carol.rando@hotmail.com.

Leslie Hopkinson is an Associate Professor in Civil and Environmental Engineering at West Virginia University. Her research focus is in hydrology, streambank stability, reclamation, and stream restoration. PO Box 6103, Morgantown, WV 26506, Leslie.Hopkinson@mail.wvu.edu.

Melissa O'Neal is a Project Manager for the West Virginia Water Research Institute where she oversees the Three Rivers QUEST (3RQ), a collaborative water monitoring program in the Upper Ohio River basin. Other work includes watershed based restoration, acid mine drainage abatement, and GIS mapping. PO Box 6064, Morgantown, WV 26506, Melissa.O'Neal@mail.wvu.edu.

Jason Fillhart is an Environmental Scientist for the West Virginia Water Research Institute. He specializes in environmental field work and reporting and is the lead for the National Mine Land Reclamation Center (NMLRC). His research focus in in acid mine drainage abatement and comprehensive watershed analysis. PO Box 6064, Morgantown, WV 26506, Jason.Fillhart@mail.wvu.edu.

Appendix: Rapid Stability Assessment Field Form (Figures Al and A2)

Alpine Lake, Rapid Stability Assessment Field Form (1/2) **SCORE:** _____

I. Personnel			
Date:	**Time begin:**	**Time end:**	**Name(s) of crew:**
Weather:		**Rain in the last two days?** □ Yes □ No	**Photo number range:**

II. LOCATION

Site Name: _____

GPS waypoint #:_____ **GPS name:** Garmin etrex 20 **GPS datum: (e.g. NAD 83)** WGS 1984

UTM field reading: Longitude_____**Latitude**_____**GPS Error: ±** 49.213 ft

Elevation:_____ (ft)

Length of Reach: _____ (ft)

Water Depth: _____ (ft) (representative of reach)

Representative Reach photo: □ Yes **Photo Number(s):**_____

III. PHYSICAL ASSESSMENT

Bank Height:_____ (ft)

< 1.6 ft (low)	1.6-3.3 ft (moderate)	> 3.3 ft (high)	(circle one)
0	***5***	***10***	***(Score, circle one)***

Exposed Bank Face Length:_____ (ft)

Bank Angle:

0-20°	21-60°	61-80°	81-90°	>90°	(circle one)
0	***2.5***	5	***7.5***	***10***	***(Score, circle one)***

Evidence of Recent Mass Wasting/Erosion (Percentage of Shoreline):

0-10%	11-25%	26-50%	51-75%	76-100%	(circle one)
0	***2.5***	5	***7.5***	***10***	***(Score, circle one)***

Gullies?: □ Yes □ No Number:_____; Average width: _____ (ft); Average depth: _____(ft)

Mass wasting/Erosion?: □ Yes □ No

Number of locations:_____; Average width: _____ (ft); Length of shoreline affected:_____ (ft)

Picture of Erosion: □ Yes □ No (Take pictures of significant failure/erosion)

Picture Number(s)	**Description(s)**

Evidence of Armoring (Big particles at toe, low transport):

High	Medium	Low	(circle one)	Average rock size: _____
0	***5***	***10***	***(Score, circle one)***	

Figure A1. Rapid stability assessment field form, page 1.

Alpine Lake, Rapid Stability Assessment Field Form (2/2) **SCORE:** _____

Wind and wave action

// to wind direction, low action	45° to wind direction	90° to wind direction; high action	(circle one)
0	***2.5***	***5***	***(Score, circle one)***

Unconsolidated Material (Percentage of Shoreline)

0-10%	11-25%	26-50%	51-75%	76-100%	(circle one)
0	***2.5***	5	***7.5***	***10***	***(Score, circle one)***

Shoreline Protection (Percentage of shoreline covered by plant roots, vegetation, downed logs, branches, rocks, etc.)

0-10%	11-25%	26-50%	51-75%	76-100%	(circle one)
10	***7.5***	5	***2.5***	***0***	***(Score, circle one)***

Description of protection:

Picture of protection: □ Yes □ No (Take pictures of representative vegetation if not captured in reach photo)

Picture Number(s)	**Description(s)**

Vegetation Contributing to Instability (Percentage of shoreline covered by trees leaning at shoreline)

0-10%	11-25%	26-50%	51-75%	76-100%	(circle one)
0	***2.5***	5	***7.5***	***10***	***(Score, circle one)***

Number of trees: _____

Picture of Trees: □ Yes □ No

Picture Number(s)	**Description(s)**

Occurrence of Accretion (Percentage of shoreline with deposition)

0-10%	11-25%	26-50%	51-75%	76-100%	(circle one)
10	***7.5***	***5***	***2.5***	***0***	***(Score, circle one)***

Notes:

Total Score_____

Hazard Class:

0-30 points	**30.5-40 points**	**40.5-50 points**	**50.5-60 points**	**60.5-85 points**
Very Low	**Low**	**Moderate**	**High**	**Very High**

Good candidate for erosion monitoring? (Circle one based on field experience)

YES NO

Why yes?

Figure A2. Rapid stability assessment field form, page 2.

References

Allmendinger, N.E., J.E. Pizzuto, N. Potter, T.E. Johnson, and W.C. Hession. 2005. The influence of riparian vegetation on stream width, eastern Pennsylvania, USA. *GSA Bulletin* 117(1/2): 229-243.

Alpine Lake Resort. 2016. Welcome to Alpine Lake Resort. Available at: http://www.alpinelake.com/welcome-alpine#. Accessed August 26, 2016.

Davies-Colley, R. 1997. Stream channels are narrower in pasture than in forest. *New Zealand Journal of Marine and Freshwater Research* 31: 599-608.

Gabriel, A.O. 2004. Impacts, perceptions, and management of shoreline hazards and water levels on a fluctuating reservoir: A case study of the Winnebago system, Wisconsin. *Lake and Reservoir Management* 20(3): 197-210.

Guthrie, R.H. and P.D. Law. 2005. *Lakeshore erosion hazard mapping.* Technical Handbook No. TH 1, British Columbia Ministry of Environment, Nanaimo, British Columbia.

Heeren, D.M., A.R. Mittelstet, G.A. Fox, D.E. Storm, A.T. Al-Madhhachi, T.L. Midgley, A.F. Stringer, K.B. Stunkel, and R.D. Tejral. 2012. Using rapid geomorphic assessments to assess streambank stability in Oklahoma Ozark streams. *Transactions of the ASABE* 55(3): 957-968.

Johnson, P.A. 2005. Preliminary assessment and rating of stream channel stability near bridges. *Journal of Hydraulic Engineering* 131(10): 845-852.

Lawson, D.E. 1985. Erosion of northern reservoir shores: An analysis and application of pertinent literature. Monograph 85-1. U.S. Army Corps of Engineers, Cold Regions Research and Engineering Laboratory.

Liu, X. and B. Huang. 2002. Mowing effects on root production, growth, and mortality of creeping bentgrass. *Crop Science* 42: 1241-1250.

Mamo, M. and G.D. Bubenzer. 2001a. Detachment rate, soil erodibility and soil strength as influenced by living plant roots. Part I: Laboratory study. *Transactions of the ASABE* 44(5): 1167-1174.

Mamo, M. and G.D. Bubenzer. 2001b. Detachment rate, soil erodibility and soil strength as influenced by living plant roots. Part II: Field study. *Transactions of the ASABE* 44(5): 1175-1181.

Mukundan, R., D.E. Radcliffe, and J.C. Ritchie. 2011. Channel stability and sediment source assessment in streams draining a Piedmont watershed in Georgia, USA. *Hydrological Processes* 25(8): 1243-1253.

Northeast Regional Climate Center (NRCC). 2016. CLIMOD 2 Data Access. Available at: http://www.nrcc.cornell.edu. Accessed September 9, 2016.

Rinaldi, M., N. Surian, F. Comiti, and M. Bussettini. 2013. A method for the assessment and analysis of the hydromorphological condition of Italian streams: The Morphological Quality Index (MQI). *Geomorphology* 180-181(1): 96-108.

Rosgen, D.L. 2001. A practical method of computing streambank erosion rate. In: *Proceedings of the Seventh Federal Interagency Sedimentation Conference II*, Reno, Nevada, Subcommittee on Sedimentation, pp. 9-15.

Simon, A. and L. Klimetz. 2008. Magnitude, frequency, and duration relations for suspended sediment in stable ("reference") southeastern streams. *Journal of the American Water Resources Association* 44(5): 1270-1283.

Simon, A. and P.W. Downs. 1995. An interdisciplinary approach to evaluation of potential instability in alluvial channels. *Geomorphology* 12: 215-232.

Soil Survey Staff. 2014. *Soil survey field and laboratory methods manual*. Soil Survey Investigations Report No. 51, Version 2.0. R, U.S. Department of Agriculture, Natural Resources Conservation Service.

Staley, N.A., T. Wynn, B. Benham, and G. Yagow. 2006. Modeling channel erosion at the watershed scale: Model review and case study. BSE Document Number 2006-0009. Center for TMDL and Watershed Studies, Blacksburg, Virginia.

Thorne, C.R., ASCE Task Committee on Hydraulics, Bank Mechanisms, and Modelling River Width Adjustment. 1998. River width adjustment. I: Processes and mechanisms. *Journal of Hydraulic Engineering* 124(9): 881-902.

Trimble, S.W. 1997. Stream channel erosion and change resulting from riparian forests. *Geology* 25(5): 467-469.

Wynn, T.M. and S. Mostagnimi. 2006. Effects of riparian vegetation on stream bank subaerial processes in southwestern Virginia, USA. *Earth Surface Processes and Landforms* 31: 399-413.

Wynn, T.M., S. Mostaghimi, J.A. Burger, A.A. Harpold, M.B. Henderson, and L. Henry. 2004. Variation in root density along stream banks. *Journal of Environmental Quality* 33: 2030-2039.

Zimmerman, R.C., J.C. Goodlett, and G.H. Comer. 1967. The influence of vegetation on channel form of small streams. In: *Symposium on River Morphology*. International Association of Scientific Hydrology, Bern, Switzerland, pp. 255-275.

Universities Council on Water Resources
Journal of Contemporary Water Research & Education
Issue 160, Pages 100-118, April 2017

Reduced Phytoplankton and Zooplankton Diversity Associated with Increased Cyanobacteria in Lake Champlain, USA

*Katelyn A. Bockwoldt[1,5], Emily R. Nodine[2,6], Timothy B. Mihuc[3], Angela D. Shambaugh[4], and Jason D. Stockwell[2]

[1]*Department of Environmental Studies, Roanoke College, Salem, VA, USA*
[2]*Rubenstein Ecosystem Science Laboratory, University of Vermont, Burlington, VT, USA*
[3]*Lake Champlain Research Institute, SUNY Plattsburgh, NY, USA*
[4]*Lakes and Ponds Program, Vermont Department of Environmental Conservation, Montpelier, VT, USA*
[5]*Currently at School of Freshwater Sciences, University of Wisconsin Milwaukee, Milwaukee, WI, USA*
[6]*Currently at Department of Environmental Studies, Rollins College, Winter Park, FL, USA*
**Corresponding Author*

Abstract: Anthropogenic inputs of nutrients threaten water quality around the world, causing eutrophication and altering phytoplankton communities. In freshwater systems, certain physiochemical conditions, including high TP, low TN:TP, and warm temperatures, can lead to problematic cyanobacteria blooms. Cyanobacteria can decrease phytoplankton diversity and phytoplankton diversity has been positively linked to zooplankton diversity, suggesting that cyanobacteria may have indirect negative effects on zooplankton diversity. Using monitoring data from Lake Champlain, we tested three hypotheses: (1) cyanobacteria density and phytoplankton diversity are inversely related; (2) phytoplankton diversity and zooplankton diversity are positively related; and by extension (3) cyanobacteria density and zooplankton diversity are inversely related. Relationships were investigated separately at shallow (4-15 m) and deep (25-100 m) sites using several diversity metrics. At deep sites, cyanobacteria density was only related (positively) to zooplankton Shannon diversity. At shallow sites, all three hypotheses were supported by three of four diversity metrics; low phytoplankton richness appears to be the link between high cyanobacteria density and low zooplankton diversity. Our results suggest that cyanobacteria may indirectly reduce zooplankton diversity by decreasing resource heterogeneity, although our results based on observational data were also consistent with well-known direct pathways. Because low biodiversity can alter ecosystem processes and impair functioning, our results suggest that shallow systems may be more responsive to global change than deeper systems.

Keywords: *eutrophication, climate change, biodiversity, ecosystem functioning*

Climate change and anthropogenic inputs of nutrients pose threats to water quality around the world (Smith et al. 1999; Michalak 2016). Nitrogen and phosphorus are typically the limiting nutrients in aquatic systems; changes in their concentrations and nutrient ratios result in changes in system productivity and phytoplankton community composition (Rhee and Gotham 1980; Smith 1983; Hecky and Kilham 1988). In freshwater systems, increased phosphorus inputs, warm temperatures, and water column stability can lead to problematic cyanobacteria blooms (Schindler 1977; Brookes and Carey 2011). While nutrient and temperature conditions are the most commonly recognized drivers of cyanobacteria growth, several other physiochemical conditions (e.g., low CO_2 supply, light limitation, etc.) have also been proposed as significant contributors to development of cyanobacteria blooms in freshwater lakes (Havens et al. 2003; Poste et al. 2013). While much debate currently exists on the primary causes of cyanobacteria blooms, the negative consequences of their presence are difficult to dispute. Intense

blooms often release harmful toxins, cause fish kills, and decrease recreational value (Paerl et al. 2001; Dodds et al. 2009). Cyanobacteria blooms are expected to intensify in the future with warmer temperatures from climate change and increased nutrient runoff resulting from intensified land use associated with population growth (Paerl and Huisman 2008; O'Neil et al. 2012). As a result, the need to fully understand the causes and effects of cyanobacteria blooms in freshwater systems has never been greater (Michalak 2016).

In recent decades, the relationship between biodiversity and ecosystem functioning has received significant attention due to the reduction of local and global biodiversity caused by anthropogenic activities (Loreau et al. 2001). Observational and experimental studies have revealed the importance of species richness and evenness in controlling ecosystem processes (i.e., productivity, nutrient cycling) and ecosystem functioning (i.e., invasibility, resilience to environmental fluctuations; Loreau et al. 2001; Hillebrand et al. 2008). In eutrophic systems, however, the community response of the lower food web to global change is not entirely clear due to a limited number of studies investigating biodiversity relationships both within (Ptacnik et al. 2008) and across trophic levels (Filstrup et al. 2014). To better develop this body of knowledge, particular emphasis must be placed on further understanding the effects of cyanobacteria on phytoplankton and zooplankton community diversity. Such efforts may provide insight into how ecosystem processes, functioning, and services may change in the future with increased cyanobacteria blooms (Cardinale et al. 2012).

Cyanobacteria dominance under high nutrient concentrations is associated with lower biomass of phytoplankton taxa and lower community diversity (Watson et al. 1997; Bouvy et al. 2001). Altered phytoplankton community composition has the potential to affect higher trophic levels by changing the quantity, quality, and diversity of food resources available for consumers (Carpenter et al. 1985; Tilman and Kareiva 1997; Brett et al. 2006). For example, the resource heterogeneity hypothesis states that species should have a positive response to variation in their resources (Connell 1978; Cardinale et al. 2012). Therefore, zooplankton abundance and diversity should be highest at high levels of phytoplankton diversity because resource variation provides opportunities for niche partitioning and reduces resource limitation (Connell 1978; Tilman and Kareiva 1997). Zooplankton and phytoplankton diversity have been shown to be positively correlated by some metrics (i.e., phytoplankton richness, Shannon diversity), adding further support for this hypothesis in freshwater systems (Soininen and Luoto 2012; Striebel et al. 2012). Conversely, low phytoplankton diversity should result in low zooplankton diversity due to resource limitation and decreased niche partitioning (Connell 1978; Tilman and Kareiva 1997).

Taken together, theory and observations suggest that because cyanobacteria can alter phytoplankton communities and decrease taxonomic diversity (Watson et al. 1997; Bouvy et al. 2001), cyanobacteria may have indirect effects on zooplankton diversity. However, studies examining the relationships between cyanobacteria and zooplankton have typically focused on the direct effects of cyanobacteria nutrition, toxicity, or morphology on zooplankton individuals and species (Ger et al. 2016). Cyanobacteria generally are a nutritionally poor, toxic, or difficult to graze food source for zooplankton, and have been found to decrease zooplankton growth, reproduction, and abundance when dominant (Lampert 1987; Brett et al. 2000; Ger et al. 2016). Less attention has been paid to the effects of cyanobacteria density on zooplankton taxonomic diversity. Bouvy et al. (2001) found an increase in zooplankton diversity (Shannon index) during and after a single cyanobacteria bloom, while Leonard and Pearl (2005) found low zooplankton diversity during periods of high cyanobacteria density. Given these contradicting results and the expected increase of cyanobacteria blooms with climate change and intensified land use, a more complete understanding of the impacts of cyanobacteria on zooplankton diversity is needed to elucidate how cyanobacteria could potentially affect intermediate trophic levels and biodiversity (Loreau et al. 2001).

In this study, we tested three linked hypotheses: (1) cyanobacteria density and phytoplankton diversity are inversely related; (2) phytoplankton diversity and zooplankton diversity are positively

related; and by extension (3) cyanobacteria density and zooplankton diversity are inversely related. The hypotheses were tested using monitoring data from Lake Champlain, a highly heterogeneous, large-lake system with habitats ranging from shallow eutrophic bays to deep oligotrophic/mesotrophic basins (Facey et al. 2012). The frequency and intensity of cyanobacteria blooms in Lake Champlain have been increasing (Smeltzer et al. 2012), providing an excellent system in which to test our hypotheses. Our goal is to expand the understanding of biodiversity in eutrophic and mesotrophic systems by testing a conceptual model that indirectly connects cyanobacteria density to zooplankton diversity (Figure 1).

Methods

Lake Champlain is a large, temperate lake with a surface area of 1,127 km^2, mean and maximum depths of 20 and 122 m, and a drainage basin of 21,326 km^2 (Facey et al. 2012). The lake is divided into five major basins: South Lake, Main Lake, Northeast Arm, Malletts Bay, and Missisquoi Bay. South Lake and Missisquoi Bay are shallow, warm, and eutrophic and the Main Lake, Malletts Bay, and Northeast Arm are mesotrophic to oligotrophic (Table 1; Figure 2; Facey et al. 2012). Existing phytoplankton and zooplankton data from the Lake Champlain Long-Term Monitoring Program (LTMP; http://dec.vermont.gov/watershed/lakes-ponds/monitor/lake-champlain) were used to test hypotheses. The LTMP monitors 15 sites distributed across all five basins, encompassing the physical, chemical, and biological heterogeneity of Lake Champlain (Figure 2; Table 1). Phytoplankton data were available from 2006 to 2014, and zooplankton data were available from 2006 to 2010. In 2006, zooplankton data were only available from five sites during July.

Phytoplankton and zooplankton sampling protocols are outlined elsewhere (Vermont DEC and New York State DEC 2015). Briefly, sites were sampled approximately twice per month from May to October each year. Phytoplankton samples were collected during the day using a 13-cm diameter, 63-µm mesh net towed vertically from twice the Secchi depth to surface. Samples were preserved in 1% Lugol's solution and species counts were completed by the Vermont Department of Environmental Conservation (Montpelier, VT) using settling chambers or Sedgewick Rafter cells and an Olympus CKX41 inverted microscope. Phytoplankton densities were calculated as the number of cells/L. Zooplankton were sampled during the day with a 30-cm diameter, 153-µm mesh net towed vertically from just above the sediment to surface. Samples were narcotized with carbonated water and preserved in formalin. Species counts were completed by the Lake Champlain Research Institute (Plattsburgh, NY) using Sedgewick Rafter cells and a Leica DM IL inverted microscope. Zooplankton densities were calculated as the number of individuals/m^3.

For phytoplankton and zooplankton, individuals were delineated to the species level whenever

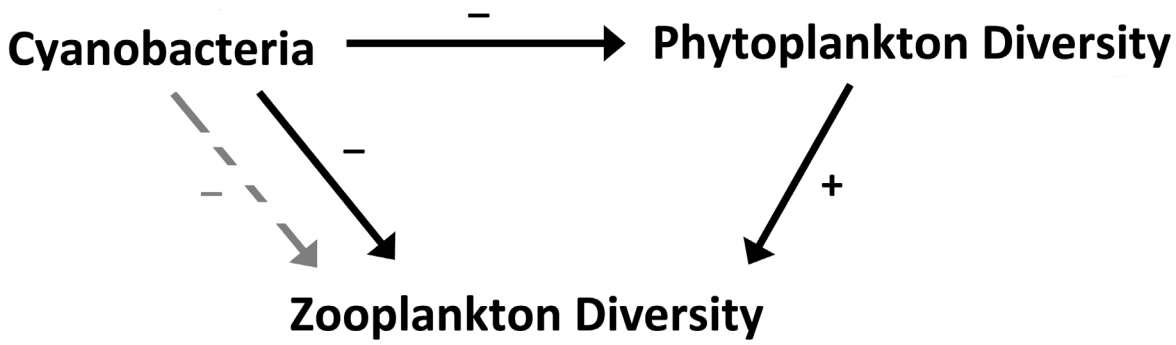

Figure 1. Established and hypothesized relationships among cyanobacteria, phytoplankton diversity, and zooplankton diversity. Solid lines represent observed direct relationships and dashed line represents hypothesized indirect relationships.

Table 1. Characteristics of 15 Lake Champlain sampling sites used in the long-term monitoring program (LTMP). Sites numbers are LTMP station numbers. Total phosphorus (TP) values are averages for each site from 2006 to 2010.

Site #	Site Name	Basin	TP (µg/L)[1]	Trophic Status[1]	Depth (m)	Latitude	Longitude
50	Missisquoi Bay	Missisquoi Bay	49.18	Eutrophic	4	45.013	-73.174
51	Missisquoi Bay Central	Missisquoi Bay	52.18	Eutrophic	5	45.042	-73.130
2	South Lake B	South Lake	49.15	Eutrophic	5	43.715	-73.383
46	Isle LaMotte (Rouses Point)	Main Lake	16.54	Mesotrophic	7	44.948	-73.340
40	St. Albans Bay	Northeast Arm	27.89	Eutrophic	7	44.785	-73.162
4	South Lake A	South Lake	34.27	Eutrophic	10	43.952	-73.408
33	Cumberland Bay	Main Lake	13.83	Mesotrophic	11	44.701	-73.418
21	Burlington Bay	Main Lake	13.62	Mesotrophic	15	44.475	-73.232
16	Shelburne Bay	Main Lake	13.14	Mesotrophic	25	44.426	-73.232
25	Malletts Bay	Mallets Bay	11.85	Oligotrophic	32	44.582	-73.281
7	Port Henry Segment	Main Lake	16.44	Mesotrophic	50	44.126	-73.413
34	Northeast Arm	Northeast Arm	20.89	Mesotrophic	50	44.708	-73.227
36	Isle LaMotte (Grand Isle)	Main Lake	12.62	Mesotrophic	50	44.756	-73.355
9	Otter Creek Segment	Main Lake	17.23	Mesotrophic	97	44.242	-73.329
19	Main Lake	Main Lake	13.32	Mesotrophic	100	44.471	-73.299

[1]Lake Champlain Basin Program data

possible (Tables S1 and S2). In cases when species could not be resolved, identification was to genus level. Genera level taxa were counted as a single taxon in diversity calculations. Diversity indices based on both species and genera level data are not ideal for diversity studies. Certain genera have species that are hard to resolve, such that the diversity of these taxa will be underrepresented compared to genera with species easier to resolve. Using genera taxa in our study, however, is consistent with the methods of other large-lake studies because many phytoplankton and zooplankton genera are difficult to delineate to species (Filstrup et al. 2014; Reavie et al. 2014; Burgess et al. 2015).

Four common measures of diversity were

used because no single metric can perfectly characterize community diversity (Hillebrand et al. 2008; Morris et al. 2014). Diversity metrics were calculated using the 'vegan' package in R (Oksanen et al. 2013):

(1) Species richness: S

(2) Shannon index: $H' = -\sum_{i=1}^{S} p_i \log_{10} p_i$

(3) Simpson index: $D' = 1-\sum_{i=1}^{S} p_i^2$

(4) Evenness: $H'/log(S)$

where S is the total number of species (or genera) and p_i is the proportion of species i based on cell and individual densities for phytoplankton and zooplankton, respectively. Briefly, D' measures the probability that two random individuals will be from different species; H' is an abstract index measuring the uncertainty of unknown individual's identity in systems of varying diversity; and evenness is a measure of the relative abundance of all species present (Morris et al. 2014).

Cyanobacteria density and phytoplankton diversity metrics were averaged for each site-year from 2006 to 2014. Cyanobacteria were included in all measures of phytoplankton diversity. Zooplankton diversity was averaged for each site and year from 2006 to 2010. Only data from July, August, and September were included in the analyses because these months encompassed the period of highest cyanobacteria density in Lake Champlain. Generalized linear models were used to test the relationships among $\log_{10}$-transformed cyanobacteria densities, phytoplankton diversity, and zooplankton diversity metrics. Each site-year was used as an observation and grouped by depth (shallow or deep with 25 m as the threshold; Table 1) for statistical tests. Sites were grouped in this manner due to expected differences resulting from the influence of basin characteristics on nutrient distributions (Smeltzer et al. 2012). Shallow sites had an average total phosphorus concentration of 32.08 µg/L during the study period, while deep sites had an average concentration of 15.07 µg/L (Table 1). Site classification in this manner allowed for the comparison of plankton diversity in generally eutrophic versus mesotrophic sites. All statistical analyses ($\alpha = 0.05$) were performed using R version 3.2.0 (R Core Development Team 2014).

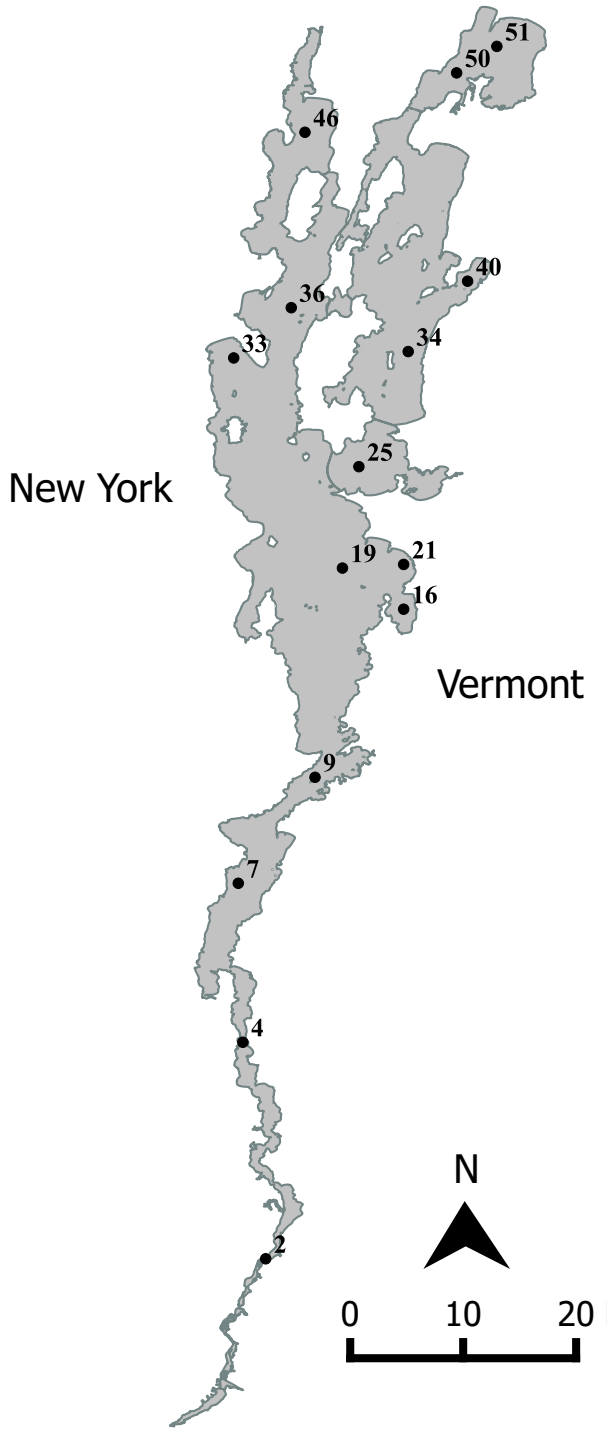

Figure 2. Locations of the 15 sampling sites used in the Lake Champlain Long-Term Monitoring Program. See Table 1 for specific site information.

Results

Relationships among cyanobacteria density, phytoplankton diversity, and zooplankton diversity metrics were generally stronger at shallow sites and rarely significant at deep sites. Cyanobacteria density was inversely related to phytoplankton diversity at shallow sites, but variable across the four diversity metrics (Figure 3). Phytoplankton richness, *H′*, and *D′* each showed a negative relationship with cyanobacteria density at shallow sites (all $p < 0.01$; Figures 3a, 3c, 3d); phytoplankton evenness was not significantly correlated with cyanobacteria density (Figure 3b). At deep sites, no significant relationships were observed between cyanobacteria density and any measure of phytoplankton diversity (Figures 3a-d).

Phytoplankton richness was the only phytoplankton diversity metric that showed significant relationships with zooplankton diversity metrics (Figure 4); phytoplankton evenness, *H′*, and *D′* were not significantly correlated with zooplankton diversity metrics ($p \geq 0.18$ for each; data not shown). The relationship between phytoplankton richness and zooplankton diversity was significant at shallow sites, but insignificant at deep sites ($p \geq 0.34$ for each). At shallow sites, zooplankton evenness, H′, and D′ were positively related to phytoplankton richness ($p < 0.05$; Figures 4b-d).

Relationships between cyanobacteria density and zooplankton diversity metrics were also strongest at shallow sites by most metrics, but revealed one significant relationship at deep sites (Figure 5). Zooplankton evenness, *H′*, and *D′* were negatively

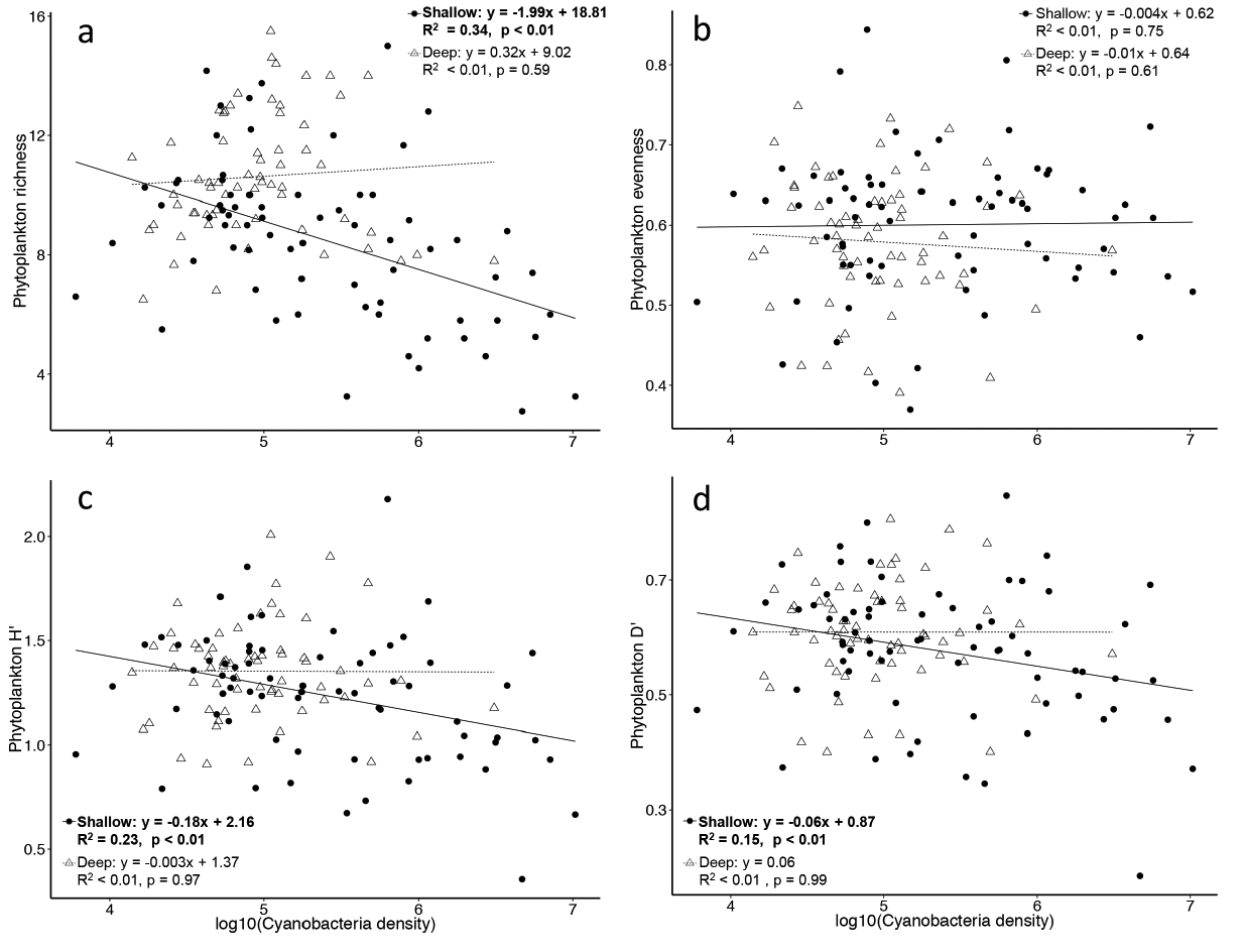

Figure 3. Relationships between $\log_{10}$-transformed cyanobacteria density and (a) phytoplankton richness, (b) phytoplankton evenness, (c) Shannon diversity, and (d) Simpson diversity for deep and shallow sites in Lake Champlain 2006-2014. Significant relationships bolded.

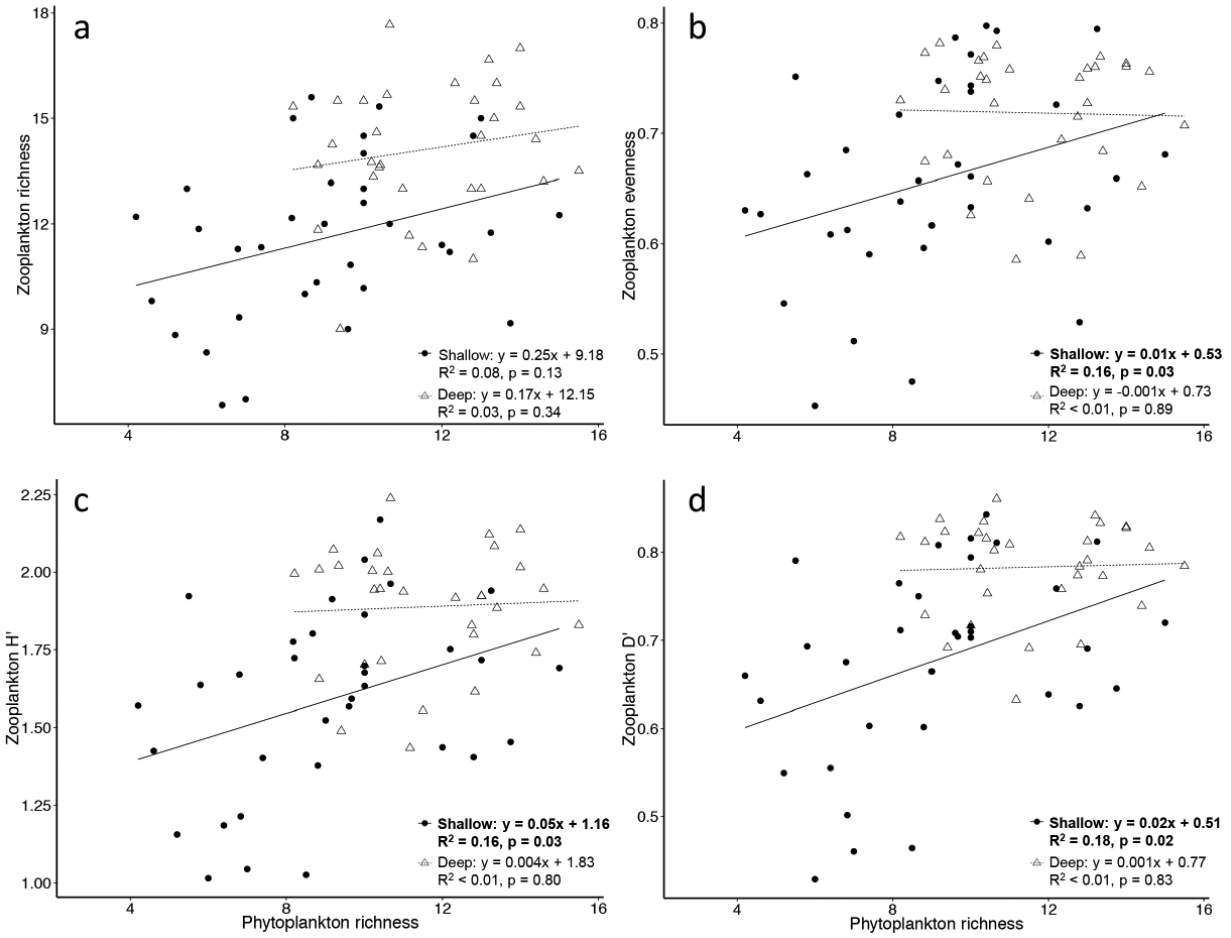

Figure 4. Relationships between phytoplankton richness and (a) zooplankton richness, (b) zooplankton evenness, (c) Shannon index, and (d) Simpson index for deep and shallow sites in Lake Champlain 2006-2010. Significant relationships bolded.

related to cyanobacteria density at shallow sites (all $p < 0.01$; Figures 5b-d); zooplankton richness was not significantly correlated with cyanobacteria density (Figure 5a). Interestingly, while the relationships with all metrics at shallow sites were negative as predicted, zooplankton *H′* was positively related to cyanobacteria density at deep sites ($p < 0.05$; Figure 5c). No other significant relationships between zooplankton diversity and cyanobacteria density were found at deep sites, although generally positive relationships were observed with each metric (Figures 5a, b, and d).

Discussion

Research on the relationships between cyanobacteria density and zooplankton has typically focused on the direct effects of cyanobacteria on zooplankton grazing and growth (e.g., Lampert 1987; Brett et al. 2000; Paerl et al. 2001). To our knowledge, our study is the first to investigate potential indirect relationships between cyanobacteria density and zooplankton diversity through phytoplankton diversity. Across shallow sites in Lake Champlain, we found negative relationships between cyanobacteria density and both phytoplankton and zooplankton diversity metrics, and positive relationships between phytoplankton and zooplankton diversity metrics, providing support for our conceptual model of indirect effects of cyanobacteria on zooplankton diversity (Figure 1). In contrast, our model was not supported at deep sites, as no relationships were observed among most of the comparisons.

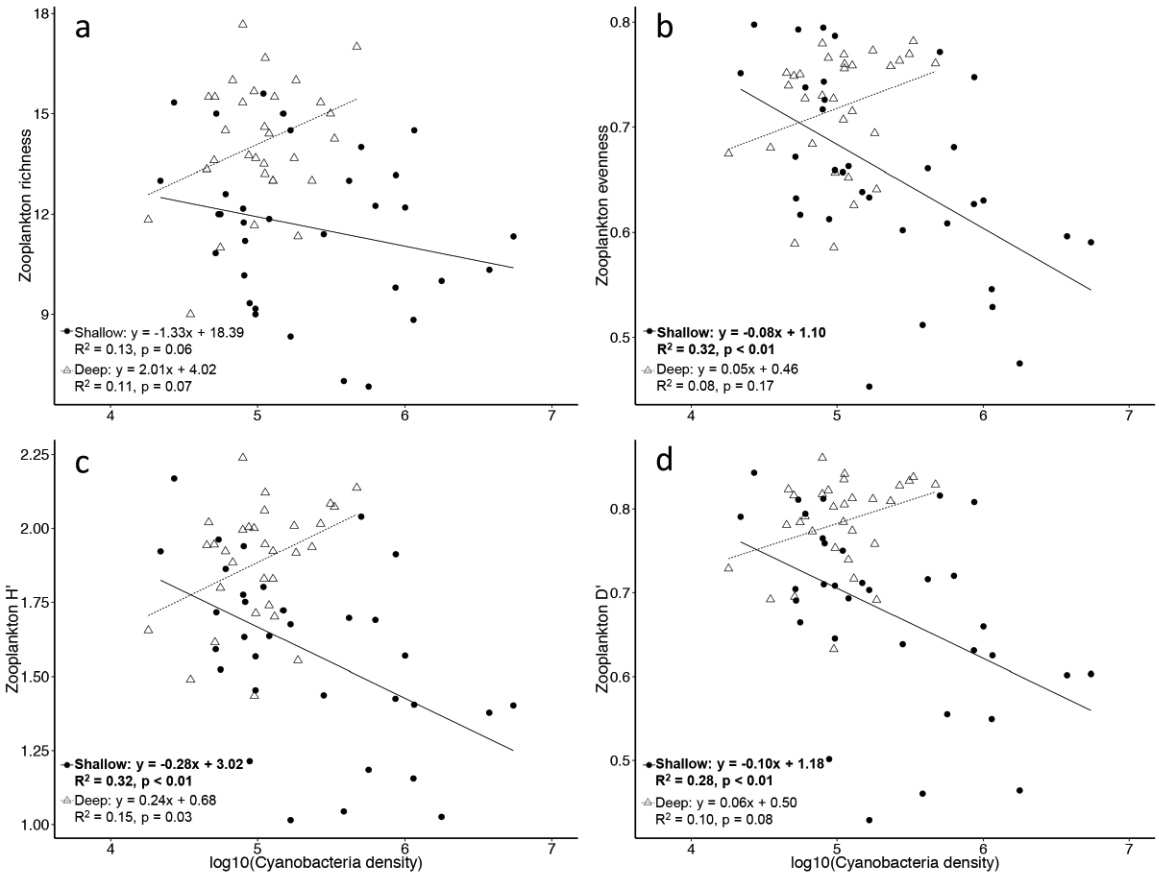

Figure 5. Relationships between cyanobacteria density and (a) zooplankton richness, (b) zooplankton evenness, (c) Shannon index, and (d) Simpson index for deep and shallow sites in Lake Champlain 2006-2010. Significant relationships bolded.

The positive relationships between phytoplankton richness and zooplankton diversity metrics at shallow sites are consistent with the resource heterogeneity hypothesis (Figure 1; Connell 1978; Tilman and Kareiva 1997). Striebel et al. (2012) also found an increase in zooplankton *H′* with phytoplankton richness, and inferred that phytoplankton richness corresponded to an increase in phytoplankton cell shapes, sizes, structures, and nutritional value that benefited the zooplankton community. The reduced phytoplankton richness we observed with increased cyanobacteria density at shallow sites suggests cyanobacteria may indirectly reduce zooplankton diversity by reducing resource heterogeneity (i.e., phytoplankton richness). While we did not assess specific taxonomic relationships in light of the resource heterogeneity hypothesis, high phytoplankton richness has a greater probability of representing higher phenotypic diversity in the phytoplankton community (Loreau et al. 2001). Thus, phytoplankton richness may be an important connection between cyanobacteria and zooplankton diversity.

Unexpectedly, phytoplankton evenness was not related to cyanobacteria density in Lake Champlain (Figure 3b). Phytoplankton evenness is expected to decrease under eutrophic conditions when the relative abundance of cyanobacteria increases with increasing phosphorus concentrations (Watson et al. 1997; Downing et al. 2001). The absence of such a relationship in our data may be a result of (1) reliance on samples from a 63-µm mesh net which selects against smaller phytoplankton taxa, or (2) the limited scope of our data set.

Filstrup et al. (2014) found lower phytoplankton evenness with high cyanobacteria densities using a 9-year, 131-lake data set. Our phytoplankton analyses were limited to a single temperate lake sampled over nine years. The analysis of a single lake or filtered samples could have limited the spatial or taxonomic ranges under which relationships between phytoplankton evenness and cyanobacteria density could be detected.

Our conceptual model (Figure 1) was not supported at deep sites, where few relationships were observed among the comparisons. The overall lack of relationships between cyanobacteria and phytoplankton and zooplankton diversity metrics at deep sites is perhaps not surprising. The deeper regions of Lake Champlain may be less suitable for cyanobacteria dominance than the shallow, protected sites (e.g., lower P concentrations, Table 1). Cyanobacteria densities were lower at deep sites compared to shallow sites (Figures 3, 5), consistent with general theory and observations that deeper lakes are less susceptible to cyanobacteria blooms due to less favorable nutrient and physical conditions for cyanobacteria (Finnendegg 1966; Ghadouani et al. 2003; Nixdorf et al. 2003). The one significant relationship at deep sites between cyanobacteria density and zooplankton H', and the general (but insignificant) patterns of positive relationships between cyanobacteria and the other zooplankton metrics, were contrary to expectations and our observations at shallow sites (Figure 5). Zooplankton growth can be enhanced by mixed diets of cyanobacteria and high-quality phytoplankton (e.g., chrysophytes, chlorophytes) compared to unmixed diets (Lundstedt and Brett 1991; DeMott 1998; Alva-Martinez et al. 2007). Thus, regions of lakes where cyanobacteria are present but do not reach dominance may enhance zooplankton diversity by contributing to resource heterogeneity, although further investigations are needed. Overall, the differences in the relationships we observed between deep and shallow sites suggest a tighter coupling of cyanobacteria dynamics to primary consumers in shallow systems (Ghadouani et al. 2003).

Arguably, attribution of cyanobacteria impacts on zooplankton diversity as indirect or direct is a tenuous proposition when based on observational data alone. Our inference of indirect effects is also complicated by the complexity of cyanobacteria-zooplankton relationships. Cyanobacteria can negatively affect zooplankton in many direct ways, including low nutritional quality (i.e., lack of essential fatty acids and sterols), harmful metabolites (i.e., cyanotoxins), and defensive morphology (Ger et al. 2016). Such direct effects of cyanobacteria on zooplankton could plausibly lead to the patterns we observed. Experiments are needed to draw conclusions about pathways. Nonetheless, the results of our observational study provide suggestive evidence of an additional channel through which cyanobacteria may affect zooplankton diversity (i.e., reduced resource heterogeneity).

Our analyses relied on phytoplankton and cyanobacteria samples collected from a long-term monitoring program using a 63-µm mesh net. Thus, we cannot fully account for phytoplankton and cyanobacteria community changes and their relationships because the net selects against picoplankton, nanoplankton, and some microplankton. If phytoplankton community responses to cyanobacteria blooms include shifts to smaller species, then our diversity metrics would be biased. Despite such limitations, the data were standardized across all sampling events and thus represent valid comparisons of the representative taxa sampled by the net. That we did observe changes in diversity relationships with changes in cyanobacteria density points to important food web changes as a result of increasing cyanobacteria density, albeit within limited size ranges of the communities sampled. Any retrospective analyses of long-term monitoring data, for which the data were not originally intended, can suffer from similar limitations as our study, but do not necessarily preclude the usefulness of such analyses.

Many studies have illustrated the negative effects of decreased biodiversity on ecosystem functioning, health, and services (Loreau et al. 2001; Hillebrand et al. 2008; Cardinale et al. 2012). The combined decreases in phytoplankton and zooplankton diversity associated with cyanobacteria blooms observed in our study suggest potential for declines in shallow, freshwater ecosystem functioning, given the

expected increase in cyanobacteria blooms with climate change (Paerl and Huisman 2008). Shallow, nearshore ecosystems will likely experience greater changes in biodiversity and ecosystem functioning than deep, pelagic communities because they will be more strongly affected by global change (e.g., higher direct nutrient inputs resulting from increased land use from population growth, faster warming water temperatures due to climate change; Mooij et al. 2007). As biodiversity and ecosystem health are valued intrinsically and economically, collaboration between scientists and policy makers to develop ways to reduce the impacts of anthropogenic activities on freshwater systems is needed.

Acknowledgements

Research was funded by the National Science Foundation (Award DBI-1358838) and supported by the Rubenstein Ecosystem Science Laboratory at the University of Vermont. Special thanks to everyone who supported the 2015 REU Program: "Interdisciplinary Research on Human Impacts in Lake Champlain." Michael McDonald and Alan Howard provided advice on statistical analyses. Many thanks to Steven Powers for providing Honors Thesis guidance.

Funding for the Champlain Long-term Water Quality and Biological Monitoring Program was provided by the Lake Champlain Basin Program. Field work was conducted by the Lakes and Ponds Program at the Vermont DEC, and by the students and staff at the Lake Champlain Research Institute at the State University of New York – Plattsburgh.

Author Bio and Contact Information

Katelyn A. Bockwoldt received a Bachelor of Science in Environmental Studies and Biology from Roanoke College in December 2016. As an undergraduate, she served as a research assistant in the Biology Department, and also participated in the 2015 REU program at UVM's Rubenstein Ecosystem Science Laboratory. Katelyn is currently pursuing a MS in Freshwater Sciences at the University of Wisconsin-Milwaukee. Her current research is quantifying lower food web production and trophic efficiency in post-dreissenid Lake Michigan. She may be reached at bockwol2@uwm.edu or School of Freshwater Sciences, 600 E Greenfield Ave., University of Wisconsin Milwaukee, Milwaukee, WI 53204.

Emily R. Nodine served as a mentor for the 2015 REU program as a post-doctoral associate at UVM's Rubenstein Ecosystem Science Laboratory. She is now an assistant professor in the Environmental Studies department at Rollins College, and may be contacted at enodine@rollins.edu or Department of Environmental Studies, 1000 Holt Avenue, Rollins College, Winter Park, FL 32789.

Timothy B. Mihuc may be reached at mihuctb@plattsburgh.edu or Lake Champlain Research Institute, 101 Broad Street, SUNY Plattsburgh, Plattsburgh, NY 12901 USA.

Angela D. Shambaugh may be reached at angela.shambaugh@vermont.gov or Lakes and Ponds Program, Vermont Department of Environmental Conservation, 1 National Life Drive, Main 2, Montpelier, VT 05620.

Jason D. Stockwell may be reached at jason.stockwell@uvm.edu or Rubenstein Ecosystem Science Laboratory, 3 College Street, University of Vermont, Burlington, VT 05401.

Supplemental Tables (S1-S2)

Table S1. Phytoplankton taxonomic data for the 15 Lake Champlain sampling sites. X indicates presence of taxon on at least one occasion from 2006 to 2014.

Taxon	Shallow Sites								Deep Sites						
	50	51	2	46	40	4	33	21	16	25	7	34	36	9	19
Asterionella formosa	X	X	X	X	X	X	X	X	X	X	X	X	X	X	X
Asterionella spp.	X	X	X			X			X	X	X		X		X
Attheya spp.			X	X		X					X			X	
Aulocoseira granulata	X	X	X	X	X	X	X	X	X		X	X	X		X
Aulocoseira spp.	X	X	X	X	X	X	X	X	X	X	X	X	X	X	X
Centrales spp.	X	X	X	X	X	X	X				X	X	X		
Cymatopleura spp.			X			X				X		X			
Cymbellaceae			X												
Diatoma spp.	X	X	X	X	X	X	X	X	X	X	X	X	X	X	X
Fragilaria crotonensis	X	X	X	X	X	X	X	X	X	X	X	X	X	X	X
Fragilaria spp.	X	X	X	X	X	X	X	X	X	X	X	X	X	X	X
Gyrosigma spp.			X	X											
Pennales spp.	X	X	X	X	X	X	X	X	X	X	X	X	X	X	X
Rhizosolenia spp.		X	X	X	X	X	X	X	X	X	X	X	X	X	X
Stephanodiscus spp.	X	X		X	X	X	X	X	X	X	X	X	X	X	X
Surirella spp.						X				X					
Synedra spp.	X								X	X					
Synedra ulna	X	X	X	X	X	X	X	X	X	X	X	X	X	X	X
Tabellaria flocculosa	X	X	X	X						X			X		
Tabellaria spp.	X	X	X	X		X	X	X	X	X	X		X	X	X
Total Bacillariophyta	**14**	**14**	**17**	**15**	**11**	**16**	**12**	**11**	**13**	**15**	**14**	**12**	**14**	**11**	**12**

Table S1 (continued).

Taxon	Shallow Sites								Deep Sites							
	50	51	2	46	40	4	33	21	16	25	7	34	36	9	19	
Ankyra spp.													X			
Arthrodesmus spp.					X		X			X		X				
Botryococcus spp.					X	X	X	X								
Bulbochaete spp.					X		X	X	X		X	X	X	X	X	
Chaetophorales				X	X		X	X	X		X	X	X	X	X	
Closteriopsis spp.				X	X		X	X	X		X	X	X	X	X	
Closterium spp.	X															
Coelastrum microporum		X														
Cosmarium spp.															X	
Dictyosphaerium spp.	X	X	X	X	X	X	X	X	X	X	X	X	X	X	X	
Elakatothrix viridis										X						
Eudorina spp.	X	X	X	X	X	X	X	X	X	X	X	X	X	X	X	
Gloeocystis gigas							X									
Gloeocystis spp.	X	X		X	X		X			X		X				
Gonium spp.	X	X		X												
Kirchneriella spp.	X												X		X	
Micractinium pusillum			X		X				X		X			X	X	
Mougeotia spp.	X	X	X	X	X	X	X	X	X	X	X	X	X		X	
Nephrocytium spp.	X															

Table S1 (continued).

Taxon	Shallow Sites								Deep Sites						
	50	51	2	46	40	4	33	21	16	25	7	34	36	9	19
Oedogonium spp.				X	X		X	X	X	X	X	X	X	X	X
Oocystis spp.		X									X	X			
Pandorina morum	X		X			X	X			X	X				
Pediastrum boryanum					X			X						X	
Pediastrum duplex	X	X	X	X	X			X				X			X
Pediastrum simplex	X	X	X		X	X		X	X		X	X	X		X
Quadrigula spp.							X			X					
Scenedesmus quadricauda			X			X									
Schizochlamys spp.					X										
Schroederia spp.		X													
Sphaerocystis spp.	X				X			X	X	X	X				
Spirogyra spp.	X		X	X	X	X									
Spondylosium spp.												X			
Staurastrum spp.	X	X	X	X	X	X	X	X	X	X	X	X	X	X	X
Staurodesmus spp.					X							X			
Stigeoclonium spp.							X								
Tetraspora lamellosa				X	X										X
Tetraspora spp.	X			X	X	X	X	X	X	X	X	X	X	X	X
Ulothrix spp.			X			X	X	X			X			X	
Volvox spp.			X	X		X	X		X						X
Total green algae	**15**	**11**	**12**	**14**	**21**	**12**	**18**	**15**	**13**	**12**	**15**	**16**	**12**	**11**	**16**

Table S1 (continued).

Taxon	Shallow Sites								Deep Sites						
	50	51	2	46	40	4	33	21	16	25	7	34	36	9	19
Dinobryon bavaricum	X	X	X	X		X	X			X	X			X	
Dinobryon cylindricum			X	X	X	X		X		X	X	X	X	X	
Dinobryon divergens	X	X	X	X	X	X	X	X	X	X	X	X	X	X	X
Dinobryon sertularia	X		X	X		X			X	X	X			X	
Dinobryon sociale	X	X	X			X	X						X		
Dinobryon spp.	X	X	X	X		X		X	X	X	X		X	X	X
Mallomonas spp.	X		X				X	X	X	X			X		X
Synura spp.	X	X	X	X	X	X	X	X	X	X	X		X	X	X
Uroglenopsis spp.						X			X		X				X
Total Chrysophyta	**7**	**5**	**8**	**6**	**3**	**8**	**5**	**5**	**6**	**7**	**7**	**2**	**6**	**6**	**5**
Anabaena circinalis	X	X		X	X	X			X		X	X			
Anabaena flos-aquae	X	X		X	X	X	X	X	X	X	X	X		X	X
Anabaena planctonica			X	X	X	X	X	X	X		X		X	X	X
Anabaena spp.	X	X	X	X	X	X	X	X	X	X	X	X	X	X	X
Aphanizomenon flos-aquae	X	X	X	X	X	X	X	X	X	X	X	X	X	X	X
Aphanizomenon gracile	X											X	X		
Aphanizomenon spp.		X			X		X	X	X	X			X	X	X
Aphanocapsa spp.	X	X	X	X	X	X	X	X	X	X	X	X	X	X	X
Aphanothece spp.	X	X	X	X	X	X	X	X	X	X	X	X	X		X
Chroococcales	X	X			X			X	X				X		
Chroococcus prescotti							X		X	X	X			X	X
Chroococcus spp.		X					X			X	X	X			X
Coelosphaerium spp.				X			X	X		X	X			X	X

Table S1 (continued).

Taxon	Shallow Sites								Deep Sites						
	50	51	2	46	40	4	33	21	16	25	7	34	36	9	19
Dactylococcopsis spp.															X
Gloeotrichia spp.					X		X						X		
Gomphosphaeria lacustris									X			X			
Hormonogonales spp.			X	X		X				X	X	X			
Lyngbya spp.				X											
Microcystis spp.	X	X	X	X	X		X	X	X	X	X	X	X	X	X
Microcystis wesenbergii	X	X			X	X	X	X				X	X		
Oscillatoria spp.				X	X										
Oscillatoriaceae		X		X		X	X			X		X		X	
Pannus spp.			X												
Phormidium mucicola	X	X		X			X		X		X	X		X	X
Phormidium spp.	X										X	X	X		
Radiocystis spp.								X	X	X					X
Romeria spp.				X											
Snowella spp.	X	X	X				X		X	X		X	X	X	X
Woronichinia spp.	X			X	X	X	X	X	X	X	X	X	X	X	X
Total Cyanobacteria	**14**	**14**	**10**	**16**	**14**	**11**	**17**	**13**	**16**	**15**	**15**	**17**	**14**	**13**	**16**
Ceratium hirundinella	X	X	X	X	X	X	X	X	X	X	X	X	X	X	X
Ceratium spp.	X	X	X		X							X			
Glenodinium spp.		X			X	X									
Peridinium spp.			X	X	X	X	X			X	X	X		X	
Total Pyrrophyta	**2**	**3**	**3**	**2**	**4**	**3**	**2**	**1**	**1**	**2**	**2**	**3**	**1**	**2**	**1**

Table S2. Zooplankton taxonomic data for the 15 Lake Champlain sampling sites. X indicates presence of taxon on at least one occasion from 2006 to 2010.

Taxon	Shallow Sites								Deep Sites						
	50	51	2	46	40	4	33	21	16	25	7	34	36	9	19
Alona bicolor						X									
Alonella spp.										X		X		X	
Bosmina longirostris	X	X	X	X	X	X	X	X	X	X	X	X	X	X	X
Bosmina spp.	X	X	X	X	X	X	X	X	X	X	X	X	X	X	X
Ceriodaphnia spp.	X	X	X	X	X	X	X	X	X	X	X	X	X	X	X
Chydorus spp.	X	X	X	X	X	X	X	X	X	X	X	X	X	X	X
Daphnia spp.	X	X	X	X	X	X	X	X	X	X	X	X	X	X	X
Diaphanosoma birgei	X	X	X	X	X	X	X	X	X	X	X	X	X	X	X
Diaphanosoma spp.	X	X	X	X	X	X	X	X	X	X	X	X	X	X	X
Epischura spp.		X	X	X		X		X	X	X		X	X	X	X
Eubosmina spp.	X	X	X	X	X	X	X	X	X	X	X	X	X	X	X
Eurycercus spp.						X									
Holopedium gibberum	X	X		X	X	X	X	X	X	X	X	X	X	X	X
Leptodora kindti	X	X	X	X	X	X		X	X	X	X	X	X		X
Pleuroxus spp.						X									
Polyphemus pediculus		X		X	X	X	X	X	X	X	X		X	X	X
Sida crystallina	X	X		X		X		X	X				X		X
Total Cladocera	**11**	**13**	**10**	**13**	**11**	**16**	**10**	**13**	**12**	**13**	**11**	**12**	**13**	**12**	**13**
Acanthocyclops spp.	X	X	X	X	X	X	X	X	X	X	X	X	X	X	X
Cyclops scutifer					X			X							
Diacyclops thomasi	X	X	X	X	X	X	X	X	X	X	X	X	X	X	X
Eucyclops serrulatus	X	X		X	X	X	X	X	X	X	X	X	X	X	X
Mesocyclops edax	X	X	X	X	X	X	X	X	X	X	X	X	X	X	X
Mesocyclops spp.	X	X	X	X	X	X	X	X	X	X	X	X	X	X	X
Thermocyclops crassus	X	X	X	X	X	X	X	X	X	X	X	X	X	X	X
Tropocyclops spp.				X	X	X	X	X	X			X	X		X
Total Cyclopoida	**6**	**6**	**5**	**7**	**8**	**7**	**7**	**8**	**7**	**6**	**6**	**7**	**7**	**6**	**7**

Table S2 (continued).

Taxon	Shallow Sites								Deep Sites						
	50	51	2	46	40	4	33	21	16	25	7	34	36	9	19
Leptodiaptomus spp.	X	X	X	X	X	X	X	X	X	X	X	X	X	X	X
Limnocalanus spp.		X	X	X	X	X	X	X	X	X	X	X	X	X	X
Senecella calanoides	X	X	X	X	X	X	X	X	X	X	X	X	X	X	X
Total Calanoida	**2**	**3**	**3**	**3**	**3**	**3**	**3**	**3**	**3**	**3**	**3**	**3**	**3**	**3**	**3**
Ascomorpha/Gastropus spp.	X		X			X		X	X		X	X	X	X	X
Asplanchna spp.	X	X	X	X	X	X	X	X	X	X	X	X	X	X	X
Brachionus calyciflorus		X								X					
Collotheca spp.	X	X			X	X	X		X	X			X		
Conochilus spp.	X	X	X	X	X	X	X	X	X	X	X	X	X	X	X
Euchlanis spp.	X	X	X	X	X	X	X			X		X	X		X
Filinia spp.	X	X		X	X	X	X	X	X			X	X	X	X
Kellicottia spp.	X	X	X	X	X	X	X	X	X	X	X	X	X	X	X
Keratella cochlearis	X	X	X	X	X	X	X	X	X	X	X	X	X	X	X
Keratella quadrata	X	X	X	X	X	X	X	X	X	X	X	X	X	X	X
Keratella spp.	X			X						X					
Lecane spp.			X	X		X	X								
Monostyla spp.					X	X									
Nothalca laurentiae		X		X	X	X	X	X	X	X			X	X	X
Nothalca squamula		X	X	X		X	X		X			X	X	X	X
Ploesoma spp.			X	X		X	X	X	X		X	X	X	X	X
Polyarthra spp.	X	X	X	X	X	X	X	X	X	X	X	X	X	X	X
Synchaeta spp.	X					X									
Trichocerca spp.	X	X	X	X	X	X	X	X	X	X	X	X	X	X	X
Total Rotifera	**13**	**13**	**12**	**14**	**12**	**17**	**14**	**11**	**13**	**12**	**9**	**12**	**14**	**12**	**13**
Harpaticoid spp.			X			X			X		X				
Ergasilus spp.			X	X		X						X			

References

Alva-Martínez, A.F., S.S. Sarma, and S. Nandini. 2007. Effect of mixed diets (cyanobacteria and green algae) on the population growth of the cladocerans *Ceriodaphnia dubia* and *Moina macrocopa*. *Aquatic Ecology* 41: 579-585.

Bouvy, M., M. Pagano, and M. Troussellier. 2001. Effects of a cyanobacterial bloom (*Cylindrospermopsis raciborskii*) on bacteria and zooplankton communities in Ingazeria reservoir (northeast Brazil). *Aquatic Microbial Ecology* 25: 215-227.

Brett, M.T., D.C. Muller-Navarra, and S.K. Park. 2000. Empirical analysis of the effect of phosphorus limitation on algal food quality for freshwater zooplankton. *Limnology and Oceanography* 45: 1564-1575.

Brett, M.T., D.C. Muller-Navarra, A.P Ballantyne, J.L. Ravet, and C.R. Goldman. 2006. *Daphnia* fatty acid composition reflects that of their diet. *Limnology and Oceanography* 51: 2428-2437.

Brookes, J.D. and C.C. Carey. 2011. Resilience to blooms. *Science* 334: 46-47.

Burgess, S., E.W. Jackson, L. Schwarzman, N. Gezon, and J.T. Lehman. 2015. Improved estimates of calanoid copepod biomass in the St. Lawrence Great Lakes. *Journal of Great Lakes Research* 41: 484-491.

Cardinale, B.J., J.E. Duffy, A. Gonzalez, D.U. Hooper, C. Perrings, P. Venail, A. Narwani, G.M. Mace, D. Tilman, D.A. Wardle, and A.P. Kinzig. 2012. Biodiversity loss and its impact on humanity. *Nature* 486(7401): 59-67.

Carpenter, S.R., J.F. Kitchell, and J.R. Hodgson. 1985. Cascading trophic interactions and lake productivity. *BioScience* 35: 634-639.

Connell, J.H. 1978. Diversity in tropical rain forest and coral reefs. *Science* 199: 1302-1310.

DeMott, W.R. 1998. Utilization of a cyanobacterium and a phosphorus-deficient green alga as complementary resources by daphnids. *Ecology* 79: 2463-2481.

Dodds, W.K., W.W. Bouska, J.L. Eitzmann, T.J. Pilger, K.L. Pitts, A.J. Riley, J.T. Schloesser, and D.J. Thornburgh. 2009. Eutrophication of U.S. freshwaters: Analysis of potential economic damages. *Environmental Science and Technology* 43: 12-19.

Downing, J.A., S.B. Watson, and E. McCauley. 2001. Predicting cyanobacteria dominance in lakes. *Canadian Journal of Fisheries and Aquatic Sciences* 58: 1905-1908.

Facey, D.E., J.E. Marsden, T.B. Mihuc, and E.A. Howe. 2012. Lake Champlain 2010: A summary of recent research and monitoring initiatives. *Journal of Great Lakes Research* 38: 1-5.

Filstrup, C.T., H. Hillebrand, A.J. Heathcote, W.S. Harpole, and J.A. Downing. 2014. Cyanobacteria dominance influences resource use efficiency and community turnover in phytoplankton and zooplankton communities. *Ecology Letters* 17: 464-474.

Findenegg, I. 1966. Factors controlling primary productivity, especially with regard to water replenishment, stratification, and mixing. In: *Primary Productivity in Aquatic Environments*, University of California Press, Berkeley and Los Angeles, pp. 105-119.

Ger, K.A., P. Urrutia-Cordero, P.C. Frost, L.A. Hansson, O. Sarnelle, A.E. Wilson, and M. Lürling. 2016. The interaction between cyanobacteria and zooplankton in a more eutrophic world. *Harmful Algae* 54: 128-144.

Ghadouani, A., B. Pinel-Alloul, and E. Prepas. 2003. Effects of experimentally induced cyanobacterial blooms on crustacean zooplankton communities. *Freshwater Biology* 48: 363-381.

Havens, K.E., R.T. James, T.L. East, and V.H. Smith. 2003. N:P ratios, light limitation, and cyanobacterial dominance in a subtropical lake impacted by non-point source nutrient pollution. *Environmental Pollution* 122: 379-390.

Hecky, R.E. and P. Kilham. 1988. Nutrient limitation of phytoplankton in freshwater and marine environments: A review of recent evidence on the effects of enrichment. *Limnology and Oceanography* 33: 796-822.

Hillebrand, H., D.M. Bennett, and M.W. Cadotte. 2008. Consequences of dominance: A review of evenness effects on local and regional ecosystem processes. *Ecology* 89: 1510-1520.

Lampert, W. 1987. Laboratory studies on zooplankton-cyanobacteria interactions. *New Zealand Journal of Marine and Freshwater Research* 21: 483-490.

Leonard, J.A. and H.W. Paerl. 2005. Zooplankton community structure, micro-zooplankton grazing impact, and seston energy content in the St. Johns river system, Florida as influenced by the toxic cyanobacterium *Cylindrospermopsis raciborskii. Hydrobiologia* 537: 89-97.

Loreau, M., S. Naeem, P. Inchausti, J. Bengtsson, J.P. Grime, A. Hector, D.U. Hooper, M.A. Huston, D. Fafaelli, B. Schmid, and D. Tilman. 2001.

Biodiversity and ecosystem functioning: Current knowledge and future challenges. *Science* 294: 804-808.

Lundstedt, L. and M.T. Brett. 1991. Differential growth rates of three cladoceran species in response to mono- and mixed- algal cultures. *Limnology and Oceanography* 36: 159-165.

Michalak, A. 2016. Study role of climate change in extreme threats to water quality. *Nature* 535: 349-350.

Mooij, W.M., J.H. Janse, L.D.S. Domis, S. Hülsmann, and B.W. Ibelings. 2007. Predicting the effect of climate change on temperate shallow lakes with the ecosystem model PCLake. *Hydrobiologia* 584: 443-454.

Morris, E.K., T. Caruso, F. Buscot, M. Fischer, C. Hancock, T.S. Maier, T. Meiners, C. Muller, E. Obermaier, D. Prati, and S.A. Socher. 2014. Choosing and using diversity indices: Insights for ecological applications from the German Biodiversity Exploratories. *Ecology and Evolution* 18: 3514-3524.

Nixdorf, B., U. Mischke, and J. Rücker. 2003. Phytoplankton assemblages and steady state in deep and shallow eutrophic lakes—An approach to differentiate the habitat properties of Oscillatoriales. In: *Phytoplankton and Equilibrium Concept: The Ecology of Steady-State Assemblages,* Springer Netherlands, pp. 111-121.

Oksanen, J., F.G. Blanchet, M. Friendly, R. Kindt, P. Legendre, D. McGlinn, P.R. Minchin, R.B. O'Hara, G.L. Simpson, P. Solymos, M.H. Stevens, E. Szoecs, and H. Wagner. 2013. Vegan: Community ecology package, version 2.0-9. Available at: http://cran.r-project.org/package=vegan. Accessed February 10, 2017.

O'Neil, J.M., T.W. Davis, M.A. Burford, and C.J. Gobler. 2012. The rise of harmful cyanobacteria blooms: The potential roles of eutrophication and climate change. *Harmful Algae* 14: 313-334.

Paerl, H.W., R.S. Futton, P.H. Moisander, and J. Dyble. 2001. Harmful freshwater algal blooms, with an emphasis on cyanobacteria. *The Scientific World Journal* 1: 76-113.

Paerl, H.W. and J. Huisman. 2008. Blooms like it hot. *Science* 320: 57-58.

Poste, A.E., R.E. Hecky, and S.J. Guildford. 2013. Phosphorus enrichment and carbon depletion contribute to high *Microcystis* biomass and micocystin concentrations in Ugandan lakes. *Limnology and Oceanography* 58: 1075-1088.

Ptacnik, R., A.G. Solimini, T. Andersen, T. Tamminen, P. Brettum, L. Lepistö, E. Willén, and S. Rekolainen. 2008. Diversity predicts stability and resource use efficiency in natural phytoplankton communities. *Proceedings of the National Academy of Sciences* 105: 5134-5138.

R Development Core Team. 2014. R: A language and environment for statistical computing. R Foundation for Statistical computing. Vienna, Austria. Available at: www.r-project.org. Accessed February 10, 2017.

Reavie, E.D., R.P. Barbiero, L.E. Alliner, and G.J. Warren. 2014. Phytoplankton trends in the Great Lakes, 2001-2011. *Journal of Great Lakes Research* 40: 618-639.

Rhee, G.Y. and I.G. Gotham. 1980. Optimum N:P ratios and coexistence of planktonic algae. *Journal of Phycology* 16: 486-489.

Schindler, D.W. 1977. Evolution of phosphorous limitation in lakes. *Science* 195: 260-262.

Smeltzer, E., A. Shambaugh, and P. Stangel. 2012. Environmental change in Lake Champlain revealed by long-term monitoring. *Journal of Great Lakes Research* 38: 6-18.

Smith, V.H., G.D Tilman, and J.C. Nekola. 1999. Eutrophication: Impacts of excess nutrient inputs on freshwater, marine, and terrestrial ecosystems. *Environmental Pollution* 100: 179-196.

Soininen, J. and M. Luoto. 2012. Is catchment productivity a useful predictor of taxa richness in lake plankton communities? *Ecological Applications* 22: 624-633.

Striebel, M., G. Singer, H. Stibor, and T. Andersen. 2012. "Trophic overyielding": Phytoplankton diversity promotes zooplankton productivity. *Ecology* 93: 2719-2727.

Tilman, D. and P.M. Kareiva. 1997. *Spatial Ecology: The Role of Space in Population Dynamics and Interspecific Interactions.* Princeton University Press, Princeton, New Jersey.

Vermont Department of Environmental Conservation and New York State Department of Environmental Conservation. 2015. Long-term water quality and biological monitoring project for Lake Champlain: 2015 quality assurance project plan. Available at: http://dec.vermont.gov/watershed/lakes-ponds/monitor/lake-champlain. Accessed February 10, 2017.

Watson, S.B., E. McCauley, and J.A. Downing. 1997. Patterns in phytoplankton taxonomic composition across temperate lakes of differing nutrient status. *Limnology and Oceanography* 42: 487-495.

Universities Council on Water Resources
Journal of Contemporary Water Research & Education
Issue 160, Pages 119-131, April 2017

Erodibility Parameters Derived from Jet and Flume Erosion Tests on Root-Permeated Soils

Bailey McNichol[1], Kayla Kassa[2], *Garey Fox[3], Ron Miller[4], and Lucie Guertault[4]

[1]Graduate Student, Forest Resources, University of Georgia (formerly, NSF REU Student, University of Connecticut); [2]NSF REU Student, Civil Engineering, Gonzaga University; [3]Professor and Department Head, North Carolina State University; [4]Post-Doctoral Research Associate, Oklahoma State University
**Corresponding author*

Abstract: Flume tests and *in situ* jet erosion tests (JETs) allow for the process-based quantification of erodibility parameters of cohesive soils. In the excess shear stress model used to predict soil detachment, the critical shear stress (τ_c) corresponds to the stress at which fluvial forces can detach soil particles or aggregates and the erodibility coefficient (k_d) governs the rate at which detachment occurs when the imposed shear exceeds τ_c. The primary objective of this research was to derive and compare erodibility parameters from flume tests and JETs on various root-permeated soil samples. Based on statistical analysis, erodibility coefficients from the flume tests were typically statistically similar to those derived with JETs. In order to further determine the capability of the JET to indicate differences in erodibility of root-permeated soils, this research then performed JETs on side-by-side *in situ* soils. The JETs on root-permeated soils estimated significantly higher τ_c but insignificant differences in k_d compared to JETs on adjacent bare soil. A significant correlation was observed between exposed root surface area (TRSA) and τ_c, but no correlation between TRSA and k_d or the equilibrium scour depth was observed. More flume and JET experiments are needed to clarify the relationship between root-permeated soils and erodibility parameters, and address a wider range of average root diameters than was considered in this research.

Keywords: *critical shear stress, erodibility coefficient, jet erosion test, flume test, fluvial erosion, roots, streambank, vegetation*

The erosion rate of cohesive soils is often expressed using the excess shear stress equation:

$$\varepsilon_r = k_d (\tau - \tau_c)^a \qquad \text{(Equation 1)}$$

where ε_r (cm/s) is the erosion rate, k_d (cm^3/N-s) is the erodibility coefficient, τ (Pa) is the average hydraulic boundary shear stress, τ_c (Pa) is the critical shear stress, and a is an empirical exponent that is typically assumed to be unity (Partheniades 1965; Hanson 1990). The τ_c and k_d are collectively referred to as the erodibility parameters of a soil. Generally, k_d represents the capacity of a soil to erode; higher values indicate the soil is more erodible. The applied shear stress necessary to initiate erosion is represented by τ_c (Partheniades 1965).

Cohesive sediment detachment caused by fluvial erosion occurs when the τ applied by the hydraulic flow exceeds τ_c, the point at which erosion begins (Clark and Wynn 2007). Vegetation acts to lessen fluvial erosion of soil in two ways: by reducing τ imposed by hydraulic flow and increasing the resistive strength of soil (Gyssels et al. 2005; Pollen-Bankhead and Simon 2010; Burylo et al. 2012). Previous research has focused primarily on the role of above-ground biomass in reducing cohesive sediment detachment (e.g., Beeson and Doyle 1995; Hession et al. 2003). Research by Gyssels et al. (2005) reported an exponential decrease in fluvial erosion as either vegetative root mass or vegetative cover increased, suggesting both factors play an important role in reducing fluvial erosion (Figure 1). Gyssels et

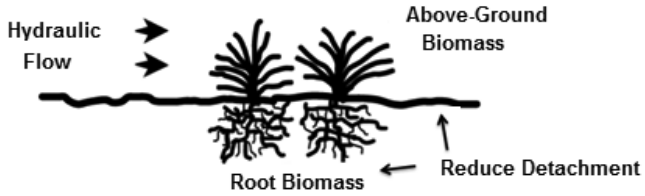

Figure 1. Vegetative cover and root networks both play a role in reducing soil detachment rates.

al. (2005) reported shallow, dense root networks characteristic of grass species as more effective than other root structure types in lessening fluvial erosion by concentrated flow. Burylo et al. (2012) argued root density alone was not sufficient in predicting the erosion-reducing effect of the root network. The vast majority of previous research investigating τ_c and k_d used an empirical approach such as simple adjustment factors of erodibility to estimate erosion in root-permeated soils. This method is limited because it fails to consider the impact of plant roots on erosion resistance and tends to underestimate τ_c (Clark and Wynn 2007).

The conventional method for deriving erodibility parameters for soils is to conduct replicated flume erosion tests in an open channel (Hanson 1990; Al-Madhhachi et al. 2013). Either disturbed and repacked or bulk samples are brought from the field, placed in the flume, and exposed to controlled flow conditions. Jet erosion tests (JETs) allow for a process-based, *in situ* determination of soil erodibility parameters (Hanson 1990; Hanson and Simon 2001). The JET impinges a stream of water through a submergence tank perpendicular to the soil surface and scours the soil, mimicking fluvial erosion caused by hydraulic flow (Hanson 1990, 1991; Hanson and Simon 2001). The depth of the resulting scour hole is recorded over gradually increasing time intervals until an equilibrium depth is reached. The applied τ is equivalent to τ_c when the scour hole reaches the equilibrium scour depth (Hanson and Simon 2001), and the time to reach the equilibrium scour depth is related to the k_d for the soil.

"Mini" JETs are smaller, more portable versions of original JETs developed by Greg Hanson in Stillwater, OK at the USDA-ARS Hydraulic Engineering Research Unit (HERU) that are more suitable for *in situ* determination of erodibility parameters. Research performed by Al-Madhhachi et al. (2013) examined erodibility parameters derived from the original and mini JET devices and reported comparable results. Using JETs specifically on root-permeated soils, Pollen-Bankhead and Simon (2010) showed that for root-permeated soils the volume of scour decreased non-linearly with an increase in root volume, root length density, and root biomass.

Research is still needed to evaluate techniques for measuring erodibility parameters of root-permeated soils and investigating the interrelation between root properties and erodibility parameters derived from JETs. In addition, a need exists to determine if JETs provide equivalent erodibility parameters as compared to the more conventional flume tests. Consequently, this study derived and compared erodibility parameters from flume tests and JETs on various root-permeated soils. It was hypothesized that flume tests performed on root-permeated soils would provide statistically similar erodibility parameters to JETs performed in similar soils. Next, side-by-side *in situ* JETs were performed on bare soils and soils near grasses with shallow, dense grass root networks. The volume of scour and rate of erosion was examined relative to measured root characteristics to determine which, if any, had an effect in reducing soil erodibility. It was hypothesized that JETs performed on soils with greater root surface area would have a shallower equilibrium scour depth, a higher τ_c, and a lower k_d than JETs in similar soils without roots.

Materials and Methods

Laboratory Flume Tests versus JETs

Ten side-by-side flume tests and JETs were conducted on root-permeated soils of two grass types: Fescue grass (*Festuca arundinacea*) and Bermuda grass (*Cynodon dactylon*). Therefore, a total of 20 erodibility tests were conducted for this part of the research. Root-permeated soil samples (25 cm wide by 25 cm long by 10 cm deep samples) were acquired from the USDA-ARS HERU grounds. Care was taken to avoid disturbance of the sample as much as possible. Adjacent samples were used for paired flume tests and JETs in an attempt to achieve similar root and soil properties between the two types of tests.

Open-channel erosion tests were conducted in a flume at the USDA-ARS HERU in Stillwater, Oklahoma. The flume consisted of the following parts: water delivery pipe, upstream water reservoir, flume channel, and a soil box. The water delivery pipe, 30.5 cm in diameter, delivered the required discharge from Lake Carl Blackwell to the water reservoir. Initial control of water supply was established in the delivery pipe with an orifice plate, a device used for measuring flow rate, reducing pressure, or restricting flow. The water reservoir was 1.2 m long, 1.2 m wide, and 1.4 m deep and provided inflow to the flume. A manometer and corresponding chart in the lab established the water height in the reservoir and flow rate for each test. The flume channel was 9 m long by 0.6 m wide and 0.6 m deep. A soil box 0.25 m long, 0.25 m wide, and 0.1 m deep was located at the center of the flume (Figure 2), and root-permeated soil samples were placed into the soil box (Figure 3).

Flows ranging from 0.056 m^3/s to 0.142 m^3/s were used to erode the soil samples. The minimum flow rate was based on trial experiments to determine when the flow rate was sufficient to initiate scour. The applied shear stress across the surface of the soil for the various flow rates was calculated following Hanson (1990) and Al-Madhhachi et al. (2014). In order to prevent excess scour caused by the introduced flow, a 25 cm by 25 cm metal square was placed on the soil surface before the initial flow began. Once a constant flow

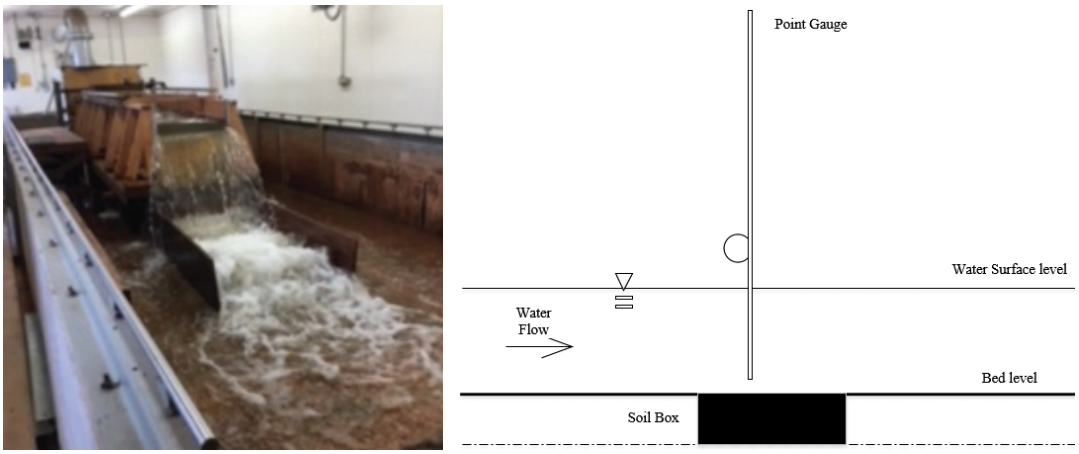

Figure 2. View of flume apparatus from below the outlet (left), and cross sectional drawing of flume apparatus at the soil box showing attached point gauge and soil sample for testing (right).

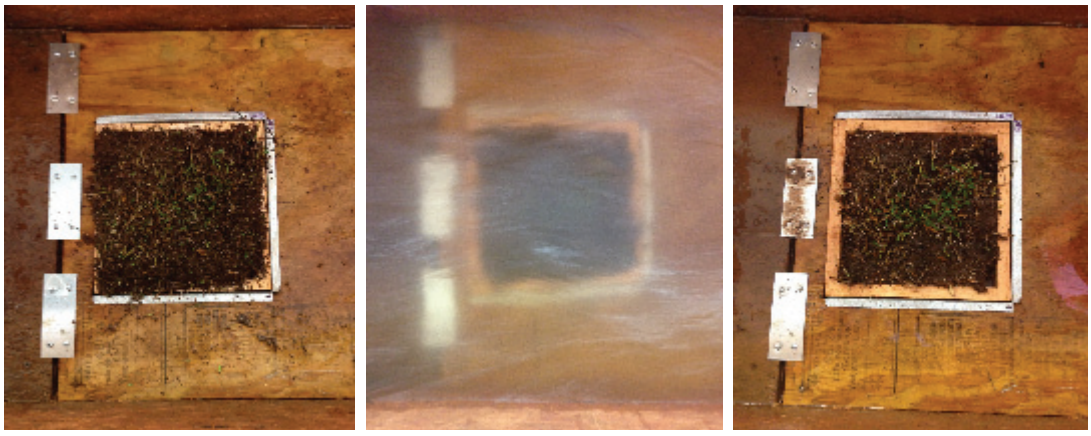

Figure 3. Soil samples positioned in the flume soil box before (left), during (middle), and after (right) hydraulic testing.

was reached, the metal square was released from the soil sample and the timer was started. The elevations of 25 points within the soil sample were measured with a point gauge before and after the test to calculate the volume of eroded soil for each flume test. In addition, during each flume test, nine points were measured around the center of the soil sample every 15 minutes for a total of 90 minutes. The water and bed surface levels were measured throughout each test.

The mini JET apparatus (Figure 4) consisted of a point gauge, rotatable plate, submergence tank, foundation ring, and jet valve. An adjustable constant head tank was used to provide the desired water head (89 cm) for the duration of the JET. The 180 mm diameter foundation ring was hammered into the surface of each soil sample. The submergence tank was positioned below the rotatable plate and point gauge, and measured 70 mm high and 101.6 mm in diameter, with a 6.4 mm wall thickness. The release of the 3.18 mm jet of water was controlled by the rotation of the brass plate, allowing scour to occur over a given time interval and preventing water from impinging on the soil at the beginning of testing and during scour depth readings (Al-Madhhachi et al. 2013). Measurements of the depth of the scour hole created by the JET were taken using a point gage and time intervals of scour were increased until the depth reading was constant, or the equilibrium scour depth was reached (Hanson 1990, 1991). The initial scour time interval for both the root-permeated and bare soil JETs began at 15 s and continued until three constant depth readings were taken. Following the standard protocol for JETs (Khanal et al. 2016), the time interval between measurements was increased to 30 s, followed by 60 s, 120 s, and 300 s, if necessary, until an equilibrium scour depth was reached and the test concluded.

The JET data were used to determine k_d and τ_c using the spreadsheet tool described by Daly et al. (2013). The JET spreadsheet tool solves for and compares variability in erodibility parameters using the Blaisdell solution, the scour depth method (Daly et al. 2013), and the iterative method (Simon et al. 2010). The Blaisdell solution remains the current standard for analyzing JET data and therefore was used as the solution technique in this research.

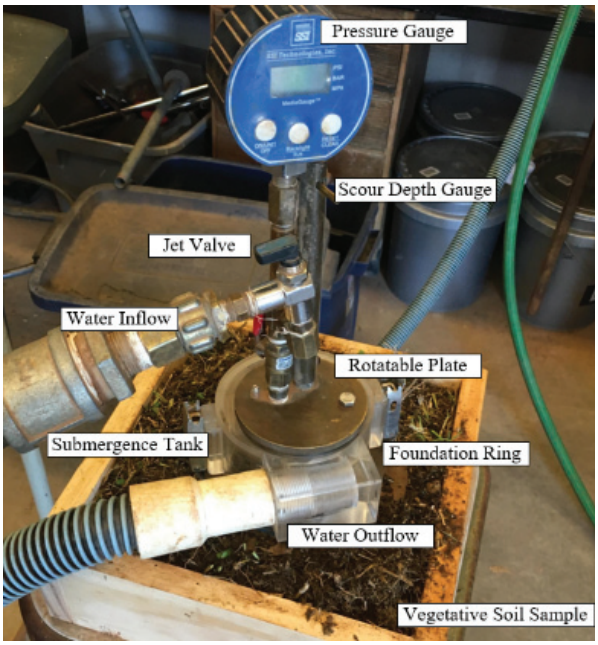

Figure 4. Mini Jet Erosion Test (JET) device installed in soil sample with important instrument components labeled. The pressure gauge shown was not utilized in the experiments.

For each of the ten paired samples, a sample 5 cm in diameter by 5 cm long was acquired to quantify bulk density, moisture content, and root characteristics. Each sample was weighed before and after 24 hours in an oven set at 105°C to obtain the bulk density and moisture content. Each sample was rinsed until only roots were present and then scanned using WinRHIZO analysis software (Regent's Instruments, Canada) (Clark and Wynn 2007). WinRHIZO scans roots lying flat in a tray of water to determine the total exposed surface area and range of root diameters.

Field Experiments: Bare versus Root-Permeated Soils

Field mini JETs were performed along Cow Creek at the Stream Restoration and Streambank Stabilization Site in Stillwater, OK. The restored reach of Cow Creek is a meander bend east of the Oklahoma State University (OSU) Botanic Garden, bounded to the north by West Virginia Avenue and to the south by Highway 51 (Lovern et al. 2013). The initial restoration activities were performed in 2011, and included the creation of a 1:1 slope stabilization research area on the

meander. Further mitigation activities in 2012 and 2013 included the establishment of a wider riparian buffer, the implementation of J-hooks, cross-vanes, and riffles, and the construction of a floodplain overflow channel and backwater constructed wetland. The research site for the JETs was on the bench of the restored meander, located between the 1:1 stabilized slope and a 2:1 vegetated slope just above the edge of Cow Creek. Lovern et al. (2013) reported the soil types located on the filled streambank of the meander as primarily loams, clay loams, and sandy clay loams. The research site was compacted during project construction and reinforced with erosion matting, with the final step being revegetation with grass seeds and native plants (Lovern et al. 2013). Three riparian grasses with relatively shallow root networks, Little bluestem (*Schizachyrium scoparium*), Bermuda grass (*Cynodon dactylon*), and Switch grass (*Panicum virgatum*), were identified on the Cow Creek meander bench. Ten sites supporting these grasses, separated from other vegetation types and next to bare, unvegetated soil, were marked with survey flags. These areas were selected to conduct 10 pairs of side-by-side JETs (20 tests total) on root-permeated and bare soils to compare erodibility parameters between the tests while holding soil type, bulk density, moisture content, and pH as constant as possible under field conditions (Figure 5).

A 5 cm diameter by 5 cm long soil sample adjacent to the JET location was collected before running the test for measurement of bulk density, and grab samples were acquired for analysis of soil texture and pH. A constant head tank was set up with the surface approximately 61 cm above the outflow of the JET device to maintain constant water pressure for the duration of the JET. Water from the OSU Botanic Garden irrigation system was directed through a garden hose to the head tank (Figure 5). The foundation ring of the JET was hammered into the soil and secured with two nails, and the JET device was attached to the base and fastened into place with two clips. For the JETs on root-permeated soil, the foundation ring was placed with the plant stems off center to ensure the impinging jet would contact soil and roots rather than stem. Grass stems were cut to approximately 1 cm above the soil surface before the test following the method of Pollen-Bankhead and Simon (2010). Outflow hoses were attached to both the head tank and the JET and directed downslope to avoid saturating the soil surrounding the JET.

The operation of the JET matched the procedures previously described. Unique to this part of the study, after each JET, the device was then disconnected from the foundation ring and residual water was allowed to runoff and infiltrate until the scour hole was empty. Water was poured into the hole from a graduated cylinder and the



Figure 5. Field JET site with side-by-side root-permeated and bare soils (left), mini JET device installed on streambank (middle), and constant head tank connected to the JET device (right).

amount recorded to obtain an approximate volume measurement of the scour hole. The foundation ring was removed and a soil corer was placed around the scour hole and hammered into the ground to collect two 91-cm^3 samples, each 5 cm in depth, of exposed roots for analysis. Roots located in the top 5 cm were referred to as the upper roots in the soil profile, and roots in the bottom 5 cm were referred to as the lower roots. Analysis of the data focused on correlations between JET variables and the upper roots due to their greater apparent influence on the results of the tests.

As noted earlier, JET data were used to derive k_d and τ_c using the spreadsheet tool described by Daly et al. (2013) with the Blaisdell solution. If the scour depth was greater than 15 mm in the first two 15 s time intervals, the data were removed from the analysis assuming that the scour depth measurements were for loosened soil created during the insertion of the foundation ring for these *in situ* soils. These first measurements typically represented only one or two of 20 to 25 total data points acquired during each of the JETs.

The root surface area and diameters were analyzed using WinRHIZO as described previously. Grab soil samples were taken to analyze the particular soil texture at each JET site. The samples were left to air dry and particle sizes were analyzed using sieves and a hydrometer following the current ASTM standards (ASTM 2002). Soil pH was measured by adding 5 g of soil from each grab sample to 15 mL of deionized (DI) water in a vial to maintain a 1:3 soil to water ratio. Samples were shaken for 1 minute to wet all soil particles and left for 20 minutes to equilibrate, then shaken for another minute. After the second equilibration period, a calibrated pH probe was placed in the mixture and upon stabilization, a reading was taken to the nearest hundredth value. The pH probe was rinsed thoroughly with DI water between each pH measurement (Smith and Doran 1996).

Statistical Analyses

Experimental data were analyzed statistically to determine the difference between paired variables. For normally distributed variables, paired t-tests were performed to determine statistical differences in means; for non-normally distributed data, a Mann Whitney Rank sum test was used to determine statistical differences in the medians. Soil, root, flume, and JET data were analyzed statistically to determine correlations between variables. Pearson product moment correlations were also performed to determine statistically significant correlations between the soil parameters, root characteristics, and erodibility parameters. All statistical tests were based on a significance level of $\alpha = 0.05$ and used SigmaPlot 13 (Systat Software, Inc., Germany).

Results and Discussion

Laboratory Flume Tests versus JETs

Comparison of images generated with WinRHIZO software indicated that samples with Fescue grass (#1 through #5) generally had smaller root surface areas (P = 0.010) and greater diameters (although not statistically different, P = 0.473) compared to samples with Bermuda grass (#6 through #10) (Table 1). It was concluded that Bermuda grass samples had denser, more fibrous root networks than the Fescue grass samples. Although the root characteristics varied between both grass types, the soil bulk densities and moisture contents for the samples were similar. Therefore, this result shows that the desired study design of varying primarily the root characteristics was achieved.

Flume data resulted in k_d values ranging from 0.1 to 6.6 cm^3/N-s and τ_c values ranging from 0.1 to 4.8 Pa. Analysis of the JET data resulted in k_d values ranging from 0.8 to 4.3 cm^3/N-s and τ_c values ranging from 0.7 to 6.4 Pa (Figure 6). An inverse relationship was observed between τ_c and k_d derived from the flume tests and JETs as reported in previous literature (Hanson and Simon 2001; Al-Madhhachi et al. 2013; Daly et al. 2013). In general, there was greater scour observed in the Fescue grass samples than for the Bermuda samples in both flumes and JETs. The denser, more fibrous root networks in the Bermuda samples, especially in the upper layers of the soil, limited detachment or scour. Such results could be useful when considering types of grasses or cover crops for erosion control, specifically when considering the influence of roots on detachment.

No significant differences were observed in the τ_c and k_d values when comparing Fescue grass samples to the Bermuda grass samples for the side-

Table 1. Soil and root characteristics from WinRHIZO analysis software for a representative sample of the soil samples used in flume tests and JETs.

Sample #	Vegetation Type	Soil Bulk Density (g/cm^3)	Soil Moisture Content (%)	Root Surface Area (cm^2)	Average Root Diameter (mm)	Root Length Per Volume (cm/m^3)	Root Volume (cm^3)
1	Fescue	1.7	24.7	300.3	1.7	5.45×10^6	12.8
2	Fescue	1.3	20.6	344.1	2.0	5.40×10^6	17.0
3	Fescue	1.5	24.4	226.2	2.5	2.75×10^6	14.4
4	Fescue	1.3	32.9	337.6	1.9	5.51×10^6	16.0
5	Fescue	1.3	32.1	401.1	2.4	5.12×10^6	24.3
6	Bermuda	1.1	15.9	464.7	2.6	5.43×10^6	30.7
7	Bermuda	1.0	21.9	455.5	1.8	7.98×10^6	20.1
8	Bermuda	1.2	20.1	343.6	1.6	6.53×10^6	14.0
9	Bermuda	1.0	29.6	467.0	1.6	8.93×10^6	18.9
10	Bermuda	1.3	32.1	423.9	1.5	8.47×10^6	16.4

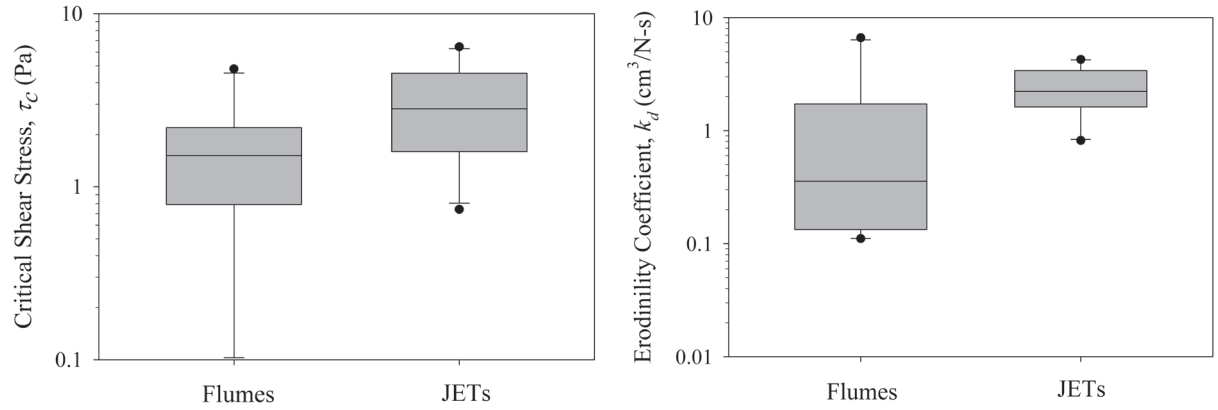

Figure 6. Box plots comparing the distribution of critical shear stress (τ_c) and the erodibility coefficient (k_d) derived from the flume tests and JETs. The mean is indicated by the solid line within the box.

by-side flume tests and JETs (Table 2). Significant differences were observed in τ_c when comparing the flume tests to the JETs across both grass types (Table 3), but not for the Fescue samples alone (Table 3). No significant differences were observed in k_d when comparing the JETs to the flume for either vegetation type or when considering both grass types together. Al-Madhhachi et al. (2013) reported no significant differences in both k_d and τ_c between the flume and JETs for bare soil samples when analyzed with the Blaisdell solution after applying a correction factor to account for differences in the equilibrium scour hole depth. No correction factor was applied in this study. Therefore, this research provides further support for the use of the JET as an appropriate tool for *in situ* and/or laboratory erodibility characterization.

While the majority of the side-by-side flume test and JET comparisons reported no statistically significant differences in the derived erodibility parameters, it should still be pointed out that differences exist in the operation of the flume tests and JETs; for example, the direction of the hydraulic flow between the flume and JETs differed.

Table 2. Results of statistical analysis of flume tests versus jet erosion test (JET) erodibility parameters for Bermuda and Fescue grass samples. For all tests $\alpha = 0.05$.

Comparisons	P-Value	Significant
τ_c *Flume Fescue* vs. τ_c *Flume Bermuda*	0.166	No
τ_c *JET Fescue* vs. τ_c *JET Bermuda*	0.056	No
k_d *Flume Fescue* vs. k_d *Flume Bermuda*	0.625	No
k_d *JET Fescue* vs k_d *JET Bermuda*	0.679	No

Table 3. Results of statistical analysis of flume tests versus jet erosion test (JET) erodibility parameters. For all tests $\alpha = 0.05$.

Comparisons	Vegetation Type	P-Value	Significant
* $\tau_{c\,JET}$ vs. $\tau_{c\,Flume}$	Both	0.031	Yes
τ_{cJET} vs. $\tau_{c\,Flume}$	Fescue	0.340	No
$\tau_{c\,JET}$ vs. $\tau_{c\,Flume}$	Bermuda	0.066	Yes
$k_{d\,JET}$ vs. $k_{d\,Flume}$	Both	0.156	No
$k_{d\,JET}$ vs. $k_{d\,Flume}$	Fescue	0.444	No
$k_{d\,JET}$ vs. $k_{d\,Flume}$	Bermuda	0.204	No

* significantly different at P-value < 0.05.

In a flume test, the shear was applied horizontally across the entire surface of the soil sample whereas during a JET the applied stress was vertical at one scour hole location. Also, while running a JET, it was more likely for the impinged water to hit a distinctively large root or conglomeration of roots exposed in the scour hole, limiting erosion during the test and skewing results. Increasing the number of tests could help reduce the skew from those tests.

Field Experiments: Bare versus Root-Permeated Soils

A total of ten side-by-side (20 total) JETs were performed on the restored meander bench at Cow Creek: ten on root-permeated soil and ten on bare soil. Of the root-permeated trials, six were on little bluestem root networks, three were on Bermuda grass, and one was on switch grass. Legacy roots from surrounding vegetation were observed during analysis in all of the bare soil samples taken from around the scour hole, primarily in the lower root samples. Additionally, pieces of erosion matting placed during the meander restoration were discovered in several of the lower root cores and influenced scour depths when the JET scoured greater than 40 mm. Both of these factors may have had an effect on the equilibrium scour depth of JETs. With that said, a significant correlation was observed between the scour hole volume and equilibrium scour depth (Figure 7).

The k_d values of both bare and root-permeated soil samples ranged over one order of magnitude (3.1 to 23.7 cm^3/N-s, Figure 8), and τ_c values ranged over two orders of magnitude (0.01 to 1.60 Pa, Figure 8). As predicted by the hypothesis, most JETs on root-permeated soils exhibited a lower erosion rate relative to the applied τ as compared to the bare soil. The τ_c value was typically higher for the root-permeated tests (Figure 8), suggesting the greater surface area of the upper roots may relate to the overall higher range of τ_c values. The k_d values did not vary significantly between the root-permeated and bare soil JETs, which does not support the hypothesis that greater root surface area would correlate with a lower k_d (Figure 8). Again,

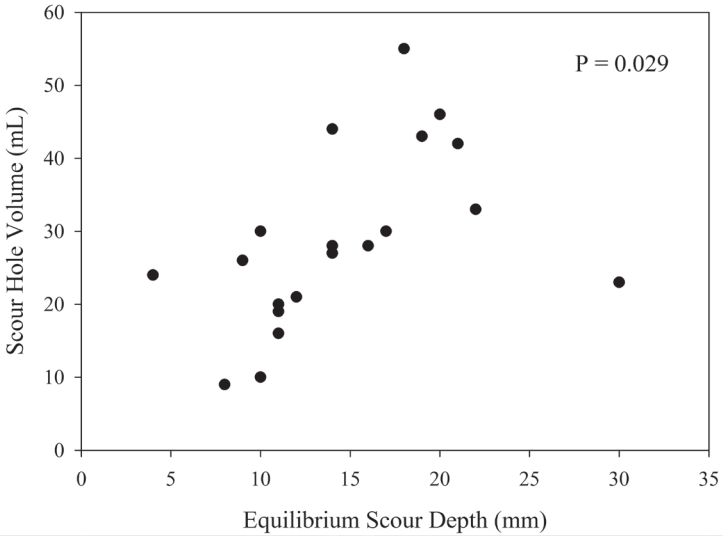

Figure 7. Relationship between equilibrium scour depth and approximated scour hole volume for all field tests, with correlation coefficient.

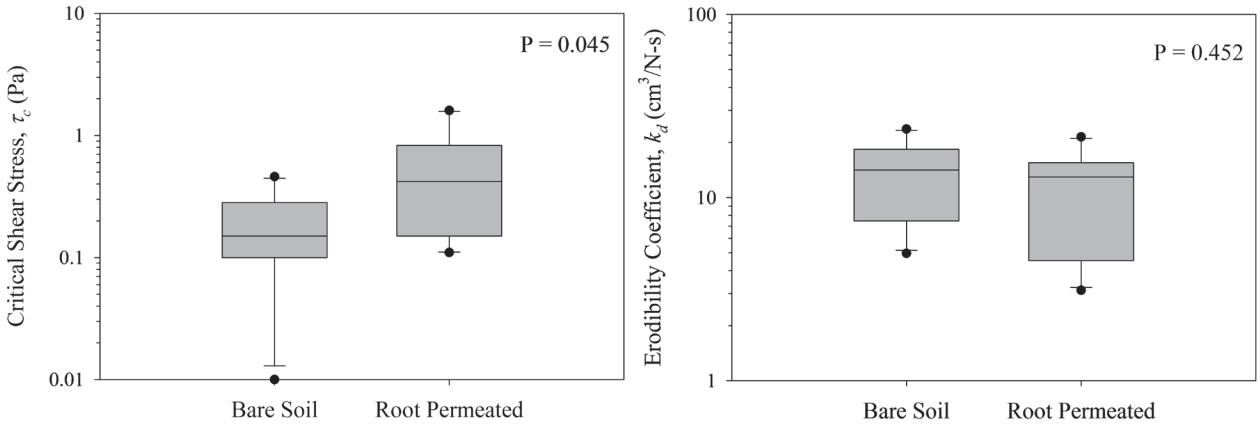

Figure 8. Distribution of critical shear stress, τ_c (Pa) and erodibility coefficient, k_d (cm^3/N-s) between JETs from field tests on bare and root-permeated soil. Shown also is the p-value for a t-test of the difference of means.

such results have implications for considering types of grasses or cover crops for erosion control, specifically when considering the influence of roots on the initiation of detachment. Interestingly, there was as much variability in the flumes and JETs under controlled conditions (Figure 6) as observed in the side-by-side JETs in the field (Figure 8). Typically, much greater variability is reported under field as compared to laboratory or flume conditions.

The Pearson product moment was used to determine correlation coefficients between τ_c, k_d, and the other measured JET, soil, and root variables (Figure 9). There was a statistically significant inverse correlation between τ_c and the equilibrium scour depth and scour hole volume, and a positive correlation with the upper root surface area. The k_d was significantly correlated to the equilibrium scour depth and the scour hole volume, and inversely correlated to the volumetric moisture content.

Sieve and hydrometer tests for soil texture analysis determined all soils were sandy clay loams. Previous research suggested a correlation

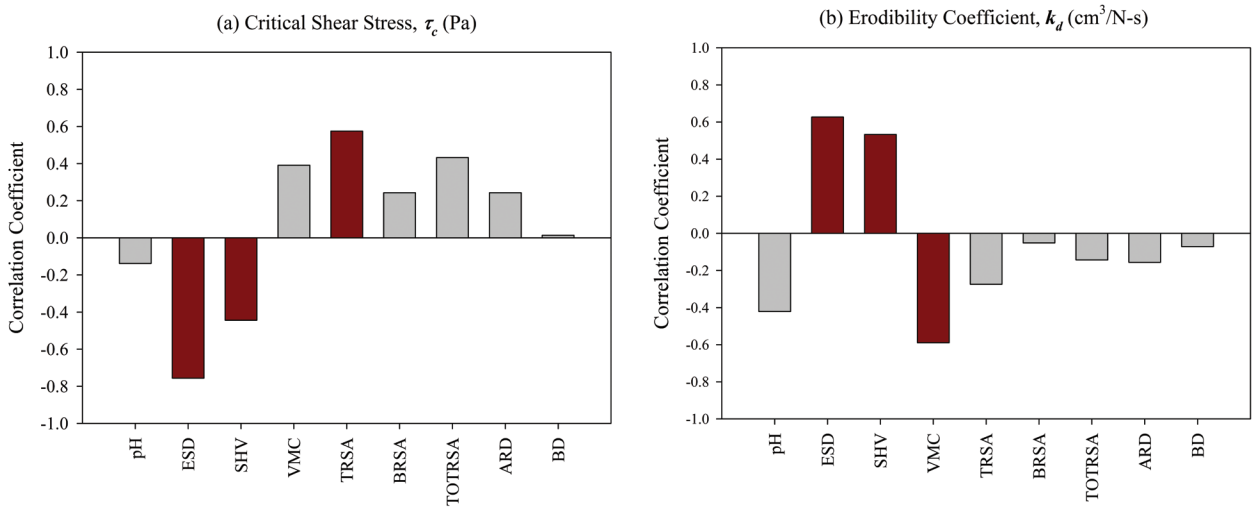

Figure 9. Correlation coefficients for relationships between (a) critical shear stress and (b) erodibility coefficient with other test, soil, and root variables. Significant correlations ($\alpha < 0.05$) are highlighted in red. ESD = equilibrium scour depth, SHV = scour hole volume, VMC = volumetric moisture content, TRSA = upper root surface area, BRSA = lower root surface area, TOTRSA = total root surface area, ARD = average root diameter, BD = soil bulk density.

between the silt-clay content of a soil and τ_c (Julian and Torres 2006), but the data from this research do not show a significant relationship (P = 0.490). The silt-clay content data were used as input into an empirical equation proposed by Julian and Torres (2006) to estimate τ_c for both bare soil and root-permeated soil, and the resulting empirically-estimated τ_c values were more than one order of magnitude higher than the JET-derived τ_c values, supporting the need for process-based determination of erodibility parameters using *in situ* JETs. This research further supports previous findings that erodibility coefficients for cohesive soils are difficult to estimate and empirical relationships should be used with caution.

A significant inverse correlation (P = 0.006) was observed in the data between k_d and the volumetric moisture content (Figure 10). The higher the moisture content, the lower the erodibility of the soil until a threshold at which the soil becomes saturated and erodibility increases. At the same time, increased moisture content helps promote plant growth and hence greater root development over the long term. This is similar to results from a study by Wynn et al. (2008) which showed k_d varied monthly and seasonally due to changes in moisture content. Their results suggest lower soil moisture content was correlated to higher k_d, but it was unclear what direct effect moisture content had on the k_d, if any. Similarly, Ziadat et al. (2010), in a study that measured changes in soil properties along arid hillslopes, observed that increased moisture content and reduced soil erodibility were associated with increased soil clay content. The data from the JETs on the meander bench similarly showed a significant correlation between clay content and volumetric moisture content (P = 0.014). There was also a strong relationship in the data between k_d and the clay content of the soil (P = 0.002).

The presence of "legacy roots" was noted in the bare soil cores. The total exposed root surface area for the bare soil JETs ranged from 5.3 to 80.3 cm^2 and from 25.7 to 284.3 cm^2 for the root-permeated JETs. The average root diameter for the 20 JETs ranged from 0.4 to 0.7 mm. As expected, there was a strong relationship in the data between the total root surface area and average root diameter for the root-permeated soils (P < 0.001). A significant positive correlation was also observed between τ_c and the surface area of the upper roots (TSRA) (Figure 10), although considerable variability was present in the data. This result supports the hypothesis that a greater exposed root surface area will result in a higher τ_c, suggesting that dense, shallow roots allow soils to resist higher detachment forces before the initiation of scour. Lower root surface area was not significantly correlated to τ_c (P = 0.316), which

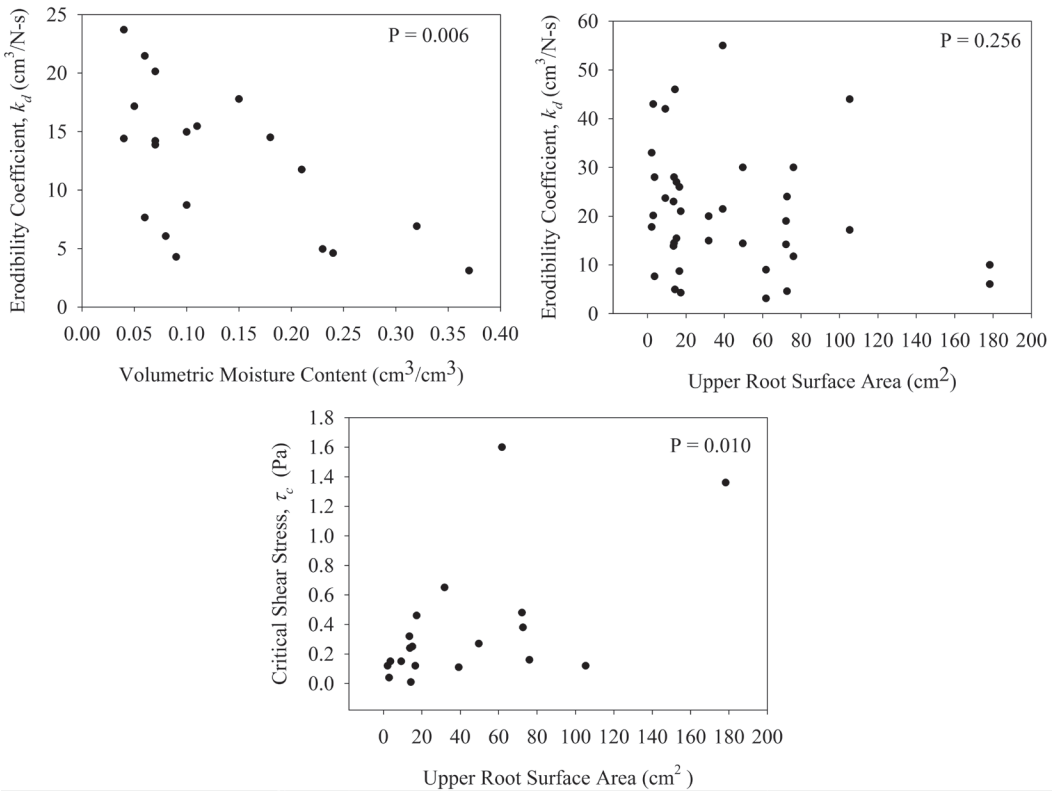

Figure 10. Relationships and associated correlation coefficients between several soil, root, and erodibility parameters from the *in situ* field tests.

was not surprising given that the JET scour depth did not reach to the lower soil depth (Figure 7). There was no significant relationship between the upper root surface area and k_d (Figure 10), which did not support the hypothesis that greater exposed root surface area will be correlated with a lower k_d. This implies that once soil begins to detach, roots have no further influence. The subsequent increase in moisture content in the soil once detachment begins could lead to similar erosion rates after the initiation of detachment.

Summary and Conclusions

This research hypothesized that conventional flume tests on root-permeated soils should result in similar derived erodibility parameters to JETs. The flume tests and the JETs typically provided statistically similar erodibility parameters. The τ_c value was typically lower in Fescue grass compared to Bermuda grass samples, suggesting the greater root surface area of the latter may result in higher τ_c values. We then hypothesized that if *in situ* JETs performed on riparian grass species with shallow root systems have a greater exposed root surface area around the scour hole, then the surrounding soil will have a shallower equilibrium scour depth, a higher τ_c, and a lower k_d. Results from root-permeated soils indicated that near-surface roots had the most significant effect on the erodibility parameters. Upper root surface area was more strongly correlated with these variables than total (combined upper and lower) or lower root surface area. A significant difference was observed in τ_c between root-permeated soil and bare soil. The JETs on root-permeated soils resulted in a higher τ_c range (0.11-1.60 Pa) than bare soil (0.01-0.46 Pa), indicating erosion was initiated at a higher τ_c in root-permeated soils where there was a greater exposed surface area of upper roots. Based on these results, the impact of roots was noticeable in influencing the τ_c. Additional paired bare soil versus root-permeated soil flume tests and JETs would be beneficial on soils with a wider range of average root diameters to expand the analyses beyond the specific conditions of this study.

Acknowledgments

The authors acknowledge the financial support provided by the National Science Foundation through award number EAR1358908 titled "REU Site: Evaluating the Effectiveness of Stream Restoration Projects Based on Natural Channel Design Concepts Using Process-Based Investigations". The authors also acknowledge the USDA-ARS Hydraulic Engineering Research Unit (HERU) led by Dr. Sherry Hunt for access to the flume. The authors thank Dr. Anish Khanal, Dr. Abdul-Sahib Al-Madhhachi, Holly Enlow, Whitney Lisenbee, and Joanna Quiah for their assistance with the research.

Author Bio and Contact Information

Bailey McNichol is currently a graduate student at the University of Georgia in Forest Resources. Bailey received her undergraduate degree in December 2015 from the University of Connecticut. She participated in a National Science Foundation (NSF) Research Experience for Undergraduates (REU) in the summer of 2015 conducting research on JETs. She can be contacted at bailey.mcnichol@gmail.com.

Kayla Kassa is currently an undergraduate student at Gonzaga University in Civil Engineering. Kayla participated in the same NSF REU program as above in the summer of 2016 conducting flume tests and JETs. She can be contacted at kkassa@zagmail.gonzaga.edu.

Dr. Garey Fox is currently a Professor and Department Head in the Department of Biological and Agricultural Engineering at North Carolina State University. He served as the PI of an NSF REU project on stream restoration and rehabilitation from 2016-2017 (EAR1358908). He can be contacted at garey_fox@ncsu.edu.

Dr. Ron Miller is currently a Post-Doctoral Research Associate in Biosystems and Agricultural Engineering at Oklahoma State University. He completed his Ph.D. in Environmental Science from Oklahoma State University. He is working on modeling coupled human-natural system responses to climate change, development, and water export scenarios in a sparsely populated forested watershed in Oklahoma. He can be contacted at ron.miller@okstate.edu.

Dr. Lucie Guertault is currently a Post-Doctoral Research Associate in Biosystems and Agricultural Engineering at Oklahoma State University. She completed her Ph.D. in Fluid Mechanics from Claude Bernard University in Lyon, France. She is working on reservoir sedimentation, performing field surveys as well as numerical modeling. She can be contacted at lucie.guertault@okstate.edu.

References

Al-Madhhachi, A.T., G.J. Hanson, and G.A. Fox. 2013. Measuring soil erodibility using laboratory "mini" JETs. *Transactions of the ASABE* 56(3): 901-910.

Al-Madhhachi, A.T., G.A. Fox, G.J. Hanson, A.K. Tyagi, and R. Bulut. 2014. Mechanistic detachment rate model to predict soil erodibility due to fluvial and seepage forces. *Journal of Hydraulic Engineering* 140(5). doi:10.1061/(ASCE)HY.1943-7900.0000836. Accessed January 25, 2017.

ASTM. 2002. Standard test method for particle-size analysis of soils. *Standard D422-63, ASTM International* 1-8.

Beeson, C.E. and P.F. Doyle. 1995. Comparison of bank erosion at vegetated and non-vegetated channel bends. *Water Resources Bulletin* 31(6): 983-990.

Burylo, M., F. Rey, N. Mathys, and T. Dutoit. 2012. Plant root traits affecting the resistance of soils to concentrated flow erosion. *Earth Surface Processes and Landforms* 37(14): 1463-1470.

Clark, L.A. and T.M. Wynn. 2007. Methods for determining streambank critical shear stress and soil erodibility: Implications for erosion rate predictions. *Transactions of the ASABE* 50(1): 95-106.

Daly, E.R., G.A. Fox, and R.B. Miller. 2013. A scour depth approach for deriving erodibility parameters from Jet Erosion Tests. *Transactions of the ASABE* 56(6): 1343-1351.

Gyssels, G., J. Poesen, E. Bochet, and Y. Li. 2005. Impact of plant roots on the resistance of soils to erosion by water: A review. *Progress in Physical Geography* 29(2): 189-217.

Hanson, G.J. 1990. Surface erodibility of earthen channels at high stresses part II – Developing an *in situ* testing device. *Transactions of the ASAE* 33(1): 132-137.

Hanson, G.J. 1991. Development of a jet index to characterize erosion resistance of soils in earthen spillways. *Transactions of the ASAE* 34(5): 2015-2020.

Hanson, G.J. and A. Simon. 2001. Erodibility of cohesive streambeds in the loess area of the Midwestern USA. *Hydrological Processes* 15(1): 23-38.

Hession, W.C., J.E. Pizzuto, T.E. Johnson, and R.J. Horwitz. 2003. Influence of bank vegetation on channel morphology in rural and urban watersheds. *Geology* 31(2): 147-150.

Julian, J.P. and R. Torres. 2006. Hydraulic erosion of cohesive riverbanks. *Geomorphology* 76: 193-206.

Khanal, A., G.A. Fox, and A.T. Al-Madhhachi. 2016. Variability of erodibility parameters from laboratory mini jet erosion tests. *Journal of Hydrologic Engineering* 21(10): 04016030. doi: 10.1061/(ASCE)HE.1943-5584.0001404. Accessed January 25, 2017.

Lovern, S.B., G.A. Fox, and R.B. Miller. 2013. Quantifying the erodibility and geotechnical strength of cohesive alluvial soils following streambank reconstruction. *Proceedings ASCE Environmental Water Resources Institute Annual Meeting*, pp. 1-10.

Partheniades, E. 1965. Erosion and deposition of cohesive soils. *Journal of the Hydraulics Division American Society of Civil Engineering* 91: 105-139.

Pollen-Bankhead, N. and A. Simon. 2010. Hydrologic and hydraulic effects of riparian root networks on streambank stability: Is mechanical root-reinforcement the whole story? *Geomorphology* 116(3-4): 353-362.

Simon, A., R.E. Thomas, and L. Klimetz. 2010. Comparison and experiences with field techniques to measure critical shear stress and erodibility of cohesive deposits. In: 2nd Joint Federal Interagency Conference, Las Vegas, NV.

Smith, J.L. and J.W. Doran. 1996. Measurement and use of pH and electrical conductivity for soil quality analysis. In: *Methods for Assessing Soil Quality*, J.W. Doran and A.J. Jones (Eds.). Soil Science Society of America, Madison, WI, pp. 169-185.

Wynn, T.M., M.B. Henderson, and D.H. Vaughan. 2008. Changes in streambank erodibility and critical shear stress due to subaerial processes along a headwater stream, southwestern Virginia, USA. *Geomorphology* 97(1-4): 260-273.

Ziadat, F.M., A.Y. Taimeh, and B.I. Hattar. 2010. Variation of soil physical properties and moisture content along toposequences in the arid to semiarid area. *Arid Land Research and Management* 24(2): 81-97.

Universities Council on Water Resources
Journal of Contemporary Water Research & Education
Issue 160, Pages 132-143, April 2017

2D-Fe_3O_4 Nanosheets for Effective Arsenic Removal

Hongxi Luo[1], Fangwei Cheng[1], Weiming Hu[2], Jinpeng Wang[1], Shuting Xiang[1], and *Maria Fidalgo de Cortalezzi[2]

[1]*Department of Chemical Engineering, University of Missouri, Columbia, MO, USA*
[2]*Department of Civil & Environmental Engineering, University of Missouri, Columbia, MO, USA*
**Corresponding author*

Abstract: Fe_3O_4 adsorbent with 2D structures was synthesized via solvothermal method and its application in arsenic removal was investigated. Isotherms were generated at pH=4.7 and 7.6 and the results were best fitted by the Freundlich isotherm model; good As(V) adsorption capacity was achieved for the Fe_3O_4 adsorbent at both pH values. Furthermore, pH effects were evaluated; the optimal pH value for adsorption was 8.27 with the adsorption capacity and the removal efficiency being 18.55 mg/g and 93.69%, respectively. Based on the measurements of the zeta potential and particle size of the adsorbent, we proposed that the overall pH dependence was a result of the combined effects of the zeta potential, particle size of the adsorbent, and existing form of As(V). From kinetics studies, the As(V) adsorption by Fe_3O_4 adsorbent followed the pseudo-second-order model and could be described by a two stage mechanism. When initial As(V) concentration was 1 ppm, 73% of the As(V) was adsorbed within the first 2.5 minutes and an overall removal efficiency of 82.5% was achieved in 2 hours. Increased removal efficiency is expected at higher adsorbent loading, thus allowing the post-treatment water to meet drinking water quality standards.

Keywords: *adsorption, Fe_3O_4 adsorbent, arsenic removal, 2D structure, water treatment*

Arsenic, a toxic element commonly found in waters and soils, has become a huge threat to public health in the recent years (Hughes 2002; Smedley and Kinniburgh 2002). Both organic and inorganic forms of arsenic exist in the environment, while the latter is of higher toxicity and frequently found in groundwater (Styblo et al. 2000; Mandal and Suzuki 2002). Inorganic arsenic typically has two oxidation states, As(III) and As(V), and its presence in groundwater is a severe environmental problem (Hughes 2002; Mandal and Suzuki 2002; Hung et al. 2004). It is believed that long term exposure to arsenic contaminated water increases the risk of skin, lung, kidney, and liver cancer as well as skin pigmentation and neurological disorders (Mandal and Suzuki 2002). In 1993, the World Health Organization (WHO) revised its guideline value for arsenic in potable water, lowering it from 50 µg/L to 10 µg/L, to limit the adverse effects of arsenic contamination (Jain and Singh 2012). However, some countries, like Bangladesh, maintain the earlier WHO standard even though research proves that exposure to arsenic at low levels (<10 ppb) increases the risk of skin cancer (Mandal and Suzuki 2002). In the typical range of groundwater pH (6.0-8.5) (Heath 1984), As(III) mainly exists as the neutral molecule (H_3AsO_3) while As(V) exists as anions ($H_2AsO_4^-$ and $HAsO_4^{2-}$). In the absence of electrostatic interactions, the adsorption of As(III) is limited by the available surface sites of the adsorbent. The adsorption of As(V) is usually more favorable under the same conditions so the removal of arsenic as As(V) is more effective (Yazdani et al. 2016). Hence, this study will focus on As(V); furthermore, As(III) can be treated following a pretreatment (oxidation) step.

During the past decades, studies have focused on the development of effective arsenic removal techniques such as membrane separation, coagulation/precipitation, ion exchange, and adsorption (Hung et al. 2004; Litter et al. 2010).

Adsorption is a competitive method due to its simplicity, low-cost, and good adsorbent reusability (Mohan and Pittman 2007; Cheng et al. 2016). Several categories of adsorbents including activated carbon (Litter et al. 2010; Amano et al. 2014), activated alumina (Guan et al. 2009; Litter et al. 2010), and iron-oxide-based adsorbents (Dixit and Hering 2003; Giles et al. 2011) have been studied intensely and applied in arsenic removal. In particular, iron-oxide-based adsorbents such as amorphous hydrous ferric oxide (FeO-OH), goethite (α-FeO-OH), hematite (α-Fe_2O_3), and magnetite (Fe_3O_4) are very effective due to the high affinity of iron towards arsenic (Litter et al. 2010). The magnetic response feature of Fe_3O_4 makes it possible for adsorbent separation by simply applying an external magnetic field after adsorption (Yavuz et al. 2006), therefore great efforts have been devoted to design Fe_3O_4 (Shipley et al. 2009) and its composites (Chang et al. 2012) with special structures to achieve effective arsenic removal. Recently, the synthesis of 2D ultrathin nanosheet for several metal oxides, including Fe_3O_4, was reported by Sun et al. (2014). Compared with conventional metal oxide nanoparticles, the unique 2D structures offered significantly higher specific surface areas (Sun et al. 2014), which is beneficial in the adsorption processes. Moreover, such structure has the potential to reduce the mass transfer resistance aroused from the tortuosity factors, resulting in improved kinetics. These properties led us to investigate its performance in arsenic removal.

In this work, we report the application of 2D Fe_3O_4 nanosheets in arsenic removal. The main objectives of the present work are (i) to examine the adsorption behavior of the adsorbent at different initial As(V) concentrations, (ii) to clarify the effects of pH on As(V) removal, and (iii) to investigate the adsorption kinetics of the adsorbent. Isotherms were generated at pH=4.7 and pH=7.6 and their results were fitted with Freundlich and Langmuir isotherm models. Single batch adsorption tests were carried out at different pH values ranging from 2 to 12. The zeta potential and particle size of the adsorbent material were also evaluated in the same interval for a better understanding of the influence of pH on adsorption. In addition, the adsorption kinetics was investigated. In general, 2D Fe_3O_4 nanosheets possessed good adsorption capacity and fast adsorption kinetics and therefore constitute a promising candidate material for effective arsenic removal.

Materials

Pluronic P123 (PEO_{20}-PPO_{70}-PEO_{20}, Sigma-Aldrich), absolute ethanol (C_2H_5OH, Sigma-Aldrich), iron nitrate nonahydrate ($Fe(NO_3)_3 \cdot 9H_2O$, Sigma-Aldrich), hexamethylenetetramine (HMTA, $C_6H_{12}N_4$, Sigma-Aldrich), ethylene glycol (EG, $(CH_2OH)_2$, Sigma-Aldrich), and DI water (H_2O) were used in the iron oxide synthesis. Dibasic sodium arsenate heptahydrate ($Na_2HAsO_4 \cdot 7H_2O$, Sigma-Aldrich), MES ($C_6H_{13}NO_4S \cdot H_2O$, Sigma-Aldrich), and DI water were used to prepare arsenic stock solution for adsorption studies. Hydrochloric acid (HCl, Sigma-Aldrich) and sodium hydroxide (NaOH, Sigma-Aldrich) were used for pH adjustments. Sodium nitrate ($NaNO_3$, Sigma-Aldrich) was used to control the ionic strength of the arsenic solution. All chemicals were of analytical reagent (AR) and used directly without further purification.

Preparation of 2D Fe_3O_4 Adsorbent

2D Fe_3O_4 adsorbent was synthesized via the route reported by Sun et al. (2014). In a typical experiment, 1.33 g P123 was added into 20 g absolute ethanol and the mixture was stirred for 15 minutes to form a homogeneous solution. 1.33 g iron nitrate nonahydrate and 0.467 g HMTA were then added into the ethanolic solution and the solution was stirred for another 15 minutes. After that, 86.7 mL EG was added and the solution was stirred for 30 minutes. The transparent dark orange precursor solution was obtained and allowed to age for two days. After two days, the precursor solution was transferred to a 200 mL autoclave with Teflon liner for solvothermal reaction. The autoclave was heated from room temperature (25 °C) to 150 °C at a rate of 5 °C/min and held at 150 °C for 15 hours. The precipitate was washed with absolute ethanol and DI water by three cycles of centrifugation (6000 rpm for 15 min at room temperature) and resuspension, dried at 80 °C overnight and sintered at 400 °C (heating rate =10 °C/min) for 10 hours in stagnant air to form the dark magnetic powder.

Material Characterizations

The crystal structures of the as-synthesized Fe_3O_4 adsorbent were characterized by X-ray diffraction in a Rigaku Ultima IV X-ray diffractometer using Cu Kα radiation (tension = 40 kV, current = 20 mA). Transmission electron microscopy (Tecnai F30 Twin transmission electron microscope (FEI)) was applied to investigate the structures and morphologies of the sample. The specific surface areas (calculated with BET method) of the Fe_3O_4 adsorbent were measured by isothermal nitrogen adsorption-desorption analysis (Beckman Coulter SA3100). The zeta potential and particle size of Fe_3O_4 adsorbent were measured by Dynamic Light Scattering (DLS) (Nanosizer ZS, Malvern).

Arsenic Adsorption Studies

Adsorption Isotherms

To investigate the adsorption performances of Fe_3O_4 adsorbent towards arsenate, adsorption isotherms were generated and studied. A determined amount of $Na_2HAsO_4{\cdot}7H_2O$ was dissolved in 1 L DI water to obtain 20 ppm As(V) stock solution. The solution was buffered by adding 9.5 g MES and its ionic strength was controlled by adding 0.85 g $NaNO_3$ (10 mM). In a typical experiment, 100 mL of the As(V) stock solution prepared was taken and its pH value was adjusted to 4.7 by adding 1M HCl solution. The total volume of HCl added was small compared to that of the As(V) solution, so that dilution effects could be neglected. The solution was then divided and diluted with 10 mM $NaNO_3$ at same pH to nine different initial concentrations, namely 1 ppm, 2 ppm, 3 ppm, 5 ppm, 7.5 ppm, 10 ppm, 12.5 ppm, 16 ppm, and 20 ppm. Then, a mass of 10 mg of Fe_3O_4 adsorbent was added to a 20 mL glass vial containing 10 mL as-prepared solution at each concentration. The vials were sealed and shaken by a vertical rotational shaker (shaking rate=80 rpm) for 24 hours to reach equilibrium. Fe_3O_4 adsorbent was separated from each vial by membrane filtration (Millipore GSWP2500, pore size 0.22 μm) after adsorption tests and the residual arsenic concentration in each solution was analyzed by Graphite Furnace Atomic Absorption Spectroscopy (GFAAS) using a BUCK Scientific, Model 220-GF. Hence, the amount of arsenic adsorbed per mass of adsorbent (g As/g Fe_3O_4) was determined with the following equation:

$$\text{As adsorbed (g As/g } Fe_3O_4) = \frac{(C_0 - C_1) * V}{m_{ad}} \quad \text{(Eq. 1)}$$

where C_0 and C_1 represented the initial and final As concentrations, V was the volume of the solution, and m_{ad} was the mass of Fe_3O_4 applied.

Another isotherm at pH=7.6 was obtained following the same procedures but the pH of As(V) solution was adjusted by adding 1M NaOH solution rather than HCl solution.

pH Effects on Adsorption

The effects of pH on adsorption were studied by carrying out batch adsorption experiments at nine different pH values, ranging from 2 to 12. It should be noted that the As(V) solution used for pH effects studies was not buffered with MES, but its ionic strength was still controlled by adding 10 mM $NaNO_3$. The pH value was adjusted to the desired value using small volumes of 1M HCl/NaOH solution. In a typical experiment, 10 mg Fe_3O_4 adsorbent was dispersed in 10 mL 20 ppm As(V) solution in each 20 mL glass vial. These vials were sealed and shaken by a vertical rotational shaker (shaking rate=80 rpm) for 24 hours to reach equilibrium. After adsorption tests, the adsorbent was removed by filtration and the final As(V) concentrations were measured by GFAAS. Equilibrium pH values for each solution measured by pH meter were 2.30, 3.15, 3.95, 5.19, 7.30, 8.27, 9.07, and 11.65, respectively.

Adsorption Kinetics

Adsorption kinetics were studied around pH=8.3, an optimal value determined by the pH tests. Herein, 2 ppm As(V) stock solution was prepared and buffered with MES. Its pH value was adjusted to 8 using a small volume of 1M NaOH and its ionic strength was again controlled by 10 mM $NaNO_3$. Unlike the previous tests, 2 mg Fe_3O_4 adsorbent was first added to a 20 mL vial containing 5 mL solution with the same pH and ionic strength, but in the absence of arsenate. The mixture was then shaken for 30 minutes to guarantee full dispersion of the adsorbent particles. At t=0, 5 mL 2 ppm As(V) solution, prepared previously, was

added to the vial to start adsorption. The vial was shaken by a vertical rotational shaker (shaking rate=80 rpm) for a determined time period and the Fe_3O_4 adsorbent was separated from the solution by filtration immediately after sampling to prevent further adsorption. The tests were carried out for nine different time periods, namely 2.5 min, 5 min, 10 min, 15 min, 20 min, 30 min, 40 min, 60 min, and 120 min; the final As(V) concentrations were measured by GFAAS.

Results and Discussion

Characterizations of Fe_3O_4 Adsorbent

The crystal structures of Fe_3O_4 were investigated by XRD. A typical diffraction pattern with 2θ ranging from 20˚ to 70˚ is shown in Figure 1. Diffraction peaks at 30.38˚, 35.63˚, 43.48˚, 54.03˚, 57.45˚, and 62.92˚, corresponding to (220), (311), (400), (422), (511), and (440) planes of magnetite (JCPDS No. 75-0449), were found in the pattern, verifying the presence of Fe_3O_4 in the bulk phase (He et al. 2007; Fan et al. 2011). Meanwhile, the sharp peaks indicate the formation of good crystallinity in the sample. However, peaks labeled with red circles at 24.15˚, 33.25˚, 41.03˚, and 49.50˚, corresponding to (012), (104), (113), and (024) plane of hematite (JCPDS No. 79-1741), were also observed, demonstrating the existence of α-Fe_2O_3 (Xu et al. 2015). The Fe_2O_3 phase might arise from the partial oxidation of the Fe_3O_4 phase during the drying and calcination process. Rietveld refinement was performed to estimate the content of each phase. As shown in Figure 1 (b), the refined sample XRD pattern could be broken down into the refined patterns for pure magnetite and hematite, respectively. The estimated content of the Fe_3O_4 phase was 80.9% and that of the Fe_2O_3 phase was 19.1%, indicating that only a small portion of Fe_3O_4 was oxidized. Moreover, the XRD pattern in Figure 1 (a) was also compared with that obtained by Sun et al. (2016); all peaks with the same shapes were found at identical locations.

The morphology of as-synthesized Fe_3O_4 was characterized by TEM and typical images are presented in Figure 2, at three different magnifications. From Figure 2 (a) and (b), it can be observed that the as-synthesized Fe_3O_4

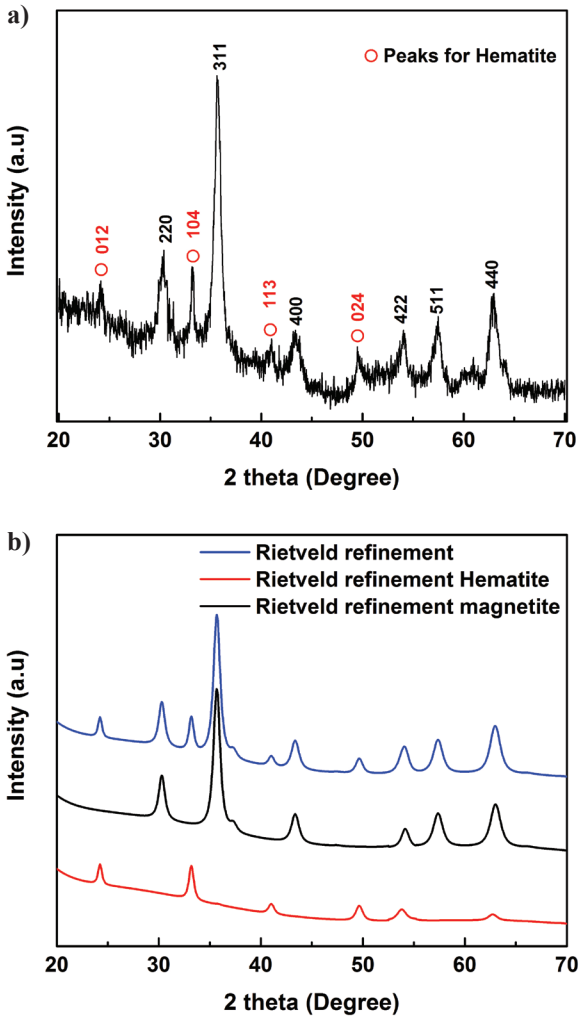

Figure 1. (a) Typical XRD pattern of as-synthesized Fe_3O_4 adsorbent. (b) Rietveld refinement of the obtained XRD pattern.

particles were mostly thin sheets, showing their 2D structure. It should also be noted that the particles did not exhibit uniformity, either in shape or size, and aggregation was observed, which can be explained from the high surface energy nature of 2D materials (Sun et al. 2016). Additionally, branched structures, with a thickness ranging from 5 nm to 20 nm, were found, as shown for example in Figure 2 (c). Such structures might be interpreted as stacks of several single layer sheets, which further verified the existence of the 2D structure in the Fe_3O_4 adsorbent fabricated. The BET specific surface area of the adsorbent was 94.07 m^2/g.

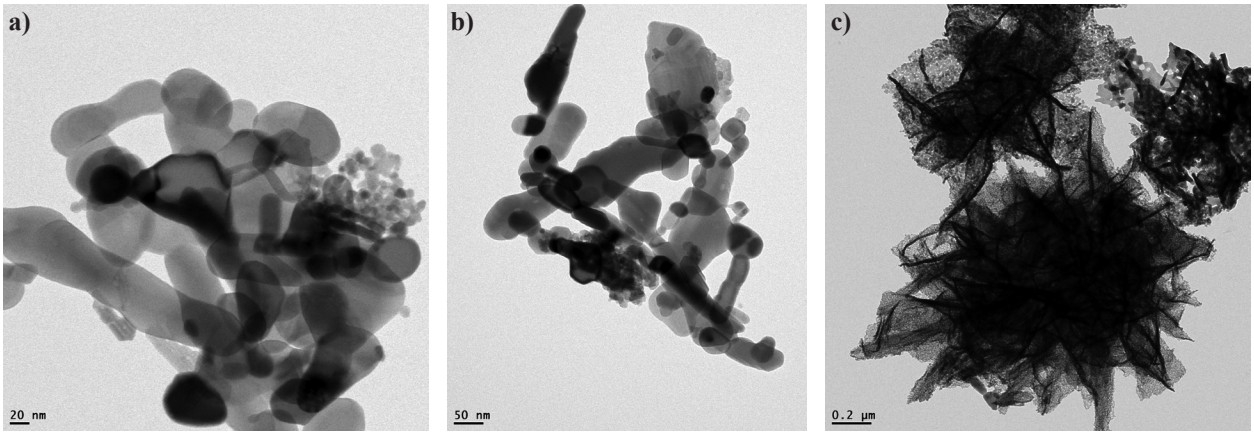

Figure 2. TEM images of as-synthesized Fe_3O_4 at different magnifications; Scale bar: (a) 20 nm, (b) 50 nm, and (c) 0.2 µm.

As(V) Adsorption Studies

Adsorption Isotherms

To investigate the As(V) adsorption capacity of Fe_3O_4 adsorbent, an adsorption isotherm at pH=4.7 was generated and the results are presented in Figure 3 (a). When the initial As(V) concentration was 20 ppm, the corresponding equilibrium adsorption capacity for Fe_3O_4 adsorbent was calculated to be 14.14 mg As/g adsorbent. For a better understanding of the adsorption behaviors, two commonly used adsorption models, the Freundlich (Borys and Grzywna 2016) and Langmuir (Ajay et al. 2014) isotherm models, were applied in data fitting.

The Freundlich isotherm model is presented by the following equation:

$$Q_e = K_f C_e^{\frac{1}{n}} \qquad \text{(Eq. 2)}$$

where Q_e and C_e represent the mass of As(V) adsorbed per mass of adsorbent (mg/g) and the equilibrium concentration of As(V) in solution (mg/L). The Freundlich isotherm constant K_f is an indication of the adsorption capacity (mg/g) of the adsorbent, and $1/n$ is the adsorption intensity (Borys and Grzywna 2016). The linear form of the Freundlich isotherm model is obtained by taking the logarithm of both sides and is given as:

$$\ln(Q_e) = \ln(K_f) + \frac{1}{n}\ln(C_e) \qquad \text{(Eq. 3)}$$

As shown in Figure 3 (b), the coefficient of determination R^2 is 0.99. The values for K_f and $1/n$ are 6.5562 mg/g and 0.4609, respectively. The data points are well fitted by the curve, demonstrating that the Freundlich isotherm model gives an excellent prediction for As(V) adsorption.

The Langmuir isotherm model is described as follows:

$$Q_e = \frac{Q_{max} K_l C_e}{1 + K_l C_e} \qquad \text{(Eq. 4)}$$

where the Langmuir isotherm constant K_l (L/mg) is related to the energy of adsorption, and Q_{max} is the maximum monolayer adsorption capacity (mg/g) (Ajay et al. 2014). The Langmuir isotherm model is linearized to the following form to determine Q_{max} and K_l:

$$\frac{1}{Q_e} = \frac{1}{Q_{max}} + \frac{1}{Q_{max} K_l C_e} \qquad \text{(Eq. 5)}$$

Clearly from Figure 3 (c), the data points do not match the linear fitting very well and the corresponding R^2 is 0.9607. The values for Q_{max} and K_l are 6.3591 mg/g and 11.6217 L/mg, respectively. Compared with the Freundlich model, the Langmuir model is less accurate in predicting the adsorption of As(V) in this case.

A second adsorption isotherm at pH=7.6 was also generated and the corresponding results are shown in Figure 4 (a). When the initial As(V) concentration was 20 ppm, the corresponding equilibrium adsorption capacity for Fe_3O_4

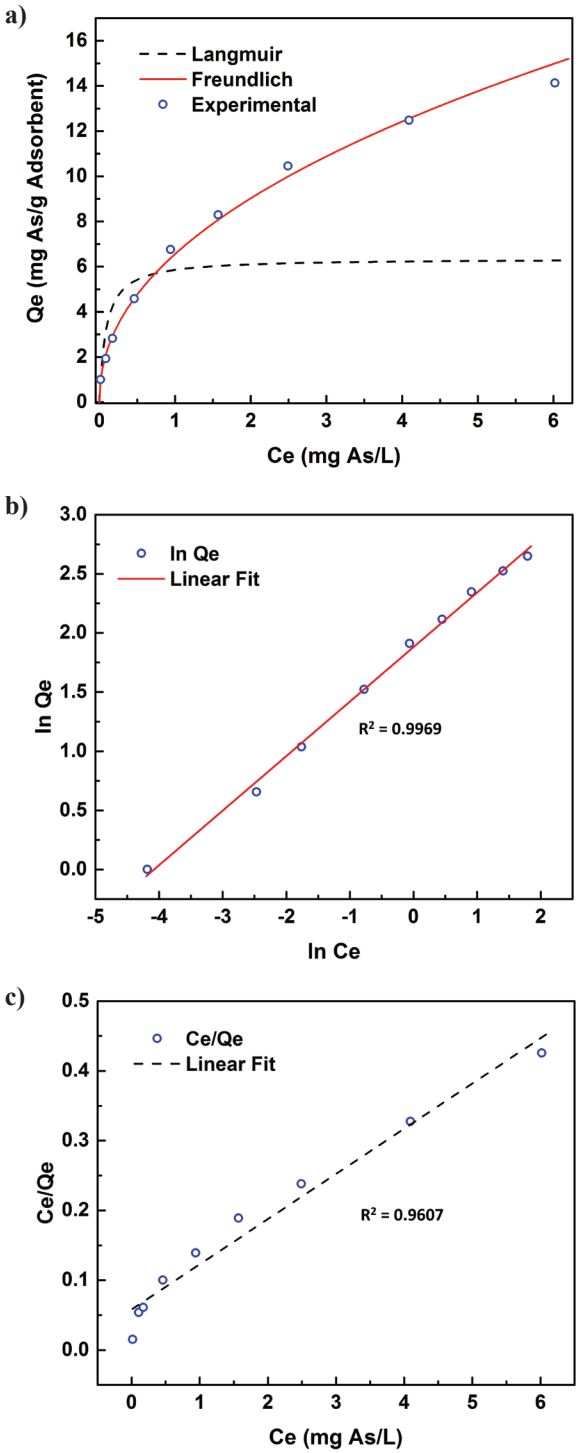

Figure 3. (a) Adsorption isotherm obtained at pH=4.7. Linear fitting curve for experimental data with (b) Freundlich model and (c) Langmuir model.

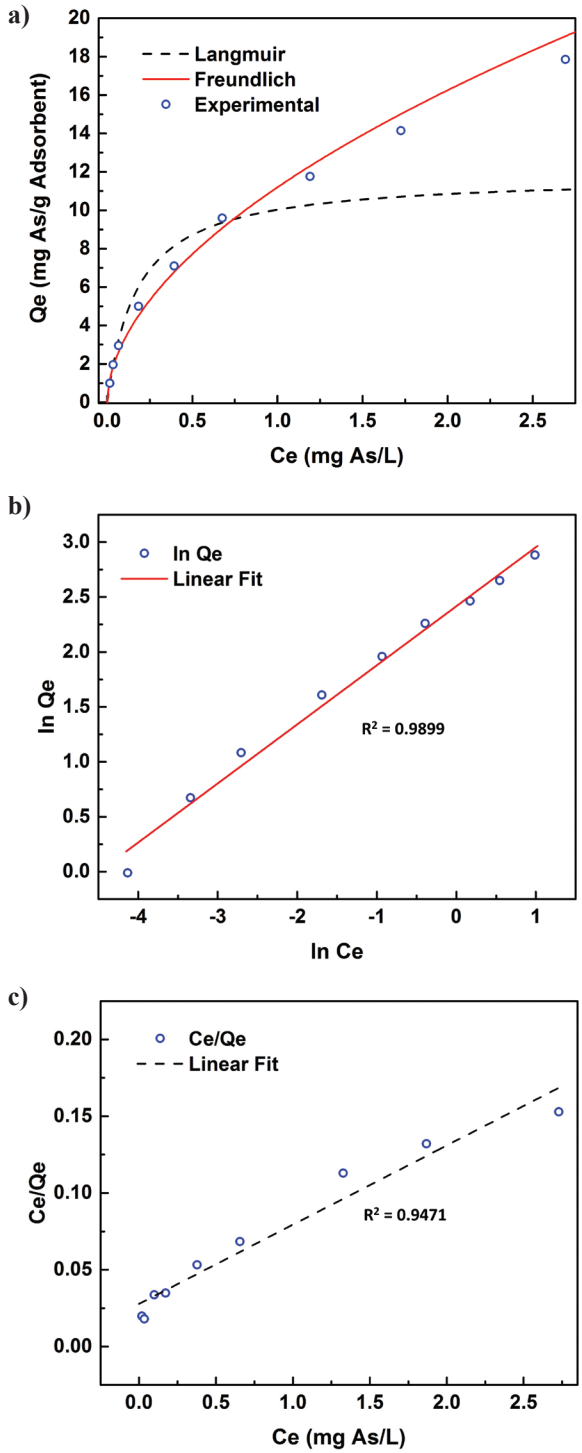

Figure 4. (a) Adsorption isotherm obtained at pH=7.6. Linear fitting curve for experimental data with (b) Freundlich model and (c) Langmuir model.

adsorbent was calculated to be 17.85 mg As/g adsorbent. Compared with the results obtained at pH=4.7, an increase in As(V) adsorption capacity was observed, indicating that As(V) adsorption became more favorable when pH was elevated from 4.7 to 7.6.

The data points were also fitted with the Freundlich and Langmuir isotherm models, as shown in Figure 4 (b) and (c). The Freundlich constants K_f and $1/n$ are 11.194 mg/g and 0.5376 while Q_{max} and K_l predicted from the Langmuir model are 11.8075 mg/g and 5.6323 L/mg. Similar to the results found at pH=4.7, the Freundlich model better fits the data points and gives a higher coefficient of determination R^2 than the Langmuir model (0.9889 vs. 0.9471). Therefore, As(V) adsorption by Fe_3O_4 adsorbent is better predicted by the Freundlich isotherm model at both pH values.

pH Effects on Adsorption

Adsorption of arsenate on iron oxides has been reported to be strongly pH dependent (Pierce and Moore 1980, 1982; Manning and Fendorf 1998) forming inner sphere complexes on the iron oxide surfaces (Hingston et al. 1971; Anderson and Malotky 1979; Lumsdon et al. 1984; Waychunas et al. 1993; Manceau 1995; Sun and Doner 1996, 1998; O'Reilly et al. 2001).

In metal oxides, specific adsorption occurs by the replacement of surface hydroxyl groups by the adsorbing species, (As_2O_3), (Cornell and Schwertmann 2003)

$$\equiv FeOH + As_2O_3^- \leftrightarrow \equiv FeOAs_2O_3 + OH^- \quad \text{(Eq. 6)}$$

$$\equiv (FeOH)_2 + As_2O_3^- \leftrightarrow \equiv FeOAs_2O_3^+ + 2OH^- \quad \text{(Eq. 7)}$$

representing the monodentate and bidentate mode or coordination respectively.

The relationship between pH values and As(V) adsorption capacity of Fe_3O_4 is revealed in Figure 5 (a). The As(V) adsorption capacity of Fe_3O_4 at each equilibrium pH (2.30, 3.15, 3.95, 5.19, 7.30, 8.27, 9.07, and 11.65) is 7.98, 9.68, 10.62, 14.38, 17.64, 18.55, 15.35, and 4.99 mg/g. It is clear that adsorption capacity of Fe_3O_4 increases with increasing pH when pH is lower than 8.27, and further increase in pH will result in reduction in the adsorption capacity. At either strong acidic (pH=2.30) or basic (pH=11.65) conditions, the adsorption capacity of Fe_3O_4 is remarkably lower compared with its maximum value at pH=8.27. Two opposing effects arise with increasing pH: 1) the relative concentration of the anionic form increases due to further deprotonation of $H_3As_2O_3$, and 2) a decrease in the number of surface ≡FeOH groups, producing a maximum in the adsorption envelope. A similar trend was observed for fluoride and silicate on goethite (Hingston et al. 1968), the peak corresponding to the pH of highest concentration of the complex at the surface. It should also be noted that the adsorption capacity obtained at pH=5.19 and pH=7.30 are in agreement with the results from isotherm studies in the previous section at adjacent pH values (4.70 and 7.6). Therefore, the performance of the as-prepared Fe_3O_4 adsorbent in arsenic removal is highly reliable.

The arsenic removal efficiency at each pH was calculated from adsorption capacity via Equation 1 and the results are presented in Figure 5 (b). Clearly, pH has the same influence on arsenic removal efficiency as it does on adsorption capacity. When pH is 8.27, the Fe_3O_4 adsorbent could realize its maximum As(V) removal efficiency of 93.69%. However, this value decreases significantly to 40.3% and 25.18% at pH=2.3 and 11.65, respectively. For the maximum performance of Fe_3O_4 adsorbent, the optimal working pH lies between 7.5 and 8.5, which falls within the typical pH range of groundwater (Heath 1984), and therefore makes the material highly promising for that application.

For a better understanding of the pH effects on adsorption, the zeta potential and particle size were measured at several different pH values, ranging from 2 to 12, and the results are presented in Figure 6.

The relationships between the zeta potential and pH are revealed in Figure 6 (a) and a major trend of decrease in zeta potential with increasing pH is observed. When pH is lower than 6, the zeta potential decreases quickly as pH increases, from 22.53 mV at pH=2.26 to -32.3 mV at pH=6.07, and the isoelectric point is found at pH=4.28 by interpolation. At pH higher than 6, the zeta potential decreases slowly to -42.3 mV as pH increases to 11.44. Figure 6 (b) shows the correlations between the particle size of Fe_3O_4 and pH. At lowest pH of 2.26, the particle size was estimated to be 1081 nm. As pH approaches the isoelectric point, the

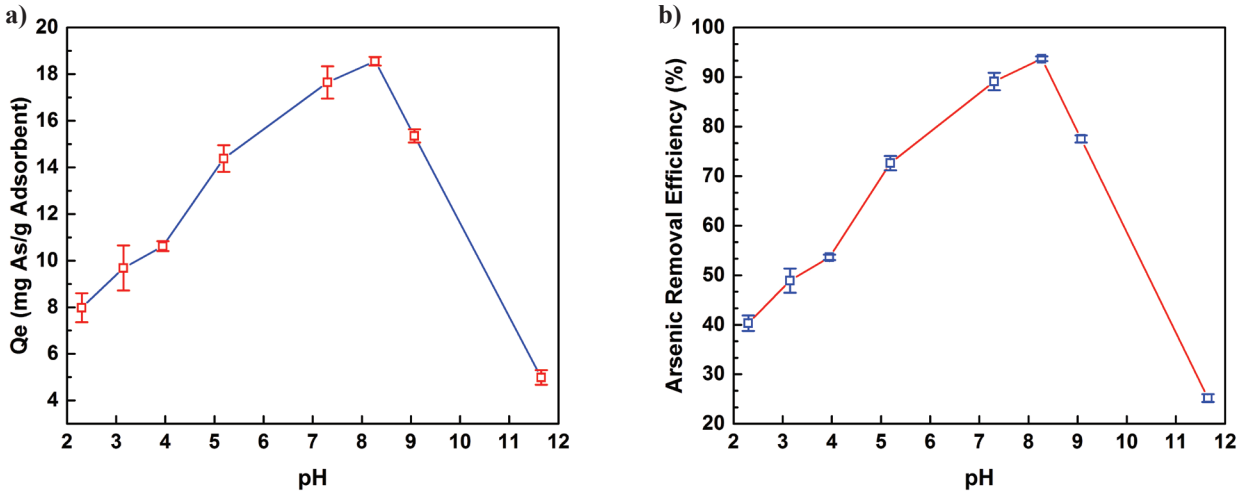

Figure 5. (a) Adsorption capacity of Fe_3O_4 at different pH. (b) Arsenic removal efficiencies at different pH.

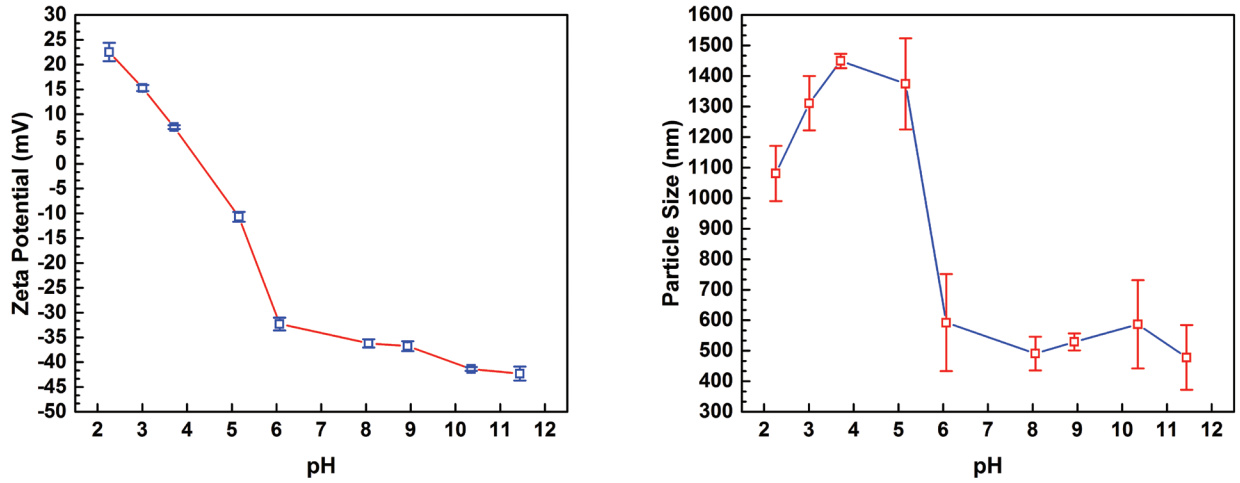

Figure 6. (a) Zeta potential of Fe_3O_4 at different pH. (b) Particle size of Fe_3O_4 in solution at different pH.

particle size gradually increases to 1449.5 nm at pH=3.71, indicating the adsorbent is less dispersed and coagulation would occur. Once above the isoelectric pH, the particle size will decrease with further increase in pH. It should be noted that the particle size decreased significantly from 1374.5 nm to 592.07 nm as pH changed from 5.16 to 6.07, suggesting the dispersion of adsorbent is much better. Meanwhile, for a fixed amount of adsorbent, smaller particle size means more available surface area for adsorption. When pH is elevated from 8.06 to 11.44, the change in the particle size is relatively small (490.75 nm at pH=8.06, 529 nm at pH=8.93, 586.5 nm at pH=10.35, and 478.2 nm at pH=11.44), which is in agreement with the small change in zeta potential.

The pH effects on adsorption could be considered as comprehensive effects of the zeta potential, particle size of the adsorbent, and existing form of As(V). As a triprotic acid, the deprotonation dissociation constants (pK_a) of arsenate are 2.20 ($H_3AsO_4/H_2AsO_4^-$), 6.97 ($H_2AsO_4^-/HAsO_4^{2-}$), and 11.53 ($HAsO_4^{2-}/AsO_4^{3-}$). When pH increases from 2.3 to 3.95, the zeta potential of Fe_3O_4 decreases while $H_2AsO_4^-$, the species with a negative charge, gradually becomes the dominating existing form of arsenate. We conjecture that the transformation of uncharged H_3AsO_4 into negative charged $H_2AsO_4^-$ could overcome the decreases in zeta potential of the adsorbent and the overall adsorption capacity increases. As mentioned previously, a sharp decrease in the particle size is observed when

pH is higher than 5 and the particle size hits its minimum value at pH around 8. In this region, though the zeta potential of Fe_3O_4 is negative and arsenate exists as anions ($H_2AsO_4^-$/$HAsO_4^{2-}$), the significant decrease in particle size provides more surface areas for adsorption and the formation of surface complexation compounds (Cornell and Schwertmann 2003). Therefore, the adsorption capacity increases and reaches its maximum value at pH=8.27. Further increase in pH has little effects on the zeta potential and particle, but arsenate will gradually transform into a more negative charged species, AsO_4^{3-}, leading to higher electrostatic repulsion. Meanwhile, the competition adsorption of OH^- on the surface of Fe_3O_4 was also reported (Cornell and Schwertmann 2003). Consequently, the adsorption capacity of Fe_3O_4 decreases quickly with increasing pH. The fact that significant adsorption of the negatively charged As(V) at pHs where the surface is also negative further indicates that the interaction is specific in nature as initially proposed.

Adsorption Kinetics

The kinetics of As(V) removal by Fe_3O_4 adsorbent was determined with an initial As(V) concentration of 1 ppm (Figure 7 (a)). A sharp decrease in As(V) concentration, from 1000 ppm to 270 ppm, is observed for the first 2.5 minutes and the corresponding As(V) removal efficiency during this period is 73%. Since then, the rate of As(V) is much lower and gradually decreases with time. The adsorption of As(V) on goethite and hematite has also been reported to follow a two stage mechanism, with a fast initial rate followed by a much slower rate (Singh et al. 1988; Grossl et al. 1997; Sabbatini et al. 2010). The adsorption-desorption equilibrium is established after 120 minutes with a residual As(V) concentration of 175 ppb and a removal efficiency of 82.5%. Considering that the adsorbent loading is much lower in kinetics studies than in other experiments (100 mg/L vs. 1000 mg/L), it is believed that fast As(V) removal with better efficiency could be obtained with higher adsorbent loading. For comparison, in the isotherm studies at pH=7.6, the residual As(V) concentration is only 8.02 ppb when initial As(V) concentration is 1 ppm.

Two kinetics models, pseudo-first-order and pseudo-second-order model, were applied to fit experimental data. Pseudo-first-order model is expressed as:

$$\log(Q_e - Q_t) = \log(Q_e) - k_1 t \qquad \text{(Eq. 8)}$$

where Q_e and Q_t represent the mass of As(V) adsorbed per mass of adsorbent (mg/g) at equilibrium and at time t; k_1 is the rate constant of pseudo-first-order model. The logarithm term $\log(Q_e - Q_t)$ is plotted against t in Figure 7 (b) and the correlation coefficient R^2 is 0.8399, thus indicating the adsorption of As(V) by Fe_3O_4 is unlikely to follow the pseudo-first-order model.

Pseudo-second-order model is then used for data fitting and its rate equation in differential form is given as:

$$\frac{dQ_t}{dt} = k_2(Q_e - Q_t)^2 \qquad \text{(Eq. 9)}$$

where k_2 is the rate constant of pseudo-first-order model ($g \cdot mg^{-1} \cdot min^{-1}$). Equation 9 is then linearized by taking integration from t=0 to t=t:

$$\frac{t}{Q_t} = \frac{1}{Q_e} t + \frac{1}{K_2 Q_e^2} \qquad \text{(Eq. 10)}$$

$\frac{t}{Q_t}$ is plotted against t in Figure 7 (c) and the model has a stronger coefficient of determination than the pseudo-first-order model, with an R^2 of 0.9908.The initial adsorption rate r_0 ($mg \cdot g^{-1} \cdot min^{-1}$) is derived from Equation 9 by setting Q_t equal to zero and substituting Q_e and k_2:

$$r_0 = k_2 Q_e^2 \qquad \text{(Eq. 11)}$$

Q_e, k_2, and r_0 are calculated to be 4.30 mg/g, 0.2754 $g \cdot mg^{-1} \cdot min^{-1}$, and 5.0985 $mg \cdot g^{-1} \cdot min^{-1}$, respectively. It should also be noted that Q_e predicted from pseudo-second-order model is in agreement with the adsorption capacity from equilibrium experiments.

Conclusions

In this work, 2D Fe_3O_4 nanosheets were synthesized and their arsenic removal performance was evaluated. XRD analysis of the adsorbent verified the presence of Fe_3O_4 in the bulk phase; peaks for Fe_2O_3 were also observed. The BET specific surface area of the adsorbent was 94.07 m^2/g and 2D structures were confirmed by TEM.

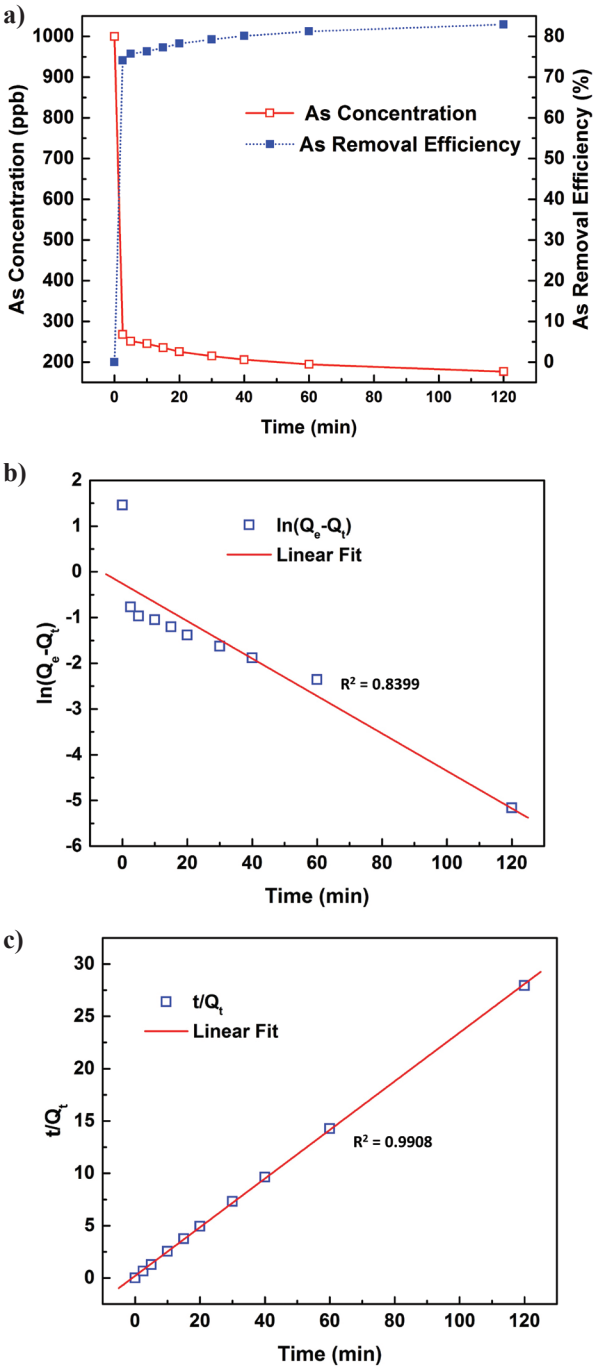

Figure 7. (a) Kinetic adsorption data for As(V) by Fe_3O_4 adsorbent. Data fitting with (b) pseudo-first-order kinetic model and (c) pseudo-second-order kinetic model.

Isotherm studies at both pH=4.7 and 7.6 proved that the adsorption behaviors of As(V) onto Fe_3O_4 adsorbent were better described by the Freundlich isotherm model. Corresponding parameters K_f and $1/n$ were 6.5562 mg/g and 0.4609 at pH=4.7 and 11.194 mg/g and 0.5376 at pH=7.6, respectively. The effect of pH was studied and the optimal value was found at 8.27, where the adsorption capacity and the removal efficiency were 18.55 mg/g and 93.69%. Further investigation suggested that the pH dependence was the result of the influence of the zeta potential, particle size of the adsorbent, and existing form of As(V). Kinetics studies showed that the As(V) adsorption by Fe_3O_4 adsorbent followed the pseudo-second-order model; 73% of the As(V) was adsorbed within the first 2.5 minutes and an overall removal efficiency of 82.5% was achieved in 2 hours of reaction. However, enhanced removal efficiency could be expected at higher adsorbent loading. Therefore, we believe that Fe_3O_4 nanosheets are a competitive adsorbent material for arsenic removal due to their good adsorption capacity, fast kinetics, and easy separation.

Acknowledgments

The manuscript was prepared through contributions of all authors. All authors have approved the final version of the manuscript.

Author Bio and Contact Information

Hongxi Luo received a B.S. in Chemical Engineering (2016) from University of Missouri, where he conducted research under the supervision of Dr. Maria Fidalgo and East China University of Science & Technology. He is currently a graduate student in Chemical Engineering at University of Virginia. His current research interests includes tuning polymer backbone structures for new membrane design and understanding the effects of polymer backbones on ion transport across the membrane. He may be contacted at hldm5@mail.missouri.edu.

Fangwei Cheng holds a B.S. degree in Chemical Engineering (2015) from Wuhan Institute of Technology and a M.S degree in Chemical Engineering (2016) from University of Missouri. She is currently a graduate student in Civil & Environmental Engineering at University of Virginia. Her current research interests include designing new organoclays and improving the efficiency and efficacy of wastewater

treatments for removal of certain organic contaminants. She may be contacted at fcnp3@mail.missouri.edu.

Weiming Hu is a Ph.D. candidate in Department of Civil & Environmental Engineering at University of Missouri – Columbia. His research interests include water/wastewater treatment processes, adsorption process, and materials science in environmental applications. He may be contacted at why78@mail.missouri.edu.

Jinpeng Wang received a B.S. degree in Chemical Engineering from University of Missouri (2015) and a Master of Engineering (MEng) degree in Chemical Engineering & Applied Chemistry from University of Toronto in Feb 2017. His current research interests are focused on Ultraviolet (UV) light reactors for drinking water treatment. He may be contacted at jinpeng.wang@mail.utoronto.ca.

Shuting Xiang received her B.S. degree in Chemical Engineering from University of Missouri (2017). She joined Dr. Maria Fidalgo's group from September 2015. Her current research interests are focused on fabrication and characterization of highly porous films, designed for the capture of pollutants in water. She may be contacted at sx6cf@mail.missouri.edu.

Maria Fidalgo is an Associate Professor in the Department of Civil and Environmental Engineering at the University of Missouri. She holds a B.S. in Chemical Engineering from Instituto Tecnologico de Buenos Aires, Argentina, and M.S. and Ph.D. degrees in Environmental Engineering from Rice University. Her area of interest includes the interactions of nanomaterials and natural systems, physicochemical processes (membrane separations and advanced oxidation) and nano-enabled environmental sensors. She may be contacted at fidalgom@missouri.edu.

References

Ajay, K., M. Agrawal, P. Chandrashekhar, L. Ishwardas, and L. Muthreja. 2014. Langmuir, Freundlich and BET adsoprtion isotherm studies for zinc ions onto coal fly ash. *International Journal of Application or Innovation in Engineering Management* 3(1): 7.

Amano, Y., Y. Matsushita, and M. Machida. 2014. Arsenic adsorption by activated carbon with different amounts of basic sites under different solution pH and coexistent ions. *Separation Science and Technology* 49(3): 345-353.

Anderson, P. and D. Malotky. 1979. The adsorption of protolyzable anions on hydrous oxides at the isoelectric pH. *Journal of Colloid Interface Science* 72: 15.

Borys, P. and Z. Grzywna. 2016. On the fractality of the Freundlich adsorption isotherm in equilibrium and non-equilibrium cases. *Physical Chemistry Chemical Physics* 18(30): 20784-20789.

Chang, S., Y. Yu, C. Li, C. Wu, and H.-Y. Lei. 2012. Highly efficient arsenic removal using a composite of ultrafine magnetite nanoparticles interlinked by silane coupling agents. *International Journal of Environmental Research & Public Health* 9(10): 3711-3723.

Cheng, F., H. Luo, L. Hu, B. Yu, Z. Luo, and M. Fidalgo de Cortalezzi. 2016. Sludge carbonization and activation: From hazardous waste to functional materials for water treatment. *Journal of Environmental Chemical Engineering* 4(4A): 4574-4586.

Cornell, R. and U. Schwertmann. 2003. *The Iron Oxides: Structure, Properties, Reactions, Occurences and Uses, 2nd edition*. WILEY-VCH Verl. GmbH Co KGaAWeinheim.

Dixit, S. and J. Hering. 2003. Comparison of arsenic(V) and arsenic(III) sorption onto iron oxide minerals: Implications for arsenic mobility. *Environmental Science & Technology* 37(18): 4182-4189.

Fan, T., D. Pan, and H. Zhang. 2011. Study on formation mechanism by monitoring the morphology and structure evolution of nearly monodispersed Fe_3O_4 submicroparticles with controlled particle sizes. *Industrial & Engineering Chemistry Research* 50(15): 9009-9018.

Giles, D., M. Mohapatra, T. Issa, S. Anand, and P. Singh. 2011. Iron and aluminium based adsorption strategies for removing arsenic from water. *Journal of Environmental Management* 92(12): 3011-3022.

Grossl, P., M. Eick, D.L. Sparks, S. Goldberg, and C.C. Ainsworth. 1997. Arsenate and chromate retention mechanism on goethite. 2: Kinetic evaluation using a pressure-jump relaxation technique. *Environmental Science & Technology* 31: 6.

Guan, X., T. Su, and J. Wang. 2009. Quantifying effects of pH and surface loading on arsenic adsorption on NanoActive alumina using a speciation-based model. *Journal of Hazard Materials* 166(1): 39-45.

He, Z., C.-Y. Xu, L. Zhen, and W.-Z. Shao. 2007. Hydrothermal synthesis and characterization of single crystalline Fe3O4 nanowires with high aspect ratio and uniformity. *Materials Lett*ers 61(14-15): 3159-3162.

Heath, R.C. 1984. *Ground-water Regions of the United States.* Report 2242.

Hingston, F., A. Posner, and J. Quirk. 1968. Adsorption of selenite by goethite. *Advances in Chemistry Series* 79: 9.

Hingston, F., A. Posner, and J. Quirk. 1971. Competitive adsorption of negatively charged ligands on oxide surfaces. *Discussions of the Faraday Society* 52: 9.

Hughes, M.F. 2002. Arsenic toxicity and potential mechanisms of action. *Toxicology Letters* 133(1): 1-16.

Hung, D., O. Nekrassova, and R. Compton. 2004. Analytical methods for inorganic arsenic in water: A review. *Talanta* 64(2): 269-277.

Jain, C. and R. Singh. 2012. Technological options for the removal of arsenic with special reference to South East Asia. *Journal of Environmental Management* 107: 1-18.

Litter, M., M. Morgada, and J. Bundschuh. 2010. Possible treatments for arsenic removal in Latin American waters for human consumption. *Environmental Pollution* 158(5): 1105-1118.

Lumsdon, D., A. Fraser, J. Russell, and N. Livesey. 1984. New infrared band assignments for the arsenate ion adsorbed on synthetic goethite (a-FeOOH). *Journal of Soil Science* 35: 6.

Manceau, A. 1995. The mechanism of anion adsorption on iron oxides. Evidence for the bonding of arsenate tetrahedra at free Fe(O, OH) edges. *Geochimica et Cosmochimica Acta* 59: 7.

Mandal, B. and K. Suzuki. 2002. Arsenic round the world: A review. *Talanta* 58(1): 201-235.

Manning, B. and S. Fendorf. 1998. Surface structures and stability of arsenic(III) on goethite: Spectroscopic evidence for inner-sphere complexes. *Environmental Science & Technology* 34: 6.

Mohan, D. and C. Pittman. 2007. Arsenic removal from water/wastewater using adsorbents--A critical review. *Journal of Hazard Materials* 142(1-2): 1-53.

O'Reilly, S., D. Strawn, and D.L. Sparks. 2001. Residence time effects on arsenate adsorption/ desorption mechanisms on goethite. *Soil Science Society of America Journal* 65: 2.

Pierce, M. and C. Moore. 1980. Adsorption of arsenite on amorphous iron hydroxide from dilute aqueous solution. *Environmental Science & Technology* 14: 3.

Pierce, M. and C. Moore. 1982. Adsorption of arsenite and arsenate on amorphous iron hydroxide. *Water Research* 16: 7.

Sabbatini, P., F. Yrazu, F. Rossi, G. Thern, A. Marajovsky, and M. Fidalgo de Cortalezzi. 2010. Fabrication and characterization of iron oxide ceramic membranes for arsenic removal. *Water Research* 44: 11.

Shipley, H., S. Yean, A. Kan, and M. Tomson. 2009. Adsorption of arsenic to magnetite nanoparticles: Effect of particle concentration, pH, ionic strength, and temperature. *Environmental Toxicology Chem*istry 28(3): 509-515.

Singh, D., G. Prasad, D. Rupainwar, and V. Singh. 1988. As(III) removal from aqueous solution by adsorption. *Water, Air, & Soil Pollution* 42: 14.

Smedley, P. and D. Kinniburgh. 2002. A review of the source, behaviour and distribution of arsenic in natural waters. *Applied Geochemistry* 17(5): 517-568.

Styblo, M., L.M. Del Razo, L. Vega, D.R. Germolec, E.L. LeCluyse, G.A. Hamilton, W. Reed, C. Wang, W.R. Cullen, and D.J. Thomas. 2000. Comparative toxicity of trivalent and pentavalent inorganic and methylated arsenicals in rat and human cells. *Archives of Toxicology* 74(6): 289-299.

Sun, J., P. Zan, X. Yang, L. Ye, and L. Zhao. 2016. Room-temperature synthesis of Fe3O4/Fe-carbon nanocomposites with Fe-carbon double conductive network as supercapacitor. *Electrochimica Acta* 215: 483-491.

Sun, X. and H. Doner. 1996. An investigation of arsenate and arsenite bonding structures on goethite by FTIR. *Soil Science* 161: 865-872.

Sun, X. and H. Doner. 1998. Adsorption and oxidation of arsenite on goethite. *Soil Science* 165: 10.

Sun, Z, T. Liao, Y. Dou, S.M. Hwang, M. Park, L. Jiang, J.H. Kim, and S.X. Dou. 2014. Generalized self-assembly of scalable two-dimensional transition metal oxide nanosheets. *Nature Communications* 5: 3813.

Waychunas, G., B. Rea, C. Fuller, and J. Davis. 1993. Surface chemistry of ferrihydrite: Part 1. EXAFS studies of the geometry of coprecipitated and adsorbed arsenate. *Geochimica et Cosmochimica Acta* 57: 19.

Xu, G., L. Li, Z. Shen, Z. Tao, Y. Zhang, H. Tian, X. Wei, G. Shen, and G. Han. 2015. Magnetite Fe3O4 nanoparticles and hematite α-Fe2O3 uniform oblique hexagonal microdisks, drum-like particles and spindles and their magnetic properties. *Journal of Alloys & Compounds* 629: 36-42.

Yavuz, C, J.T. Mayo, W.W. Yu, A. Prakash, J.C. Falkner, S. Yean, L. Cong, H.J. Shipley, A. Kan, M. Tomson, D. Natelson, and V.L. Colvin. 2006. Low-field magnetic separation of monodisperse Fe3O4 nanocrystals. *Science* 314(5801): 964-967.

Yazdani, (Roza) M., T. Tuutijärvi, A. Bhatnagar, and R. Vahala. 2016. Adsorptive removal of arsenic(V) from aqueous phase by feldspars: Kinetics, mechanism, and thermodynamic aspects of adsorption. *Journal of Molecular Liquids* 214: 149-156.

Universities Council on Water Resources
Journal of Contemporary Water Research & Education
Issue 160, Pages 144-156, April 2017

Design and Manufacturing of High Surface Area 3D-Printed Media for Moving Bed Bioreactors for Wastewater Treatment

Olivia Elliott[1], Stephanie Gray[2], Michael McClay[2], Bakr Nassief[2], Ann Nunnelley[1], Eric Vogt[1], Joseph Ekong[2], Kamran Kardel[3], Ali Khoshkhoo[2], Gabriel Proaño[2], David M. Blersch[1], and *Andres L. Carrano[2]

[1]Department of Biosystems Engineering, Auburn University, Auburn, AL, USA
[2]Department of Industrial and Systems Engineering, Auburn University, Auburn, AL, USA
[3]Department of Manufacturing Engineering, Georgia Southern University, Statesboro, GA, USA
**Corresponding author*

Abstract: The specific surface area and topology of a biofilter media carrier is one of the most important parameters that determines the performance and efficiency of the system. In this work, mathematical models and 3D printing technologies were used to design and fabricate complex media designs that provide high specific surface area and refugia to protect biofilm from premature sloughing. Several gyroid based designs were proposed with specific surface area well beyond 2300 m^2/m^3. However, wall thicknesses and pore sizes that are prone to clogging determined a design that yields 1168 m^2/m^3 (133% larger than the baseline commercial K1 Kaldnes). Several moving bed bioreactors were constructed for laboratory testing with inoculation provided by wastewater from a fisheries operation. Preliminary results indicate that the 3D printed media can withstand the prevalent conditions in moving bed bioreactors, and that the NH_3 removal rate of gyroid media is comparable to that of K1 Kaldnes. This work establishes the feasibility of using 3D printing for bioreactor media fabrication and allows for future topology optimization for enhanced operation. Future work is needed to investigate how these complex media designs might stimulate novel microbial assemblages and community metabolism that translate into yield efficiency gains in reactor performance.

Keywords: *specific surface area, biofilter, carrier, topology, gyroid, nitrification, efficiency*

Water pollution is a global problem and is found wherever human activity takes place. Every 20 seconds a child dies from a preventable illness caused by unsafe drinking water, poor hygiene, and inadequate sanitation (UNICEF/WHO 2009). Although the United Nations Millennium Development Goals (MDGs) for water access have been met ahead of schedule, the world did not meet the 2015 goals for sanitation (WHO 2012) as nearly half of the people living in developing regions still lack improved sanitation (WHO/UNICEF 2010). In addition, the Natural Resources Defense Council states that dirty water is the world's biggest health risk and threatens quality of life as well as public health (NRDC 2014). Water is considered polluted when impaired by anthropogenic contaminants and thereby rendered unusable as drinking water. These contaminants typically comprise a combination of organic and inorganic substances, and different remediation methods exist for various pollutants.

One approach for water pollution remediation is through the use of biofilters that employ attached-growth microbial biofilms to metabolize pollutant constituents. In these reactors, microbial biofilms colonize an artificial substratum and capture or transform dissolved pollutants, rendering them less harmful or removing them via losses to the atmosphere. There are different types of biofilm-based bioreactors, including biofilters with suspended (moving bed) media, and biofilters with static (trickling) media, among others. The

potentially low operational costs of biofilters have led to their implementation in many applications for water and wastewater remediation, including for both remediation of organic and nitrogen contaminants (Mendoza-Espinoza and Stephenson 1999).

Moving-bed bioreactors (MBBR) are popular in many wastewater treatment processes because of their simple operation and potential efficiency, combining the advantages of both attached and suspended growth systems. MBBR treatment reactors use carrier media for the growth of biofilms on their surfaces (Biswas et al. 2014). Suitable carrier media present a high surface area per unit volume and are light-weight for buoyancy in the moving fluid flow of the reactor vessel (Ødegaard et al. 2000). Typical carrier media designs employed in biofilter reactors are often simple structures patterned along a single axis of symmetry such that they are amenable to traditional tool-and-die manufacturing processes (e.g., polymer extrusion, injection molding, etc.). Figure 1 shows several types of biofilter media that are commercially available.

Reliably high performance of these media in biofilters has been shown in many pollutant remediation applications. However, limitations in manufacturing processes place restrictions on shape diversity of the media, potentially limiting the ultimate performance gains that might be realized through novel media shapes with recursive surface area complexity for biofilm colonization. The potential exists to develop new media concepts that might stimulate novel microbial assemblages and community metabolism to yield efficiency gains in reactor performance.

The performance of a carrier media in an MBBR is typically evaluated as a function of the media's specific surface area (SSA), which is the ratio of the total surface area to the bulk volume. Media geometries that have high SSA values offer more opportunities for biofilm establishment and are generally considered to be more effective than media with lower SSA values (Guerdat et al. 2010). Other factors, such as material, surface texture (Felföldi et al. 2015), carrier orientation, pore spacing, and geometry (Herrling et al. 2015; Li et al. 2015), have been shown to impact the overall performance of MBBR systems. Young et al. (2016) concluded that high surface area to volume carriers demonstrate a high propensity for clogging due to small pore space configuration, thus reducing the effective surface area of the media and significantly lowering ammonia removal rates in nitrification reactors (Forrest 2014). Herrling et al. (2015) demonstrated that carrier geometry and orientation could dynamically alter local flow velocities in the inner face of the carrier. Odegaard et al. (2000) showed that the shape and size of the carrier do not significantly influence the water treatment process efficiency if the effective surface area is the same. However, the carrier size and surface area often dictate the maximum feed loading rate (Pfeiffer and Wills 2011). Kriklavova and Lederer (2010) proposed the use of a unique design to achieve greater surface area by attaching nano-fibers to commercial bio-carriers.

Carriers made with natural materials have been investigated for their low cost. Various carriers such as sand, gravel, peanut shells, rice husk, coconut shells, cane bagasse, and maize stubble

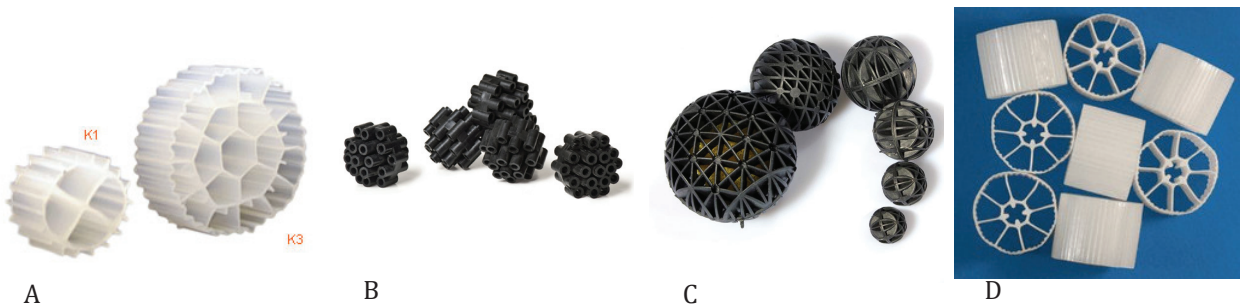

Figure 1. Commercial biofilter media: (A) K1, K3, (B) Atlantic bio-balls, (C) honeycomb bio-balls, and (D) MB3 media .

have been used as carriers in bio-filters (Ramirez-Lopez et al. 2003; Shao et al. 2009). Also, fireclay (Tilaki 2011), bamboo charcoal (Chen et al. 2012), fiber threads (Jin et al. 2012), geotextiles (Mukkulath and Thampi 2012), and peach pits (Soltani et al. 2013) have been investigated as potential carriers in bio-filters. A sample of different kinds of bio-carriers used in a MBBR, along with a brief summary of their characteristics, is given by Shrestha (2013). While these types of media are inexpensive, the variability of carrier characteristics, lack of buoyancy, unpredictability of SSA, and contamination issues stemming from the use of biodegradable materials have diverted attention towards the use of manufactured polymer carrier media to enhance the interaction between the fluid and the biofilm (Bolton et al. 2006; Martinez-Huerta et al. 2009). The patent literature also offers a wide variety of carrier media designs, with most of them aimed at increasing the SSA of the carrier element. From a geometric standpoint, most are variations of a known shape that is amenable to traditional manufacturing. Examples include cylindrical (Brockdorff 2010; Flournoy and Pehrson 2010; McKean et al. 2011), spherical (Cullimore 2013), or cuboidal prisms (Loken 2011; Dempster et al. 2012; Rusten et al. 2014a; Rusten et al. 2014b). Others offer combinations of complex shapes (Barrett 2013). Many incorporate elements such as fins, grooves, and ridges. Several of these designs were too complex for feasible manufacturing at the time of the disclosure and have remained as conceptual designs.

One unexplored yet promising avenue for development and manufacture of biofilter media is additive manufacturing, or 3D printing. Recent advances in 3D printing technologies allow for precise fabrication of complex, biomimetic shapes and topologies in plastic polymer with fidelity at the micron scale. This can be used to design and manufacture ultra-high surface area carriers with complex geometries. Microbial colonization of 3D printed materials has been demonstrated for use in phototrophic biofilm reactors (Kardel et al. 2015; Carrano et al. 2016; Blersch et al. 2017). With 3D printing, shapes might be produced that have no other method of manufacture, and with a complexity that potentially stimulates unique heterogeneous biofilm development through establishment of diverse pathways for diffusion and advective transport of dissolved constituents. For example, media designs might be developed that encourage the growth of mixed bacteria and algal biofilms, creating heterogeneous networks of autotrophic and heterotrophic metabolisms that more completely transform targeted water contaminants. Currently, the potential set of 3-dimensional geometrical patterns for biofilter media remains relatively unexplored, especially with regards to biofilm complexity and biofilter performance. The objective of this work is to challenge the predominant paradigms for microbial biofilm-based reactors by designing and producing novel high-surface area biofiltration media and demonstrate functional feasibility in a mixed-bed bioreactor for nitrogen removal.

Materials and Methods

The overall methodology involved three stages: (*i*) development of mathematical models of various complex shapes of carrier media with ultra-high surface area; (*ii*) fabrication of carrier media with a 3D printer; and (*iii*) preliminary testing and analysis of carrier media performance. In this section, each one of these stages is described.

Mathematical Modeling of Complex Carrier Media

A benchmarking survey of polymer-based biofilter media currently available on the market yields a wide array of shapes, sizes, and performance characteristics. Table 1 presents a list of commercially available products with their corresponding reported SSA values. From this selection, the carrier design with the highest SSA that is commercially available is the MB3 media (604 m^2/m^3). Another similar media shape, the Kaldnes K1, is arguably one of the most popular products due to its pricing, availability, and material (high density polypropylene) and presents a SSA of 500 m^2/m^3. It should be noted that, in many of these designs, much of the area available for biofilm establishment is on the outer perimeter surfaces of the shape, where exposure to high shear stress from local flow velocities may occur and limit biofilm attachment under certain reactor conditions.

Table 1. Polymer-based manufactured biofilter media.

Medium	Specific Surface Area (SSA) (m^2/m^3)	Sources
MB3 Media	604	Pfeiffer & Wills 2011
K1 Kaldnes Media	500	Rusten et al. 2006; Lekang & Kleppe 2000
K3 Kaldnes Media	500	Rusten et al. 2006; Lekang & Kleppe 2000
AMB Media	500	Pfeiffer & Wills 2011
Kaldnes Rings	500	Lekang & Kleppe 2000
BioBall	378	Maslon & Tomaszek 2015
K2 Kaldnes Media	350	Rusten et al. 2006
BactoBalls	300	Godoy-Olmos et al. 2016
Finturf Artificial Grass	284	Lekang & Kleppe 2000
Norton Rings	220	Lekang & Kleppe 2000
Type A Biofill	180	Godoy-Olmos et al. 2016

Modeling was performed for various geometries in an effort to develop shapes with a higher SSA than those found in commercially available products. The approach in this effort incorporated mathematical models of a gyroid, a surface based on *sine* and *cosine* functions of an infinitely connected periodic minimal surface containing no straight lines (Schoen 1970; Osserman 1986). The gyroid is the only known embedded triply periodic minimal surface with triple junctions; does not possess any reflectional symmetries (Große-Brauckmann 1997); and is biomimetic of other surface-area dependent biological processes (Deng and Mieczkowski 1998). The gyroid surface can be described with Equation 1 and further manipulated with scaling parameters.

$$\sin x * \cos y + \sin y * \cos z + \sin z * \cos x = 0 \quad \text{(Equation 1)}$$

Once fabricated, a spherical gyroid exhibits a high degree of internal channel interconnectivity that can potentially facilitate nutrient delivery to attached biofilms. The infinite gyroid function was modeled using Mathematica® software and truncated into a sphere with further mathematical manipulation. A range of options obtained through parametric manipulation is shown in Figure 2. Taking into consideration pore size and other design constraints (e.g., overall size, manufacturability, etc.), the parameters for the chosen carrier media model were determined. It has been shown that efforts to increase SSA in a constant volume might result in topologies that are prone to clogging through accumulation of biofilm thickness (Loupasaki and Diamadopoulos 2013). Clogging in the media can reduce the amount of mass transfer between the water and the biofilm, thereby reducing the efficiency of the system (Colt 2006). Clogging considerations for the spherical gyroid media design yielded estimates for the minimum hole size of a gyroid carrier of 1500 µm.

The chosen gyroid-based media design has an overall diameter of 19 mm and a wall thickness of 500 µm. The model surface area and volume were measured with Netfabb® software (Autodesk, Mill Valley, California) and the specific surface area was estimated at 1168 m^2/m^3, which represents an increase of almost 130% in SSA over the nominal specifications reported for commercial media design Kaldnes K1. Kaldnes K1 was chosen for baseline comparison in this study because of its

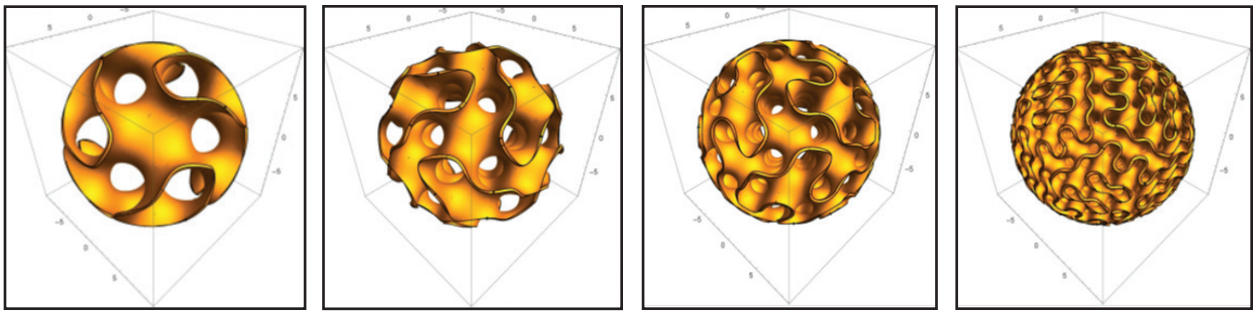

SSA= 585 m^2/m^3 SSA= 863 m^2/m^3 SSA= 1168 m^2/m^3 SSA= 2309 m^2/m^3

A B C D

Figure 2. Computer model and mathematical manipulation of a spherical gyroid.

widespread adoption and use in local fisheries. Further confirmation was pursued by performing reverse engineering of the K1 Kaldness media followed by solid modeling (Figure 3) and estimation of the surface and volume. Likely because of manufacturing variability, the bulk SSA for the actual batch of K1 Kaldness media used in this experiment was estimated at a higher SSA of 810 m^2/m^3.

As seen in Figure 2, further mathematical manipulation rendered designs with much higher SSA. However, preliminary testing showed high tendency towards rapid pore clogging in such designs, thus the choice for a gyroid design with larger pore sizes. The spherical gyroid design presented complex internal surfaces, suggesting that this media has increased regions of refugia where biofilm might be protected from fluid shear forces. It is also hypothesized that this could promote the establishment of nitrifying microbial biofilms of *Nitrosomonas* and *Nitrobacter* on the different regions of the carrier (Figure 4), thereby supporting enhanced rates of conversion of ammonia (NH_3^+) into the less toxic nitrate (NO_3^-) (Pfeifeer and Wills 2011).

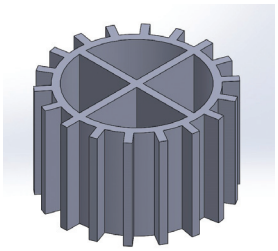

Figure 3. Reverse engineered solid model of K1 Kaldnes media.

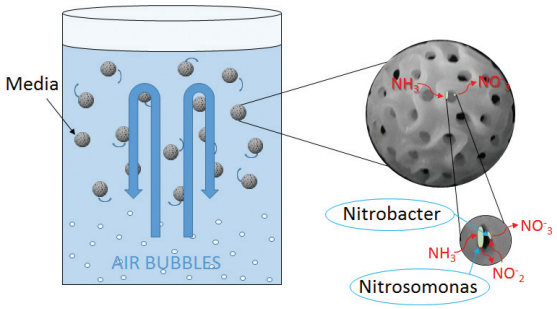

Figure 4. Mixed-bed bioreactor concept for nitrification with spherical gyroids.

Fabrication of Carriers Using 3D Printing

The media design was exported from Mathematica® software (Wolfram, Champaign, IL) into an STL file format and sent to a material jetting 3D printer (Objet30, Stratasys®, Eden Prairie, MN). Like most 3D printers, this one builds an object layer by layer, which allows for the manufacturing of complex shapes. This is especially well suited for media designs that contain complex internal channel geometries, such as the gyroid shape. The 3D printer uses a polyjet principle to deposit droplets of a liquid acrylate-based monomer resin through 200 nozzles. Once the deposition for a layer is complete, ultra-violet lamps ensure proper curing of the resin into a solid. To accommodate the build of hollow structural shapes, the printer also deposits a paraffin support material, allowing for the manufacture of holes, cavities, and channels in the media. This material

is then removed by a combination of chemical dissolution (2% NaOH solution), high-pressure water cleansing, and mechanical scraping. Figure 5 depicts the actual gyroid media fabricated with this process. A batch of 220 gyroid media carriers was fabricated for inoculation and preliminary testing.

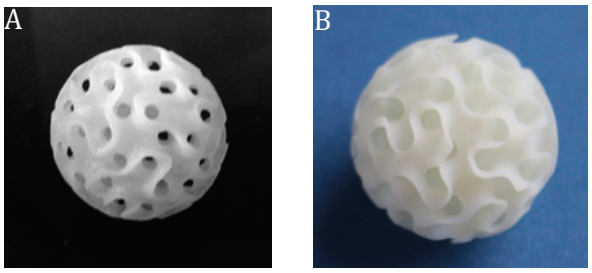

Figure 5. 3D-printed gyroid media with orientation aligned with (A) internal channels, and (B) random orientation.

Preliminary Testing and Analysis of Carrier Media Performance

Several bench-scale bioreactors were designed and constructed for testing, with scaling based on an existing system used in Auburn University's E.W. Shell North Auburn Fisheries Unit (Figure 6A). This system is a MBBR used for nitrification conversion of ammonia to nitrate in a fish aquaculture facility. Two pilot-scale bioreactors (1/10 scale by volume) were designed (Figure 6B) and constructed (Figure 6C) to implement the different test protocols. Each of the bioreactors recirculated to a 5-gallon reservoir with a 1/10 hp sump pump providing the flow. The outlet and inlet channels of the bioreactor were made of nominal ½-in PVC pipe and had valves to allow control over the volumetric flow rate into the bioreactor. Inlet flow velocities from the bottom of the bioreactor provided circulatory velocity vectors that maintained the media in suspension. Using panel-mount air flow meters, the rate of air into the

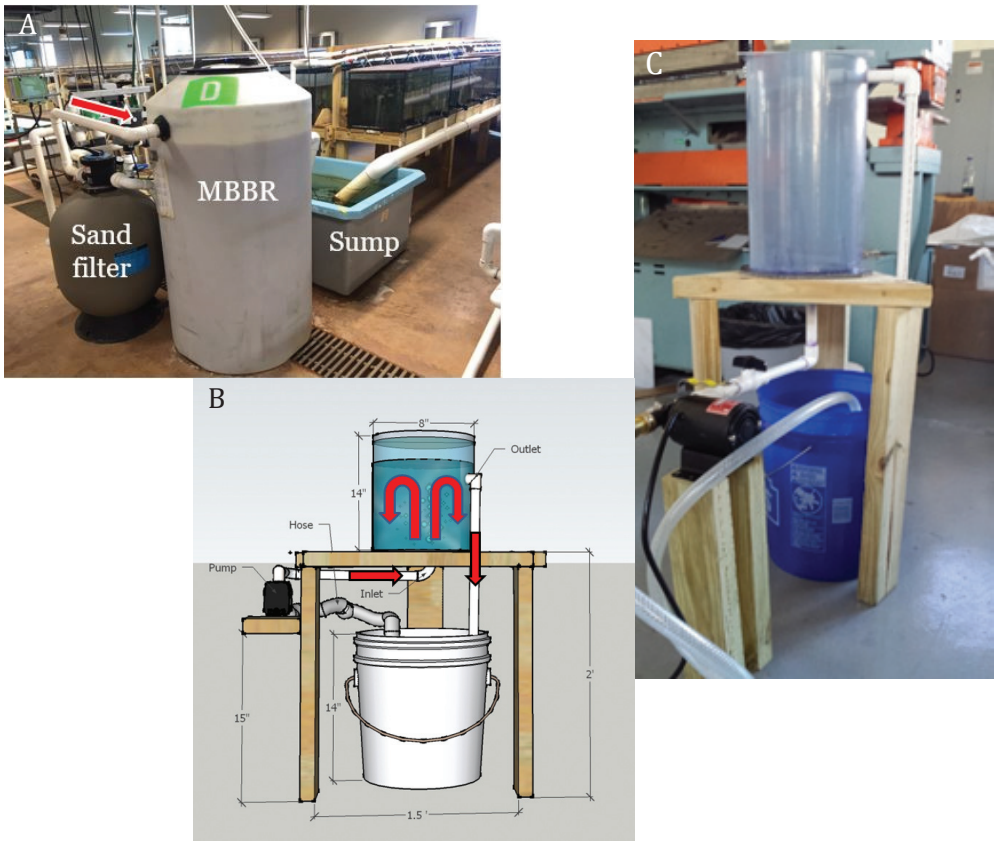

Figure 6. (A) Industrial-scale bioreactor at Auburn University North Auburn Fisheries Unit, (B) sketch of pilot-scale bioreactor for media testing, and (C) photograph of actual pilot-scale bioreactor.

bioreactor was controlled and injected to aerator stones at the bottom of the bioreactor vessel.

A series of functional tests, including tests of buoyancy, durability, and flow, were conducted with small batches of the gyroid carrier media (n<12). The buoyancy test consisted of releasing a gyroid media element at the top of a 500-mL graduated cylinder filled with water (Figure 7A), and recording the time elapsed until it reached the bottom of the water column. This was repeated 25 times and was used to calculate the sinking velocity, an important parameter for moving-bed media, as it determines the energy needed to recirculate the media. The density of each of the media was measured as well by measuring displacement of water of 20 individual elements of known dry mass placed in a graduated cylinder. The wet weight of each element was measured after removal from submergence in water and blot-drying with absorbent towels.

A durability test was conducted to determine the amount of mass, if any, lost during a 48-hour period of vigorous agitation. Ten pre-weighed media elements were placed in 400-mL of water in an Erlenmeyer flask, and agitated with compressed air at an air flow rate of 990 L/hr for 48 hours (Figure 7B). This air flow rate was selected based on the rate used in the bioreactors at the Auburn University Fisheries facility. The media elements were then air-dried for 24 hours and the final mass was recorded.

The flow test involved placing a volume of 0.6 L of gyroid carrier media in a flat plate tank that was built by inserting a sheet of Plexiglas to partition a 10-gallon fish aquarium (Figure 7C). A 1 cm OD silicon tube fitted with air holes was placed at the bottom of the tank to provide air supply. Ten gyroid carriers were marked with permanent ink of different colors so that their motion paths could be tracked through video recording. Using an air flow meter, the pressure was set to 110, 170, 220, and 280 L/hr in order to record the behavior of the media under various flow conditions. These flows were not necessarily meant to mimic the bioreactor in the field, but simply used as a standard to directly compare the media designs to one another based on movement and energy requirements. The edges of the tank were marked with a ruler, and a stopwatch was placed in the recording window so that a frame-by-frame analysis could be conducted. This helped in the determination of patterns of circulation as correlated to air flow, the energy required to adequately circulate the media, as well as the best arrangement of air flow to minimize dead zones.

After the buoyancy, durability, and flow tests were conducted, a batch of gyroid media and K1 Kaldnes was inoculated for a period of 19 days, starting on March 9, 2016 and ending on March 27, 2016. The amount of each media type used in the inoculation and experimentation process was determined by calculating the number needed to occupy 50% of the volume in the bioreactor. The inoculation process involved depositing each media batch into a 5-gallon reservoir containing three gallons of tilapia wastewater from North

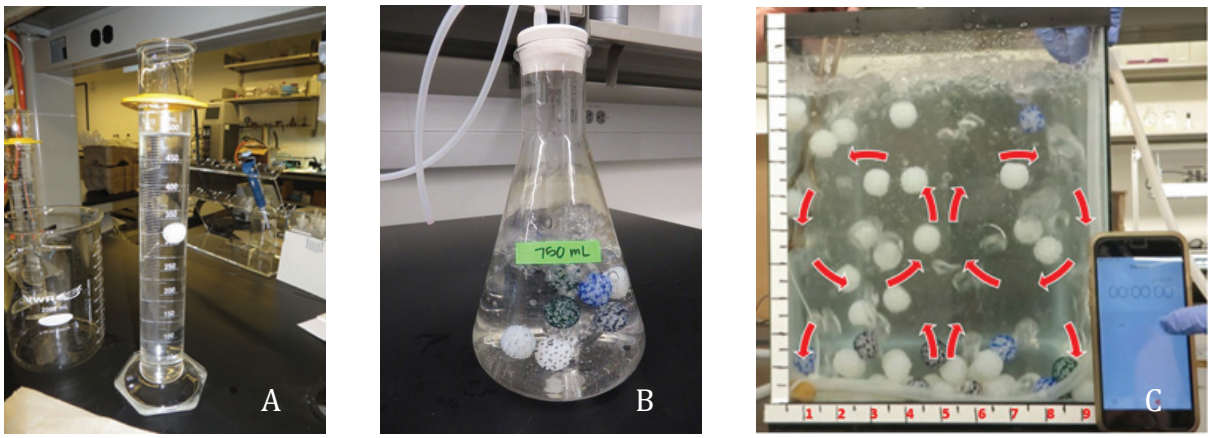

Figure 7. (A) Buoyancy test of Gyroid media, (B) Gyroid media undergoing a durability test, and (C) flow characterization test of Gyroid media.

Auburn Fisheries and keeping it constantly aerated. Each media type was inoculated with a cup (250 mL) of K1 Kaldnes covered in a biofilm of nitrifying bacteria, retrieved from the MBBR at the fisheries facility. Samples of 250 mL of water were taken daily from both reservoirs and measured for pH, temperature, and concentration (in mg/L) of ammonia, nitrite, and nitrate. The nutrient analysis was carried out using an EcoSense 9500 photometer (YSI, Yellow Springs, Ohio) and the temperature and pH were measured using a pH probe (Hanna Instruments, Limena, Italy). Every three days, 25% of the water volume was removed and replaced with fresh wastewater. The data obtained throughout this inoculation process was analyzed graphically to observe the biochemical patterns taking place. The media was deemed inoculated when the ammonia levels had decreased and the nitrate levels had increased.

Once the biofilms reached maturity, the inoculated gyroid and K1 Kaldnes media were incorporated into two separate bioreactors and were monitored during a period of two weeks. The protocol consisted of drawing water samples every six hours and testing for the presence of ammonia and nitrates using standard methods (APHA 2012). Fresh wastewater was added daily to replenish losses due to evaporation and testing, while a 25% wastewater replacement occurred every three days to ensure nutrient levels and pH remained relatively constant.

Results and Discussion

The results from the functional tests indicate that the spherical gyroid carrier, after submergence, was negatively buoyant, with a sinking velocity of 5.5 cm/s in water and a calculated buoyant force of 0.012 N. Density measures for the gyroid result in a dry specific gravity of 0.851±0.036 (n=20), and effective wet specific gravity of 1.033±0.072 (n=20), suggesting that the gyroid becomes negatively buoyant following absorption and adsorption of water. This compares to the positively-buoyant K1 Kaldnes media, found to have a specific gravity of 0.660±0.048 and 0.714±0.065 (n=20) for dry and wet conditions, respectively. Results of the durability testing show that the gyroid carrier experiences an average mass loss of 0.075% by weight over 48 hours. This corresponds to a mass loss of approximately 6.75% over the expected media life of six months in a full-scale bioreactor industry. Also, in the gyroid media design, a shear stress of 7.83 x 10^{-6} lb/ft^2 (47.9 N/m^2) at the spherical surface is estimated.

With respect to the ammonia removal test, the anticipated trends were that the NH_3 levels would decrease, while the concentration of NO_3^- would increase. The graphs below represent the average daily ammonia and nitrate time series curves for the spherical gyroid (Figure 8) and the K1 Kaldnes (Figure 9). For both media, ammonia was generally seen to decrease over time, suggesting nitrification processes were occurring. Additionally, nitrate was seen to decrease over time for both media. Nitrate removal processes are difficult to explain; the loss rate suggests possible denitrification as a removal process for the nitrate, but the high rate of aeration in the bioreactors argues against this as a possibility.

Preliminary data show that the estimated rate of NH_3 removal rates were 1.620 and 0.710 ppm/day for the spherical gyroid and the K1 Kaldnes, respectively. However, due to the difficult, lengthy processing and cost of producing 3D printed media in large batches, only a single, preliminary run was performed, thus these results are not conclusive or statistical significant. However, results do show that the 3D printed media can withstand the conditions that are prevalent in typical MBBR operations for fisheries. It also appears that the performance of the 3D printed media is at least comparable to that from the K1 Kaldnes. Although neither media reached the water quality standards required for these systems during the short nutrient testing period, given more time, it might be expected that the NH_3 and NO_3^- levels would continue to decline.

Conclusions

This preliminary work shows that complex carrier media designs can be achieved with the 3D printing technologies available today and successfully implemented in MBBR environments. Feasibility of such carrier media has been demonstrated with this effort, and features such as sheltered refugia and optimized nutrient delivery flow can be pursued in future work. Also, the

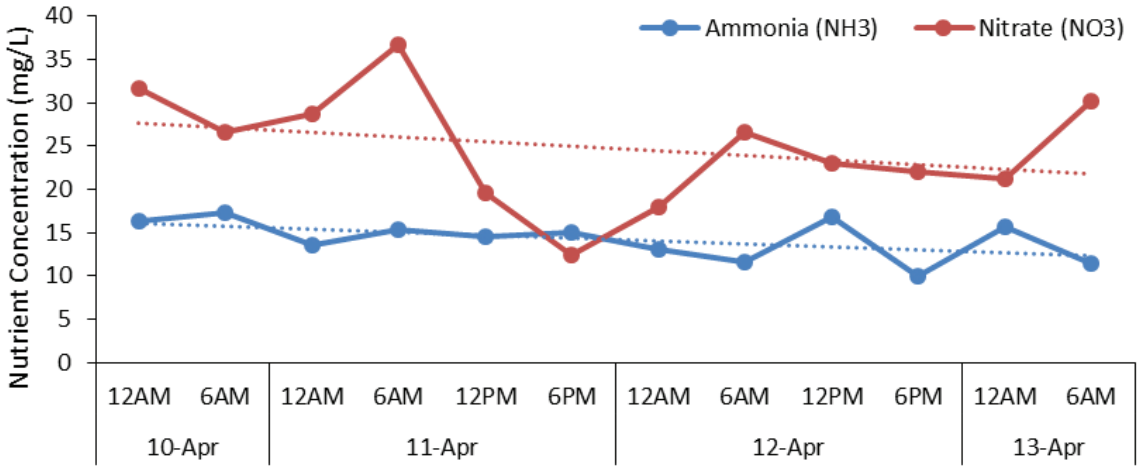

Figure 8. Ammonia and nitrate concentration time series for the bioreactor using gyroid media.

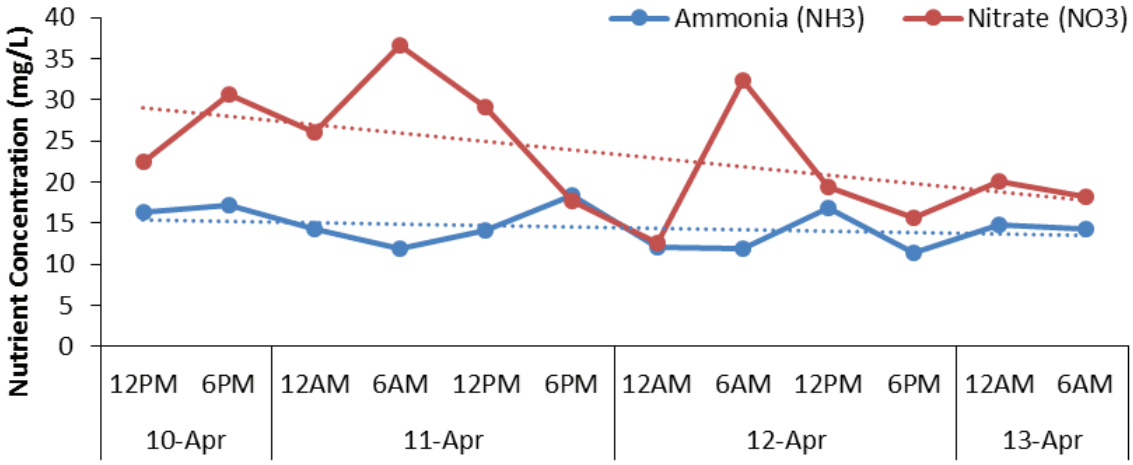

Figure 9. Ammonia and nitrate concentration time series for the bioreactor using K1 Kaldnes media.

approaches with 3D printing can push the frontier on specific surface area limitations. The pursuit of custom topologies that create unique flow pathways through internal features, minimizing sloughing while creating "dead zones" ideal for anaerobic bacteria growth, is now within reach. It is expected that design of heterogeneous flow environments in the media can result in heterogeneous microbial metabolism that can yield increased performance of media-based bioreactors (for example, media design for combined nitrification-denitrification processes). The cost of the 3D production process currently prevents large-scale commercial implementation of the new media designs, but prototyping next generation carrier designs for specialty applications such as high-efficiency wastewater treatment in remote locations or extreme environments can be addressed. There is little doubt that 3D printing will be instrumental in the design of next generation biofilter media.

Undergraduate Education Component

The work presented in this paper was conducted as part of a Phase I award from the Environmental Protection Agency's P3 student design competition (EPA 2016). This program funds student teams to develop solutions to challenges that include a wide range of categories: water, energy, agriculture,

built environment, materials, and chemicals. As a requirement of this program, the student team presented their research at the 2016 National Sustainable Design Expo in Washington D.C. From a curricular standpoint, this work was carried out during the 2015 spring semester and within the Senior Design courses in two departments at Auburn University: Biosystems Engineering and Industrial & Systems Engineering. The team was composed of seven undergraduate students at the senior level and four graduate students. The students relied on each other's expertise to address the multidisciplinary challenge of this project and educated their counterparts in the aspects of the project that were discipline specific. The senior design course constitutes the capstone experience in each of the engineering disciplines at Auburn University and enforces a rigorous engineering design process throughout the semester. This experience emphasizes competencies in areas essential for contemporary new product and process development: multidisciplinary teamwork, technical communication, and the consideration of multidisciplinary design constraints, among others. Other important skills, such as problem solving and awareness of contemporary issues, are imparted through seminars and guest speakers throughout the semester. This project was selected from among 45 entries for Phase II funding for the period 2017-2019 by the Environmental Protection Agency.

Author Bio and Contact Information

Olivia Elliott received a B.S. degree in Biosystems Engineering in May 2016 from Auburn University in Alabama. She is a member of the American Society of Agricultural and Biological Engineering (ASABE). She may be contacted at obe0001@auburn.edu.

Stephanie Gray graduated from Auburn University in 2016 with a degree in Industrial and Systems Engineering. She currently lives in South Carolina and works as an Industrial Engineer for The Boeing Company. As a founding member of Alpha Omega Epsilon, an engineering and technical science sorority, she was heavily involved with it during her college career. She may be contacted at spg0009@auburn.edu.

Michael McClay received a B.S. degree in Industrial and Systems Engineering from Auburn University (Main Campus) in 2016. He is working towards a M.S. degree in Industrial and Systems Engineering, also at Auburn University. He is currently the treasurer for the Industrial Engineering Honor Society ΑΠΜ. His main areas of interest include Lean Manufacturing and Technologies, Stochastic Modeling, and Linear Programming. He may be contacted at mjm0040@auburn.edu.

Bakr Nassief received a B.S. degree in Industrial and Systems Engineering in 2016 from Auburn University in Auburn, Alabama. He plans on enrolling in graduate school in fall 2017 and continue his research in additive manufacturing applications in biosystems engineering. He may be contacted at ban0006@auburn.edu.

Ann Nunnelley graduated from Auburn University with a Bachelors of Biosystems Engineering in 2016. She currently works as an Assistant Engineer in the Water Resource Practice Group at Hazen and Sawyer in Atlanta, GA. She is a member of the American Society of Agricultural and Biological Engineers (ASABE) and the Georgia Association of Water Professionals (GAWP). She may be contacted at agn0005@auburn.edu.

Eric Vogt received a B.S. degree in Biosystems Engineering in 2016 from Auburn University in Alabama. He is a member of the American Society of Agricultural and Biological Engineers (ASABE). He may be contacted at edv0002@auburn.edu.

Joseph Ekong received his M.Sc. Degree in Industrial and Systems Engineering from Georgia Institute of Technology. He is currently working towards his Ph.D. in Industrial and Systems Engineering at Auburn University. His research interests include biomaterials engineering, additive manufacturing and production systems. He is a member of the Institute of Industrial Engineers (IIE) and the Institute for Operations Research and the Management Sciences (INFORMS). He may be contacted at jje0003@auburn.edu.

Kamran Kardel received a B.S. degree in Industrial Engineering in 2003 from Iran University of Science and Technology and a M.S. degree in Economic Systems Engineering from Mazandaran University of Science and Technology in 2008. He also received a Masters degree and a Ph.D in Industrial and Systems Engineering from Auburn University in 2013 and 2016, respectively. Dr. Kardel is a member of the Institute of Industrial and Systems Engineering (IISE) and Society of Manufacturing Engineering (SME). He may be contacted at kkardel@georgiasouthern.edu.

Ali Khoshkhoo received a B.S. degree in Industrial and Systems Engineering in 2011 from University of Tehran and a M.S. degree in Industrial and

Manufacturing Systems from University of Missouri-Columbia in 2013. He is currently working towards his Ph.D. in Industrial and Systems Engineering at Auburn University. His research interests include Additive Manufacturing (AM), manufacturing systems, tribology, surface metrology, and production systems. He may be contacted at azk0057@auburn.edu.

Gabriel Proaño received a B.S. degree in Electronics and Telecommunications and a M.S. degree in Physics in Ecuador from Escuela Superior Politecnica del Litoral (ESPOL) in 2007 and 2013, respectively. He currently is a sponsored scholar from the Ecuadorian government pursuing a Ph.D. in Industrial and Systems Engineering at Auburn University. His research interests include automated bioreactors design and fuzzy modeling on environmental applications. He may be contacted at gzp0009@auburn.edu.

David M. Blersch is Assistant Professor of Ecological Engineering in the Biosystems Engineering Department at Auburn University. He received his Master of Science and Ph.D. degrees in Bioresources Engineering from the University of Maryland in College Park, Maryland in 2004 and 2010, respectively. Dr. Blersch directs the Algae Systems and Ecological Engineering Laboratory in Biosystems Engineering, and with Dr. Carrano co-directs the 3D-Printed Biosurfaces Laboratory at Auburn University. He may be contacted at dmb0040@auburn.edu.

Andres L. Carrano is the Philpott WestPoint Stevens Associate Professor in the Department of Industrial and Systems Engineering at Auburn University. Previously, he served on the faculty of the Kate Gleason College of Engineering at the Rochester Institute of Technology, in New York. He received his Master of Science and Ph.D. degrees from North Carolina State University in 1997 and 2000, respectively. Along with Dr. Blersch, he co-directs the 3D-Printed Biosurfaces Laboratory in Auburn's Research Park. He may be contacted at carrano@auburn.edu or at 3301 Shelby Engineering Center, Department of Industrial and Systems Engineering, Auburn University, Auburn, Alabama 36849.

Acknowledgements

This work was supported by the U.S. Environmental Protection Agency Grant Number SU836122. Any opinions, findings, and conclusions or recommendations expressed in this material are those of the authors and do not necessarily reflect the views of the EPA. The majority of this work was conducted by a team of undergraduate students under the auspices of the senior design courses in the Departments of Industrial and Systems Engineering as well as Biosystems Engineering at Auburn University. The support and valuable feedback from Karen Veverica (Director, E.W. Shell Fisheries Research Center), Steven Taylor, Jorge Valenzuela, Jeremiah Davis, and Mark Dougherty is also acknowledged.

References

American Public Health Association (APHA). 2012. Standard Methods for the Examination of Water and Wastewater. Washington D.C., USA. Available at: https://www.standardmethods.org/. Accessed February 28, 2017.

Barrett, M. 2013. Biomedia. U.S. Patent No: D0696744 S1.

Biswas, K., M.W. Taylor, and S.J. Turner. 2014. Successional development of biofilms in moving bed biofilm reactor (MBBR) systems treating municipal wastewater. *Applied Microbiology and Biotechnology* 98: 1429-1440.

Blersch, D.M., K. Kardel, A.L. Carrano, and K. Kaur. 2017. Customized 3D-printed surface topography governs species attachment preferences in a fresh water periphyton community. *Algal Research* 21: 52-57.

Bolton, J., A. Tummala, C. Kapadia, M. Dandamudi, and J.M. Belovich. 2006. Procedure to quantify biofilm activity on carriers used in wastewater treatment systems. *Journal of Environmental Engineering* 132: 1422-1430.

Brockdorff, K.P. 2010. Bacterial carrier for water purification. U.S. Patent No: D612,007S.

Carrano, A.L., D.M. Blersch, K. Kardel, and A. Khoshkhoo. 2016. Understanding attachment preferences of benthic algae through controlled surface topographies on 3D printed substrata. In: *5th International Conference on Surface Metrology (ICSM 2016).* April 4-7, 2016. Poznan, Poland.

Chen, C.J., X.X. Huang, C.X. Lei, W.J. Zhu, Y.X. Chen, and W.X. Wu. 2012. Improving anammox start-up with bamboo charcoal. *Chemosphere* 89: 1224-1229.

Colt, J. 2006. Water quality requirements for reuse systems. *Aquacultural Engineering* (34)3: 143-156.

Cullimore, D.R. 2013. Floating microbiological growth ball. U.S. Patent No: D687,512S.

Dempster, G., G. Seidl, S. Angappan, and J.C. Gardiner. 2012. Moving bed bioreactor carrier. U.S. Patent No: D661778.

Deng, Y. and M. Mieczkowski. 1998. Three-dimensional periodic cubic membrane structure in the mitochondria of amoebae *Chaos carolinensis*. *Protoplasma* 203(1-2): 16-25.

Environmental Protection Agency (EPA). 2016. People, prosperity and the planet (P3) student design competition. Available at: http://www.epa.gov/P3. Accessed March 1, 2017.

Felföldi, T., L. Jurecska, B. Vajna, K. Barkács, J. Makk, G. Cebe, A. Szabó, G. Záray, and K. Márialigeti. 2015. Texture and type of polymer fiber carrier determine bacterial colonization and biofilm properties in wastewater treatment. *Chemical Engineering Journal* 264: 824-834.

Flournoy, W.J. and R.L. Pehrson. 2010. Extruded media for supporting growth biology within a wastewater treating system. U.S. Patent No: D618760 S1.

Forrest, D. 2014. Tertiary nitrifying moving bed-biofilm reactor: A study of carrier and loading effects on nitrifying kinetics, biologically produced solids and microbial community. Dissertation, University of Ottawa, Ottawa, Canada.

Godoy-Olmos, S., S. Martínez-Llorens, A. Tomás-Vidal, and M. Jover-Cerdá. 2016. Influence of filter medium type, temperature and ammonia production on nitrifying trickling filters performance. *Journal of Environmental Chemical Engineering* 4(1): 328-340.

Große-Brauckmann, K. 1997. Gyroids of constant mean curvature. *Experimental Mathematics* 6: 33-50.

Guerdat, T.C., T.M. Losordo, J.J. Classen, J.A. Osborne, and D.P. DeLong. 2010. An evaluation of commercially available biological filters for recirculating aquaculture systems. *Aquacultural Engineering* 42: 38-49.

Herrling, M.P., G. Guthausen, M. Wagner, S. Lackner, and H. Horn. 2015. Determining the flow regime in a biofilm carrier by means of magnetic resonance imaging. *Biotechnology and Bioengineering* 112: 1023-1032.

Jin, Y., D. Ding, C. Feng, S. Tong, T. Suemura, and F. Zhang. 2012. Performance of sequencing batch biofilm reactors with different control systems in treating synthetic municipal wastewater. *Bioresource Technology* 104: 12-18.

Kardel, K., A.L. Carrano, D.M. Blersch, and M. Kaur. 2015. Preliminary development of 3D-printed custom substrata for benthic algal biofilms. *3D Printing and Additive Manufacturing* 2: 12-19.

Kriklavova, L. and T. Lederer. 2010. The use of nanofiber carriers in biofilm reactor for the treatment of industrial wastewaters. *In: Nanocon.* October 12-14, 2010. Olomouc, Czech Republic.

Lekang, O.-I. and H. Kleppe. 2000. Efficiency of nitrification in trickling filters using different filter media. *Aquacultural Engineering* 21(3): 181-199.

Li, C., M. Wagner, S. Lackner, and H. Horn. 2015. Assessing the influence of biofilm surface roughness on mass transfer by combining optical coherence tomography and two-dimensional modeling. *Biotechnology and Bioengineering* 113(5): 989-1000.

Loken, S. 2011. Moving bed bioreactor carrier. U.S. Patent No: D645161.

Loupasaki, E. and E. Diamadopoulos. 2013. Attached growth systems for wastewater treatment in small and rural communities: A review. *Journal of Chemical Technology and Biotechnology* 88(2): 190-204.

Martinez-Huerta, G., B. Prendes-Gero, F. Ortega-Fernandez, and J.M. Mesa-Fernandez. 2009. Design of a carrier for wastewater treatment using moving bed bioreactor. In: *Proceedings of the 2nd International Conference on Environmental and Geological Science and Engineering (EG'09)*. ISBN: 978-960-474-119-9.

Masłoń, A. and J.A. Tomaszek. 2015. A study on the use of the BioBall® as a biofilm carrier in a sequencing batch reactor. *Bioresource Technology* 196: 577-585.

McKean, C., T. Schwingle, and M.C. Whittier. 2011. Moving bed biofilm reactor media. U.S. Patent No: D645,116.

Mendoza-Espinosa, L. and T. Stephenson. 1999. A review of biological aerated filters (BAFs) for wastewater treatment. *Environmental Engineering Science* 16(3): 201-216.

Mukkulath, G. and S.G. Thampi. 2012. Performance of coir geotextiles as attached media in biofilters for nutrient removal. *International Journal of Environmental Sciences* 3(2): 784-794.

National Resources Defense Council (NRDC). 2014. Available at: https://www.nrdc.org/. Accessed March 2, 2017.

Ødegaard, H., B. Gisvold, and J. Strickland. 2000. The influence of carrier size and shape in the moving bed biofilm process. *Water Science and Technology* 41: 383-391.

Osserman, R. 1986. *Frontispiece to a Survey of Minimal Surfaces*. New York, Dover.

Pfeiffer, T.J. and P.S. Wills. 2011. Evaluation of three types of structured floating plastic media in moving

bed biofilters for total ammonia nitrogen removal in a low salinity hatchery recirculating aquaculture system. *Aquacultural Engineering* 45: 51-59.

Ramırez-López, E., J. Corona-Hernández, L. Dendooven, P. Rangel, and F. Thalasso. 2003. Characterization of five agricultural by-products as potential biofilter carriers. *Bioresource Technology* 88: 259-263.

Rusten, B., E. Bjørnar, Y. Ulgenes, and E. Lygren. 2006. Design and operations of the Kaldnes moving bed biofilm reactors. *Aquacultural Engineering* 34(3): 322-331.

Rusten, B., J.G. Siljudalen, T. Andersen, S. Smith, and L. Marcolini. 2014a. Grate. U.S. Patent No: D697,168.

Rusten, B., J.G. Siljudalen, T. Andersen, S. Smith, and L. Marcolini. 2014b. Biofilm media. U.S. Patent No: D697169 S1.

Schoen, A.H. 1970. Infinite Periodic Minimal Surfaces without Self-Intersections. NASA Technical Note No. D-5541. Washington D.C.

Shao, L., Z. Xu, W. Jin, and H. Yin. 2009. Rice husk as carbon source and biofilm carrier for water denitrification. *Polish Journal of Environmental Studies* 18: 693-699.

Shrestha, A. 2013. Specific moving bed biofilm reactor in nutrient removal from municipal wastewater. Master Thesis, University of Technology, Sydney, Australia.

Soltani, R., A. Rezaee, H. Godini, A. Khataee, and S. Jorfi. 2013. Organic matter removal under high loads in a fixed-bed sequencing batch reactor with peach pit as carrier. *Environmental Progress & Sustainable Energy* 32: 681-687.

Tilaki, R.A.D. 2011. A study on using fireclay as a biomass carrier in an activated sludge system. *Journal of Industrial Microbiology and Biotechnology* 38: 209-213.

UNICEF/World Health Organization (WHO). 2009. *Diarrhoea: Why Children are Still Dying and What Can Be Done*. Available at : http://whqlibdoc.who.int/publications/2009/9789241598415_eng.pdf. Accessed March 2, 2017.

World Health Organization (WHO). 2012. Millennium Development Goal Drinking Water Target Met. Available at: http://www.who.int/mediacentre/news/releases/2012/drinking_water_20120306/en/. Accessed March 2, 2017.

WHO/UNICEF Joint Monitoring Programme (JMP) for Water Supply and Sanitation. 2010. Progress on sanitation and drinking-water, 2010 update. Available at: http://www.unicef.org/media/files/JMP-2010Final.pdf. Accessed March 2, 2017.

Young, B., B. Banihashemi, D. Forrest, K. Kennedy, A. Stintzi, and R. Delatolla. 2016. Meso and micro-scale response of post carbon removal nitrifying MBBR biofilm across carrier type and loading. *Water Research* 91: 235-243.

UCOWR
UNIVERSITIES COUNCIL ON WATER RESOURCES

Register Now!

NIWR
The National Institutes for Water Resources

2017 UCOWR/NIWR Annual Conference
Water in a Changing Environment
Fort Collins, CO

June 13-15, 2017
Colorado State University campus



Register at http://ucowr.org/conferences/registration-2017.
Early-bird registration deadline is May 19, 2017.

Gaps in projected water supply and demand, water quality and reuse issues, increased food and energy needs, and a changing climate bring water resources to center stage, not only in the Western U.S., but across the continent and around the world. Please join the dialogue as we seek to develop transdisciplinary and disciplinary solutions to complex water problems and explore bridges between science and policy.

For upcoming details:
Check our website (www.ucowr.org) and like us on Facebook (facebook.com/ucowr).

Contents

The Importance of Scientific Publishing: Teaching an Undergraduate How to Swim the Entire Length of the Pool
Garey A. Fox, Emma L. Kuster, and Amanda K. Fox 1

The Cost of Stability: Consumption-Based Fixed Rate Billing for Water Utilities
Amy Schmidt and Lynne Lewis 5

Assessing Models of Arsenic Occurrence in Drinking Water from Bedrock Aquifers in New Hampshire
Caroline M. Andy, Maria Florencia Fahnestock, Melissa A. Lombard, Laura Hayes, Julia G. Bryce, and Joseph D. Ayotte 25

Searching for Antibiotic Resistance Genes in a Pristine Arctic Wetland
Krystalle S. Diaz, Virginia I. Rich, Jean E. McLain 42

Assessing Biomineral Formation by Iron-oxidizing Bacteria in a Circumneutral Creek
Nohemi Almaraz, Andrew H. Whitaker, Megan Y. Andrews, and Owen W. Duckworth 60

Anthropogenic Litter Abundance and Accumulation Rates Point to Seasonal Litter Sources on a Great Lakes Beach
Anna E.S. Vincent and Timothy J. Hoellein 72

A Method for Assessing Shoreline Stability of Alpine Lake, West Virginia
Carolina Rando, Leslie Hopkinson, Melissa O'Neal, and Jason Fillhart 85

Reduced Phytoplankton and Zooplankton Diversity Associated with Increased Cyanobacteria in Lake Champlain, USA
Katelyn A. Bockwoldt, Emily R. Nodine, Timothy B. Mihuc, Angela D. Shambaugh, and Jason D. Stockwell 100

Erodibility Parameters Derived from Jet and Flume Erosion Tests on Root-Permeated Soils
Bailey McNichol, Kayla Kassa, Garey Fox, Ron Miller, and Lucie Guertault 119

2D-Fe_3O_4 Nanosheets for Effective Arsenic Removal
Hongxi Luo, Fangwei Cheng, Weiming Hu, Jinpeng Wang, Shuting Xiang, and Maria Fidalgo de Cortalezzi 132

Design and Manufacturing of High Surface Area 3D-Printed Media for Moving Bed Bioreactors for Wastewater Treatment
Olivia Elliott, Stephanie Gray, Michael McClay, Bakr Nassief, Ann Nunnelley, Eric Vogt, Joseph Ekong, Kamran Kardel, Ali Khoshkhoo, Gabriel Proaño, David M. Blersch, and Andres L. Carrano 144



2017 UCOWR / NIWR Annual Conference
Water in a Changing Environment
Colorado State University
Fort Collins, CO
June 13-15, 2017

UCOWR
UNIVERSITIES COUNCIL ON WATER RESOURCES

Universities Council on Water Resources
Mail Code 4526
Southern Illinois University Carbondale
1231 Lincoln Drive
Carbondale, IL 62901
www.ucowr.org